MODELLING OF UNBAFFLED LONG ENCLOSURES FOR NOISE CONTROL

YANG WEIPING

PhD

The Hong Kong Polytechnic University

2021

The Hong Kong Polytechnic University

Department of Mechanical Engineering

Modelling of Unbaffled Long Enclosures for Noise Control

Yang Weiping

A thesis submitted in partial fulfillment of the requirements for the degree of Doctor of Philosophy

June, 2021

CERTIFICATE OF ORIGINALITY

I hereby declare that this thesis is my own work and that, to the best of my knowledge and belief, it reproduces no material previously published or written, nor material that has been accepted for the award of any other degree or diploma, except where due acknowledgement has been made in the text.

________________________________ (Signed)

YANG Weiping (Name of student)

Department of Mechanical Engineering

The Hong Kong Polytechnic University

Hong Kong, China

June, 2021

ABSTRACT

Unbaffled long enclosures can be widely observed in practice, such as ventilation systems, traffic tunnels, and railway stations. These facilities bring people convenience however also cause noise pollution. Sound waves inside a long space do not dissipate but rather reverberate if they are not properly treated. Excessive exposure to such noisy acoustical environments exerts adverse effects on people's physical and psychological health. Besides, the sound radiated from the openings of long enclosures also produce noise pollution to the surroundings. To predict and reduce the radiated noise, the sound pressure fields of unbaffled long enclosures are investigated, according to which, noise attenuation strategies are proposed.

A theoretical model is first formulated based on the Wiener-Hopf (W-H) technique in conjunction with the mode-matching method to predict the sound radiated from an unbaffled long enclosure. The geometrical configuration represents a practical scenario in which noise is produced inside the long enclosure and radiates to the outside through the opening. The sound field inside the long enclosure is expressed in terms of the superposition of acoustical modes, while the radiated sound field is described by a far-field directivity pattern that can calculate large acoustic domains effectively. The detailed implementation procedures of the model are introduced and the physics behind the sound radiation phenomenon is explored. The modelling procedures using the W-H technique build a theoretical foundation for problems regarding sound radiation from unbaffled long enclosures.

For the purpose of predicting and attenuating the noise radiated from sound-proof tunnels, a theoretical model is proposed applying the W-H technique. Both the ground and impedance boundary conditions are taken into consideration. As a result, the sound distribution in the current configuration is totally different from that of the rigid long

enclosure without the ground. Owing to the ground reflections, more directivity lobes appear outside the long enclosure. Besides, from the investigations on the impedance boundary conditions, the inner wall of the long enclosure is the most effective location to mount noise control devices. Subsequently, a partial lining is employed to abate the radiated noise. The results demonstrate that SPLs inside and outside the unbaffled long enclosure are significantly decreased.

Aiming at suppressing the peaks in the SPL spectra of the sound fields, Helmholtz resonators (HRs) are proposed to reduce the modal responses inside the long enclosure so that the radiated SPL field around the targeted frequencies are suppressed. A hybrid method based on the finite element method (FEM) and the W-H technique is established for the purpose of dealing with discrete noise control devices mounting on the enclosure wall. The mechanisms of using HRs to suppress the SPL peaks are then explored using the hybrid method. In addition, the interaction between the HRs and the acoustical field inside the long enclosure is investigated. The HR locations, optimized to achieve a high sound reduction, are obtained. Numerical results demonstrate that noise reduction can be achieved inside and outside the long enclosure around the targeted frequencies with an appropriate number and locations of HRs.

To attenuate the higher-order acoustical modes inside an unbaffled long enclosure and achieve a broadband sound absorption performance, A Z-shaped micro-perforated panel absorber (ZMPPA) is proposed. To calculate the sound absorption coefficient of a ZMPPA under an oblique plane-wave incidence, an FEM-based numerical method is established. The acoustical performance of a ZMPPA is compared with that of flat and corrugated MPPAs. Numerical results demonstrate that the ZMPPA outperforms the others, especially at the first dip and middle-frequency range of the sound absorption coefficient curve. Parametric studies are carried out to study the effects of corrugation depth, offset distance, and the incident angle on the sound absorption performance of the ZMPPA. Besides, a liner consisting of an array of ZMPPAs is employed to reduce the noise radiated from an unbaffled long enclosure including the ground. Satisfactory insertion loss is obtained.

In addition to theoretical formulas, FEM-based simulation results are presented to validate the proposed models. Indoor and outdoor experiments are also implemented to figure out the spectrum characteristics of environmental noise. Furthermore, a scaled-down quasi-two-dimensional test rig is developed. The theoretical models are verified and the sound attenuation performance of HRs and ZMPPAs are investigated using the experimental results.

PUBLICATIONS ARISING FROM THE THESIS

Journal papers:

Yang, W. P., Wang, Z. B., & Choy, Y. S. (2021). "Prediction of sound radiation from an unbaffled long enclosure with the ground," *Mechanical Systems and Signal Processing*, 149, 107232.

Yang, W. P., Choy, Y. S., Wang, Z. B., & Li, Y. (2022). "Sound radiation and suppression of an unbaffled long enclosure using Helmholtz resonators," *Mechanical Systems and Signal Processing*, 165, 108408.

Conference papers:

Yang, W. P., & Choy, Y. S. (2019). "Theoretical model for the prediction of sound radiated from unbaffled long enclosure with the ground effect," In: *23rd International Congress on Acoustics*, Aachen, Germany.

Yang, W. P., & Choy, Y. S. (2020). "Analytical and numerical investigations of sound radiation from traffic tunnels," In: *INTER-NOISE and NOISE-CON Congress and Conference Proceedings*, Seoul, Korea.

Wang, Z. B., **Yang, W. P.**, & Choy, Y. S. (2020). "Meta-surface by multiple perforated panels in a coiled arrangement," In: *INTER-NOISE and NOISE-CON Congress and Conference Proceedings*, Seoul, Korea.

Choy, Y. S., Wang, Z. B., & **Yang, W. P.** (2021). “Noise reduction of Parallel barrier integrated with compact flexible panel device,” In: *INTER-NOISE and NOISE-CON Congress and Conference Proceedings*, Washington, D.C., USA.

ACKNOWLEDGEMENTS

I would like to express my sincere gratitude to my chief supervisor, Dr. ***Yatsze Choy****, for her inspiring ideas and professional guidance throughout the whole period of my study. Over the past four years, she has given me lots of encouragement and support to accomplish my study. I also wish to thank my co-supervisor Dr.* ***Jie Zhu*** *who gives me inspirations and insightful advice.*

Special thanks go to my colleagues, Dr. ***Yankei Chiang****, Dr.* ***Zhibo Wang****, Dr.* ***Long Cheng****, Dr.* ***Long Wei****, and Mr.* ***Ying Li*** *for their kind assistance and comments during my study. I also want to thank the generous help from the technicians in the department.*

Last but most importantly, I would like to deeply thank my parents and family for their love, care, and encouragement. I am particularly grateful to my wife, Mrs. Zhang, who supports me all the time. It is really challenging to maintain a long-distance relationship. Thanks for her patience and understanding. Without her, this thesis cannot be finished. Thank her for giving birth to a beautiful daughter, Amy. I will sacrifice everything to love you both in the rest of my life.

NOMENCLATURE

Symbol	Description
$A(\alpha)$	Spectral coefficient in the complex α-plane
$B(\alpha)$	Spectral coefficient in the complex α-plane
b_j	Modal response coefficients
$\mathbf{B}$	Matrix form of the modal response coefficients
$C(\alpha)$	Spectral coefficient in the complex α-plane
c_0	Sound speed in the air
C_d	Diffraction coefficient
c_j	Modal response coefficient
$C = 0.57721...$	Euler's constant
$C_{\pm}$	Cut lines in the complex α-plane
$\mathbf{C}$	Matrix form of the modal response coefficients
d	Derivative
d_{MPP}	Hole diameter of an MPP
d_j	Modal response coefficient
D	Cavity depth of an MPPA
$D(\alpha)$	Spectral coefficient in the complex α-plane
$\mathbf{D}$	Matrix form of the modal response coefficients
e	Even index
$f(y)$	Sound pressure gradient at the opening

f_m	Modal response coefficients of pressure gradient
F	Matrix form of modal response coefficients
$g(y)$	Sound pressure at the opening
g_m	Modal response coefficients of pressure
G	Green's function
G	Matrix form of modal response coefficient
h	Height of the unbaffled long enclosure
H	Corrugation depth
H	Matrix form of coefficient
i	Imaginary variable
j	Subscription index
J	Matrix form of coefficient
k	The wavenumber in the free space
k_1	Real part of wavenumber in the free space
k_2	Imaginary part of wavenumber in the free space
K	Matrix form of coefficient
l	Distance from the edge to the receiver in the shadow zone
$L(\alpha), L^{+}(\alpha), L^{-}(\alpha)$	Kernel function and its factorized forms
L_p	Length of the partial lining
L_R	The sound pressure level at the receiver
L_W	The sound power level at the source
L	Matrix form of coefficient
m	Subscription index

$\mathbf{M}$	Matrix form of coefficient
M_{π}	Maliuzhinets function
n	Normal direction, subscription index
$N(\alpha), N^{+}(\alpha), N^{-}(\alpha)$	Kernel function and its factorized forms
o	Odd index
O	Offset distance
p_A, p_B, p_C, p_D	Sound pressure in regions A, B, C, and D
P_A, P_B, P_C, P_D	Transformed sound pressure in regions A, B, C, and D
$P_A^{+}, P_B^{+}, P_C^{+}, P_D^{+}$	Factorized sound pressure in the spectral domain
$P_A^{-}, P_B^{-}, P_C^{-}, P_D^{-}$	Factorized sound pressure in the spectral domain
$\dot{P}_A^{+},\ \dot{P}_D^{+}$	Unknowns in the Wiener-Hopf equation
p_i	Incident sound pressure field in the GTD
p_d	Diffracted sound pressure field in the GTD
p_{cavity}	Sound pressure field inside the cavity
p_{duct}	Sound pressure field inside the duct
$p_{incident}$	Incident sound pressure field
p_{MPP}	Perforation ratio of an MPP
$p_{reflected}$	Reflected sound pressure field
p_{total}	Total sound pressure field
$\mathbf{P}$	Matrix form of coefficient
P_{mn}	Sound pressure of (m, n) image source
Q_{mn}	The combined complex wave reflection coefficient

Q_n	Volume velocity strength of the n-th point source
r	Observation radius
$(ro\theta)$	The polar coordinate system
R	Receiver point, distance from the source to receiver
$R^+(\alpha)$	An unknown in the Wiener-Hopf equation
S_n	The n-th monopole point source
$\mathbf{S}$	Matrix form of coefficient
t	Time
t_{MPP}	Thickness of an MPP
$\mathbf{T}$	Transfer function of the quasi-2D test rig
$\mathbf{U}$	Matrix form of coefficient
v_n	Normal particle velocity at the opening
$\mathbf{V}$	Matrix of particle velocity along the enclosure opening
$w = \mu + i\nu$	Complex w-plane
w_s	The saddle point
W	Width of the cavity
$W(\alpha)$	Characteristic function
x_n	Abscissa coordinate of the n-th monopole point source
(xoy)	The Cartesian coordinate system
$\mathbf{X}$	Matrix of unit signal
y_n	Ordinate coordinate of the n-th monopole point source
Y_j^B, Y_m^C	Modal functions in sub-regions B and C.

$\mathbf{Y}$	Matrix form of coefficient, collected signal
Z_{MPP}	Acoustical impedance of an MPP
Z_p	Acoustical impedance of the partial lining
$Z_z, z = 1, 2, 3, 4.$	Acoustical impedance on different boundaries
$\alpha = \sigma + i\tau$	Complex α-plane
α_θ	Oblique sound absorption coefficient
α_r	Random sound absorption coefficient
α_m	Wavenumbers in the horizontal direction
β_j	Wavenumbers in the horizontal direction
η_j	Wavenumbers in the transversal direction
φ	Incident angle in the GTD
$\mu = 1.84\times10^{-5}$	Coefficient of kinematic viscosity
ς	Integration variable
χ, χ^+, χ^-	Kernel function and its factorized forms
$\kappa(\alpha), \kappa^+(\alpha), \kappa^-(\alpha)$	Kernel function and its factorized forms
ω	Radian frequency
θ	Observation angle, incident angle
θ_l	Local incident angle on MPP surface
ϕ	Diffracted angle in the GTD
ϕ_j	Wavenumbers in the horizontal direction
ξ_j	Wavenumbers in the transversal direction
ρ	Density of air

δ	The Dirac delta function
O	The infinitesimal of higher-order
Ω_A	Sub-region A
Ω_B	Sub-region B
Ω_C	Sub-region C
Ω_D	Sub-region D
Λ	Normalize coefficient of modal expansion
∇^2	2D Laplace operator
$\Delta\Gamma$	Small distance near the saddle point
ΔL_d	Correction term for diffraction effect
ΔL_g	Correction term for the ground effect
Γ	Integration path in the complex α-plane
Γ_w	Integration path in the complex w-plane
Γ_s	Steepest descent path (SDP)

TABLE OF CONTENTS

LIST OF FIGURES

LIST OF TABLES

CHAPTER 1

INTRODUCTION AND LITERATURE REVIEW

1.1 Background

During the process of China's urbanization, numerous traffic tunnels have been built to make full use of land resources and shorten the distance of roads. According to incomplete statistics (Fei & Xing, 2013), the total length of road tunnels in China had reached 5122.6 kilometers by the end of 2013. However, the number has been growing continuously in the last 18 years. Undoubtedly, they are playing increasingly important roles in cities' traffic systems. Their advantages are obvious in certain situations when the roads are designed to pass through rivers and mountains. However, they also bring a lot of problems, such as poor ventilation, lighting, and noise pollution, in which the noise pollution is particularly serious. As a long space with openings on both ends, the propagation, distribution, attenuation, and reverberation of sound inside traffic tunnels are completely different from that in the open space (Kang, 1996a; 1996b; 1996c; 1997; 2002). Serious excess of noise standard for road tunnels exerts harmful effects on the maintenance staff, drivers, and passengers. People feel uncomfortable after exposing to such high noise environments.

Abatement of traffic noise using a single sound barrier or parallel barriers is very common in densely populated cities like Hong Kong. The noise level behind a barrier can be greatly reduced as the line-of-sight from the source to the receiver is intercepted and only the diffracted sound waves can reach the shadow zone. To further enhance the performance, barriers with T-shaped, Y-shaped, circular, and branched edge profiles have been designed to minimize the diffracted noise (Ishizuka & Fujiwara, 2004). Their performance, however, might still not be good if the barriers are built near high-rise buildings, as the noise can still deteriorate the living conditions of high-floor residents who are exposed to the illuminated zones of these barriers (Li, Kwok, et al., 2008; Li, Law, et al., 2008). To reduce the traffic noise effectively, tunnel-shaped sound barriers or the so-called sound-proof tunnels were built along the roads which can greatly reduce the noise to a relatively low level. However, apart from the problems like the traditional tunnels, the noise radiated from tunnel openings is becoming increasingly prominent which has severely impacted the living conditions of residents nearby. Therefore, it is of great significance to establish a prediction model for sound radiation from tunnels so that the formation mechanisms of sound fields can be investigated and appropriate noise attenuation approaches can be proposed to minimize noise pollution.

Apart from the noise radiated from tunnels in the outdoor environment, the noise radiated from pipework systems inside buildings is another issue to be solved. In Hong Kong, to make full use of the land resources, ground floors are used. However, the air circulation underground is bad which needs ventilation systems to provide fresh air. As a result, the noise radiated from the outlet of the pipework become serious which exerts negative impacts on the working efficiency of staff. The noise is mostly generated by the internal flow within the pipework, which might be sufficient to cause vibration and structure damage. The rough surfaces inside pipework can also cause noise, which can be modeled as monopole point sources (Goyder, 2011). Such noise problems can also be found in public facilities like air-conditioning systems of metro stations and gas pipes in buildings. The annoying noise radiated from the openings of pipework has adversely affected people's physical and mental health. As people's requirements for acoustical environments are getting higher and higher, the prediction and suppression of radiation noise from pipes have become an urgent issue to be considered.

Both the sound-proof tunnel and pipework in a ventilation system can be modeled as an unbaffled long enclosure (Yang et al., 2021). Researches on sound propagation inside an unbaffled long enclosure have been conducted. However, relatively less effort has been devoted to the issue of sound radiation from the long enclosure. The formation mechanisms of the radiated sound fields and the relationship between the sound fields inside and outside the unbaffled long enclosure need to be investigated so that suitable noise control devices can be applied to attenuate the noise pollution.

1.2 Literature review

1.2.1 Sound pressure field inside long enclosures

The sound field inside a long enclosure is complex due to multiple reflections and interferences of sound waves. Inside a practical tunnel, there are many factors affecting the sound distribution, such as the variation of traffic flows and vehicle types, different tunnel dimensions, and interior boundary conditions. Theoretically, the classical mode theory has been frequently employed to predict the sound pressure distribution inside a duct and long enclosure. The excitation, transmission, and radiation of sound in a duct of hard walls were systematically analyzed by Doak (1973). In addition, the sound field produced by a monopole point source in an infinite rectangular duct was calculated by using the mode theory (Pierce & Acoustics, 1981). The image source method (ISM) is another frequently applied method to calculate the sound field in a long enclosure, such as corridors (Redmore, 1982), street canyons (Iu & Li, 2002), and traffic tunnels (Li & Iu, 2002). Based on the principles of ray tracing techniques, an incoherent ISM (Lemire & Nicolas, 1989) was proposed and developed which can evaluate the sound pressure level (SPL) of a particular receiver by the summation of intensities from direct and all image sources. However, this energy-based ISM cannot account for the interferences between the direct and reflected sound waves. Recently, a coherent ISM was presented by Min et al. (2011) to predict the sound field in a two-dimensional (2D) waveguide with locally reactive impedance boundary conditions. A three-dimensional (3D) model was subsequently developed and validated in a long space with reflective ground and an absorptive ceiling (Min et al., 2014). The primary and image sources in the model are presented in Figure 1.1.

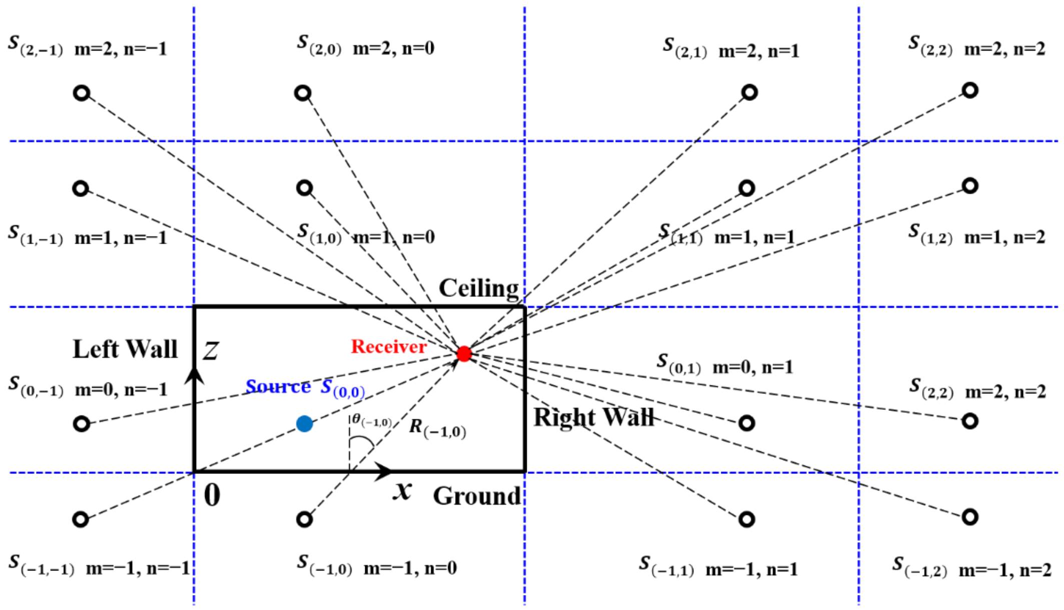

Figure 1.1 Coherent image source method (ISM) to predict the sound pressure field inside a long space (Min et al., 2014).

The total sound pressure field at the receiver in this space can be approximated as the summation of successive sound reflections on the four boundaries, which can be modeled as image sources:

$$p_{total} = \sum_{m=-\infty}^{\infty} \sum_{n=-\infty}^{\infty} Q_{mn} P_{mn} \tag{1.1}$$

where Q_{mn} stands for the combined complex wave reflection coefficient at each surface which contains the phase effect, and P_{mn} denotes the pressure. In addition, scaled-down experiments were conducted to study the properties of sound propagation inside a long enclosure (Li & Iu, 2004).

In brief, the sound field inside an unbaffled long enclosure can be determined by using the mode theory and ISM. However, these theoretical models can only be applied to deal with regular geometries such as rectangular and cylindrical enclosures. ISM is based on acoustical rays which is applicable in point source excitation. Besides, all the models mentioned above assumed that the enclosure is infinite long which ignored the reflected sound waves at the opening. Therefore, it is necessary to propose a prediction model that can couple the sound fields inside and outside a long enclosure.

1.2.2 Sound pressure field outside long enclosures

The prediction of the noise level in the vicinity of an unbaffled long enclosure is difficult due to the complexity of the radiated sound field which is formed by various acoustical phenomena including the direct sound radiation, reflections on the walls, and diffraction at the sharp edge. In the past 30 years, numerous computational models were put forward by researchers from different angles on the sound radiation and diffraction at openings which provide us a theoretical basis for the research of tunnel noise. Since the end of the last century, an increasing number of inhabitants who live near a tunnel had been complaining about the insufferable noise radiated from the tunnel opening. In order to avoid this annoying problem, prediction models (Sasaki, 1984) were proposed to investigate the noise level radiated from traffic tunnels. However, most of them are unsatisfactory even for ordinary engineering applications because of poor precision or specific preconditions. Woehner (1992) presented measurement results both inside and around some tunnels in Germany. Absorptive treatment was applied to the interior of the tunnels, and an average of 3 dB to 6 dB sound reduction was found. Olafsen (1996) described a mathematical model, where the tunnel is assumed to be a circular tube, and the sound power generated inside the tunnel is equal to the sound power radiated at the openings multiplied by a reduction factor. All the above-introduced methods are the initial explorations of tunnel noise which lay a foundation for the later researches.

In 1998, the Research Committee of Road Traffic Noise in Acoustic Society of Japan (ASJ) established the ASJ model (Sakamoto, 2015; Sakamoto et al., 2020) to predict the noise level radiated from the tunnel opening. Based on the energy balance inside the tunnel, the total sound power produced by a point source was divided into two parts and each of them propagates to the receiver point either directly or through multiple reflections. The sound pressure level at the receiver can be expressed as

$$L_R = L_W - 8 - 20\log_{10} R + \Delta L_d + \Delta L_g \tag{1.2}$$

where L_W denotes the sound power level at the source, ΔL_d and ΔL_g are correction terms for diffraction and ground effect, R stands for the distance from the sound source to the receiver. A schematic diagram of the ASJ model (Sakamoto, 2015) is illustrated in Figure 1.2.

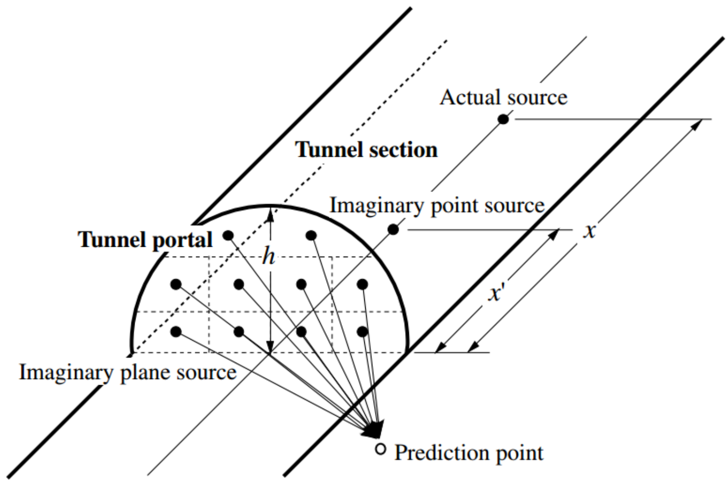

Figure 1.2 Schematic diagram of the ASJ model to predict the sound radiated from a traffic tunnel (Sakamoto, 2015).

Numerically, it is a simple model with certain accuracy. But it can only be used as an approximate approach to estimate the noise radiated from the tunnel openings as most of the correction terms in the formula are from experiments rather than analytical derivation. The correction term for the diffraction is calculated as a function of the path difference using Maekawa's engineering chart (Maekawa, 1968; Yamamoto & Takagi, 1992). The correction term for the ground effect is evaluated by summing attenuations due to all surfaces, independently of the types of road surface pavement. Moreover, the monopole point source was assumed to be on the central line of the ground which limits its applicability. Later, the sound power at the point source as well as along the opening surface was calculated analytically by Heutschi and Bayer (2006). Then, an empirical algorithm was proposed, in which a part of the sound energy from the source transmits to the receiver directly with certain shielding effects at the edges. The rest of the sound energy was assumed to radiate from the center point of the opening to the receiver with corresponding directivities. Although improvements were done compared to the ASJ model, no validation or experiments were presented.

In addition to theoretical investigations, scaled-down experimental studies have been conducted to explore the properties of sound radiated from tunnels. Tachibana et al. (1999) performed 1:40 scaled-down experiments to validate the calculation scheme for sound radiation from road tunnel openings described in the ASJ model. They studied a tunnel with a semicircular cross-section and different absorption characteristics of the surface. They found that a sound absorptive treatment of a limited area near the tunnel opening reduces the emitted sound power. Full-scale experiments were conducted in the Tai Lam Tunnel and the Western Harbor Crossing Tunnel of Hong Kong to validate the coherent ISM model in practical situations (Li & Iu, 2005). In most of the cases, the results obtained by the coherent ISM and the experiments agree well with each other and the discrepancies are within 3 dB. Moreover, A 1:10 scaled-down model has been established to validate the theoretical ISM and the ASJ model (Li & Iu, 2004). A 1:16 scaled-down model was built to simulate the Transit Railway in Hong Kong to see if there is noise reduction after the use of sound absorption materials (Kang, 1998). Most of the investigations mentioned above are oriented to engineering applications. As a result, errors are unavoidable. Besides, the physics and formation mechanisms behind the sound radiation phenomenon are seldom explored.

1.2.3 Calculation methods for sound radiation problems

1.2.3.1 Numerical methods

The main difficulty when dealing with the problem of sound radiation from an unbaffled long enclosure is how to model the semi-infinite region outside the enclosure opening. Otherwise, the boundary value problem cannot be solved theoretically for the lack of enough equations in the physical domain. Alternatively, numerical approaches such as the finite element method (FEM), the boundary element method (BEM) can be applied. A numerical model based on a hybrid FEM was developed that seeks to couple sound pressure fields of the interior and exterior regions (Kirby, 2008; Duan & Kirby, 2012). Felix et al. (2018) proposed a method to transform the semi-infinite acoustical domain outside a duct into a waveguide region by introducing a perfectly matched layer (PML) outside the original geometry. By doing this, the sub-fields could be expressed in terms of normal modes inside the duct and the whole acoustical field can be obtained via the mode-matching method. However, the PML parameters need to be optimized in numerical computation when dealing with specific problems, such as sound radiation from tunnels. Besides, the calculation efficiency declines when the size of the geometry is large. Huang et al. (2001) investigated the sound field near the tunnel outlet through the normal mode method analytically and BEM numerically. The tunnel is simplified as a circular tube with an abrupt change of the cross-section. Obviously, the sound field outside the tunnel should be modeled as a semi-free one rather than the one constrained in a tube. These numerical methods possess the advantage of tackling irregular-shaped acoustical domains, however, have shortcomings in computational efficiency when the calculated acoustical domain is large.

1.2.3.2 Wiener-Hopf technique

Wiener-Hopf (W-H) technique is a standard approach to solve certain types of linear partial differential equations, which are subjected to mixed boundary conditions on infinite geometries. The exact solution to the problem of plane-wave radiation from a cylindrical duct has been obtained applying the W-H technique (Levine & Schwinger, 1948). The distribution of the radiated sound field which is symmetrical about the axis of the pipe was described by the directivity function. For the radiation of higher-order modes, Lordi et al. (1974) calculated the power radiated from a duct opening per unite solid angle by the W-H technique. Afterward, the magnitude of the directivity function was analyzed. Practical strategies were put forward to predict the radiated lobes, zeros, sidelines, and aft radiation (Homicz & Lordi, 1975).

The W-H technique was initially applied in the Electromagnetic field to deal with problems regarding the Electromagnetic wave radiation from parallel plate waveguide radiators. The radiation field of a parallel-plate waveguide radiator due to a plane-wave incidence and a single-mode incidence were addressed using the W-H technique (Ayub et al., 2016; Buyukaksoy & Birbir, 1998). Nevertheless, when dealing with the radiation problems with complex boundary conditions on plate surfaces (Polat, 1998), the W-H equation becomes intractable. In order to solve the wave radiation problem with mixed boundary conditions, the waveguide region was proposed to be expressed in terms of normal modes, and the Fourier transform technique was applied elsewhere. This bypass the most challenging step of the matrix W-H factorization when applying the traditional W-H procedures. Besides, the thickness of the wall (Hames, 2011), local impedance boundary conditions (Birbir & Buyukaksoy, 2000) were also taken into consideration when dealing with the radiation problem. Later, a theoretical model for sound radiation from an unbaffled annular duct with the flow (Gabard & Astley, 2006) and lined center body (Demir & Rienstra, 2006) were proposed using the W-H technique. The findings are important benchmark results for acoustical engine-aircraft engineering applications. Besides, they serve as useful tools for understanding the physics behind sound radiation phenomena and validating numerical solutions.

However, the exact solutions are not convenient for numerical calculation as they are expressed by complex integrals. Several approximation methods were put forward to simplify the problem, in which the most widely applied is Hocter’s method (Hocter, 1999; 2000). The ray structures of duct modes propagating inside a semi-infinite duct were determined by Chapman (1994). Using the modal angles, it is possible to express the propagation and radiation of modes in conjunction with Keller’s geometrical theory of diffraction. Besides, the W-H technique mentioned was applied in electromagnetics and for 2D geometries which limits its application in practical tunnels. 3D cases are seldom mentioned in literature even though they could be used in the cylindrical duct as they are symmetric along their axis.

1.2.4 Helmholtz resonators for noise control

Previous investigations have demonstrated that to predict the sound radiated from the openings of open cavities (Yang et al., 2013, Tong et al., 2017), unbaffled long enclosures (Yang et al., 2021), and ducts (Doak, 1973; Cai & Mak, 2018), the sound fields inside the enclosed regions can be expressed by the superposition of acoustical modes, and the radiated sound fields are closely related with these modes. Due to the multiple reflections on boundaries inside the enclosed regions, standing waves can be observed which gives rise to multiple peaks in the SPL spectra of receivers inside and outside the geometry which are dominated by acoustical modes. Therefore, suppressing the acoustical modes inside the bounded region of an open cavity to attenuate the SPL peaks outside the enclosed region of the cavity has been proposed and verified (Wang & Choy, 2019a).

A Helmholtz resonator (HR) is commonly used to attenuate the noise level at the resonant frequency, which is suitable for the control of a sound peak. A resonator works only within a narrow bandwidth centered at the resonant frequency of the resonator. To broaden the working frequency band, a resonator array consisting of multiple resonators with different natural frequencies has been applied to control multiple sound peaks. The sound transmission loss of a duct was improved by adding HRs at the side branch (Chen et al., 1998). Besides, serial and parallel arrangement of HRs were tested to obtain a broad impedance match (Seo & Kim, 2005). However, the mounting locations of the HRs must be optimized. Otherwise, unfavorable interactions among the HRs and the acoustical domain may occur when the distances between them are small. Apart from the duct noise control, HRs have also been applied to attenuate the noise radiated from a baffled rectangular open cavity (Wang & Choy, 2019a). They revealed that desirable noise attenuation can be achieved with the HR mounting near the point source, while the noise reduction decreases when the HR moves towards the opening of the cavity as the coupling effect between the HR and the cavity become weak. Similar results were found in parallel barriers which is a 2D configuration of an unbaffled open cavity (Wang & Choy, 2019b). In addition, HRs have been employed to suppress the noise inside enclosures (Li et al., 2007; Li & Cheng, 2007; Yu et al., 2008; Yu & Cheng, 2009). The effects of internal resistance and mounting locations of T-shaped HRs on the noised attenuation performance of enclosures are systematically investigated. Even though numerous studies on HRs were found, investigations on the interaction between multiple HRs and the acoustical field inside an unbaffled long enclosure have seldom been observed.

1.2.5 Micro-perforated panel absorbers for noise control

Micro-perforated panel absorbers (MPPAs) have been extensively used in room acoustics (Fuchs & Zha, 2006), architectural and environmental noise abatement (Kang & Brocklesby 2005; Asdrubali & Pispola, 2007). An MPPA can be simply assembled by putting an MPP in front of a backing cavity (Maa, 1998). MPPs can be manufactured from a variety of materials such as metal, plastics, and wood. Therefore, an MPPA can be used either in ordinary conditions or harsh environments. For instance, Wu (1997) proposed applying MPPs for the design of duct silencers. The sound absorption and transmission characteristics of a lightweight MPP backed by a plate were investigated by Dupont et al. (2003). The feasibility of using transparent MPPs in window systems to reduce the noise and maintain the efficiency of ventilation was examined by Kang and Brocklesby (2005). An innovative sound barrier using a transparent polycarbonate MPP was proposed and studied by Asdrubali and Pispola (2007) which shows excellent performance in both the acoustical and optical fields. Experimental investigations were carried out to explore the feasibility of applying MPPs in medical equipment such as magnetic resonance imaging scanners (Li & Mechefske, 2010). In addition, new types of mufflers (Allam & Abom, 2011) and dissipative silencers (Abom & Allam, 2013) were proposed based on MPPs.

Due to the promising potential of MPPAs in noise control, many efforts have been made to improve their acoustical performance. For instance, for the purpose of applying the MPPs to construction facilities, Liu and Herrin (2010) attempt to improve the sound absorption coefficient of an MPPA inside a rectangular enclosure by using honeycomb cavities (Herrin et al., 2011). Wang et al. (2010) developed an MPPA with a trapezoidal backing cavity which alters the coupling effect between the MPP and cavity. Gai et al. (2017) calculated the sound absorption coefficients of MPPAs with L-shaped backing cavities. Besides, the sound absorption performance of an MPPA backed by an HR was studied aiming at improving its property of absorbing low-frequency noise. Apart from the shape designs of an MPPA, flexible structures have been introduced to improve the performance of MPPAs. The vibration effect of flexible panels on the sound absorption performance of MPPAs was explored by Lee et al. (2005). Both the sound absorption and transmission performance of a flexible MPPA were investigated theoretically and experimentally (Bravo et al., 2012a; 2012b). Besides, a light MPP was used by Wang et al. (2012) to improve the noise control performance of duct silencers. In addition, multiple layered (Maa, 1987; Lee & Kwon, 2004; Sakagami et al., 2010; Bravo et al., 2017; Chang et al., 2018, Bucciarelli et al., 2019); parallel (Wang & Huang, 2011; Yairi et al., 2011; Li et al., 2016) and serial (Qian et al., 2017) arrangement of MPPAs are proposed. In general, MPPs in parallel arrangements provide wider sound absorption bandwidth compared with those in serial arrangements. To widen the sound absorption bandwidth, inhomogeneous MPPAs were proposed (Prasetiyo et al., 2016; Mosa et al., 2019; 2020). The inhomogeneous MPPAs provide good sound absorption bandwidth by designing the sub-MPPs.

The performance of MPPAs might not be good when they are applied in complex situations (Maxit et al. 2012; Yang & Cheng, 2016), even though their performance under a normal plane-wave incidence is excellent. To model practical situations, the sound absorption performance of MPPAs subjected to oblique and random plane-wave incidences has been studied (Yang et al., 2013; Wang et al., 2014; Liu et al., 2020). The sound absorption coefficient of an MPPA is dominated by the mass-spring system consisting of the air inside micro-perforations and the air inside the backing cavity. The equivalent acoustical impedance of the MPPA varies with respect to the incidence angle which in turn changes the sound absorption performance of the MPPA. Besides, for an MPPA with a rectangular cavity, only the acoustic modes normal to the MPP contribute to the sound absorption performance. Corrugated MPPA was proposed which not only changes the incidence angle of the incoming sound wave to the local MPP surface but also creates an irregular-shaped backing cavity which enables more acoustical modes to contribute to the sound absorption performance of the corrugated MPPA (Wang & Liu, 2020). Results showed that multiple modes of the corrugated configuration are excited at the peak and dip frequencies and the acoustic responses by the non-resonating modes contribute to the improvement of sound absorption performance.

The sound distribution inside a soundproof tunnel is complex which needs a noise control device that can attenuate higher-order modes. Corrugated MPPAs are promising devices for the attenuation of noise in complex situations. However, only a sinusoidal MPP profile has been considered (Wang & Liu, 2020). To enhance the sound absorption performance, the acoustical characteristics of a Z-shaped MPPA are investigated and its sound attenuation performance inside an unbaffled long enclosure is explored in the current study.

1.3 Preliminary experiments

A preliminary experiment has been performed to figure out the basic properties of traffic noise outside a tunnel in Hong Kong. According to the measurement method described in the environmental quality standard of noise (GB 3096-2008), the day-time equivalent A-weighted SPLs at different locations outside the tunnel were obtained by sound level meters (Larson Davis Model 831). For each test point, three measurements were carried out and their average SPLs are listed in Figure 1.3. The total average SPL of all the testing points reached 81.8 dB (A). It has exceeded the threshold specified in the standard which is 70 dB (A) for urban arterial roads. The noise pollution in this area has severely influenced the living condition of the nearby residents.

Figure 1.3 Measurement locations outside a sound-proof tunnel in Hong Kong and the average SPLs at each testing point.

Besides, the measured SPL spectra of the average noise radiated from the tunnel with stable traffic flow, from buses, and heavy trucks traveling at approximately 70 km/h are presented in Figure 1.4. Apart from the fluctuating results under around 200 Hz which results from the random vibration and the limitation of equipment, the noise energy concentrates mainly in the frequency range between 200 Hz and 2000 Hz. For high-frequency interval, however, the SPL decreases continuously and dissipates easily in the open space with increasing distance. Similar experimental results can be observed in the work by Can et al. (2010).

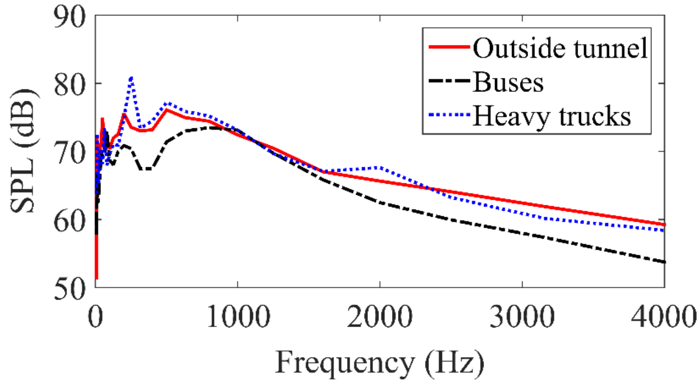

Figure 1.4 SPL spectra of noise radiated from a tunnel with stable traffic flow, from city buses, and heavy trucks traveling at about 70 km/h.

Moreover, the SPL spectra of noise radiated from the openings of 3 ventilation ducts in research offices are illustrated in Figure 1.5. The peaks stand approximately at 200 Hz with the SPLs reaching 58 dB. In the middle to high-frequency range, the SPLs decrease continuously. However, the SPLs are higher than 40 dB when the frequency is within 2000 Hz which is not conducive to efficient work. Based on the experimental results, the main noise frequency band that affects our normal life is 200 Hz to 2000 Hz which is chosen as the targeted frequency range in this thesis. Besides, the noise levels in people’s living environment have already excessed the threshold values of various noise standards which need serious consideration.

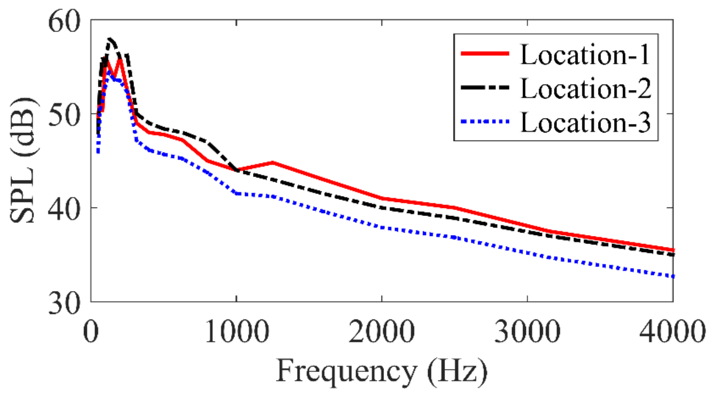

Figure 1.5 SPL spectra of noise radiated from the openings of three ventilation ducts in research offices.

1.4 Motivations and objectives

Environmental noise is particularly serious in densely populated cities like Hong Kong. To prevent the residents from noise pollution, parallel barriers have been widely constructed on both sides of roads. However, their performance is still unsatisfactory as the noise can still reach the residents in high-rise buildings. In addition, sound-proof tunnels are built to cover the roads so that the noise inside the tunnel cannot propagate directly to the outside receiver. However, the SPL and the reverberation time inside the sound-proof tunnels are high and long, respectively, which is harmful to maintenance staff, passengers, and drivers. Besides, the sound radiated from the portals also causes noise pollution to the surroundings.

From the existing works, numerous investigations have been implemented on the propagation, reverberation, and dissipation of sound inside long enclosures and traffic tunnels. However, relatively little attention has been paid to problems concerning sound radiation from unbaffled openings. Specifically, the main issues needing consideration are summarized as follows:

(1) Engineering approaches have been put forward to tackle problems regarding sound radiation from pipes and tunnels. However, theoretical investigations on sound radiation from such unbaffled long enclosures are limited.

(2) W-H technique has been applied to formulate sound radiation problems. The geometrical configurations, sound sources, and boundary conditions need to be further extended to meet engineering applications.

(3) The formation mechanisms of the sound pressure fields inside and outside an

unbaffled long enclosure are seldom explained, and the physics behind the sound radiation phenomenon is barely revealed.

(4) A simple, compact, and reliable noise control device is still needed to suppress the noise radiated from an unbaffled long enclosure. The interaction between the acoustical field of an unbaffled long enclosure and a noise control device needs to be explored.

Motivated by the serious noise pollution in Hong Kong and insufficient studies on the sound radiation problems, the prediction and attenuation of sound radiated from unbaffled long enclosures are addressed in this thesis. The objectives are summarized as follows:

(1) To establish a theoretical model for the prediction of sound radiated from an unbaffled long enclosure, validate the proposed model using the FEM, and explain the physics behind the sound radiation phenomenon.

(2) To model the sound radiation from a sound-proof tunnel, in which monopole point sources, impedance boundary conditions are taken into consideration to simulate practical scenarios; to explore the physics behind the sound radiation phenomenon, and provide a theoretical basis to the proposal of noise control strategies.

(3) To propose suitable noise control devices for the abatement of noise radiated from unbaffled long enclosures, evaluate their performance, investigate the interaction between devices and the acoustical domain, and find the optimized configurations of the proposed noise control devices.

(4) To validate the proposed theoretical models and examine the noise absorption performance of noise control devices via scaled-down quasi-two-dimensional experiments.

1.5 Outline of the thesis

The thesis is composed of 6 chapters. Chapter 1 presents the background of sound radiation from unbaffled long enclosures, such as ductwork in ventilation systems and traffic tunnels. In addition, related literature is reviewed and preliminary experiments are conducted. Motivations, objectives, and the outline of this study are illustrated.

Chapter 2 introduces the W-H technique to predict the sound radiation from an unbaffled long enclosure. In contrast to the classical formulations which led to a matrix W-H equation, the proposed model reduced the boundary value problem into two scalar modified W-H equations (MWHE) of the second kind which involve an infinite number of unknowns satisfying an infinite system of linear algebraic equations susceptible to a numerical treatment. Besides, monopole point sources are applied to simulate the noise sources which are more real and representative. Detailed formulation processes and the numerical implementation procedures are presented. The physics behind the radiation phenomenon is investigated by the mode theory. Additionally, quasi-2D experiments and FEM simulations are conducted to validate the proposed model.

Chapter 3 presents a theoretical model for the prediction of sound radiated from an unbaffled long enclosure including the ground. The geometrical arrangement forms an idealized representation of soundproof tunnels where noise propagates inside the long enclosures and radiates to the outside through the openings. Impedance boundary conditions are applied to mimic the practical scenarios. The influences of these acoustic impedances on sound radiation patterns are investigated which indicates that boundary condition on the inner wall of the long enclosure is the most suitable one to be applied for the attenuation of noise. Besides, the sound radiation pattern from an unbaffled long enclosure with a partial lining is investigated in which frequency-dependent impedance condition is applied. Finally, quasi-2D experiments are carried out to validate the model and examine the sound absorption performance of partial linings.

Chapter 4 demonstrates a hybrid method to explore the sound radiated from an unbaffled long enclosure with the ground, in which the sound pressure field inside the long enclosure is calculated by the FEM, while the radiated sound field is expressed by the W-H technique. The proposed hybrid possesses the advantages of calculating the sound fields flexibly and efficiently. Helmholtz resonators are proposed to suppress the modal responses at the opening so that the radiated sound is expected to be attenuated at the targeted frequencies. The optimized configurations and locations of multiple HRs are obtained to suppress multiple sound peaks of the radiated sound field. Finally, a quasi-2D experiment is implemented to validate the model.

Chapter 5 investigates the acoustical properties of a Z-shaped micro-perforated panel absorber (ZMPPA) in practical acoustical environments. A numerical scheme is proposed to calculate the sound absorption coefficient of corrugated MPPAs under an oblique plane-wave incidence. Then, the numerical model is validated using benchmark theoretical formulas. Parametrical studies are conducted to investigate the performance of a ZMPPA. After that, the optimized parameters of a ZMPPA are obtained, which are applied to attenuate the sound radiated from an unbaffled long enclosure. Experimental results are presented to validate the numerical model and examine the sound absorption performance of a ZMPPA in attenuating the noise radiated from an unbaffled long enclosure with the ground.

Chapter 6 summarizes the findings in this thesis. Recommendations for the future work for sound attenuation of an unbaffled long enclosure are briefly discussed.

CHAPTER 2

THEORETICAL MODEL OF SOUND RADIATION FROM AN UNBAFFLED LONG ENCLOSURE

2.1 Introduction

Sound radiation from an unbaffled long enclosure can be commonly observed in ductwork systems, such as ventilation, air conditioning, and aircraft jet engines. Various investigations have been conducted to predict and then reduce the sound radiated from the long enclosure, among which, the W-H technique was widely applied. However, in the previous studies (Levine & Schwinger, 1948; Lordi et al., 1974, Homicz & Lordi, 1975; Buyukaksoy & Cinar, 2005; Peake & Abrahams, 2020), both acoustical domains inside and outside the duct were converted into the spectral domain through the Fourier transform, which gave rise to a matrix W-H equation. To find the solution, the square matrix must be split into the product of two matrices with nonvanishing determinants such that the entries of these matrices, as well as their inverses, are regular in a certain overlapped region of the upper and lower halves of the complex plane. However, due to the non-commutativity of matrix multiplication, there is not a general approach to achieve the W-H factorization of an arbitrary square matrix. As a result, if the geometry and boundary conditions are complicated, the solution to the radiation problem cannot be obtained using traditional W-H procedures.

The distribution pattern of sound radiated from ducts or long enclosures is directly determined by the acoustical source. Plane-wave and single-mode were considered in the models mentioned above. These models are applied to predict the sound radiation from heating, ventilation, and air-conditioning systems as the sound distribution in such a system is relatively simple. However, in larger geometries such as traffic tunnels, the sound field inside the long enclosure is more complicated, which cannot be represented by a plane-wave or single-mode. Hence, in this thesis, we use a monopole point source to simulate the noise source. It produces a sound field formed by the superposition of multiple higher-order acoustical modes, which is more practical and representative.

2D configurations are considered in this thesis. Admittedly, a 2D model cannot fully represent the sound distribution in a 3D domain. However, for such a geometrical configuration, 2D models are often established in previous studies. This is due to the limitation of the W-H technique in dealing with a 3D problem. As a result, a 2D model is first established to explore the radiation patterns of noise from a long enclosure and to explain the physics behind the sound radiation phenomenon. With the development of the W-H technique, it has been extended to solve certain kinds of 3D problems such as sound radiation from annular/cylindrical ducts (Demir & Buyukaksoy, 2005; Demir & Rienstra, 2006; 2010; Tiryakioglu, 2019; Peake & Abrahams, 2020). Despite that, there are still many problems to be solved in building a 3D W-H model such as sound radiation from a rectangular long enclosure. These problems which will be studied in our future work.

In this chapter, the sound radiation from an unbaffled long enclosure is analyzed based on the W-H technique. However, only the outside acoustical domain is converted into the spectral domain. Two modified W-H equations are obtained and their solutions are obtained simultaneously by applying the standard factorization and decomposition procedures. This bypass the most challenging stage of the classical formulations, which will lead to an intractable matrix W-H factorization. Besides, the sound field inside the enclosure is expressed in terms of acoustical modes which is convenient to explain the radiation phenomenon from the perspective of the mode theory. Monopole point sound sources are applied. Detailed formulation and implementation of the theoretical model are demonstrated. Besides, the proposed theoretical model is validated using the FEM, and mechanisms behind the radiation phenomenon are explained from the perspective of mode theory. In addition, A quasi-2D experiment is also conducted to validate the proposed model.

2.2 Theoretical model

2.2.1 Description of the problem in the natural domain

A schematic diagram of the sound radiation from an unbaffled long enclosure is shown in Figure 2.1. A two-dimensional rectangular (2D) enclosure is considered. The height of the unbaffled long enclosure is 2h, and the thickness of the wall is assumed to be zero for simplicity. All boundaries are set to be acoustically rigid. In this thesis, the flow speed of the air media is ignored which may change the propagation and radiation patterns of the noise. However, the proposed theoretical model can be easily extended to contain the moving flow (Gabard & Astley, 2006). Besides, the radiation properties of sound in the frequency domain are considered here. Nevertheless, in real traffic, both the velocity and location of the sound source are changeable. Doppler effect should be considered for such situations in the time domain. As the main purpose of this research is to explore the underlying physics behind the sound radiation phenomenon, frequency analysis is considered.

The noise is produced by monopole point sources S_n with their locations and the volume velocity strengths being $\left(x_n, y_n\right)$ and Q_n , respectively. A Cartesian coordinate system (xoy) is adopted with the origin fixing at the middle point of the opening. The polar coordinate system $(ro\theta)$ is also shown to express the directivity patterns of the radiated sound field. In addition, imaginary interfaces I, II, and III are depicted for the convenience of analysis. They divide the whole acoustical domain into four sub-regions which are denoted by Ω_A, Ω_B, Ω_C, and Ω_D, respectively.

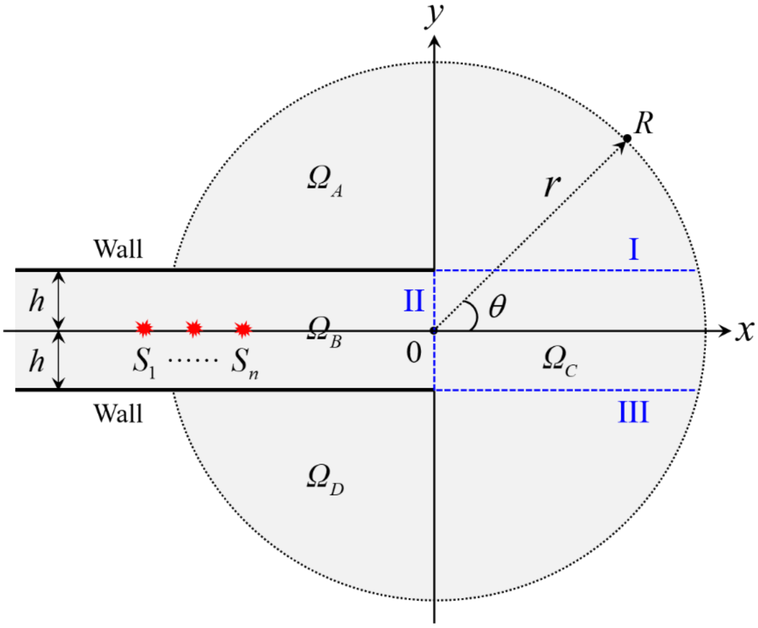

Figure 2.1 A schematic diagram of sound radiation from a two-dimensional unbaffled long enclosure.

According to the partition of the whole acoustical domain in Figure 2.1, the total sound pressure field is expressed by the following piecewise function as

$$p_{total}(x,y)=\begin{cases} p_A(x,y) & \Omega_A: x\in(-\infty,+\infty), y\in[h,+\infty) \\ p_{incident}(x,y)+p_{reflected}(x,y) & \Omega_B: x\in(-\infty,0], y\in[-h,h] \\ p_C(x,y) & \Omega_C: x\in[0,+\infty), y\in[-h,h] \\ p_D(x,y) & \Omega_D: x\in(-\infty,+\infty), y\in[-\infty,-h] \end{cases} \tag{2.1}$$

where $p_A(x,y)$, $p_C(x,y)$, and $p_D(x,y)$ are the sound pressure fields of regions Ω_A, Ω_C, and Ω_D, respectively. The incident and reflected sound pressure fields of region

Ω_B are denoted by $p_{incident}(x,y)$ and $p_{reflected}(x,y)$, respectively.

The total sound pressure field without any sound source can be described by the following homogeneous Helmholtz equation as

$$\nabla^2 p_{total}(x,y) + k^2 p_{total}(x,y) = 0 \tag{2.2}$$

where $\nabla^2 = \partial^2/\partial x^2 + \partial^2/\partial y^2$ denotes the 2D Laplace operator, and k represents the free space wavenumbers.

In any physical medium, loss is inevitable. Therefore, an ideal lossless medium which is often used in theoretical analyses can be regarded as a limiting case with a vanishingly small loss. We assume:

$$k = k_1 - ik_2,\ k_1 \gg k_2 > 0 \tag{2.3}$$

where k_1 and $-k_2$ are the real and imaginary parts of the wavenumber.

Boundary conditions on the rigid walls can be described by

$$\left.\frac{\partial p_{total}(x,y)}{\partial y}\right|_{\text{walls}} = 0 \tag{2.4}$$

Apart from that, the sound pressure and particle velocity at imaginary interfaces should be continuous which are expressed by

$$p_A = p_C, \left.\frac{\partial p_A}{\partial y} = \frac{\partial p_C}{\partial y}\right|_{\text{I}};\ p_B = p_C, \left.\frac{\partial p_B}{\partial x} = \frac{\partial p_C}{\partial x}\right|_{\text{II}};\ p_D = p_C, \left.\frac{\partial p_D}{\partial y} = \frac{\partial p_C}{\partial y}\right|_{\text{III}} \tag{2.5}$$

where p_B denotes the total sound pressure field of region Ω_B.

Besides, when boundaries at infinity or geometrical singularities are involved in the model, several mathematically acceptable solutions of the acoustical field might be obtained. However, only one of them is completely consistent with the anticipated physical phenomenon. Hence, to ensure the uniqueness of the solution to the problem, we must consider the Sommerfeld radiation condition for the infinite region outside the long enclosure (Yang et al., 2013):

$$\lim_{r\to\infty}\sqrt{r}\left[\frac{\partial p_{total}\left(r,\theta\right)}{\partial r}-ikp_{total}\left(r,\theta\right)\right]=0,\quad r=\sqrt{x^2+y^2} \tag{2.6}$$

Also, to avoid the geometrical singularities at the edges of the long enclosure, the acoustical energy stored in any finite neighborhood of the edges must be finite which is expressed by (Khan et al., 2014)

$$p_{total}\left(x,\pm h\right)=O\left(\left|x\right|^{1/2}\right),\quad \frac{\partial p_{total}\left(x,\pm h\right)}{\partial y}=O\left(\left|x\right|^{-1/2}\right),\ \left|x\right|\to 0 \tag{2.7}$$

where O denotes the infinitesimal of higher-order.

Inside the long enclosure, the incident sound pressure field produced by the n-th monopole point source satisfies the following inhomogeneous Helmholtz equation:

$$\left(\nabla^2+k^2\right)p_{incident}\left(x,y\right)=-i\rho kc_0Q_n\delta\left(x-x_n\right)\delta\left(y-y_n\right) \tag{2.8}$$

where δ, ρ, and c_0 are, respectively, the Dirac delta function, the density of air and the sound speed. The solution to Eq. (2.8) satisfying the boundary conditions on walls can be expressed in terms of the superposition of normal modes as (Doak, 1973)

$$\begin{aligned}p_{incident}\left(x,y\right)=&\sum_{n=1}^{\infty}\sum_{j=0}^{\infty}\frac{\rho kc_0Q_n\cos\left(\kappa_j^o y_n\right)\cos\left(\kappa_j^o y\right)}{2\Lambda_j^o\alpha_j^o}e^{-i\alpha_j^o\left|x-x_n\right|}\\&+\sum_{n=1}^{\infty}\sum_{j=0}^{\infty}\frac{\rho kc_0Q_n\sin\left(\kappa_j^e y_n\right)\sin\left(\kappa_j^e y\right)}{2\Lambda_j^e\alpha_j^e}e^{-i\alpha_j^e\left|x-x_n\right|}\end{aligned} \tag{2.9}$$

where the even (with superscript 'e') and odd (with superscript 'o') wavenumbers for cosine and sine modal functions are calculated by

$$\begin{aligned}&\kappa\left(\alpha_j^o\right)=\kappa_j^o=\frac{j\pi}{h}\\&\Rightarrow\alpha_j^o=\sqrt{k^2-\left(\kappa_j^o\right)^2},\ j=0,1,2,\ldots\end{aligned} \tag{2.10}$$

and

$$\begin{aligned}&\kappa\left(\alpha_j^e\right)=\kappa_j^e=\left(2j+1\right)\pi/2h\\&\Rightarrow\alpha_j^e=\sqrt{k^2-\left(\kappa_j^e\right)^2},\ j=0,1,2,...\end{aligned}\tag{2.11}$$

Besides, the normalized coefficients of the cosine and sine modal expansions are calculated by

$$\Lambda_j^o=\int_{-h}^{h}\cos^2\left(\kappa_j^o\varsigma\right)d\varsigma=h\left(1+\delta_{oj}\right),\ \Lambda_j^e=\int_{-h}^{h}\sin^2\left(\kappa_j^e\varsigma\right)d\varsigma=h\tag{2.12}$$

Due to the impedance mismatch caused by the abrupt size change at two sides of the enclosure opening, there must be a reflected sound pressure field inside the long enclosure which is expressed by

$$p_{reflected}=\sum_{n=0}^{\infty}b_n^o\cos\left(\kappa_n^o y\right)e^{i\alpha_n^o x}+\sum_{n=0}^{\infty}b_n^e\sin\left(\kappa_n^e y\right)e^{i\alpha_n^e x}\tag{2.13}$$

where b_n^o and b_n^e are modal response coefficients for cosine and sine modal functions.

The boundary value problem is described in the natural domain. However, due to the infinite boundary conditions outside the long enclosure, it is difficult to obtain the solution to the Helmholtz equation applying traditional methods. Enlightened by the corresponding relationships between the infinite boundary conditions on walls and the infinite limits in Fourier integral, next, we will apply the Fourier transform to convert the radiated sound pressure field into the spectral domain. Solvable W-H equations will be obtained and then solved through the W-H technique.

2.2.2 Radiated sound pressure field in the spectral domain

The Helmholtz equations for regions $\Omega_{A(D)}$ in the natural domain are converted into the spectral domain through the full-range Fourier transform as

$$\int_{-\infty}^{+\infty}\left[\frac{\partial^2 p_{A(D)}\left(x,y\right)}{\partial x^2}+\frac{\partial^2 p_{A(D)}\left(x,y\right)}{\partial y^2}+k^2 p_{A(D)}\left(x,y\right)\right]e^{-i\alpha x}dx=0\tag{2.14}$$

where $\alpha = \sigma + i\tau$ denotes the Fourier transform variable. The first term in the bracket of Eq. (2.14) can be integrated by parts as

$$\int_{-\infty}^{+\infty} \frac{\partial^2 p_{A(D)}(x,y)}{\partial x^2} e^{-i\alpha x} dx = \left[\frac{\partial p_{A(D)}(x,y)}{\partial x} e^{-i\alpha x} \right]_{-\infty}^{+\infty}$$
$$+ i\alpha \left[p_{A(D)}(x,y) e^{-i\alpha x} \right]_{-\infty}^{+\infty} - \alpha^2 \int_{-\infty}^{+\infty} p_{A(D)}(x,y) e^{-i\alpha x} dx = -\alpha^2 P_{A(D)}(\alpha, y) \tag{2.15}$$

where

$$P_{A(D)}(\alpha, y) = \int_{-\infty}^{+\infty} p_{A(D)}(x,y) e^{-i\alpha x} dx \tag{2.16}$$

Hereafter, we use the upper cases of the variables in the natural domain to stand for their transformed forms in the spectral domain. Note that the contributions from the bracketed terms of Eq. (2.15) at the positive and negative infinities are both zero. They result from the Sommerfeld radiation condition which implies that an outgoing wave disappears at the infinity.

Combining Eqs. (2.14) and (2.15), we have the transformed Helmholtz equations for regions $\Omega_{A(D)}$ which are expressed as

$$\left[\frac{\partial^2}{\partial y^2} + \kappa^2(\alpha) \right] \begin{bmatrix} P_A^+(\alpha, y) + P_A^-(\alpha, y) \\ P_D^+(\alpha, y) + P_D^-(\alpha, y) \end{bmatrix} = 0 \tag{2.17}$$

where

$$\begin{bmatrix} P_A^\pm(\alpha, y) \\ P_D^\pm(\alpha, y) \end{bmatrix} = \pm \int_0^{\pm\infty} \begin{bmatrix} p_A(x,y) \\ p_D(x,y) \end{bmatrix} e^{-ikx} dx \tag{2.18}$$

and $\kappa(\alpha) = \sqrt{k^2 - \alpha^2}$ is called the square root function. It is defined in the complex α-plane with two branch points $\pm k$, and branch cuts $C_\pm$ along $\alpha = k$ to $\alpha = k - i\infty$ and $\alpha = -k$ to $\alpha = -k + i\infty$ as shown in Figure 2.2.

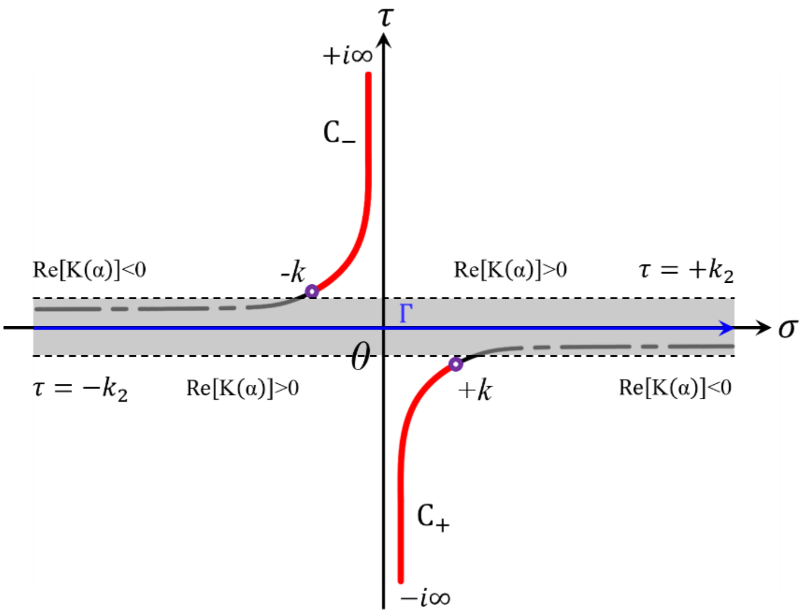

Figure 2.2 Schematic diagram of branch points (circles), branch cuts (red solid line) of the square root function, the integration path (blue arrow line) for the inverse Fourier transform.

This is a compulsory choice due to the physical existence of Green's function. Besides, it can be observed that the imaginary parts of the numbers in this cut plane are all negative, which implies that, under this configuration, the cut plane is a proper sheet. For the convenience of description, we denote that the regions $\tau > -k_2$ and $\tau < k_2$ are the upper and lower half complex α-planes, respectively.

Taking into consideration the following asymptotic behaviors:

$$\begin{bmatrix} p_A(x,y) \\ p_D(x,y) \end{bmatrix} = O\begin{bmatrix} e^{-ik|x|} \\ e^{+ik|x|} \end{bmatrix}, \quad x \to \pm\infty \tag{2.19}$$

it can be observed that $P_A^+(\alpha,y)$ and $P_D^+(\alpha,y)$ are regular functions in the upper half complex α-plane, while $P_A^-(\alpha,y)$ and $P_D^-(\alpha,y)$ are regular functions in the lower half complex α-plane. The general solution to Eq. (2.17) reads

$$\begin{bmatrix} P_A(\alpha,y) \\ P_D(\alpha,y) \end{bmatrix} = \begin{bmatrix} P_A^+(\alpha,y) + P_A^-(\alpha,y) \\ P_D^+(\alpha,y) + P_D^-(\alpha,y) \end{bmatrix} = \begin{bmatrix} A(\alpha)e^{-i\kappa(\alpha)(y-h)} \\ D(\alpha)e^{i\kappa(\alpha)(y+h)} \end{bmatrix} \tag{2.20}$$

where $A(\alpha)$ and $D(\alpha)$ are unknown spectral coefficients. Based on the transformed boundary conditions on the walls, we have the following identities:

$$\dot{P}_A^+(\alpha,h) = -i\kappa(\alpha)A(\alpha) \tag{2.21}$$

$$\dot{P}_D^+(\alpha,-h) = i\kappa(\alpha)D(\alpha) \tag{2.22}$$

Similarly, the Helmholtz equation for region Ω_C is converted into the spectral domain using the half-range Fourier transform technique:

$$\left[\frac{\partial^2}{\partial y^2} + \kappa^2(\alpha)\right] P_C^+(\alpha,y) = f(y) + i\alpha g(y) \tag{2.23}$$

where the pressure and pressure gradient at the opening are defined as

$$g(y) = p_C(0,y),\ f(y) = \frac{\partial p_C(0,y)}{\partial x} \tag{2.24}$$

and

$$P_C^+(\alpha,y) = \int_0^{+\infty} p_C(x,y)e^{-i\alpha x}dx \tag{2.25}$$

The general solution to Eq. (2.23) which is a second order inhomogeneous linear differential equation can be obtained using the method of constant variation as

$$\begin{aligned} P_C^+(\alpha,y) &= B(\alpha)\cos\left[\kappa(\alpha)y\right] + C(\alpha)\sin\left[\kappa(\alpha)y\right] \\ &+ \frac{1}{\kappa(\alpha)}\int_{-h}^{y}\left[f(\varsigma) + i\alpha g(\varsigma)\right]\sin\left[\kappa(\alpha)(y-\varsigma)\right]d\varsigma \end{aligned} \tag{2.26}$$

where $B(\alpha)$ and $C(\alpha)$ are unknown spectral coefficients.

Based on the transformed continuity relations of particle velocity at the imaginary interfaces I and III, the unknown spectral coefficients can be obtained as

$$B(\alpha) = \frac{\left\{\dot{P}_D^+(\alpha,-h) - \dot{P}_A^+(\alpha,h) + \int_{-h}^{h}\left[f(\varsigma) + i\alpha g(\varsigma)\right]\cos\left[\kappa(\alpha)(h-\varsigma)\right]d\varsigma\right\}}{2\kappa(\alpha)\sin\left[\kappa(\alpha)h\right]} \tag{2.27}$$

$$C(\alpha)=\frac{\left\{\dot{P}_D^+(\alpha,-h)+\dot{P}_A^+(\alpha,h)-\int_{-h}^{h}\left[f(\varsigma)+i\alpha g(\varsigma)\right]\cos\left[\kappa(\alpha)(h-\varsigma)\right]d\varsigma\right\}}{2\kappa(\alpha)\cos\left[\kappa(\alpha)h\right]} \tag{2.28}$$

Then, substituting Eqs. (2.27) and (2.28) into Eq. (2.26), the transformed sound pressure field of region Ω_C is obtained:

$$\begin{aligned}
&P_C^+(\alpha,y)\\
&=\frac{\cos\left[\kappa(\alpha)y\right]}{2\kappa(\alpha)\sin\left[\kappa(\alpha)h\right]}\left\{\begin{aligned}&\dot{P}_D^+(\alpha,-h)-\dot{P}_A^+(\alpha,h)\\&+\int_{-h}^{h}\left[f(\varsigma)+i\alpha g(\varsigma)\right]\cos\left[\kappa(\alpha)(h-\varsigma)\right]d\varsigma\end{aligned}\right\}\\
&+\frac{\sin\left[\kappa(\alpha)y\right]}{2\kappa(\alpha)\cos\left[\kappa(\alpha)h\right]}\left\{\begin{aligned}&\dot{P}_D^+(\alpha,-h)+\dot{P}_A^+(\alpha,h)\\&-\int_{-h}^{h}\left[f(\varsigma)+i\alpha g(\varsigma)\right]\cos\left[\kappa(\alpha)(h-\varsigma)\right]d\varsigma\end{aligned}\right\}\\
&+\frac{1}{\kappa(\alpha)}\int_{-h}^{y}\left[f(\varsigma)+i\alpha g(\varsigma)\right]\sin\left[\kappa(\alpha)(y-\varsigma)\right]d\varsigma
\end{aligned} \tag{2.29}$$

The term on the left-hand side of Eq. (2.29) is regular in the upper half complex α-plane. However, the regularity of the terms on the right-hand side of the equation is violated by the poles occurring at the zeros of denominators satisfying the following conditions:

$$\kappa\left(\alpha_m^o\right)\sin\left[\kappa\left(\alpha_m^o\right)h\right]=0 \tag{2.30}$$

$$\kappa\left(\alpha_m^e\right)\cos\left[\kappa\left(\alpha_m^e\right)h\right]=0 \tag{2.31}$$

These poles are eliminated by imposing that their residues are zero. According to the residue theorem, the terms in the bracket of Eq. (2.29) should be zero:

$$\dot{P}_A^+\left(\alpha_m^o,h\right)-\dot{P}_D^+\left(\alpha_m^o,-h\right)=(-1)^m\int_{-h}^{h}\left[f^o(\varsigma)+i\alpha_m^o g^o(\varsigma)\right]\cos\left(\kappa_m^o\varsigma\right)d\varsigma \tag{2.32}$$

$$\dot{P}_A^+\left(\alpha_m^e,h\right)+\dot{P}_D^+\left(\alpha_m^e,-h\right)=(-1)^m\int_{-h}^{h}\left[f^e(\varsigma)+i\alpha_m^e g^e(\varsigma)\right]\sin\left(\kappa_m^e\varsigma\right)d\varsigma \tag{2.33}$$

Define the following coefficients:

$$\begin{bmatrix} g_m^o \\ f_m^o \end{bmatrix} = \frac{1}{\Lambda_m^o} \int_{-h}^{h} \begin{bmatrix} g^o(\varsigma) \\ f^o(\varsigma) \end{bmatrix} \cos\left(\kappa_m^o \varsigma\right) d\varsigma \tag{2.34}$$

$$\begin{bmatrix} g_m^e \\ f_m^e \end{bmatrix} = \frac{1}{\Lambda_m^e} \int_{-h}^{h} \begin{bmatrix} g^e(\varsigma) \\ f^e(\varsigma) \end{bmatrix} \sin\left(\kappa_m^e \varsigma\right) d\varsigma \tag{2.35}$$

Then, using Eqs. (2.34) and (2.35), Eqs. (2.32) and (2.33) can be simplified to the residue solutions as

$$\dot{P}_A^+\left(\alpha_m^o, h\right) - \dot{P}_D^+\left(\alpha_m^o, -h\right) = (-1)^m \left(f_m^o + i\alpha_m^o g_m^o \right) \Lambda_m^o \tag{2.36}$$

$$\dot{P}_A^+\left(\alpha_m^e, h\right) + \dot{P}_D^+\left(\alpha_m^e, -h\right) = (-1)^m \left(f_m^e + i\alpha_m^e g_m^e \right) \Lambda_m^e \tag{2.37}$$

The sound pressure and its gradient at the opening of the long enclosure can be expanded into modal series as

$$\begin{bmatrix} g^o(y) \\ f^o(y) \end{bmatrix} = \sum_{m=0}^{\infty} \begin{bmatrix} g_m^o \\ f_m^o \end{bmatrix} \cos\left(\kappa_m^o y\right) \tag{2.38}$$

$$\begin{bmatrix} g^e(y) \\ f^e(y) \end{bmatrix} = \sum_{m=0}^{\infty} \begin{bmatrix} g_m^e \\ f_m^e \end{bmatrix} \sin\left(\kappa_m^e y\right) \tag{2.39}$$

In the residue solutions, there are still an infinite number of unknowns, which need extra equations to determine them. Next, we will obtain two W-H equations and their solutions using the W-H technique.

2.2.3 Wiener-Hopf equations and their solutions

Combining Eqs. (2.20), (2.21), (2.22), and the transformed continuity relations at imaginary interfaces I and III, we have the following identities:

$$\begin{aligned} &\frac{1}{i\kappa(\alpha)}\left[\dot{P}_D^+(\alpha, -h) + \dot{P}_A^+(\alpha, h) \right] + P_A^-(\alpha, h) - P_D^-(\alpha, -h) \\ &= P_C^+(\alpha, -h) - P_C^+(\alpha, h) \end{aligned} \tag{2.40}$$

and

$$
\begin{aligned}
&\frac{1}{i\kappa(\alpha)}\left[\dot{P}_D^{+}(\alpha,-h)-\dot{P}_A^{+}(\alpha,h)\right]-P_A^{-}(\alpha,h)-P_D^{-}(\alpha,-h)\\
&=P_C^{+}(\alpha,-h)+P_C^{+}(\alpha,h)
\end{aligned}
\tag{2.41}
$$

Substituting Eq. (2.29) into Eqs. (2.40) and (2.41), respectively, we can obtain the following W-H equations:

$$
\begin{aligned}
&-\frac{i}{\kappa^2(\alpha)N(\alpha)}\left[\dot{P}_D^{+}(\alpha,-h)+\dot{P}_A^{+}(\alpha,h)\right]\\
&=\sum_{m=0}^{\infty}\frac{2(-1)^m\left(f_m^e+i\alpha g_m^e\right)}{\alpha^2-\left(\alpha_m^e\right)^2}-P_A^{-}(\alpha,h)+P_D^{-}(\alpha,-h)
\end{aligned}
\tag{2.42}
$$

and

$$
\begin{aligned}
&\frac{1}{\kappa^2(\alpha)L(\alpha)}\left[\dot{P}_D^{+}(\alpha,-h)-\dot{P}_A^{+}(\alpha,h)\right]\\
&=2\sum_{m=0}^{\infty}\frac{(-1)^m\left(f_m^o+i\alpha g_m^o\right)}{\alpha^2-\left(\alpha_m^o\right)^2}-P_A^{-}(\alpha,h)-P_D^{-}(\alpha,-h)
\end{aligned}
\tag{2.43}
$$

where kernel functions are defined as follows:

$$
N(\alpha)=\frac{\cos\left[\kappa(\alpha)h\right]}{\kappa(\alpha)}e^{-i\kappa(\alpha)h}
\tag{2.44}
$$

and

$$
L(\alpha)=\frac{\sin\left[\kappa(\alpha)h\right]}{\kappa(\alpha)}e^{-i\kappa(\alpha)h}
\tag{2.45}
$$

In order to find the solutions of the W-H equations, the classical factorization and decomposition W-H procedures are conducted. The general procedures to solve a W-H equation are presented in Appendix-A. Taking Eq. (2.42) for example, the first step is to split (factorize) the kernel functions into positive (denoted by a superscript '+') and negative (denoted by a superscript '-') parts which are regular in the upper half and the lower half complex α-plane, respectively.

$$
\begin{aligned}
&-\frac{i}{\kappa^{+}(\alpha)\kappa^{-}(\alpha)N^{+}(\alpha)N^{-}(\alpha)}\left[\dot{P}_D^{+}(\alpha,-h)+\dot{P}_A^{+}(\alpha,h)\right] \\
&=\sum_{m=0}^{\infty}2(-1)^m\left[\frac{f_m^e+i\alpha_m^e g_m^e}{2\alpha_m^e\left(\alpha-\alpha_m^e\right)}-\frac{f_m^e-i\alpha_m^e g_m^e}{2\alpha_m^e\left(\alpha+\alpha_m^e\right)}\right]-P_A^{-}(\alpha,h)+P_D^{-}(\alpha,-h)
\end{aligned}
\tag{2.46}
$$

where the factorized kernel functions satisfy:

$$
\kappa^{+}(\alpha)=\kappa^{-}(-\alpha),\ N^{+}(\alpha)=N^{-}(-\alpha) \tag{2.47}
$$

Collecting the terms which are regular in the upper half complex α-plane at the left-hand side of the equation and those regular in the lower half complex α-plane at the right-hand side, we have

$$
\begin{aligned}
&-\frac{i}{\kappa^{+}(\alpha)N^{+}(\alpha)}\left[\dot{P}_D^{+}(\alpha,-h)+\dot{P}_A^{+}(\alpha,h)\right] \\
&+\sum_{m=0}^{\infty}\frac{\left(f_m^e-i\alpha_m^e g_m^e\right)\sin\left(\kappa_m^e h\right)N^{-}(\alpha)\kappa^{-}(\alpha)}{\alpha_m^e\left(\alpha+\alpha_m^e\right)} \\
&=\sum_{m=0}^{\infty}\frac{(-1)^m\left(f_m^e+i\alpha_m^e g_m^e\right)N^{-}(\alpha)\kappa^{-}(\alpha)}{\alpha_m^e\left(\alpha-\alpha_m^e\right)} \\
&-P_A^{-}(\alpha,h)N^{-}(\alpha)\kappa^{-}(\alpha)+P_D^{-}(\alpha,-h)N^{-}(\alpha)\kappa^{-}(\alpha)
\end{aligned}
\tag{2.48}
$$

The regularity of the left-hand side terms in the lower half complex α-plane is violated by simple poles occurring at zeros of the denominator. They can be eliminated using the following decomposition procedure:

$$
\begin{aligned}
&-\frac{i}{\kappa^{+}(\alpha)N^{+}(\alpha)}\left[\dot{P}_D^{+}(\alpha,-h)+\dot{P}_A^{+}(\alpha,h)\right] \\
&+\sum_{m=0}^{\infty}\frac{(-1)^m\left(f_m^e-i\alpha_m^e g_m^e\right)N^{-}\left(-\alpha_m^e\right)\kappa^{-}\left(-\alpha_m^e\right)}{\alpha_m^e\left(\alpha+\alpha_m^e\right)} \\
&+\sum_{m=0}^{\infty}\frac{(-1)^m\left(f_m^e-i\alpha_m^e g_m^e\right)\left[N^{-}(\alpha)\kappa^{-}(\alpha)-N^{-}\left(-\alpha_m^e\right)\kappa^{-}\left(-\alpha_m^e\right)\right]}{\alpha_m^e\left(\alpha+\alpha_m^e\right)} \\
&=\sum_{m=0}^{\infty}\frac{(-1)^m\left(f_m^e+i\alpha_m^e g_m^e\right)N^{-}(\alpha)\kappa^{-}(\alpha)}{\alpha_m^e\left(\alpha-\alpha_m^e\right)} \\
&-P_A^{-}(\alpha,h)N^{-}(\alpha)\kappa^{-}(\alpha)+P_D^{-}(\alpha,-h)N^{-}(\alpha)\kappa^{-}(\alpha)
\end{aligned}
\tag{2.49}
$$

Considering analytical continuation followed by Liouville's theorem and making full use of the properties of the split function Eq. (2.47), the W-H solution is obtained as follows:

$$\begin{aligned}&\dot{P}_D^+(\alpha,-h)+\dot{P}_A^+(\alpha,h)\\&=-i\sum_{m=0}^{\infty}\frac{(-1)^m\left(f_m^e-i\alpha_m^e g_m^e\right)N^+\left(\alpha_m^e\right)\kappa^+\left(\alpha_m^e\right)N^+(\alpha)\kappa^+(\alpha)}{\alpha_m^e\left(\alpha+\alpha_m^e\right)}\end{aligned}\tag{2.50}$$

Based on the same procedures described above, we can obtain the solution to the second W-H equation:

$$\begin{aligned}&\dot{P}_A^+(\alpha,h)-\dot{P}_D^+(\alpha,-h)\\&=\sum_{m=0}^{\infty}\frac{(-1)^m\left(f_m^o-i\alpha_m^o g_m^o\right)L^+\left(\alpha_m^o\right)\kappa^+\left(\alpha_m^o\right)L^+(\alpha)\kappa^+(\alpha)}{\alpha_m^o\left(\alpha+\alpha_m^o\right)}\end{aligned}\tag{2.51}$$

Here, the split functions are regular in the upper half complex α-plane and their explicit expressions are obtained based on the method described by Mittra (1971) as

$$\begin{aligned}N^+(\alpha)=&\sqrt{\frac{\cos(kh)}{k}}\times\exp\left\{\ln\left[\frac{\alpha-i\kappa(\alpha)}{k}\right]\frac{\kappa(\alpha)h}{\pi}\right\}\\&\times\exp\left\{\left(1-C+\ln\left(\frac{2\pi}{kh}\right)-\frac{i\pi}{2}\right)\frac{-i\alpha h}{\pi}\right\}\times\prod_{m=1}^{\infty}\left(1+\frac{\alpha}{\alpha_m^e}\right)\times\exp\left(\frac{-i\alpha h}{m\pi}\right)\end{aligned}\tag{2.52}$$

and

$$\begin{aligned}L^+(\alpha)=&\sqrt{\frac{\sin(kh)}{k}}\times\exp\left\{\ln\left[\frac{\alpha-i\kappa(\alpha)}{k}\right]\frac{\kappa(\alpha)h}{\pi}\right\}\\&\times\exp\left\{\left(1-C+\ln\left(\frac{2\pi}{kh}\right)-\frac{i\pi}{2}\right)\frac{-i\alpha h}{\pi}\right\}\times\prod_{m=1}^{\infty}\left(1+\frac{\alpha}{\alpha_m^o}\right)\times\exp\left(\frac{-i\alpha h}{m\pi}\right)\end{aligned}\tag{2.53}$$

where $C=0.57721...$ denotes the Euler-Mascheroni constant.

2.2.4 Sound pressure field in the natural domain

Then, to determine the modal response coefficients, we employ the well-known mode-matching method which has been extensively applied to analyze the sound fields inside waveguide structures. Using continuity relations of sound pressure and particle velocity at imaginary interface II, we have

$$\sum_{m=0}^{\infty} g_m^e \sin\left[\kappa_m^e y\right] - \sum_{n=0}^{\infty} b_n^e \sin\left(\kappa_n^e y\right) = \sum_{n=1}^{\infty}\sum_{j=0}^{\infty} \frac{\rho k c_0 Q_n \sin\left(\kappa_j^e y_n\right)\sin\left(\kappa_j^e y\right)}{2\Lambda_j^e \alpha_j^e} e^{i\alpha_j^e x_n} \tag{2.54}$$

and

$$\sum_{m=0}^{\infty} f_m^e \sin\left[\kappa_m^e y\right] - \sum_{n=0}^{\infty} i\alpha_n^e b_n^e \sin\left[\kappa_n^e y\right] = -\sum_{n=1}^{\infty}\sum_{j=0}^{\infty} \frac{i\rho k c_0 Q_n \sin\left(\kappa_j^e y_n\right)\sin\left(\kappa_j^e y\right)}{2\Lambda_j^e} e^{i\alpha_j^e x_n} \tag{2.55}$$

Similarly, we have

$$\sum_{m=0}^{\infty} g_m^o \cos\left[\kappa_m^o y\right] - \sum_{n=0}^{\infty} b_n^o \cos\left[\kappa_n^o y\right] = \sum_{n=1}^{\infty}\sum_{j=0}^{\infty} \frac{\rho k c_0 Q_n \cos\left(\kappa_j^o y_n\right)\cos\left(\kappa_j^o y\right)}{2\Lambda_j^o \alpha_j^o} e^{i\alpha_j^o x_n} \tag{2.56}$$

and

$$\sum_{m=0}^{\infty} f_m^o \cos\left[\kappa_m^o y\right] - \sum_{n=0}^{\infty} i\alpha_n^o b_n^o \cos\left(\kappa_n^o y\right) = -\sum_{n=1}^{\infty}\sum_{j=0}^{\infty} \frac{i\rho k c_0 Q_n \cos\left(\kappa_j^o y_n\right)\cos\left(\kappa_j^o y\right)}{2\Lambda_j^o} e^{i\alpha_j^o x_n} \tag{2.57}$$

Multiply both sides of Eqs. (2.54) and (2.55) by $\sin\left(\kappa_s^e y\right)$; Eqs. (2.56) and (2.57) by $\cos\left(\kappa_s^o y\right)$, and integrate along the opening in terms of y. Making full use of the orthogonality of trigonometric functions, we have the following identities:

$$g_s^e - b_s^e = \underbrace{\sum_{n=1}^{\infty} \frac{\rho k c_0 Q_n \sin\left(\kappa_s^e y_n\right) e^{i\alpha_s^e x_n}}{2\Lambda_s^e \alpha_s^e}}_{Y_{s1}^e} \tag{2.58}$$

$$\underbrace{f_s^e - i\alpha_s^e\, b_s^e}_{U_{ss}^e} = \underbrace{-\sum_{n=1}^{\infty} \frac{i\rho k c_0 Q_n \sin\left(\kappa_s^e y_n\right) e^{i\alpha_s^e x_n}}{2\Lambda_s^e}}_{M_{s1}^e} \tag{2.59}$$

$$\underbrace{f_s^e + i\alpha_s^e\, g_s^e}_{U_{ss}^e} = -i\sum_{m=0}^{\infty} \underbrace{\frac{(-1)^m \kappa^+\left(\alpha_m^e\right) N^+\left(\alpha_m^e\right) \kappa^+\left(\alpha_s^e\right) N^+\left(\alpha_s^e\right)}{\alpha_m^e\left(\alpha_s^e + \alpha_m^e\right)\Lambda_s^e(-1)^s}}_{H_{sm}^e} \left(\underbrace{f_m^e - i\alpha_m^e\, g_m^e}_{U_{mm}^e}\right) \tag{2.60}$$

Similarly, we have

$$g_s^o - b_s^o = \underbrace{\sum_{n=1}^{\infty} \frac{\rho k c_0 Q_n \cos\left(\kappa_s^o y_n\right) e^{i\alpha_s^o x_n}}{2\Lambda_s^o \alpha_s^o}}_{Y_{s1}^o} \tag{2.61}$$

$$\underbrace{f_s^o - i\alpha_s^o\, b_s^o}_{U_{ss}^o} = \underbrace{-\sum_{n=1}^{\infty} \frac{i\rho k c_0 Q_n \cos\left(\kappa_s^o y_n\right) e^{i\alpha_s^o x_n}}{2\Lambda_s^o}}_{M_{s1}^o} \tag{2.62}$$

$$\underbrace{f_s^o + i\alpha_s^o\, g_s^o}_{U_{ss}^o} = \sum_{m=0}^{\infty} \underbrace{\frac{(-1)^m \kappa^+\left(\alpha_m^o\right) L^+\left(\alpha_m^o\right) \kappa^+\left(\alpha_s^o\right) L^+\left(\alpha_s^o\right)}{\alpha_m^o\left(\alpha_s^o + \alpha_m^o\right)\Lambda_s^o(-1)^s}}_{H_{sm}^o} \left(\underbrace{f_m^o - i\alpha_m^o\, g_m^o}_{U_{mm}^o}\right) \tag{2.63}$$

Rewrite Eqs. (2.58) to (2.63) in matrix forms, we have

$$\mathbf{G}^e - \mathbf{B}^e = \mathbf{Y}^e \tag{2.64}$$

$$\mathbf{F}^e - \mathbf{U}^e\mathbf{B}^e = \mathbf{M}^e \tag{2.65}$$

$$\mathbf{F}^e + \mathbf{U}^e\mathbf{G}^e = \mathbf{H}^e\left(\mathbf{F}^e - \mathbf{U}^e\mathbf{G}^e\right) \tag{2.66}$$

$$\mathbf{G}^o - \mathbf{B}^o = \mathbf{Y}^o \tag{2.67}$$

$$\mathbf{F}^o - \mathbf{U}^o\mathbf{B}^o = \mathbf{M}^o \tag{2.68}$$

$$\mathbf{F}^o + \mathbf{U}^o\mathbf{G}^o = \mathbf{H}^o\left(\mathbf{F}^o - \mathbf{U}^o\mathbf{G}^o\right) \tag{2.69}$$

where $\mathbf{B}^o$, $\mathbf{B}^e$, $\mathbf{F}^o$, $\mathbf{F}^e$, $\mathbf{G}^o$, and $\mathbf{G}^e$ are unknown coefficients to be determined; $\mathbf{Y}^o$, $\mathbf{Y}^e$, $\mathbf{M}^o$, $\mathbf{M}^e$, $\mathbf{U}^o$, $\mathbf{U}^e$, $\mathbf{H}^o$, and $\mathbf{H}^e$ are the known matrices that can be constructed according to Eqs. (2.58) to (2.63), respectively. Matrix inversions are needed in the process of solving the equations. Therefore, we let all the subscript indexes be equal to guarantee that they are square matrices.

After determining the unknown coefficients, the radiated sound pressure fields of regions Ω_A and Ω_D in the natural domain can be obtained by taking the inverse Fourier transform of Eq. (2.20) as

$$\begin{bmatrix} p_A(x,y) \\ p_D(x,y) \end{bmatrix} = \frac{1}{2\pi}\int_\Gamma \begin{bmatrix} \dfrac{\dot{P}_A^+(\alpha,h)}{-i\kappa(\alpha)} e^{-i\kappa(\alpha)(y-h)} \\ \dfrac{\dot{P}_D^+(\alpha,-h)}{i\kappa(\alpha)} e^{i\kappa(\alpha)(y+h)} \end{bmatrix} e^{i\alpha x} d\alpha \tag{2.70}$$

where the integration path Γ is presented in Figure 2.3, and

$$\dot{P}_D^+(\alpha,-h) = \frac{1}{2}\left\{ \begin{aligned} &-\sum_{m=0}^{\infty} \frac{i(-1)^m \left(f_m^e - i\alpha_m^e g_m^e\right) N^+\left(\alpha_m^e\right)\kappa^+\left(\alpha_m^e\right) N^+(\alpha)\kappa^+(\alpha)}{\alpha_m^e\left(\alpha+\alpha_m^e\right)} \\ &-\sum_{m=0}^{\infty} \frac{(-1)^m \left(f_m^o - i\alpha_m^o g_m^o\right) L^+\left(\alpha_m^o\right)\kappa^+\left(\alpha_m^o\right) L^+(\alpha)\kappa^+(\alpha)}{\alpha_m^o\left(\alpha+\alpha_m^o\right)} \end{aligned} \right\} \tag{2.71}$$

$$\dot{P}_A^+(\alpha,h) = \frac{1}{2}\left\{ \begin{aligned} &-\sum_{m=0}^{\infty} \frac{i(-1)^m \left(f_m^e - i\alpha_m^e g_m^e\right) N^+\left(\alpha_m^e\right)\kappa^+\left(\alpha_m^e\right) N^+(\alpha)\kappa^+(\alpha)}{\alpha_m^e\left(\alpha+\alpha_m^e\right)} \\ &+\sum_{m=0}^{\infty} \frac{(-1)^m \left(f_m^o - i\alpha_m^o g_m^o\right) L^+\left(\alpha_m^o\right)\kappa^+\left(\alpha_m^o\right) L^+(\alpha)\kappa^+(\alpha)}{\alpha_m^o\left(\alpha+\alpha_m^o\right)} \end{aligned} \right\} \tag{2.72}$$

Eq. (2.70) can be numerically evaluated using the method introduced by Gabard and Astley (2006). However, the direct calculation of the inverse Fourier transform is expensive and time-consuming. To get an asymptotic solution to Eq. (2.70), we conduct a change of variables as follows:

$$\alpha = -k\cos w, \quad x = r\cos\theta, \quad y = r\sin\theta \tag{2.73}$$

Then, Eq. (2.70) is transformed into the complex w-plane as

$$\begin{bmatrix} p_A(r,\theta) \\ p_D(r,\theta) \end{bmatrix} = \frac{i}{2\pi}\int_{\Gamma_w} \begin{bmatrix} \dot{P}_A^+(-k\cos w, h) \\ \dot{P}_D^+(-k\cos w, -h) \end{bmatrix} e^{-ik\sin wh} e^{krg(w)} dw \tag{2.74}$$

where

$$g(w) = -i\cos(w+\theta) \tag{2.75}$$

and the new integration path Γ_w is illustrated in Figure 2.3. Next, we deform the path into a new path Γ_s known as the steepest descent path (SDP) which passes through the saddle point $w_s = -\theta$. The criterion for the selection of Γ_s are that the imaginary part of the function $g(w)$ is constant and its real part reaches the maximum value at the saddle point which can be described as $g'(w_s) = 0$.

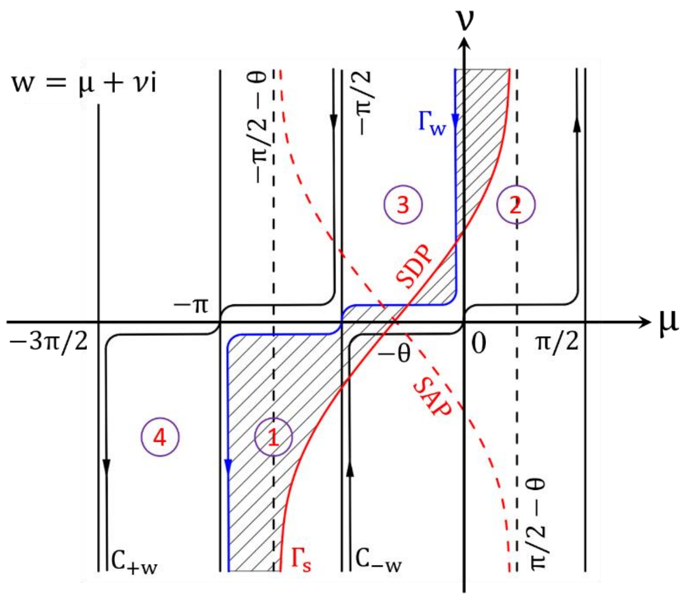

Figure 2.3 Mapping of the square root function from the complex α-plane to the new complex w-plane.

As $kr \to \infty$, the major contribution to the integral of Eq. (2.74) along Γ_s comes from a small segment around the saddle point due to the exponentially decaying factor in the integrand. Making full use of the error function, the asymptotic evaluation of the inverse Fourier transform through the saddle point method gives

$$\begin{bmatrix} p_A(r,\theta) \\ p_D(r,\theta) \end{bmatrix} = \frac{i}{\sqrt{2\pi kr}} \begin{bmatrix} \dot{P}_A^+(-k\cos\theta, h) e^{\frac{i\pi}{4}} \\ \dot{P}_D^+(-k\cos\theta, -h) e^{-\frac{3i\pi}{4}} \end{bmatrix} e^{ik\sin\theta h} e^{-ikr} \operatorname{erf}\left(\sqrt{\frac{kr}{2}}\Delta\Gamma\right) \tag{2.76}$$

where the error function is expressed as

$$\operatorname{erf}(x) = \frac{2}{\sqrt{\pi}} \int_0^x e^{-t^2} dt \tag{2.77}$$

and $\Delta\Gamma$ is a small length near the saddle point. Detailed derivations of the saddle-point method can be found in Appendix-B.

In numerical calculations, we assume that the value of the error function is always 1, which results in the far-field approximation of the radiated sound pressure field. It is sufficient for most engineering applications. For detailed analysis, the sound field near the opening of the unbaffled long enclosure is also needed which can be obtained either by evaluating the inverse Fourier transform directly or using the numerical methods.

2.3 Sound radiation from an unbaffled long enclosure

Numerical calculations and FEM simulations are done to validate the theoretical model proposed in Section 2.2, and reveal the formation mechanisms behind the sound radiation phenomenon.

The configuration of an unbaffled long enclosure, monopole point source, and the properties of the air media are listed in Table 2-1. An unbaffled long enclosure of 2 m long and 0.4 m high is considered here. A monopole point source with volume velocity strength being 0.01 $\mathrm{m^2/s}$ is located at (-1, -0.1) m. The far-field observation radius is set as 2 m, and the observation angle is between [-150 150] degrees. Besides, the speed of sound and the density of air are 340 $\mathrm{m/s}$ and 1.225 $\mathrm{kg/m^3}$, respectively.

Table 2-1 Configuration of the unbaffled long enclosure, air properties, monopole point source, and the far-field directivity pattern.

Air Properties		**Monopole Point Source**	
Density	1.225 kg/m^3	Location	(-1, -0.1) m
Sound speed	340 m/s	Volume velocity strength	0.01 m^2/s
Unbaffled Long Enclosure		**Directivity Patterns**	
Height	0.4 m	Far-field radius	2 m
Truncated length	2 m	Observation angle	[-150, 150] degrees

2.3.1 Numerical implementation of the theoretical model

2.3.1.1 Calculation of the wavenumbers

Before any calculation, the wavenumbers must be determined in advance using Eqs. (2.10) and (2.11), respectively. Part of the odd and the even wavenumbers at 1000 Hz in the horizontal and transversal directions are presented in Figure 2.4. As presented in Figure 2.4 (b) and (d), the wavenumbers in the transversal direction are pure real which are determined by the rigid boundary conditions and the height of the unbaffled long enclosure. In Figure 2.4 (a) and (c), however, the wavenumbers in the horizontal direction are either pure imaginary or real, as the free space wavenumber at 1000 Hz is 18.5. Besides, the imaginary parts are negative to represent outgoing waves.

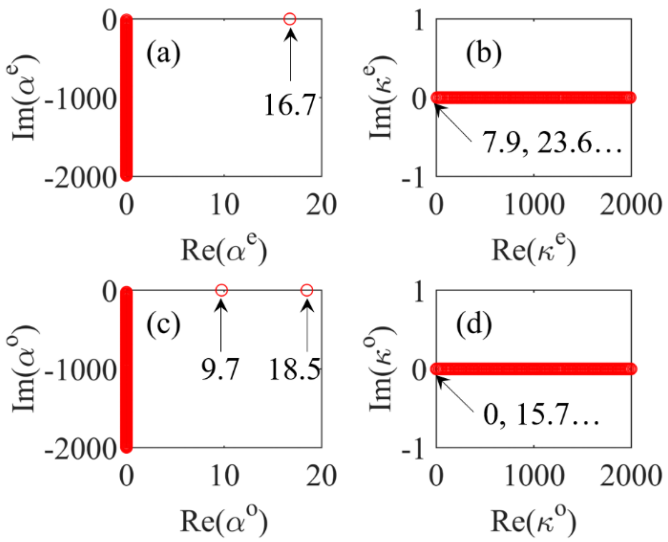

Figure 2.4 Part of the odd (a, b) and even (c, d) wavenumbers at 1000 Hz along the horizontal (a, c) and transversal (b, d) directions, respectively.

2.3.1.2 Modal truncations and convergence checks

Theoretically, the sound pressure field inside the long enclosure is composed of infinite propagating modes as presented in Eqs. (2.9) and (2.13). However, in numerical implementations, the modal series must be truncated. Therefore, a convergence check is carried out to determine the maximum mode number based on the trade-off between computation cost and accuracy. The criterion of convergence is defined that the relative error of pressure values between two successive mode numbers of arbitrary locations is less than 5%. As the maximum mode number increases as the increase of geometrical dimension and frequency, it could be determined by examining the convergence of the total sound pressure of arbitrarily picked points at 2000 Hz. The convergence of sound pressure against the modal number at locations (-2, 0) m, (-1, 0.2) m, and (0, -0.2) m are presented in Figure 2.5 (a), (b), and (c), respectively. At (-2, 0) m, the real and imaginary parts of sound pressure converge after 3 modes. At (-1, 0.2) m and (0, -0.2) m, the sound pressures become stable when the mode number is beyond approximately 10. Generally, more acoustical modes are needed near the opening as it is the interface of the incident and reflected sound waves. After some tentative calculations, 20 modes are finally considered for this configuration to ensure accuracy.

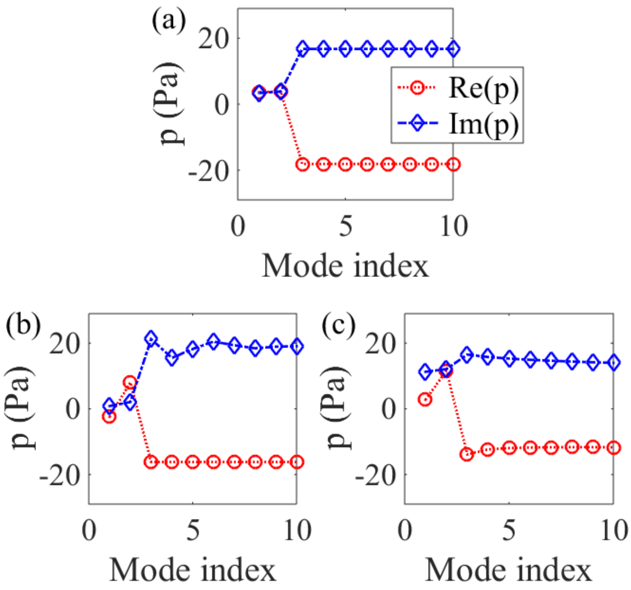

Figure 2.5 Convergence checks of sound pressure at 2000 Hz: (a) (-2, 0) m, (b) (-1, 0.2) m, and (c) (0, -0.2) m.

Then, SPL distributions inside the unbaffled long enclosure at 2000 Hz calculated by the FEM and W-H technique are compared in Figure 2.6. The commercial software COMSOL Multiphysics is applied for the FEM. When using the theoretical model, the size of the enclosure and the outside region can be infinite. However, this is impossible for the FEM. To solve this problem, the calculation domain is bounded by a perfectly matched layer (PML) which is an artificial absorption layer that allows sound waves to propagate out without reflections (Wang et al., 2015). To ensure the accuracy of the FEM and to satisfy the requirement for the acoustical elements which requires that the maximum side-length of the acoustical meshes should be less than 1/6 of the minimum wavelength in the targeted frequency range. The whole acoustical domain is discretized into more than 7.8×10^5 elements. In addition, both the curvature parameter and scaling factor of the PML are set to be 1 in the current analysis according to the finding of Hein et al. (2004). The SPL fields agree well with each other which indicates that 20 modes are sufficient to ensure an accurate result for the current configuration.

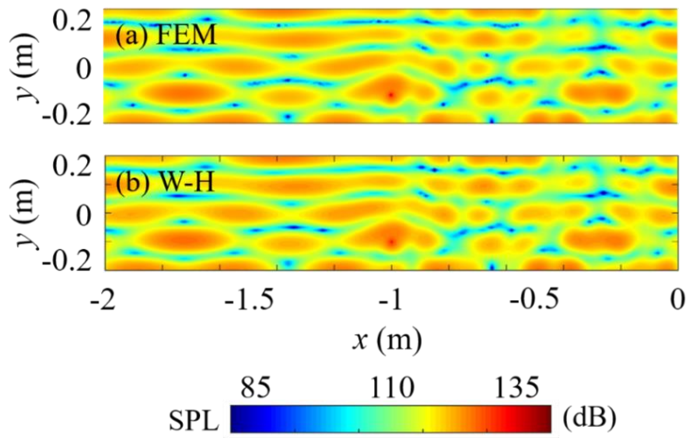

Figure 2.6 SPL distribution inside the long enclosure at 2000 Hz obtained by (a) the FEM, and (b) the W-H technique.

2.3.1.3 Accuracy analysis of the far-field approximation

Several approximations are conducted to simplify the inverse Fourier transform and obtain the explicit directivity pattern of the radiated sound field. Among them, the one that affects the calculation accuracy the most is that we assume that the value of the error function in Eq. (2.76) is always 1. However, as illustrated in Figure 2.7 (a), it approaches 1 when the input is beyond 3. Hence, to ensure an accurate result of the radiated sound field, we should guarantee that $\sqrt{kr/2}\Delta\Gamma$ is larger than 3, which limits the choice of the observation radius in the targeted frequency range.

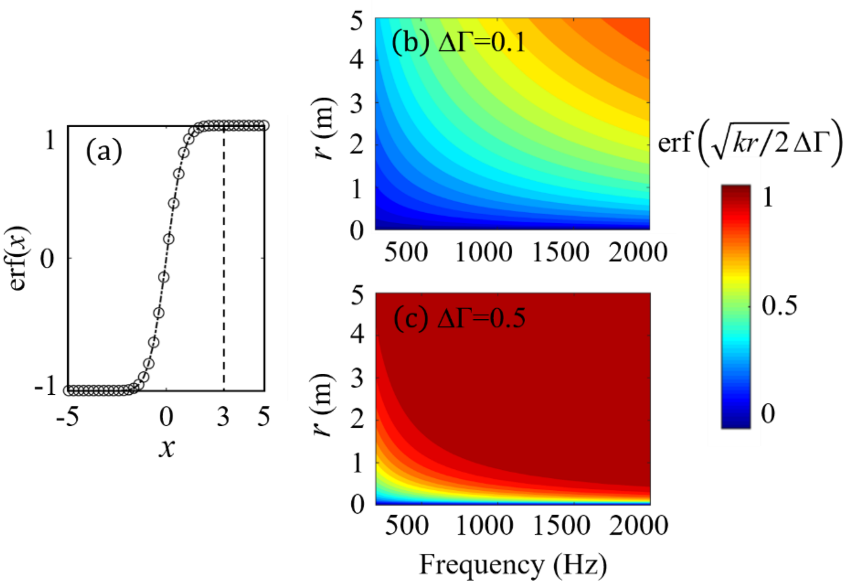

Figure 2.7 The properties of the error function and the accuracy analysis of the far-field approximation.

Besides, as $\Delta\Gamma$ is an unknown but small length near the saddle point, we choose two values of $\Delta\Gamma$ to explore the properties of the error function. As demonstrated by Figure 2.7 (b) and (c), the value of the error function approaches 1 with the increase of the observation distance and frequency. Therefore, an observation radius that is large enough to ensure the accuracy of the result should be determined when the frequency range is chosen. After some trial calculations, generally, the observation radius can be roughly chosen as three to five times the enclosure height to ensure an acceptable result of the radiated sound pressure field.

2.3.1.4 Model validation through the FEM

Comparisons of the SPLs obtained by the FEM and the W-H technique within the targeted frequency range at randomly picked receivers (-0.5, 0) m and (-2, 2) m are presented in Figure 2.8. Good agreement can be observed even though discrepancies exist at the peaks which are within the acceptable range of error. Therefore, the results verify the proposed model in the calculation of sound pressure fields inside and outside an unbaffled long enclosure.

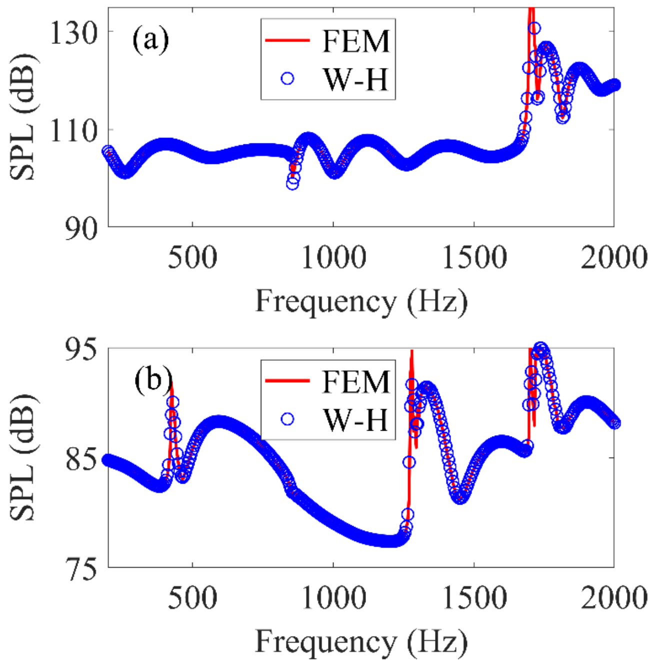

Figure 2.8 Comparisons of SPLs obtained by the FEM and the W-H technique at (a) receiver (-0.5,0) m and (b) receiver (-2, 2) m.

The directivity patterns of the radiated sound field obtained by the FEM and the W-H technique are compared in Figure 2.9. Good agreement can be observed. At 200 Hz, as shown in Figure 2.9 (a), the radiated sound field is symmetric about the central line of the long enclosure. As the cutoff frequency of the long enclosure is 425 Hz, only a plane wave exists inside the long enclosure at 200 Hz. The pressure along the opening is almost the same, so the radiated sound field exhibits symmetric distribution. At 1000 Hz and 1800 Hz, however, as presented in Figure 2.9 (b) and (c), lobes can be seen in front of the opening as higher-order acoustical modes have been excited inside the long enclosure and the sound pressure distribution at the opening is non-uniform which gives rise to the formation of lobes in front of the opening.

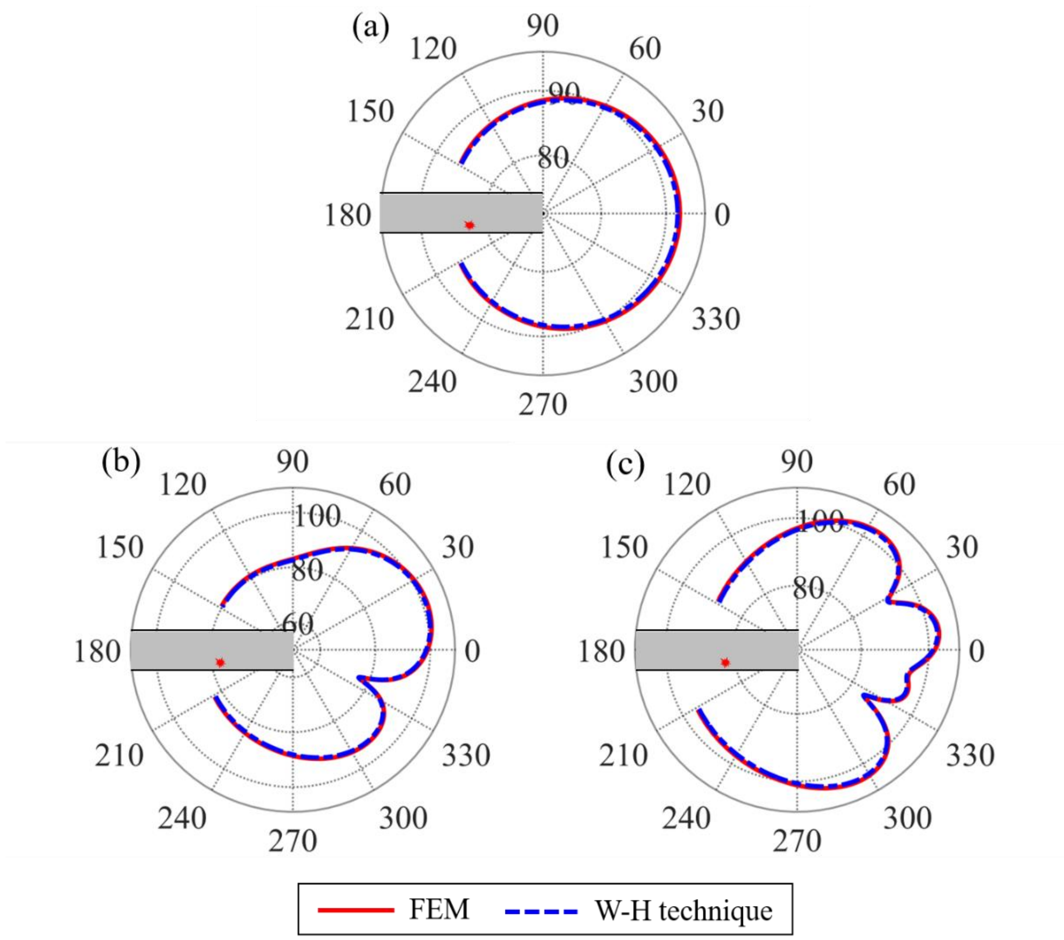

Figure 2.9 Directivity patterns of the radiated sound field obtained by the FEM and the W-H technique at (a) 200 Hz, (b) 1000 Hz, and (c) 1800 Hz.

The distribution patterns of the radiated SPL fields can be roughly explained from the perspective of acoustical rays as presented in Figure 2.10. In the shadow zones, only diffracted waves contribute to the sound fields. The SPLs in these regions are uniformly distributed. In the illuminated zone, however, direct, reflected, and the diffracted sound waves propagate to this region with different phases and over different distances which results in the lobes in front of the enclosure opening.

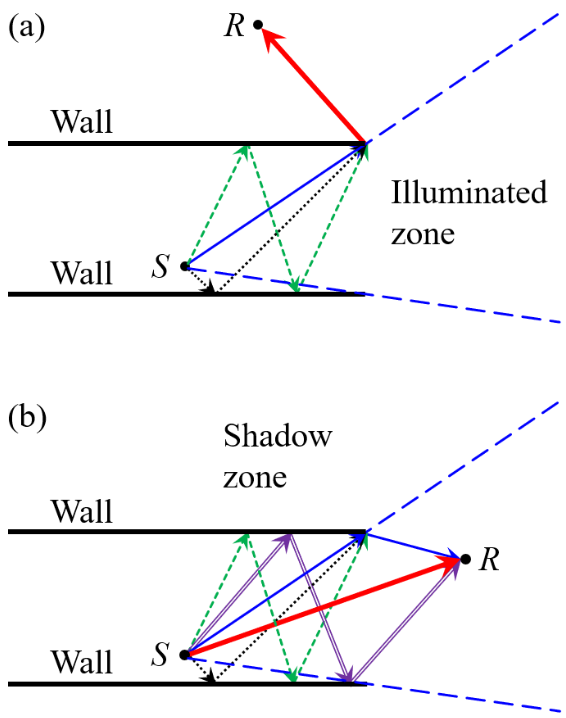

Figure 2.10 Acoustical rays from the sound source to the (a) shadow and (b) illuminated zones of an unbaffled long enclosure.

2.3.2 Modal analysis of sound pressure fields

The normalized modal response coefficients at 200 Hz and 1000 Hz are presented in Figure 2.11. At 200 Hz, as presented in Figure 2.11 (a), only plane-wave (zeroth even mode) contributes to the total sound pressure field as it is under the cut-off frequency of the long enclosure which is 475 Hz. At 1000 Hz, the first two even and odd acoustical modes contribute to the total sound pressure field. To further investigate the formation mechanisms of the sound distribution outside the long enclosure, the radiation pattern of a single-mode incidence is presented. The first three cosine and sine modal functions are given in Figure 2.12. The corresponding eigenfrequencies are 0, 850 Hz, 1700 Hz; and 425 Hz, 1275 Hz, 2125 Hz, respectively. These modes are imposed on the opening of the long enclosure as pressure boundary conditions in COMSOL. The radiated sound pressure field of these modes can then be obtained.

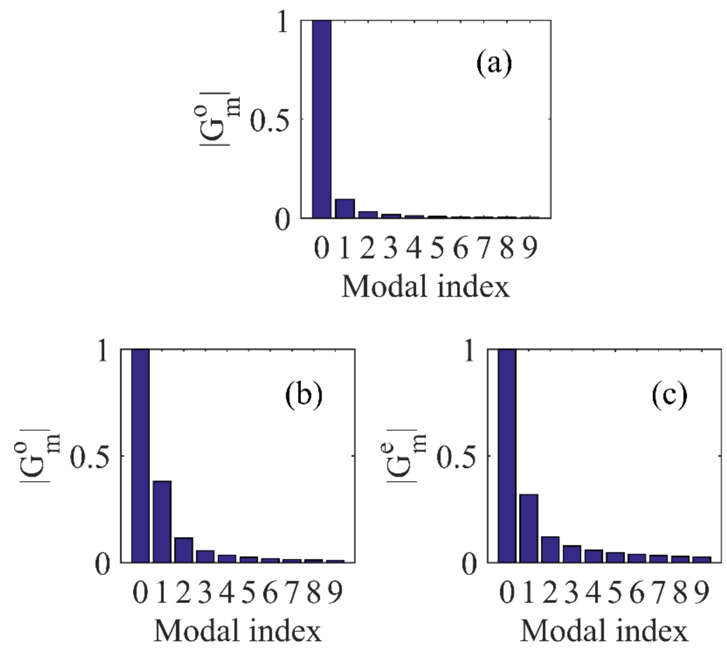

Figure 2.11 Normalized modal response coefficients of sound pressure at the opening (a) 200 Hz, odd (b), and even (c) modal response at 1000 Hz.

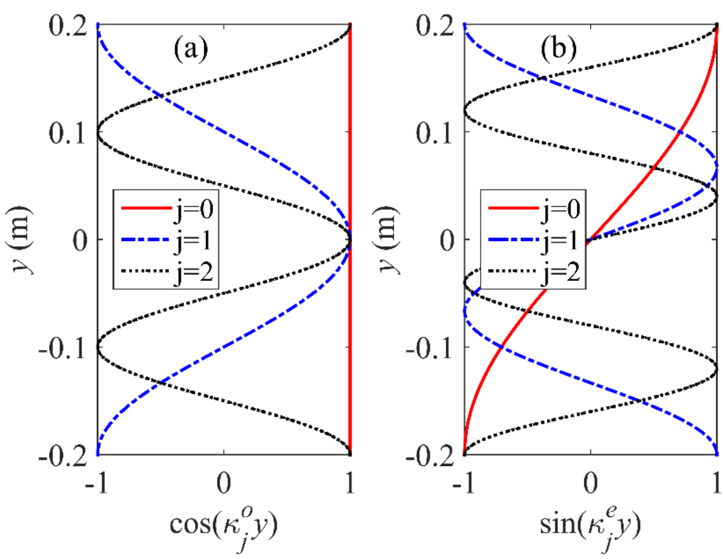

Figure 2.12 Shapes of the first three cosine (a) and sine (b) modes; the corresponding eigenfrequencies are 0, 850 Hz, 1700 Hz; and 425 Hz, 1275 Hz, 2125 Hz.

The radiated SPL fields of the zeroth cosine and sine mode incidence at 200 Hz are presented in Figure 2.13. The radiated SPLs are symmetric about the central line of the long enclosure. However, for cosine mode radiation, there is only one big lobe in front of the opening, while there are two lobes at two sides of the opening for sine mode radiation. This finding can be verified in Figure 2.14. There is an even number of lobes for the sine mode radiation, while there is an odd number of lobes for the cosine mode radiation. Their joint contributions give rise to different SPL distributions outside the unbaffled long enclosure.

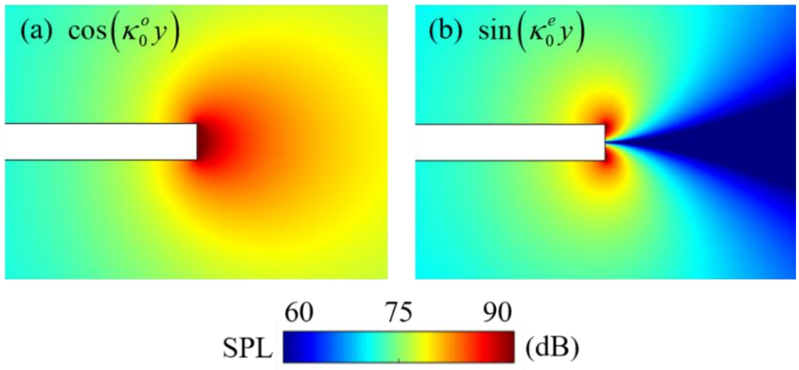

Figure 2.13 Radiated SPL field of single-mode incidence at 200 Hz: the zeroth cosine (a) and sine (b) mode.

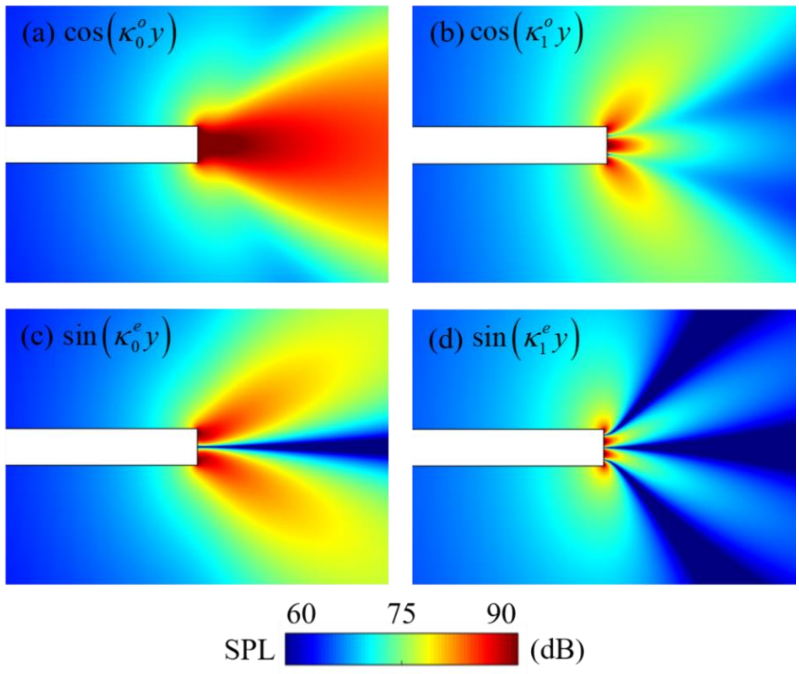

Figure 2.14 Radiated SPL fields of single-mode incidence at 1000 Hz: the zeroth (a) and the first (b) cosine mode, the zeroth (c) and the first (d) sine mode.

2.3.3 Baffled and unbaffled long enclosures

In early times, a recourse was often made to simplify the sound radiation problem in which the opening is surrounded by an infinite baffle, thereby eliminating the effect of the sharp edge. Sound radiation from a baffled opening can be solved by the Rayleigh integral method which can be expressed as (Pamies et al., 2011, McAlpine et al., 2012; Wang & Choy, 2019)

$$p(x,y) = i\rho k c_0 \int_S G v_n dS \tag{2.78}$$

where the Green's function for a baffled opening is given by

$$G = \frac{e^{-ikr}}{2\pi r},\ r = \left|(x,y)_R - (x,y)_S\right| \tag{2.79}$$

and v_n denotes the particle velocity normal to the opening.

For sound radiation from an unbaffled opening, there is no theoretical formula for Green's function of the radiated sound field. Hence, the Rayleigh integral cannot be directly applied to deal with unbaffled sound radiation problems. Besides, it is probably adequate for predicting sound radiation to the hemisphere in the front of the enclosure opening. However, the sideline radiation, as well as the sound field at the backside of the unbaffled long enclosure, is heavily influenced by the diffraction effect at the edge which cannot reasonably be predicted by the baffled model. The numerical method can be employed to obtain Green's function outside an unbaffled opening (Wang & Choy, 2019), Nevertheless, multiple calculations are required for each frequency concerned which is time-consuming.

Directivity patterns of radiated SPL fields from the opening of an unbaffled and a baffled long enclosure are compared in Figure 2.15. As can be observed, directivity patterns are roughly consistent except for the region near the infinite baffle. And the

SPLs of the baffled long enclosure are larger than that of an unbaffled enclosure in this region.

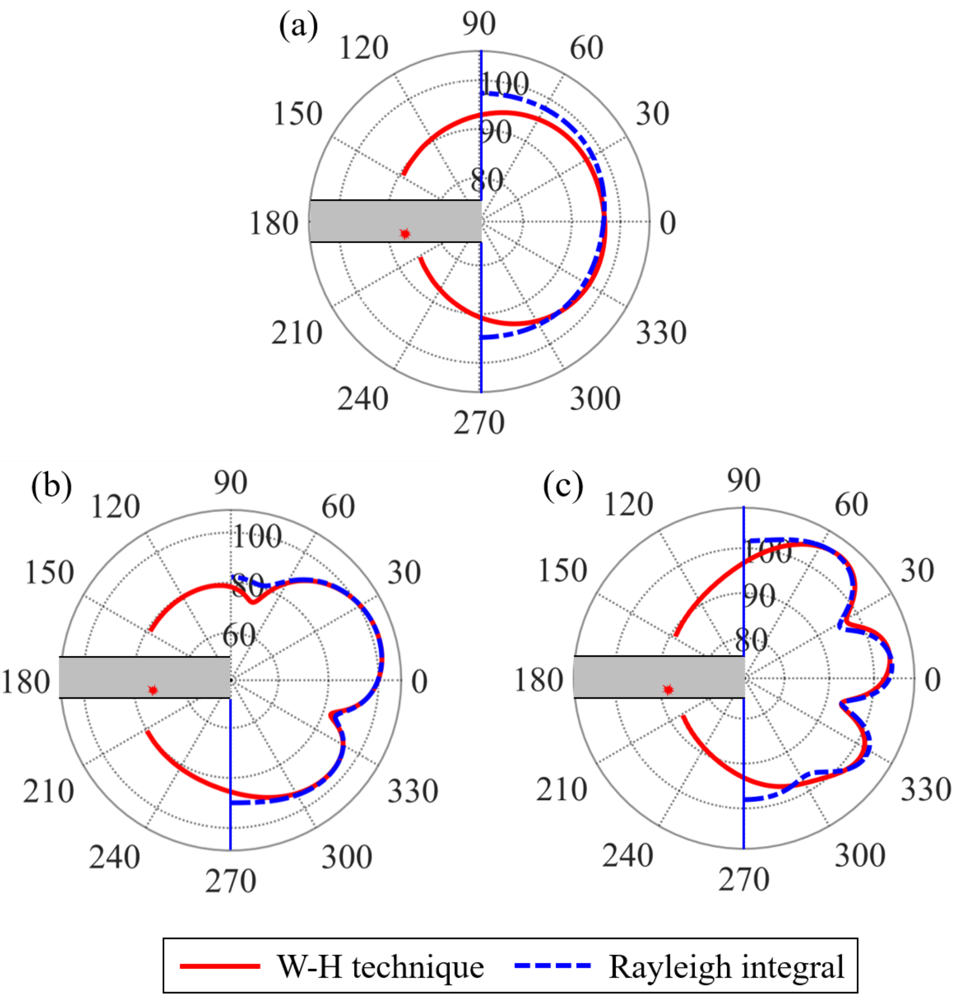

Figure 2.15 Directivity patterns of the radiated SPL fields outside an unbaffled and a baffled long enclosure at (a) 600 Hz, (b) 1200 Hz, and (c) 2000 Hz.

This phenomenon can be explained from the perspective of the conservation of sound energy. The distributions of sound intensity near the openings of a baffled and an unbaffled long enclosure at 600 Hz are presented in Figure 2.16. For an unbaffled long enclosure, part of the sound energy is diffracted into the shadow zone as shown in Figure 2.16 (a). This part of sound energy, however, is blocked by the infinite baffle which either propagates along the boundary or reflects towards the opening as shown in Figure 2.16 (b). Consequently, the calculated SPLs using the baffled model are often larger than that obtained by the unbaffled model in the region near the infinite baffle. It also implies that the Rayleigh integral method cannot be directly applied to predict the sound radiated from an unbaffled long enclosure.

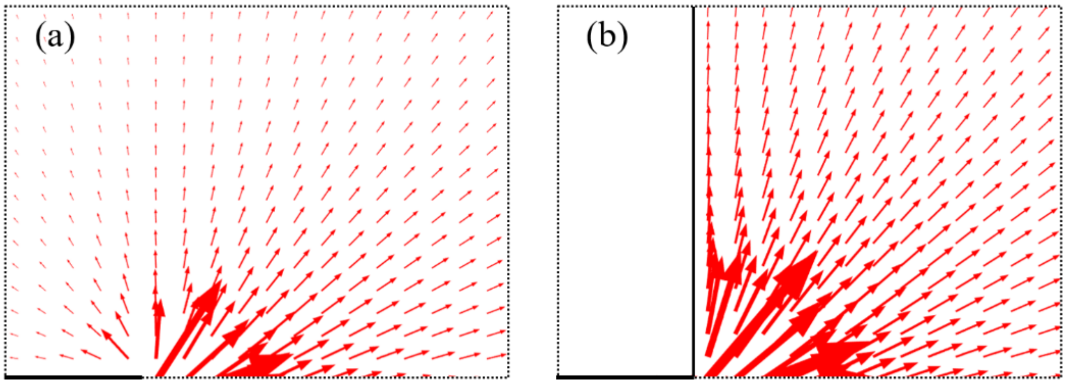

Figure 2.16 Distribution of sound intensity near the opening of an unbaffled (a) and a baffled (b) long enclosure at 600 Hz.

2.3.4 Source effect

The effect of source locations on the sound radiation phenomenon is investigated by changing one of the coordinates while keeping the other one constant. The directivity patterns of the radiated SPL field when the source is located at x = -1 m are presented in Figure 2.17. At 500 Hz, as shown in Figure 2.17 (a), the SPLs in the shadow zone increase with the decrease of y coordinates. This can be explained by the GTD that the incident angles of the sound pressure towards the sharp edge increase which gives rise to high diffraction efficiency. At higher frequencies, as illustrated in Figure 2.17 (b) and (c), the principle still holds for most of the results. However, when the point source is located at y=-0.05 m, the radiation patterns are irregular as the diffracted sound field is determined by the incident angle and sound pressure. At higher frequencies, multiple higher-order acoustical modes contribute to the sound pressure field, which leads to the complex distribution of sound pressure at the edge. Therefore, the diffracted sound field in the shadow zone is irregular.

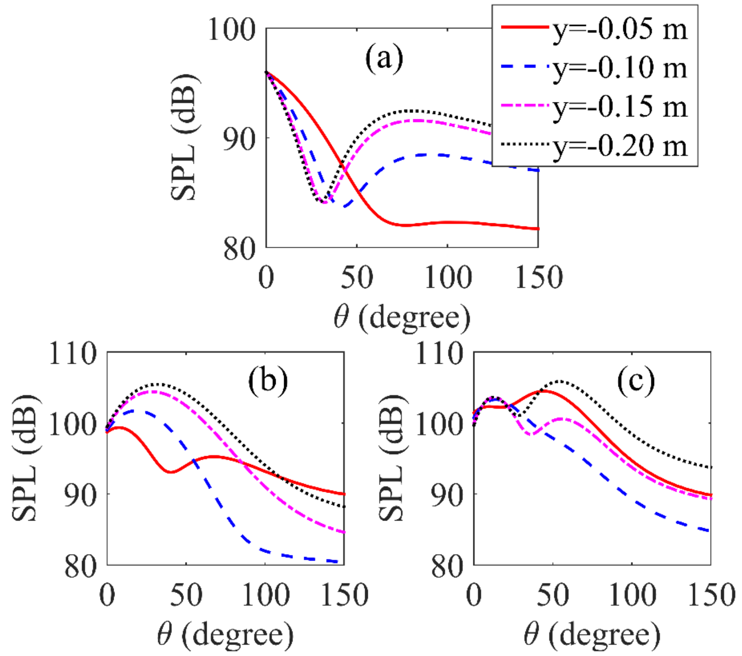

Figure 2.17 Directivity pattern of radiated SPL field (x=-1 m) at (a) 500 Hz, (b) 1000 Hz, and (c) 1500 Hz.

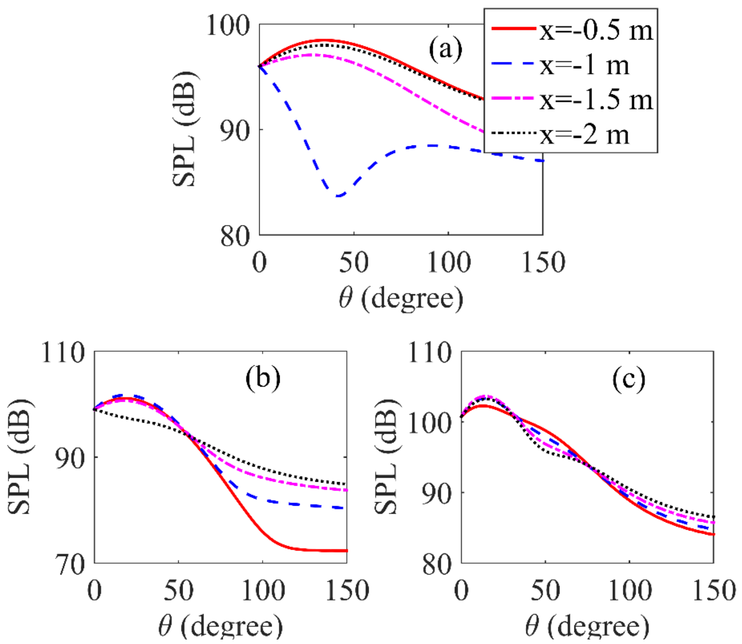

Figure 2.18 Directivity patterns of the radiated SPL field (y=-0.1 m) at (a) 500 Hz, (b) 1000 Hz, and (c) 1500 Hz.

The directivity patterns of the radiated SPL field when the source is at y =-0.1 m are presented in Figure 2.18. The results indicate that the radiated sound pressure field is complex which has no absolute correlation with the location of the point source. The results also show that various acoustical phenomena, such as direct sound propagation, sound reflection from the walls, sound diffraction to the shadow zone at the sharp edge form the final distribution of sound fields.

2.4 Experimental studies

Experimental studies are conducted to validate the theoretical model proposed in Section 2.2. The schematic diagram of the test rig is presented in Figure 2.19 (a). The experiment is carried out in an anechoic chamber of 6 m in length, 6 m in width, and 3 m in height. As the proposed model was established in a 2D configuration, we designed a quasi-2D test rig accordingly (Guo et al., 2018; Fang et al., 2019; Ji et al., 2020) which is presented in Figure 2.19 (b). It is constructed by two parallel arranged acrylic plates of 2.4 m long, 1.2 m wide, and 0.02 m thick. To eliminate the effect of the higher-order acoustical modes along vertical direction, the distance between the acrylic plates is kept at 0.04 m. Based on the cut-off rule of a channel, the plates can form a quasi-2D space under about 4250 Hz. A rectangular duct of 1.2 m long, 0.2 m wide, and 0.04 m high is inserted into the quasi-2D space to form an unbaffled long enclosure. To simulate the infinite region outside the long enclosure, a layer of wedge-shaped Melamine foam is placed at the side openings of the 2D space. The total heights of the wedges are 0. 2 m as illustrated in Figure 2.19 (b). According to the rule of a quarter wavelength, they can achieve non-reflection boundaries above around 450 Hz (Jiang et al., 2016).

The whole test rig is supported by a frame assembled by aluminum extrusions. 2 A0 papers printed with the Cartesian and polar coordinate systems are pasted on the backside of the transparent acrylic plate to locate the measurement points. A Tannoy loudspeaker connected to a long pipe of 1 m in length and 25 mm in diameter is applied to simulate a monopole point source. Measurements of the directional characteristics of this source were conducted and it was observed that the deviations in all directions were within 1 dB for frequencies above about 200 Hz (Li, Law, et al., 2008; Wang & Choy, 2019). The harmonic sound source is produced by a signal generator, output by an A/D converter (NI 4431), amplified by the power amplifier (LA 1201), and played by the Tannoy loudspeaker. Two microphones (B&K 4189) are connected to the conditioning amplifier (B&K NEXUS) and the data acquisition module (NI 9234). They move along the observation radius and collect acoustical signals every 5 degrees of observation angle. The testing system is controlled by LabVIEW which possesses the merits of good stability and high real-time performance in the targeted frequency range.

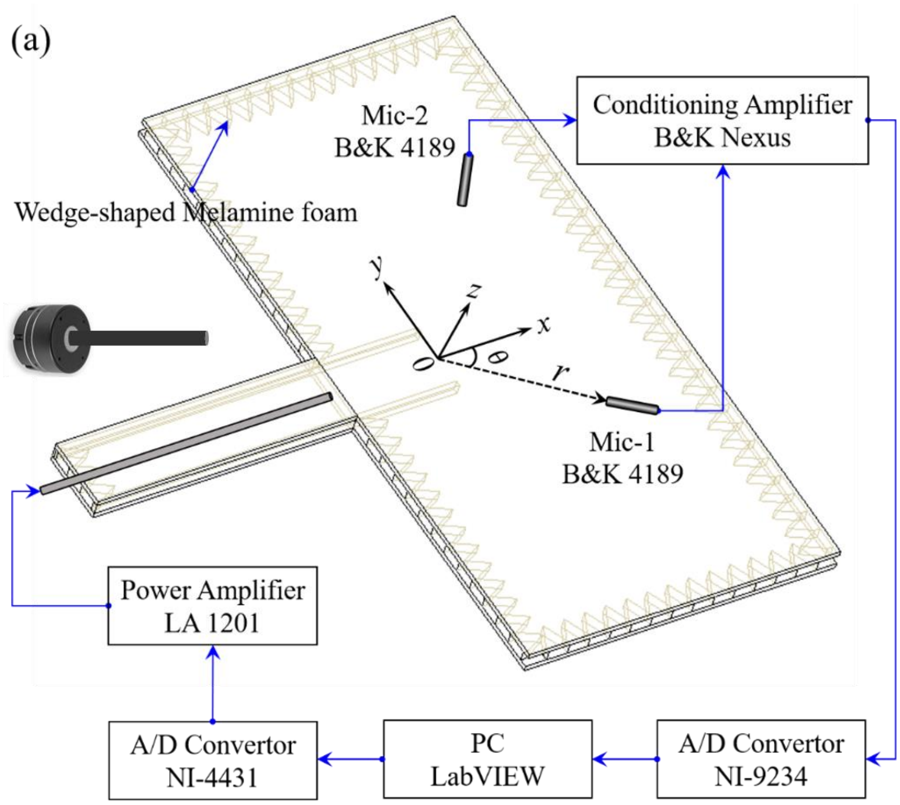

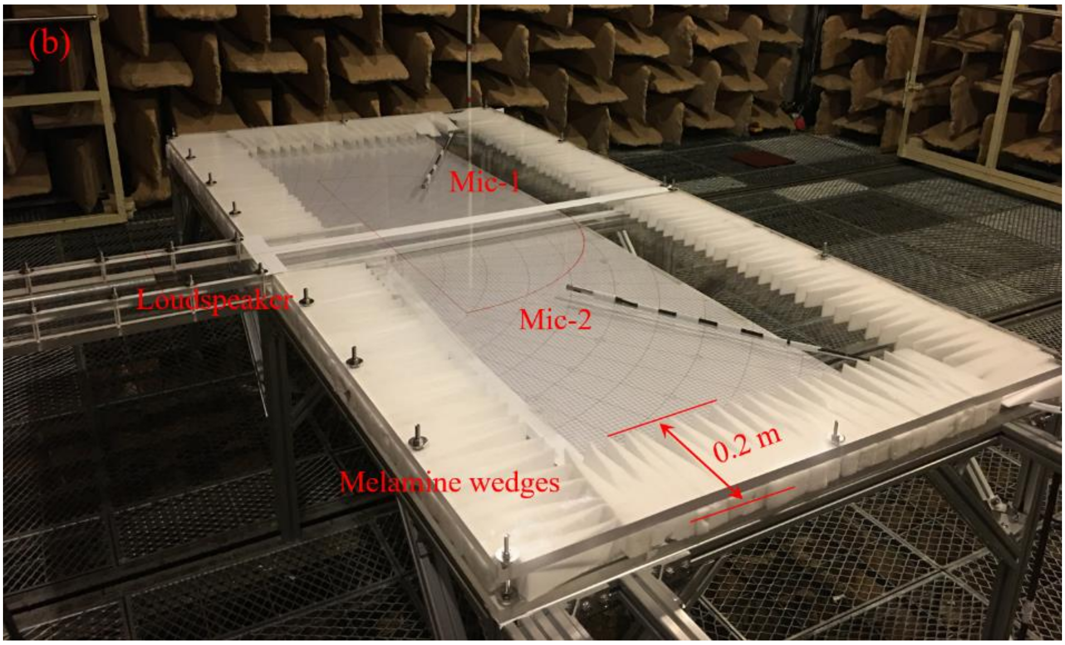

Figure 2.19 Experimental setups: (a) schematic diagram of the quasi-2D experimental test rig, (b) photography of the test rig in an anechoic chamber.

Due to the size of the test rig, it forms a scaled-down model of the traffic tunnel in practice which is about 10 m high. Then, the scaling factor is 1:50 which means the targeted frequency in practice [200, 2000] Hz must be enlarged to very high frequency range. However, limited by the sound absorption material and the quasi-2D space, the applicable frequency range of the test rig is [450, 4250] Hz. Consequently, it will fail to simulate the tunnels in practice. Instead, it is applied to validate the theoretical model by which the sound radiation patterns of large tunnel can be predicted.

Considering the performance of the loudspeaker and the dimensions of the test rig, the location coordinates and volume velocity strength of the monopole point source are set as (-0.5, 0) m and 0.002 m^2/s, respectively, in the experiment. In addition, the observation radius and angle are 0.6 m and [-90, 90] degrees, respectively. As the signal is amplified before being played by the loudspeaker, and practically, the frequency response of a loudspeaker is not always flat (Ortiz et al., 2013; Ortiz et al., 2016). The transfer function $\mathbf{T}$ between the loudspeaker and the microphone must be determined first. Their relations can be described by

$$\mathbf{XT=Y} \tag{2.80}$$

where $\mathbf{X}$ and $\mathbf{Y}$ are, respectively, the source and collected signals. A sinusoidal wave of unit amplitude $\mathbf{X}=[1,1,...1]^{\mathrm{T}}$ is stimulated and played by the loudspeaker. The sound pressure is measured by a microphone placed 20 mm in front of the pipe opening.

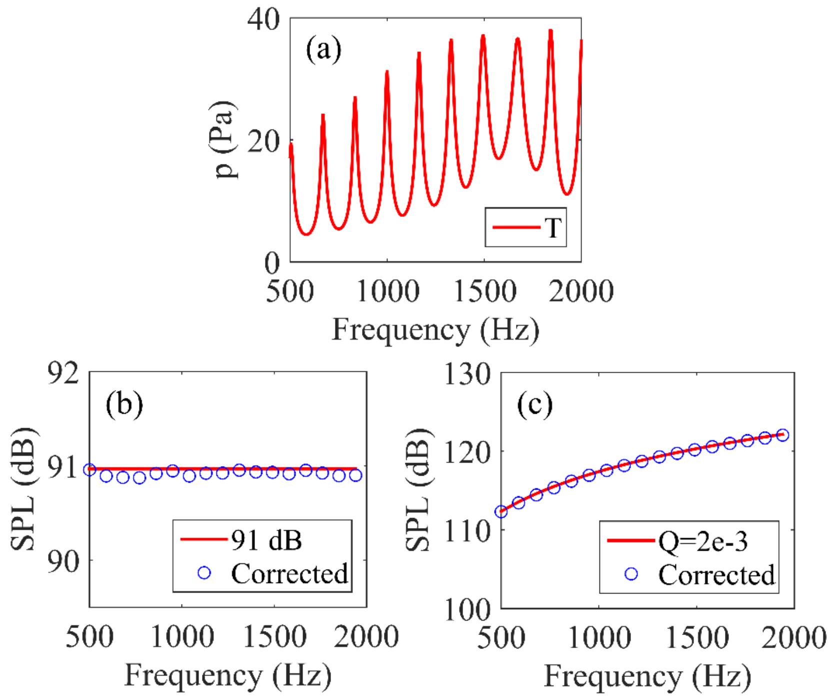

Figure 2.20 Transfer function of the testing system and sound source correction: (a) the transfer function of the testing system, (b) correction of sinusoidal wave, (c) correction of a monopole point source.

Using Eq. (2.80), the transfer function of the testing system is obtained which is illustrated in Figure 2.20 (a). Subsequently, the accuracy of the transfer function $\mathbf{T}$ is checked by specifying $\mathbf{X}=1/\mathbf{T}$ and the expected output should be $\mathbf{Y}=[1,1,...1]^{\mathrm{T}}$ which is shown in Figure 2.20 (b). The fluctuation of the SPLs radiated from the loudspeaker is within 0.3 dB in the frequency range of 500 Hz to 2000 Hz compared with the expected SPL which is 91 dB. Similarly, a monopole point source is designed and corrected using the same procedures. The designed and corrected SPLs of the point source are compared in Figure 2.20 (c). As can be observed, the results agree well with each other which can be used in the following experiment. The monopole point source in the frequency range [2000, 4000] Hz is also corrected applying the method which is not presented here.

The directivity patterns of the radiated SPL field are measured and compared with the theoretical results as demonstrated in Figure 2.21. Good agreement can be observed between the results obtained by the W-H technique and experiment. Even though only the experimental results in [-90, 90] degrees are presented, the consistency of the results validate the proposed theoretical model in calculating the radiated sound field.

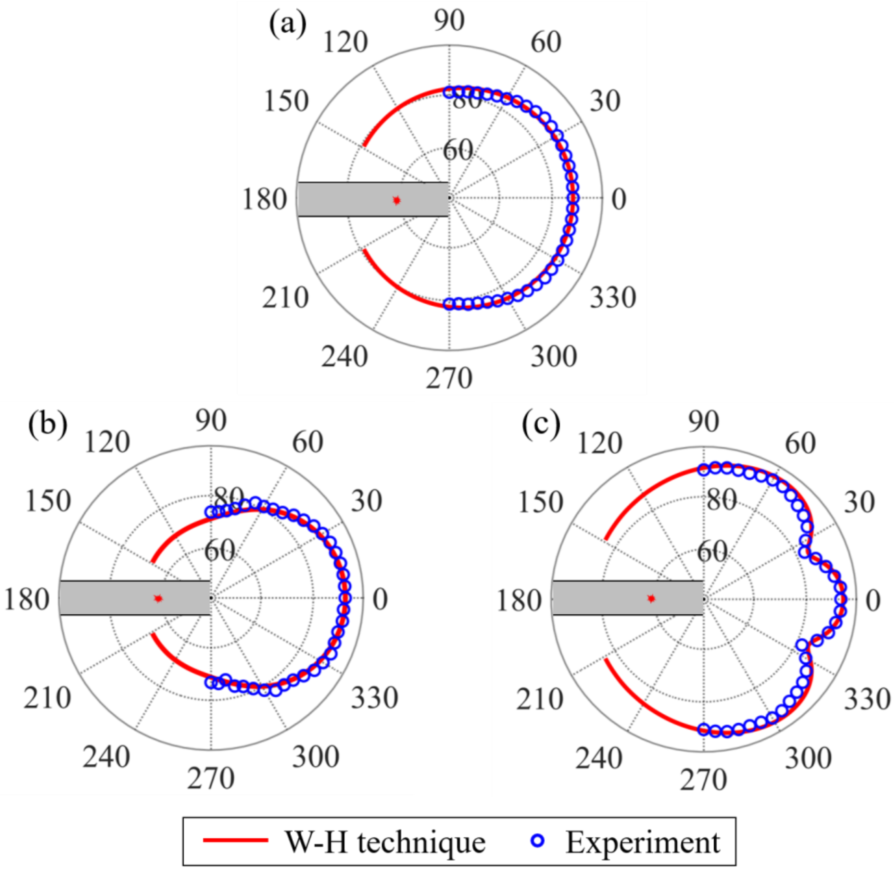

Figure 2.21 Directivity patterns of the radiated SPL field obtained by the theoretical model and experiment at (a) 500 Hz, (b) 1500 Hz, and (c) 2000 Hz.

Besides, the SPL spectra obtained by the proposed model and the experiment at randomly picked receivers (0, 0) m and (0.5, 0.5) m are compared in Figure 2.22. As the height of the unbaffled long enclosure is relatively small, the sound distributions inside and outside the long enclosure are quite simple. The SPL results coincide well with each other which validate the proposed model in predicting the sound fields inside and outside an unbaffled long enclosure.

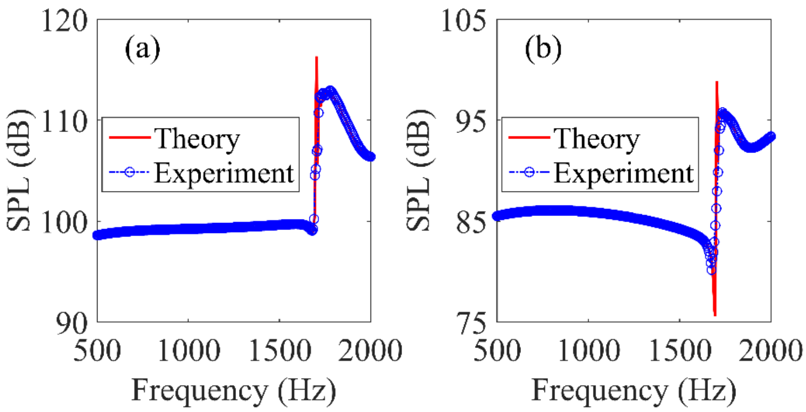

Figure 2.22 SPL spectra obtained by the W-H technique and experiment at randomly picked (a) receiver (0, 0) m and (b) receiver (0.5, 0.5) m.

2.5 Summary

This chapter concerns the W-H investigation of sound radiation from an unbaffled long enclosure. The geometrical configuration can be commonly observed in ductwork systems where noise is produced inside the enclosure and radiates to the outside through the openings. A prediction model consisting of employing the mode-matching method in conjunction with the Fourier transform is proposed to investigate the sound radiation phenomenon. The solution involves branch-cut integrals which can be evaluated by the saddle point method approximately. An explicit far-field directivity pattern of the radiated sound pressure field is obtained, which can calculate large acoustical domains with high efficiency. The detailed implementation procedures of the proposed model are introduced, such as the calculation of the wavenumbers, modal truncation, and convergency checks. It is observed that 20 modes are sufficient for an accurate result for a long enclosure of 0.4 m in height. The accuracy of the far-field approximation is analyzed and the theoretical model is validated through the FEM.

Subsequently, modal analysis is conducted to explore the formation mechanisms of the radiated sound field. The relationship between the acoustical modes and radiated sound field is investigated. Besides, the comparison between sound radiation from a baffled and an unbaffled long enclosure is carried out. Finally, quasi-2D experimental studies are implemented to validate the theoretical model. The proposed model can be applied to a broad frequency range and can be generalized into impedance boundaries which is an effective tool for the prediction and suppression of sound radiation from an unbaffled long enclosure.

CHAPTER 3

THEORETICAL MODEL OF SOUND RADIATION FROM AN UNBAFFLED LONG ENCLOSURE WITH THE GROUND

3.1 Introduction

Unbaffled long enclosures with the ground (Kang, 1996a; 1996b; 1996c) can be widely seen in traffic facilities, such as tunnels and underground stations (Heutschi & Bayer, 2006; Yang & Shield, 2001; Shimokura & Soeta, 2011). They greatly facilitate people's living conditions, however, cause many noise problems. The sound energy inside a long space is difficult to be attenuated (Kang, 1996c) which gives rise to high sound pressure levels and a long reverberation time. Such an acoustical environment produces adverse influences on drivers and passengers. Moreover, it impairs speech intelligibility. Besides, as the noise energy cannot be directly transmitted to the outside through the walls which can be considered rigid, it propagates to the openings of the long enclosure and radiates to the outside through the portals. Taking a traffic tunnel for example, if there are residents near the openings, their living environment will be seriously affected.

Therefore, in this chapter, a mathematical model is first presented to predict the sound radiation from a semi-infinite unbaffled long enclosure including the ground effect. This geometrical configuration demonstrates an idealized representation of the sound-proof tunnels, in which noise propagates along the enclosures and radiates to the outside through the portals. The prediction model described in this chapter applies only to theoretical situations and 2D configurations, however, necessary elements of realistic scenarios are included such as impedance boundary conditions, point source excitation, and ground effect, which is beneficial to understanding the physics behind the sound radiation phenomenon and significant for the proposal of suitable noise control approaches. In the first place, by expressing the sound pressure field regarding the superposition of acoustical modes inside the long enclosure and using the Fourier transform in other domains, the boundary value problem, which is intractable in the natural domain, is converted into a modified W-H equation (MWHE) of the second kind in the spectral domain. Subsequently, its solution is attained by employing the standard factorization and decomposition W-H procedures. Then, the radiated sound pressure field outside the enclosure is obtained by the inverse Fourier transform, which includes a contour integral that can be evaluated using the saddle point method approximately. In what follows, the model is validated by adopting the finite element method (FEM) and the far-field directivity patterns of the radiated sound pressure fields are shown. Besides, the properties of the sound pressure field both inside and outside three long enclosures with different boundary conditions are analyzed. Based on the results, a potential noise attenuation strategy by using acoustical liners is proposed and discussed. After that, a partial lining is applied to reduce the radiated noise from an unbaffled long enclosure and good noise reduction performance can be found. Finally, quasi-2D experiments are conducted to validate the proposed models.

3.2 Theoretical model

3.2.1 Description of the problem in the natural domain

A schematic diagram of sound radiation from an unbaffled long enclosure with the ground is presented in Figure 3.1. The height of the enclosure is h and the thickness of the wall is assumed to be zero for simplicity. The enclosure extends to the negative infinity and the ground extends to the positive infinity.

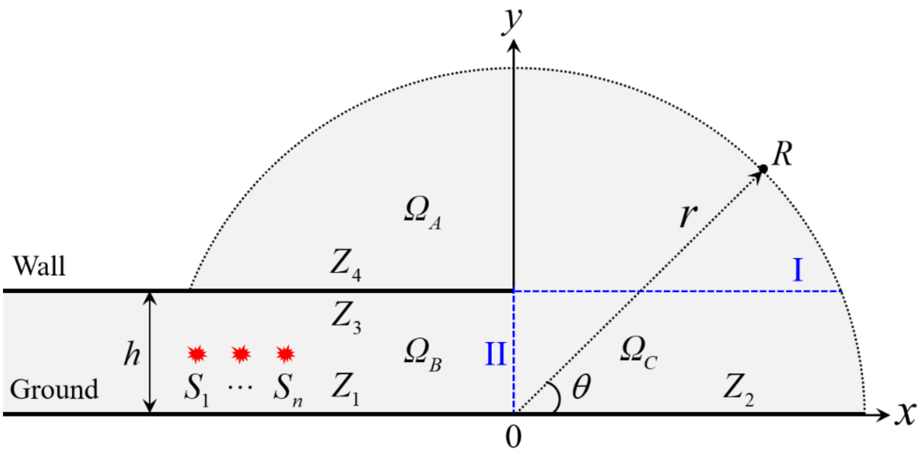

Figure 3.1 A schematic diagram of sound radiation from an unbaffled long enclosure with the ground.

The acoustical properties of the ground and wall surfaces are characterized by acoustical impedance $Z_z, z = 1, 2, 3, 4$. A Cartesian coordinate system (xoy) is applied with the origin fixing at the intersection of the opening and the ground. The sound is produced by monopole point sources with their location coordinates and the volume velocity strengths being (x_n, y_n) and Q_n, respectively. Imaginary interfaces I and II are depicted for the convenience of analysis. They divide the whole acoustical domain into three sub-regions which are Ω_A, Ω_B, and Ω_C, respectively. Besides, the polar coordinate system $(ro\theta)$ is shown to illustrate the directivity pattern of the radiated sound pressure field.

According to the partition of the whole acoustical domain in Figure 3.1, the total sound pressure field is expressed by the following piecewise function as

$$p_{total}(x,y)=\begin{cases} p_A(x,y) & \Omega_A : x\in(-\infty,+\infty)\cap y\in[h,+\infty) \\ p_{incident}(x,y)+p_{reflected}(x,y) & \Omega_B : x\in(-\infty,0]\cap y\in[0,h] \\ p_C(x,y) & \Omega_C : x\in[0,+\infty)\cap y\in[0,h] \end{cases} \quad (3.1)$$

where $p_A(x,y)$ and $p_C(x,y)$ are the sound pressure fields of regions Ω_A and Ω_C, respectively. The incident and reflected sound pressure fields of region Ω_B are denoted by $p_{incident}(x,y)$ and $p_{reflected}(x,y)$, respectively.

The Helmholtz equation of the total sound pressure field without a source, the Sommerfeld radiation condition for the semi-infinite region outside the long enclosure and the edge condition at the opening are the same as the model described in chapter 2, which are expressed by Eqs. (2.2), (2.6), and (2.7), respectively. For the current configuration, the boundary conditions on the ground and wall are expressed by

$$\left(\frac{\partial}{\partial n}+\frac{i\rho kc_0}{Z_z}\right)p_{total}\Bigg|_{z=1,2,3,4}=0 \quad (3.2)$$

where n denotes the normal direction to the boundary. Continuity relations of sound pressure and particle velocity at imaginary interfaces I and II are expressed as

$$p_A=p_C, \frac{\partial p_A}{\partial y}=\frac{\partial p_C}{\partial y}\bigg|_{\mathrm{I}} ;\ p_B=p_C, \frac{\partial p_B}{\partial x}=\frac{\partial p_C}{\partial x}\bigg|_{\mathrm{II}} \quad (3.3)$$

where p_B denotes the total sound pressure field of region Ω_B.

Inside the long enclosure, the incident sound field produced by monopole point sources satisfies the inhomogeneous Helmholtz Eq. (2.8). The solution under the boundary condition Eq. (3.2) is given by

$$p_{incident}\left(x,y\right)=\sum_{n=1}^{\infty}\sum_{j=0}^{\infty}\frac{\rho kc_0 Q_n Y_j^B\left(y_n\right)Y_j^B\left(y\right)}{2\Lambda_j^B\phi_j}e^{-i\phi_j\left|x-x_n\right|} \tag{3.4}$$

where $Y_j^B\left(y\right)$ represents the transversal modal function of region Ω_B expressed as

$$Y_j^B\left(y\right)=\cos\left(\xi_j y\right)+\frac{i\rho kc_0\sin\left(\xi_j y\right)}{Z_1\xi_j} \tag{3.5}$$

The transversal and horizontal wavenumbers of region Ω_B satisfy the following characteristic equations:

$$\begin{aligned}&L\left(\xi_j\right)=i\rho kc_0\left(\frac{1}{Z_1}+\frac{1}{Z_3}\right)\cos\left(\xi_j h\right)\\&-\left(\xi_j^2+\frac{k^2\rho^2c_0^2}{Z_1Z_3}\right)\frac{\sin\left(\xi_j h\right)}{\xi_j}=0,\ \phi_j=\sqrt{k^2-\xi_j^2},\ j=0,1,2,...\end{aligned} \tag{3.6}$$

The normalized coefficient of the modal expansion is given by

$$\Lambda_j^B=Y_j^B\left(h\right)\frac{dL\left(\xi_j\right)}{2\xi_j} \tag{3.7}$$

where d represents derivative. Due to the abrupt change of size at two sides of the opening, there is a reflected sound pressure field in region Ω_B which can be expressed in terms of normal modes as

$$p_{reflected}\left(x,y\right)=\sum_{j=0}^{\infty}b_jY_j^B\left(y\right)e^{i\phi_j x} \tag{3.8}$$

where b_j denotes the modal response coefficient.

Applying the similar procedures described in chapter 2, next, we convert the radiated sound pressure field from the natural domain into the spectral domain through the Fourier transform. The residue solution and the W-H equation will be obtained to solve the intractable boundary value problem.

3.2.2 Radiated sound fields in the spectral domain

The transformed Helmholtz equation of region Ω_A is given in Eq. (2.17) and its general solution is given by

$$P_A(\alpha, y) = P_A^+(\alpha, y) + P_A^-(\alpha, y) = A(\alpha) e^{-i\kappa(\alpha)(y-h)} \tag{3.9}$$

where the square root function $\kappa(\alpha)$ is defined in the complex α-plane illustrated in Figure 2.2. The definitions of the upper and lower complex α-planes are also applied in this chapter.

Combining Eq. (3.9) and the transformed boundary conditions of Eq. (3.2), the following identity can be obtained:

$$\left[\frac{\partial}{\partial y} - \frac{i\rho k c_0}{Z_4}\right] P_A^+(\alpha, h) = R^+(\alpha) = -i\left[\kappa(\alpha) + \frac{\rho k c_0}{Z_4}\right] A(\alpha) \tag{3.10}$$

On the other hand, the transformed Helmholtz equation for region Ω_C and the general solution are expressed by Eqs. (2.23) and (2.26), respectively. Combining the transformed continuity relations at interface I and Eq. (3.10), we have

$$R^+(\alpha) = \frac{\partial}{\partial y} P_C^+(\alpha, h) - \frac{i\rho k c_0}{Z_4} P_C^+(\alpha, h) \tag{3.11}$$

Using Eqs. (2.26) and (3.11), the transformed sound pressure of region Ω_C can be expressed as

$$P_C^+(\alpha,y)=\frac{\cos\left[\kappa(\alpha)y\right]+\dfrac{i\rho kc_0\sin\left[\kappa(\alpha)y\right]}{Z_2\kappa(\alpha)}}{W(\alpha)}$$
$$\times\left\{R^+(\alpha)-\int_0^h\left[f(\varsigma)+i\alpha g(\varsigma)\right]\left[\begin{array}{l}\cos\left[\kappa(\alpha)(h-\varsigma)\right]\\ -\dfrac{i\rho kc_0\sin\left[\kappa(\alpha)(h-\varsigma)\right]}{Z_4\kappa(\alpha)}\end{array}\right]d\varsigma\right\} \tag{3.12}$$
$$+\frac{1}{\kappa(\alpha)}\int_0^y\left[f(\varsigma)+i\alpha g(\varsigma)\right]\sin\left[\kappa(\alpha)(y-\varsigma)\right]d\varsigma$$

where

$$W(\alpha)=i\rho kc_0\left(\frac{1}{Z_2}-\frac{1}{Z_4}\right)\cos\left[\kappa(\alpha)h\right]$$
$$-\left[\kappa^2(\alpha)-\frac{k^2\rho^2c_0^2}{Z_2Z_4}\right]\frac{\sin\left[\kappa(\alpha)h\right]}{\kappa(\alpha)} \tag{3.13}$$

The term on the left-hand side of Eq. (3.12) is regular in the upper half complex α-plane. However, the regularity of right-hand side terms is violated by the presence of the poles occurring at the zeros of the denominator lying in the upper half complex α-plane satisfying

$$W(\alpha_m)=0,\quad m=0,1,2,... \tag{3.14}$$

These poles can be eliminated by imposing that their residues are zero, namely, according to the residue theorem, the terms in the curly brace of Eq. (3.13) should be zero. Then, we have the following equation:

$$R^+(\alpha_m)=\left\{\cos\left[\kappa(\alpha_m)h\right]-\frac{i\rho kc_0\sin\left[\kappa(\alpha_m)h\right]}{Z_4\kappa(\alpha_m)}\right\}$$
$$\times\int_0^h\left[f(\varsigma)+i\alpha_m g(\varsigma)\right]\left\{\cos\left[\kappa(\alpha_m)\varsigma\right]+\frac{i\rho kc_0\sin\left[\kappa(\alpha_m)\varsigma\right]}{Z_2\kappa(\alpha_m)}\right\}d\varsigma \tag{3.15}$$

According to the form of the terms in the integrand of Eq. (3.15), we define two coefficients as follows:

$$\begin{bmatrix} g_m \\ f_m \end{bmatrix} = \frac{1}{\Lambda_m^C} \int_0^h \begin{bmatrix} g(y) \\ f(y) \end{bmatrix} Y_m^C(y) dy \tag{3.16}$$

where $Y_m^C(y)$ represents the transversal modal function of region Ω_C which can be determined by the Helmholtz equation and the boundary condition on the ground:

$$Y_m^C(y) = \cos\left[\kappa(\alpha_m) y\right] + \frac{i\rho k c_0 \sin\left[\kappa(\alpha_m) y\right]}{Z_2 \kappa(\alpha_m)} \tag{3.17}$$

The normalized coefficient of the modal expansion is given by

$$\Lambda_m^C = Y_m^C(h) \frac{dW(\alpha_m)}{2\alpha_m} \tag{3.18}$$

Based on Eqs. (3.15) to (3.18), the residue solution can be obtained as

$$R^+(\alpha_m) = \left\{ \cos\left[\kappa(\alpha_m) h\right] - \frac{i\rho k c_0 \sin\left[\kappa(\alpha_m) h\right]}{Z_4 \kappa(\alpha_m)} \right\} \Lambda_m^C \left(f_m + i\alpha_m g_m \right) \tag{3.19}$$

As can be observed in Eq. (3.19), it contains an infinite number of unknowns that need more equations to determine them. Next, we will obtain the W-H equation and its solution by the W-H procedures.

3.2.3 Wiener-Hopf equation and its solution

Considering the transformed continuity relation of sound pressure at imaginary interface I, we have the following identity:

$$P_C^+(\alpha, h) + P_A^-(\alpha, h) = \frac{iR^+(\alpha)}{\kappa(\alpha) + \rho k c_0 / Z_4} \tag{3.20}$$

Substituting Eq. (3.12) into Eq. (3.20) and then applying the characteristics of trigonometric functions, we have

$$\frac{\kappa(\alpha)+\rho kc_0/Z_2}{W(\alpha)e^{-i\kappa(\alpha)h}\left[\kappa(\alpha)+\rho kc_0/Z_4\right]}+P_A^-(\alpha,h)$$
$$=\frac{1}{W(\alpha)}\int_0^h\left[f(\varsigma)+i\alpha g(\varsigma)\right]\left\{\cos\left[\kappa(\alpha_m)\varsigma\right]+\frac{i\rho kc_0\sin\left[\kappa(\alpha_m)\varsigma\right]}{Z_2\kappa(\alpha_m)}\right\}d\varsigma \tag{3.21}$$

We can express the pressure and pressure gradient at the opening in the form of series expansions as

$$\begin{bmatrix} g(y) \\ f(y) \end{bmatrix}=\sum_{m=0}^{\infty}\begin{bmatrix} g_m \\ f_m \end{bmatrix}Y_m^C(y) \tag{3.22}$$

Substituting Eq. (3.22) into Eq. (3.21) and evaluating the resulting integral, we obtain a modified W-H equation of the second kind which is valid in the overlapped region of the upper and lower complex α-plane as presented in Figure 2.2:

$$\frac{Z_4\chi(\eta_4,\alpha)R^+(\alpha)}{Z_2\chi(\eta_2,\alpha)N(\alpha)}+P_A^-(\alpha,h)=\sum_{m=0}^{\infty}\frac{f_m+i\alpha g_m}{\alpha^2-\alpha_m^2}Y_m^C(h) \tag{3.23}$$

where kernel functions are defined as

$$N(\alpha)=W(\alpha)e^{-i\kappa(\alpha)h},\quad \chi(\eta_z,\alpha)=\frac{\kappa(\alpha)}{\eta_z\kappa(\alpha)+k},\quad \eta_z=Z_z/\rho c_0,\quad z=2,4 \tag{3.24}$$

According to the factorization and decomposition W-H procedures introduced in chapter 2 and Appendix-A, the solution to the W-H equation is given by

$$R^+(\alpha)=-\sum_{m=0}^{\infty}Y_m^C(h)\frac{f_m-i\alpha_m g_m}{2\alpha_m(\alpha+\alpha_m)}$$
$$\times\frac{\chi^-(\eta_2,-\alpha_m)N^-(-\alpha_m)Z_2\chi^+(\eta_2,\alpha)N^+(\alpha)}{\chi^-(\eta_4,-\alpha_m)Z_4\chi^+(\eta_4,\alpha)} \tag{3.25}$$

where the explicit expressions of the split functions are given by

$$N^{+}(\alpha)=\sqrt{i\rho k c_0\left(\frac{1}{Z_2}-\frac{1}{Z_4}\right)\cos(kh)-k\left(1-\frac{\rho^2 c_0^2}{Z_2 Z_4}\right)\sin(kh)}$$
$$\times\exp\left\{\begin{array}{l}\frac{\kappa(\alpha)h}{\pi}\ln\left[\frac{\alpha-i\kappa(\alpha)}{k}\right]\\ -\frac{i\alpha h}{\pi}\left[1-C+\ln\left(\frac{2\pi}{kh}\right)-\frac{i\pi}{2}\right]\end{array}\right\}\prod_{m=1}^{\infty}\left(1+\frac{\alpha}{\alpha_m}\right)\exp\left(-\frac{i\alpha h}{m\pi}\right) \tag{3.26}$$

and (Buyukaksoy & Birbir, 1998)

$$\chi^{-}(\eta_z,k\cos\phi)\Big|_{z=2,4}=$$
$$\frac{4\left[M_\pi\left(\frac{3\pi}{2}-\phi-\theta\right)M_\pi\left(\frac{\pi}{2}-\phi+\theta\right)\right]^2\sin\left(\frac{\phi}{2}\right)}{\sqrt{\eta_z}\left[M_\pi\left(\frac{\pi}{2}\right)\right]^4\left[1+\sqrt{2}\cos\left(\frac{3\pi-2\phi-2\theta}{4}\right)\right]\left[1+\sqrt{2}\cos\left(\frac{\pi-2\phi+2\theta}{4}\right)\right]} \tag{3.27}$$

where $C=0.5772...$ denotes the Euler-Mascheroni constant, and the Maliuzhinets function is defined as

$$M_\pi(v)=\exp\left\{-\frac{1}{8\pi}\int_0^v\frac{1}{\cos u}\left[\pi\sin u-2\sqrt{2}\pi\sin\left(\frac{u}{2}\right)-2u\right]du\right\} \tag{3.28}$$

where

$$\sin\theta=(\eta_z)^{-1},\ z=2,4 \tag{3.29}$$

3.2.4 Sound pressure field in the natural domain

As can be found in Eq. (3.25), it contains an infinite number of unknowns. To determine them, we apply the well-known mode-matching method, which has been extensively applied to analyze the sound fields in waveguide structures. Combining Eqs. (2.24) and (3.3), we have the following identity:

$$\sum_{n=1}^{\infty}\sum_{j=0}^{\infty}\frac{\rho k c_0 Q_n Y_j^B(y_n)Y_j^B(y)}{2\Lambda_j^B\phi_j}e^{i\phi_j x_n}+\sum_{j=0}^{\infty}b_j Y_j^B(y)=\sum_{m=0}^{\infty}g_m Y_m^C(y) \tag{3.30}$$

$$-\sum_{n=1}^{\infty}\sum_{j=0}^{\infty}\frac{i\rho kc_0 Q_n Y_j^B\left(y_n\right)Y_j^B\left(y\right)}{2\Lambda_j^B}e^{i\phi_j x_n}+\sum_{j=0}^{\infty}i\phi_j b_j Y_j^B\left(y\right)=\sum_{m=0}^{\infty}f_m Y_m^C\left(y\right) \tag{3.31}$$

Multiply both sides of Eqs. (3.30) and (3.31) by mode function $Y_s^C\left(y\right)$ and then conduct an integration over the opening. Using the orthogonality of modal functions, one obtains

$$\underbrace{\sum_{n=1}^{\infty}\sum_{j=0}^{\infty}\frac{\rho kc_0 Q_n Y_j^B\left(y_n\right)\Delta_{js}}{2\Lambda_j^B\phi_j\Lambda_s^C}e^{i\phi_j x_n}}_{Y_{s1}}+\underbrace{\sum_{m=0}^{\infty}\frac{\Delta_{ms}}{\Lambda_s^C}}_{J_{sm}}b_m=g_s \tag{3.32}$$

$$\underbrace{-\sum_{n=1}^{\infty}\sum_{j=0}^{\infty}\frac{i\rho kc_0 Q_n Y_j^B\left(y_n\right)\Delta_{js}}{2\Lambda_j^B\Lambda_s^C}e^{i\phi_j x_n}}_{M_{s1}}+\underbrace{\sum_{m=0}^{\infty}\frac{i\phi_m\Delta_{ms}}{\Lambda_s^C}}_{K_{sm}}b_m=f_s \tag{3.33}$$

where

$$\Delta_{js}=\frac{i\rho kc_0\left(\dfrac{1}{Z_1}-\dfrac{1}{Z_2}\right)}{\xi_j^2-\kappa^2\left(\alpha_s\right)}+\frac{i\rho kc_0\left(\dfrac{1}{Z_3}+\dfrac{1}{Z_4}\right)}{\xi_j^2-\kappa^2\left(\alpha_s\right)}Y_j^B\left(h\right)Y_s^C\left(h\right) \tag{3.34}$$

Combining the W-H solution Eq. (3.25) and the residue solution Eq. (3.19), they should be equal at specific values. Then we have the following equation:

$$\begin{aligned} & f_s+i\alpha_s\; g_s= \\ & \quad U_{ss} \\ & \underbrace{-\frac{Z_2\chi^+\left(\eta_2,\alpha_s\right)N^+\left(\alpha_s\right)}{Z_4\chi^+\left(\eta_4,\alpha_s\right)}\sum_{m=0}^{\infty}\frac{Y_m^C\left(h\right)\chi^+\left(\eta_2,\alpha_m\right)N^+\left(\alpha_m\right)}{2\alpha_m\left(\alpha_s+\alpha_m\right)\chi^+\left(\eta_4,\alpha_m\right)\mathrm{P}\left(\alpha_s\right)\Lambda_s^C}}_{H_{sm}} \\ & \times\left(\begin{matrix} f_m-\;i\alpha_m\;\; g_m \\ U_{mm}\end{matrix}\right) \end{aligned} \tag{3.35}$$

where

$$\mathrm{P}\left(\alpha_s\right)=\cos\left[K\left(\alpha_s\right)h\right]-\frac{i\rho kc_0\sin\left[K\left(\alpha_s\right)h\right]}{Z_4K\left(\alpha_s\right)} \tag{3.36}$$

Rewrite Eqs. (3.32), (3.33), and (3.35) in matrix forms:

$$\mathbf{Y+JB=G} \tag{3.37}$$

$$\mathbf{M+KB=F} \tag{3.38}$$

$$\mathbf{F+UG=H}\left(\mathbf{F\text{-}UG}\right) \tag{3.39}$$

where $\mathbf{B}$, $\mathbf{F}$, and $\mathbf{G}$ are unknown modal response coefficients; $\mathbf{Y}$, $\mathbf{J}$, $\mathbf{M}$, $\mathbf{K}$, $\mathbf{U}$, and $\mathbf{H}$ can be constructed by Eqs. (3.32) to (3.36), respectively. In the process of solving the equations, matrix inversions are needed. Therefore, we let all the subscript indices be equal to guarantee that they are square matrices. After determining the unknowns, next, the radiated sound pressure field of region Ω_A in the natural domain can be obtained by taking the inverse Fourier transform of Eq. (3.9) as

$$p_A\left(x,y\right)=\frac{1}{2\pi}\int_{\Gamma}\frac{iR^{+}\left(\alpha\right)}{\kappa\left(\alpha\right)+\rho kc_0/Z_4}e^{-i\kappa(\alpha)(y-h)}e^{i\alpha x}d\alpha \tag{3.40}$$

where the integration path Γ is a straight line along the real axis lying in the common strip of the upper and lower complex α-planes as shown in Figure 2.2. Applying the saddle point method described in Appendix-B, the asymptotic evaluation of Eq. (3.40) is given by

$$p_A\left(r,\theta\right)=\frac{ik\sin\theta e^{ik\sin\theta h}e^{-ikr}e^{i\pi/4}}{\sqrt{2\pi kr}\left[k\sin\theta+\rho kc_0/Z_4\right]}R^{+}\left(-k\cos\theta\right) \tag{3.41}$$

The implementation of the far-field results has been elaborated in chapter 2. To obtain an accurate result of the sound fields, wavenumbers and a sufficient truncation number should be determined first. Detailed information will be presented in the next section.

3.3 Implementation of the theoretical model

To validate the proposed model, numerical calculations and FEM simulations are implemented in this section. The geometrical configuration of the unbaffled long enclosure, monopole point source, and acoustical impedances in calculations are listed in Table 3-1.

Table 3-1 Configuration of the unbaffled long enclosure, sound source, and acoustical impedances in numerical calculations.

Air Properties		**Monopole Point Source**	
Density	1.225 kg/m^3	Location	(-2, 0.5) m
Sound speed	340 m/s	Volume velocity strength	0.01 m^2/s
Unbaffled Long Enclosure		**Directivity Patterns**	
Height	1 m	Far-field radius	5 m
Truncated length	5 m	Observation angle	[0, 150] degrees
Acoustical Impedances			
Z_1=202+13i; Z_2=1840+370i; Z_3=458+517i; Z_4=630-651i			

Theoretically, the size of the calculation domain, boundary conditions, and the frequency range can be assigned arbitrarily. For the sake of calculation efficiency, we deal with a relatively small long enclosure whose height is 1 m and truncated length is 5 m. Boundary conditions imposed on the ground and wall surfaces come from ceramic tubular liners which are made of parallel cylindrical channels embedded in a ceramic matrix. These liners are commonly applied in engineering applications, and the acoustical impedances of such acoustical liners with a variety of configurations have been obtained through experiments (Jones et al. 2005). The sound propagation properties inside a lined duct were investigated and 4 acoustical impedances, namely, Z_1=202+13i, Z_2=1840+370i, Z_3=458+517i, and Z_4=630-651i were employed which come from the experimental data (Yang et al. 2018). Therefore, we apply the same acoustical impedances in the current model to investigate the performance of using an acoustical liner to reduce the noise. However, these impedance values do not uniquely associate with sound absorption materials in practice which makes it difficult to select materials according to the impedance values in the theoretical modal despite that it is convenient for calculations. The relations between impedance values and their sound absorption performance should be presented for better understanding. This will be our future work. In this thesis, we apply different acoustical impedances mainly to validate our theoretical model. In addition, a monopole point source with its volume velocity strength being 0.01 m^2/s is located at (-2, 0.5) m. The speed of sound and the density of air are 340 m/s and 1.225 kg/m^3, respectively.

3.3.1 Calculation of the wavenumbers

As the expressions of sound fields in regions Ω_B and Ω_C are based on normal modes, a correct solution to the problem requires a successful determination of the wavenumbers which are defined by Eqs. (3.6) and (3.14), respectively. Aiming at finding the roots of characteristic equations, the classical Newton-Raphson method is applied, but care should be taken in selecting proper initial values and step lengths to implement the iteration scheme. Due to the nature of trigonometric functions, the roots are symmetric about the origin and with certain periodicity which can reduce the time cost during the calculation. However, one thing that should be kept in mind is that the periods do not show up from the first root, and they exist only in either the real or the imaginary parts of the roots. Knowing this, we start the iteration from zero and define a step length that is slightly smaller than the period, which can be determined by a pilot calculation.

Taking 1000 Hz for example, a small number of wavenumbers along horizontal and transversal directions of regions Ω_B and Ω_C are listed in Figure 3.2. As can be observed in Figure 3.2 (a), the first root of Eq. (3.6) is 17.68-0.13i. It is very close to the wavenumber in the free space which is 18.32. However, it has a certain deviation and imaginary part because of the impedance boundary conditions. Additionally, the imaginary parts of these roots decrease over 2π continuously and finally tend to the minus infinity. The real parts decrease as well but ultimately converge to zero. In Figure 3.2 (b), the real parts of the roots, on the contrary, have a period of 2π and finally tend to the plus infinity, the imaginary parts, however, decrease stably and converge to zero eventually. In Figure 3.2 (c) and Figure 3.2 (d), similar changing patterns can be seen but the details are different due to different boundary conditions.

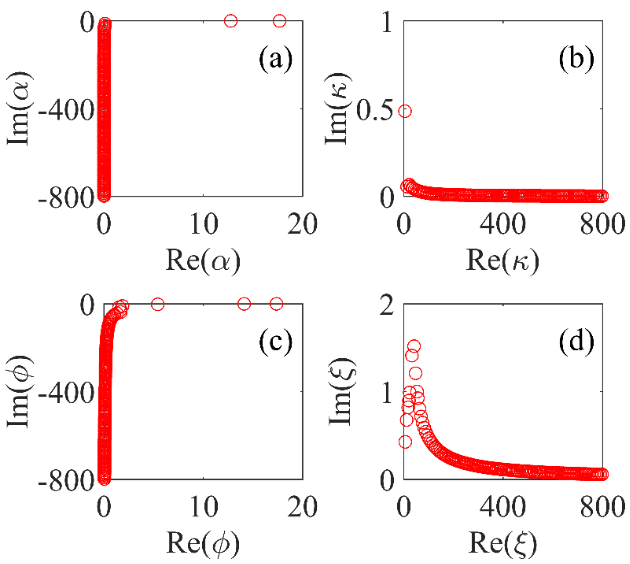

Figure 3.2 The Horizontal and transversal wavenumbers at 1000 Hz obtained by the Newton-Raphson method.

3.3.2 Model validation via the FEM

As the incident and reflected sound pressure fields inside the long enclosure share the same modal function, the number of normal modes used in the calculations is determined first. A convergence check is carried out to find out the maximum mode number based on a trade-off between the computation cost and accuracy. The criterion of convergence is defined that the relative error of sound pressure values between two successive acoustical modes at an arbitrary location is less than 1%. As the maximum mode number would increase with the increase of dimension and frequency. It can be obtained by checking the convergence of the total sound pressure of randomly picked points at 2000 Hz. Three receivers are considered here, namely, (-3, 0.1) m, (-1.5, 0.5) m, and (0, 0.9) m. The real and imaginary parts of sound pressure become stable after about 12 modes, as presented in Figure 3.3. After several calculations, 20 modes are considered for such a configuration. The results illustrate that the modal number is sufficient as a further increase in the number does not produce a significant difference in this study.

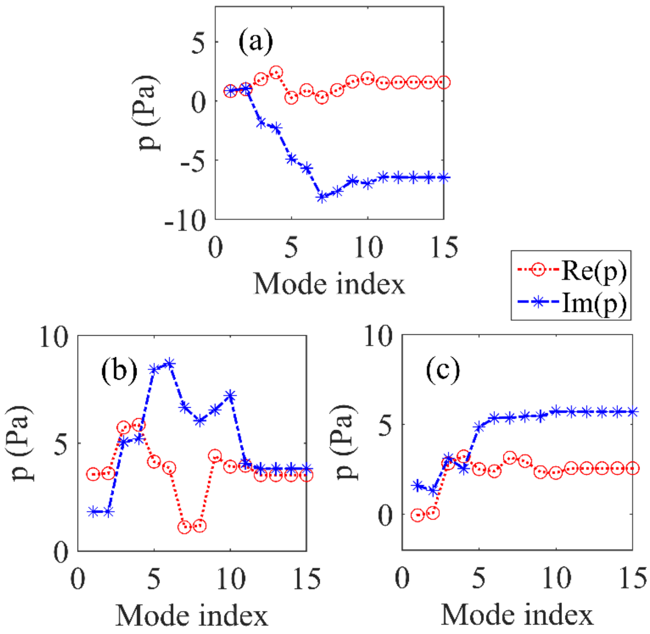

Figure 3.3 Convergence checks of the sound pressure field at 2000 Hz for arbitrarily picked receiver points (a) at (-3, 0.1) m, (b) at (-1.5, 0.5) m, (c) at (0, 0.9) m.

Subsequently, the comparison of the SPL distribution in region Ω_B obtained by the FEM and the W-H technique at 2000 Hz is conducted. The commercial software COMSOL Multiphysics is applied for the FEM. In the theoretical model, the size of the long enclosure and the radiation region can be infinite. However, this is impossible for the FEM. To avoid this problem, the calculation domain is bounded by a perfectly matched layer (PML), which is an artificial absorption layer that allows sound waves to propagate out without any reflection (Wang et al., 2015). To guarantee the accuracy of the FEM and to satisfy the basic requirement for the acoustic elements which states that the maximum side-length of acoustical meshes should be less than one-sixth of the minimum wavelength in the frequency range of interest. The acoustical domain is discretized into about 1.67×10^6 elements. Besides, the curvature parameter and the scaling factor of the PML are set to be 1 in the current simulation according to the findings of Hein et al. (2004).

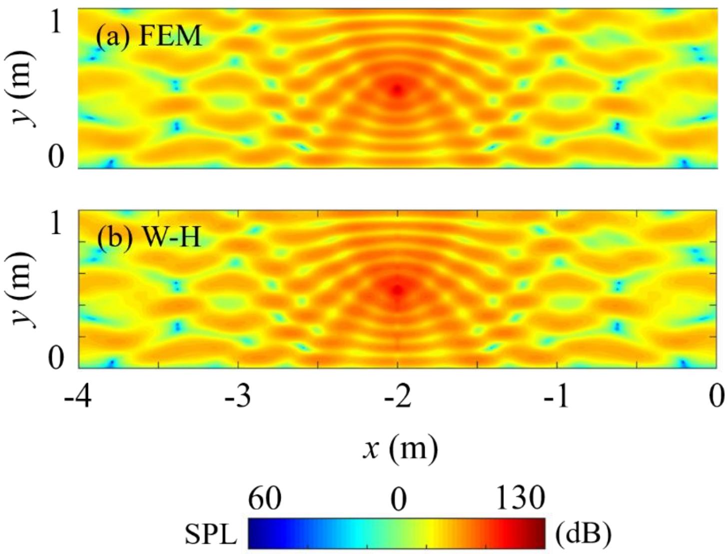

Figure 3.4 Comparison of SPL distribution inside the unbaffled long enclosure at 2000 Hz calculated by (a) the FEM and (b) the W-H technique.

As presented in Figure 3.4, a good agreement can be observed even though small discrepancies can be found, which result from unsatisfactory mesh quality in the FEM and insufficient mode number using the W-H technique. Comparisons between the SPLs obtained by the FEM and the W-H technique in the targeted frequency range at randomly picked receiver points are illustrated in Figure 3.5. Good agreement can be observed which validates the proposed model in the calculation of sound field inside and at the shadow zone of a long enclosure.

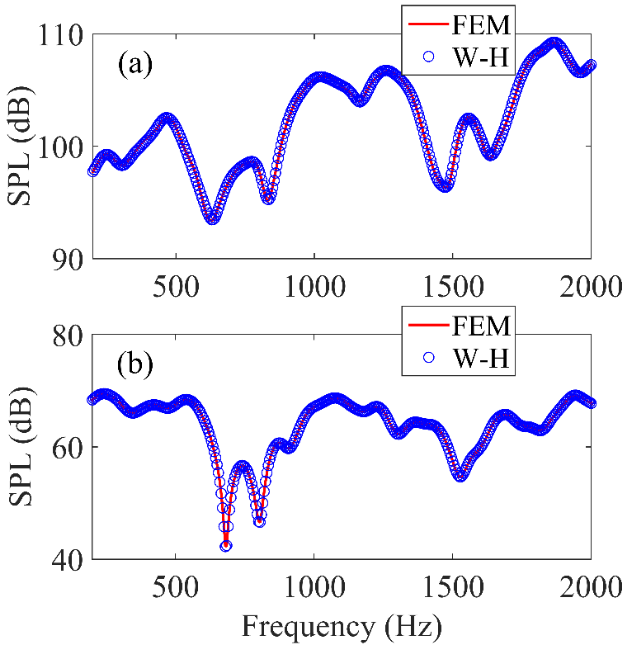

Figure 3.5 Comparison between SPL spectra obtained by the W-H technique and the FEM at two randomly picked receivers inside and at the shadow zone of the long enclosure: (a) receiver (-1, 0.5) m, (b) receiver (-3, 3) m.

The directivity patterns of the radiated SPL fields outside the long enclosure obtained by the FEM and the W-H technique are presented in Figure 3.6. The results agree well with each other despite that there are some discrepancies, which result from the far-field approximation. In front of the opening, lobes can be clearly observed, and the number of lobes increases with the increase of frequency. The sound pressure field in this region is formed by the superposition of direct, reflected, and diffracted sound waves. These sound waves propagate to the receiver over different distances and with different phases, which gives rise to the directivity patterns. At the backside of the long enclosure, the sound pressure field is the result of diffraction at the opening edge which, according to the GTD, is mainly determined by the incident angle, diffracted angle, and the distance between the edge and the receiver. This part of the sound field is quite stable and standing at relatively low SPLs.

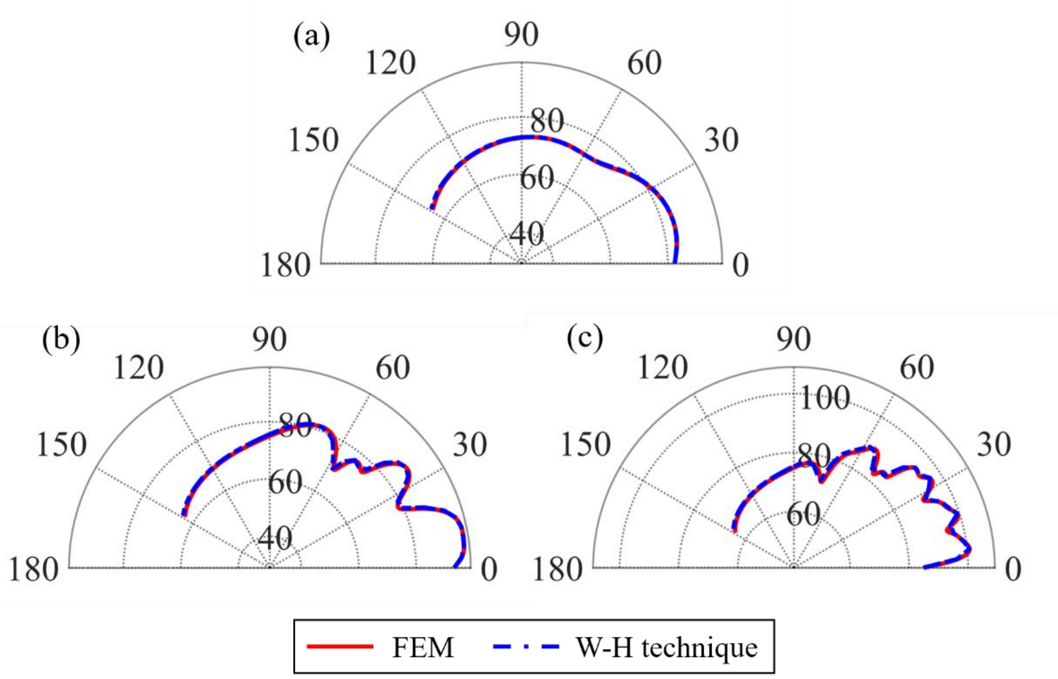

Figure 3.6 Directivity patterns of the radiated SPL field obtained by the W-H technique and the FEM at (a) 200 Hz, (b) 1000 Hz, and (c) 2000 Hz.

From the results presented in the preceding content, the W-H technique can predict the sound pressure fields both inside and outside an unbaffled long enclosure with a certain accuracy. Besides, the calculation time required by the W-H technique and the FEM is roughly the same. To verify the capability of the proposed method to deal with large-size acoustical domains, larger enclosures are considered. The results obtained using the FEM and the W-H technique are consistent which are not presented here. The main difference lies in the calculation time. When the size of the acoustical domain increases, more acoustical modes should be considered in order to obtain an accurate result using the W-H technique. Consequently, the calculation efficiency reduces. However, the advanced technologies of computers allow us to calculate summations fast. Therefore, the calculation efficiency of the proposed model for a big acoustical domain is acceptable. Moreover, the calculation efficiency of the radiated sound pressure field is not constrained by the size of the outside domain because it is an explicit expression regarding the observation radius and angle. Nevertheless, for the FEM, the element number grows rapidly with the increased size of the acoustical domain. This will result in low efficiency, particularly in the case of real traffic tunnels whose size can reach tens of meters. Therefore, to calculate the sound pressure fields of big acoustical domains, the W-H technique outperforms the FEM, especially when far-field results are preferred in engineering projects.

3.3.3 Sound radiation control using acoustic liners

Acoustic liners are widely applied to attenuate noise in ducted systems (Bauer, 1977; Tam et al., 2001; Jones et al., 2005; Brambley, 2011). Combining Eqs. (3.25) and (3.41), we notice that the radiated sound field is determined by the incident and reflected sound fields inside the long enclosure. Therefore, the radiated noise can be reduced through the control of the sound field inside the long enclosure. To verify this conjecture, and provide data to support the proposal of noise control strategies, three cases with different boundary conditions, namely, totally rigid (Case 1), an impedance on the inner wall (Case 2), and all surfaces having impedances (Case 3), are analyzed thoroughly. In these cases, the point source is located at (-2, 0.5) m, and the height of the long enclosure is 1 m. The SPL spectra for arbitrarily picked receiver (-1, 0.5) m inside the unbaffled long enclosure, and (-3, 3) m in the shadow zone are presented in Figure 3.7. In the totally rigid case, several peaks can be observed around 340 Hz, 680 Hz, 1020 Hz, 1360 Hz, and 1700 Hz which are the resonance frequencies of the long enclosure. Taking rigid case as the basis, the introduction of liners on the boundaries can significantly reduce the SPL over most of the targeted frequency range, which is mainly determined by the resistance and reactance of the acoustic impedance provided by the liner. However, the effects of the impedance values and the number of liners cannot be clearly reflected in this figure which will be considered in the future.

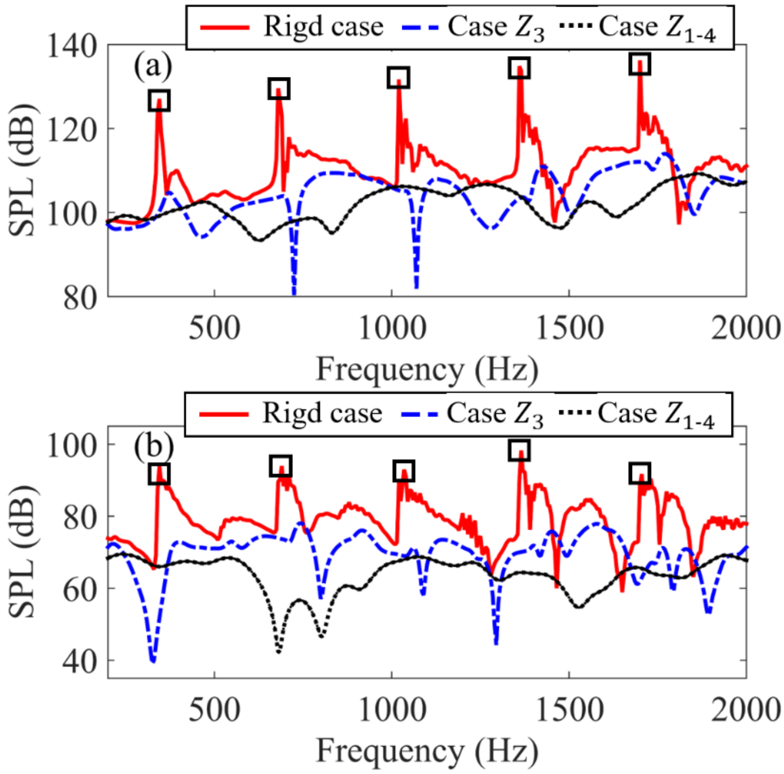

Figure 3.7 SPL spectra under different boundary conditions for (a) receiver (-1, 0.5) m inside the long enclosure and (b) receiver (-3, 3) m in the shadow zone.

As SPL spectra in Figure 3.7 can only reflect the results of a single point, SPL distributions inside and outside the long enclosure at resonant frequencies 340 Hz, 1360 Hz, and non-resonant frequencies 510 Hz, 850 Hz, are shown in Figure 3.8 and Figure 3.9, respectively, to further explore the effect of liner on the reduction of noise radiated from the long enclosure. As can be seen in the rigid cases at 340 Hz and 1360 Hz, SPLs stand at high levels and standing waves can be observed. Their distributions are along the transversal direction. After introducing the liners, the SPLs inside the long enclosure are reduced and the resonant distributions disappear which reduces the radiated noise. In general, imposing all the boundaries with liners can obtain more sound reduction than using a liner on the inner wall even though the rule is reversed at some frequencies (340 Hz) which is determined by the boundary conditions.

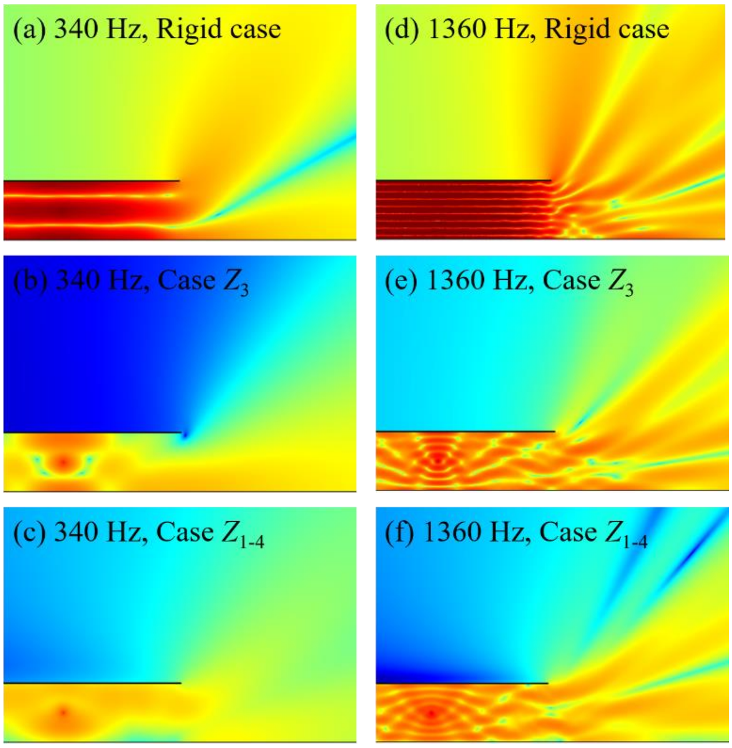

Figure 3.8 SPL distributions of a long enclosure at resonant frequencies: (a) 340 Hz, Case 1; (b) 340 Hz, Case 2; (c) 340 Hz, Case 3; (d) 1360 Hz, Case 1; (e) 1360 Hz, Case 2; (f) 1360 Hz, Case 3.

At 510 Hz and 850 Hz, the SPLs inside the long enclosure are also reduced after introducing the liners, however, not as much as the resonant frequencies. In brief, the introduction of liners can reduce the radiated noise but the performance depends on the sound distribution inside the long enclosure.

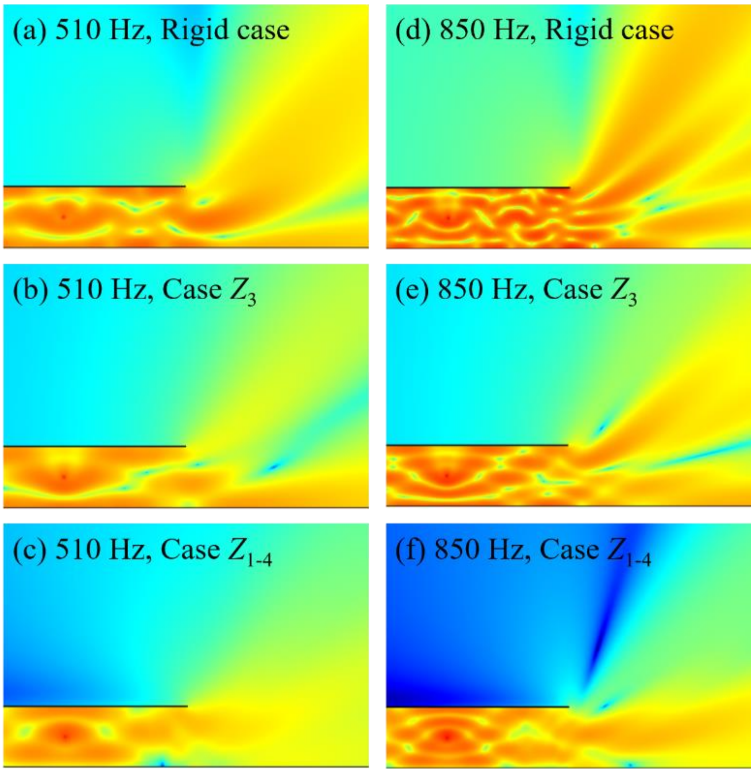

Figure 3.9 SPL distributions of a long enclosure at non-resonant frequencies: (a) 510 Hz, Case 1; (b) 510 Hz, Case 2; (c) 510 Hz, Case 3; (d) 850 Hz, Case 1; (e) 850 Hz, Case 2; (f) 850 Hz, Case 3.

Furthermore, the directivity patterns of the radiated sound fields at 340 Hz, 850 Hz, and 1360 Hz are presented in Figure 3.10. Compared to the rigid cases, the introduction of liners on the boundaries can reduce the SPLs of the radiated sound fields between the observation angles of 40~150 degrees. Generally, the case in which all surfaces have impedances reduces more SPL than the case with only Z_3. However, at 340 Hz, the result is reversed which can be explained by the GTD. We consider the enclosure edge as a secondary source. As is shown in Figure 3.8 (b), the SPL at the edge in case Z_{1-4} is larger than the case Z_3, and hence the diffracted SPL is larger accordingly. Between the observation angles of 0~60 degrees, the SPL reductions become blurred as the SPLs vary irregularly. Besides, some dips in the rigid case disappear after introducing the impedance. Despite this, the lobes in the rigid case are smoothed in the impedance cases. Another phenomenon in the rigid case that deserves attention is that, between the observation angles of 60~90 degrees, there always be one or more lobes with their SPLs standing at relatively high levels. These lobes are the so-called principal lobes and will be our focus of consideration in proposing noise control strategies.

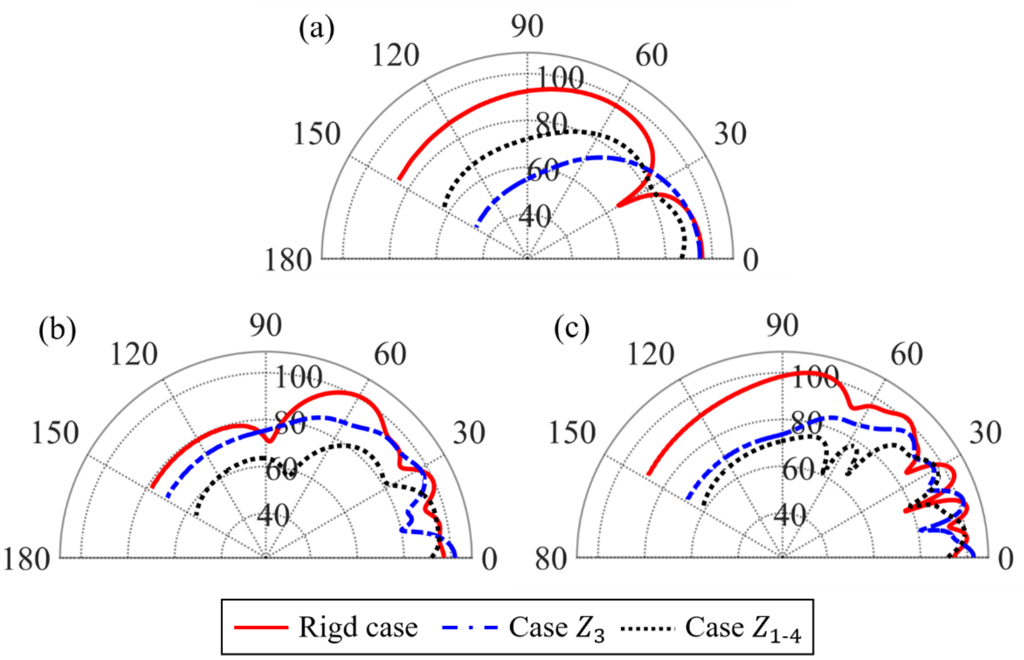

Figure 3.10 Directivity patterns of the radiated sound fields under different boundary conditions at (a) 340 Hz, (b) 850 Hz, and (c) 1360 Hz.

According to the foregoing analysis, it is practicable to control the noise both inside and outside the long enclosure using acoustic liners. In practice, however, the ground is not convenient for the introduction of noise reduction devices and is usually considered to be acoustically rigid (Attenborough, 1985). Besides, the length of these linings should be finite which is less costly and more realistic. From the result of case with only Z_3 presented above, the noise reduction is not as good as expected. Hence, the design of the location, length, and optimized value of the impedance on the wall of the enclosure will be studied. On the other hand, in this paper, liners with constant impedances are used to validate the proposed model and examine their potential to attenuate noise inside and outside the long enclosure. Currently, with the development of acoustical metamaterials, new types of liners (Guo et al., 2018) that can provide inhomogeneous impedances (Wang et al., 2015; Wang et al., 2017) are widely used for reflection wave manipulation and noise attenuation purposes. These structures have great potential for the control of noise inside and outside long enclosures.

3.3.4 Partial lining on the enclosure wall

Due to the difficulties in obtaining and solving the W-H equations, impedance boundary conditions of infinite long are usually preferred instead of finite ones (Demir & Buyukaksoy, 2003; Demir & Rienstra, 2006; Gabard & Astley, 2006). However, in practice, the length of a noise control device should be finite which is less costly and more realistic. Besides, constant impedance boundary condition was applied by Demir and Buyukaksoy (2005). However, the impedance values of any acoustical treatment in nature change with frequency. Hence, a frequency-dependent impedance boundary condition of finite length is considered here. To model the above-described scenario, a schematic diagram of the sound radiation from an unbaffled long enclosure with a partial lining on the inner wall is presented in Figure 3.11.

The length of the partial lining is denoted by L_p, and its acoustical properties are characterized by the acoustical impedance Z_p. A new imaginary interface III is depicted which divides a region Ω_D with imaginary interface II. The sound pressure field of region Ω_D can be expressed in terms of the superposition of acoustical modes as follows:

$$p_D(x,y)=\sum_{j=0}^{\infty}\left(c_j e^{i\beta_j x}+d_j e^{-i\beta_j x}\right)\cos\left(\xi_j y\right) \tag{3.42}$$

where c_j and d_j are modal response coefficients.

The transversal and horizontal wavenumbers in region Ω_D are determined by

$$\begin{aligned} &L\left(\xi_j\right)=\xi_j\sin\left(\xi_j L_p\right)-i\rho k c_0\cos\left(\xi_j L_p\right)/Z_p=0 \\ &\phi_j=\sqrt{k^2-\xi_j^2},\ j=0,1,2,\ldots \end{aligned} \tag{3.43}$$

The sound pressure fields of the other regions can be described according to the previous chapters. To simplify the model, we assume that all the other boundaries are acoustically rigid.

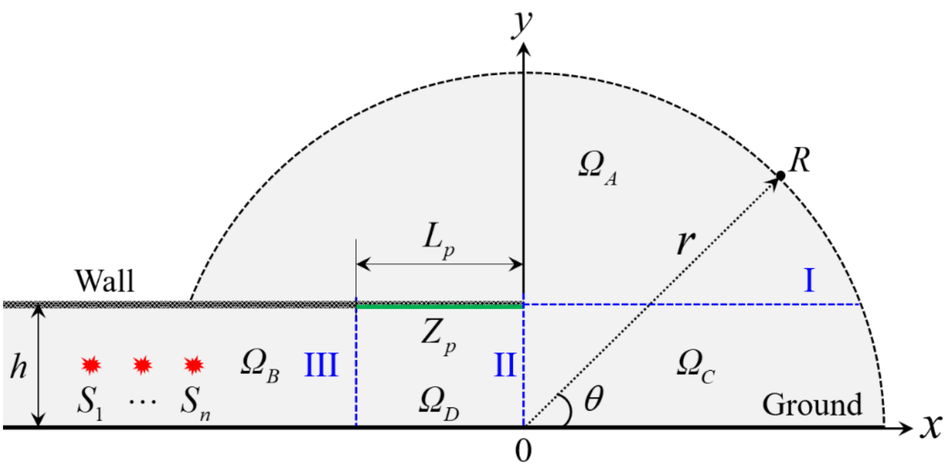

Figure 3.11 A schematic diagram of sound radiation from an unbaffled long enclosure with a partial lining.

As can be observed, two extra unknown coefficients c_j and d_j were introduced in Eq. (3.42) which need two more equations to determine them. Continuity relations of pressure and its gradient at imaginary interface III are given by

$$p_B = p_D, \frac{\partial p_B}{\partial x} = \frac{\partial p_D}{\partial x}\bigg|_{\mathrm{III}} \tag{3.44}$$

Combining the residue solution, W-H equation, continuous relations of sound pressure, and its gradient at the imaginary II and III, the unknowns can be determined simultaneously. The finally identities are listed below:

$$\begin{aligned}&\sum_{j=0}^{\infty}\left(c_j e^{-i\phi_j L_p} + d_j e^{i\phi_j L_p}\right)\cos\left(\xi_j y\right) - \sum_{j=0}^{\infty} b_j \cos\left(\eta_j y\right) e^{-i\beta_j L_p} \\ &= \sum_{n=1}^{\infty}\sum_{j=0}^{\infty} \frac{\rho k c_0 Q_n \cos\left(\eta_j y_n\right)\cos\left(\eta_j y\right)}{2\beta_j \Lambda_j^B} e^{i\beta_j\left(L_p + x_n\right)}\end{aligned} \tag{3.45}$$

$$\begin{aligned}&\sum_{j=0}^{\infty}\phi_j\left(c_j e^{-i\phi_j L_p} - d_j e^{i\phi_j L_p}\right)\cos\left(\xi_j y\right) - \sum_{j=0}^{\infty} b_j \beta_j \cos\left(\eta_j y\right) e^{-i\beta_j L_p} \\ &= -\sum_{n=1}^{\infty}\sum_{j=0}^{\infty} \frac{\rho k c_0 Q_n \cos\left(\eta_j y_n\right)\cos\left(\eta_j y\right)}{2\Lambda_j^B} e^{i\beta_j\left(L_p + x_n\right)}\end{aligned} \tag{3.46}$$

$$\sum_{j=0}^{\infty}\left(c_j + d_j\right)\cos\left(\xi_j y\right) = \sum_{m=0}^{\infty} g_m \cos\left(\kappa_m y\right) \tag{3.47}$$

$$\sum_{j=0}^{\infty} i\phi_j\left(c_j - d_j\right)\cos\left(\xi_j y\right) = \sum_{m=0}^{\infty} f_m \cos\left(\kappa_m y\right) \tag{3.48}$$

Multiply both sides of Eqs. (3.45) to (3.48) by $\cos\left(\xi_s y\right)$ and integrate along the opening. Making full use of the orthogonality of modal functions, we have

$$\begin{aligned}&c_s \underbrace{e^{-2i\phi_s L_p}}_{L_{SS}} + d_s - \sum_{j=0}^{\infty} \underbrace{\frac{(-1)^j \xi_s \sin\left(\xi_s h\right) e^{-iL_p\left(\beta_j + \phi_s\right)}}{\Lambda_s^D\left(\xi_s^2 - \eta_j^2\right)}}_{K_{sj}} b_j \\ &= \underbrace{\sum_{n=1}^{\infty}\sum_{j=0}^{\infty} \frac{\rho k c_0 Q_n (-1)^j \xi_s \sin\left(\xi_s h\right)\cos\left(\eta_j y_n\right) e^{i\beta_j\left(L_p + x_n\right) - i\phi_s L_p}}{2\Lambda_s^D \beta_j \Lambda_j^B\left(\xi_s^2 - \eta_j^2\right)}}_{E_{s1}}\end{aligned} \tag{3.49}$$

$$c_s \underbrace{e^{-2i\phi_s L_p}}_{L_{ss}} - d_s - \sum_{j=0}^{\infty} \underbrace{\frac{(-1)^j \xi_s \sin(\xi_s h) \beta_j e^{-iL_p(\beta_j+\phi_s)}}{\Lambda_s^D \phi_s (\xi_s^2 - \eta_j^2)}}_{R_{sj}} b_j$$

$$= \underbrace{-\sum_{n=1}^{\infty}\sum_{j=0}^{\infty} \frac{\rho k c_0 Q_n (-1)^j \xi_s \sin(\xi_s h) \cos(\eta_j y_n) e^{i\beta_j(L_p+x_n)-i\phi_s L_p}}{2\Lambda_s^D \phi_s \Lambda_j^B (\xi_s^2 - \eta_j^2)}}_{P_{s1}} \tag{3.50}$$

$$c_s + d_s = \sum_{m=0}^{\infty} \underbrace{\frac{\sin(\kappa_m h)\cos(\xi_s h)\kappa_m - \cos(\kappa_m h)\sin(\xi_s h)\xi_s}{\Lambda_s^D (\kappa_m^2 - \xi_s^2)}}_{M_{sm}} g_m \tag{3.51}$$

$$c_s - d_s = \sum_{m=0}^{\infty} \underbrace{\frac{\sin(\kappa_m h)\cos(\xi_s h)\kappa_m - \cos(\kappa_m h)\sin(\xi_s h)\xi_s}{i\phi_s \Lambda_s^D (\kappa_m^2 - \xi_s^2)}}_{S_{sm}} f_m \tag{3.52}$$

Applying the same procedures in chapter 2, the residue and W-H solutions for the rigid unbaffled long enclosure with the ground are obtained. We have

$$f_s + i\underbrace{\alpha_s}_{U_{ss}} g_s = \sum_{m=0}^{\infty} \underbrace{(-1)^m \frac{\kappa^+(\alpha_m) L^+(\alpha_m) \kappa^+(\alpha_s) L^+(\alpha_s)}{2\alpha_m (\alpha_s + \alpha_m) \Lambda_s^C (-1)^s}}_{H_{sm}} \left(f_m - i \underbrace{\alpha_m}_{U_{mm}} g_m \right) \tag{3.53}$$

Rewriting Eqs. (3.49) to (3.53) in matrix forms, we have

$$\mathbf{LC+D=E+KB} \tag{3.54}$$

$$\mathbf{LC\text{-}D=P+RB} \tag{3.55}$$

$$\mathbf{C+D=MG} \tag{3.56}$$

$$\mathbf{C\text{-}D=SF} \tag{3.57}$$

$$\mathbf{F+UG=H(F\text{-}UG)} \tag{3.58}$$

where $\mathbf{B}$, $\mathbf{C}$, $\mathbf{D}$, $\mathbf{F}$, and $\mathbf{G}$ are unknown coefficients to be determined; $\mathbf{L}$, $\mathbf{R}$, $\mathbf{E}$, $\mathbf{U}$, $\mathbf{K}$, $\mathbf{P}$, $\mathbf{M}$, $\mathbf{S}$, and $\mathbf{H}$ are the known matrices that can be constructed according to Eqs. (3.49) to (3.53).

To validate the theoretical model, numerical simulations are carried out. In the proposed method, the size of the acoustic domain, the number of sources, impedance boundary conditions, and the targeted frequency range are arbitrary. However, for the sake of calculation efficiency, we start with a relatively small long enclosure of 1 m in height and 5 m in length. The frequency of interest ranges between 200 Hz and 2000 Hz. The maximum wavelength is about 1.7 m at 200 Hz. So, all lengths in the following content are based on the multiples of this value. A monopole point source with its volume velocity strength being Q_1=0.01 $\mathrm{m^2/s}$ is considered first. It is placed at (-4, 0.5) m. The impedance boundary conditions applied to the partial lining come from an MPPA. The acoustical impedance of the MPPA is obtained according to the equation proposed by Maa (1998):

$$Z_p = \underbrace{-i\rho c_0 \cot\left(\frac{\omega D}{c_0}\right)}_{Z_{Cavity}} \\ + \underbrace{\frac{32\mu t_{MPP}}{p_{MPP} d_{MPP}^2}\left(\sqrt{1+\frac{K^2}{32}}+\frac{\sqrt{2}}{32}K\frac{d_{MPP}}{t_{MPP}}\right)+\frac{i\rho\omega t}{p_{MPP}}\left(1+\frac{1}{\sqrt{9+K^2/2}}+0.85\frac{d_{MPP}}{t_{MPP}}\right)}_{Z_{MPP}} \tag{3.59}$$

where $\mu = 1.84\times10^{-5}$ kg/(m*s) is the coefficient of kinematic viscosity of air, ω is the radian frequency, t_{MPP} is the thickness of the MPP, d_{MPP} is the diameter of micro-holes, p_{MPP} is the perforation ratio of the MPP, D denotes the cavity depth, and K is proportional to the ratio of the radius to the viscous boundary layer thickness inside the orifice:

$$K = (d_{MPP}/2)\sqrt{\rho\omega/\mu} \tag{3.60}$$

Figure 3.12 shows the calculated acoustical impedance of MPPA in the targeted frequency range. The MPPA parameters are summarized in Table 3-2.

Table 3-2 Parameters of MPPA used in the numerical calculation.

t_{MPP} (mm)	d_{MPP} (mm)	p_{MPP}	D (mm)	L_p (m)
0.2	0.2	1%	86	1.7

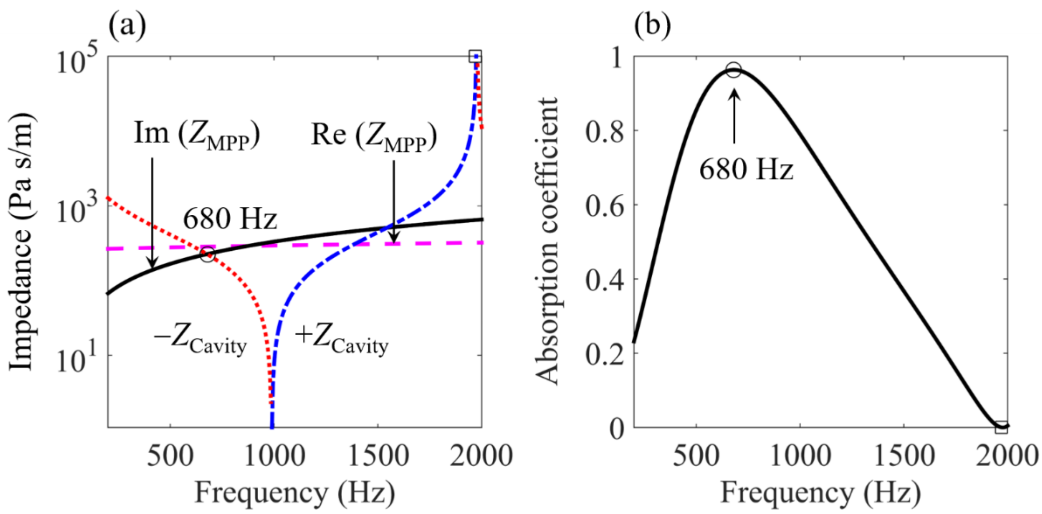

Figure 3.12 Acoustical impedance of an MPPA and corresponding sound absorption coefficient under normal plane-wave incidence.

Once the reactance of the MPP intersects with the negative part of the reactance of the backing cavity, a sound absorption peak appears. At 680 Hz, the total reactance of the MPPA vanishes and it works like a Helmholtz resonator at its resonant frequency. Under this configuration, the maximum absorption coefficient is 0.96 at 680 Hz in normal incidence. However, the in-situ performance may vary.

The directivity patterns of the radiated sound field are presented in Figure 3.13 and good agreement can be found between the results obtained by the FEM and the

W-H technique. The proposed model can be applied to predict the radiated sound field of an unbaffled long enclosure with a partial lining. The applicability of the proposed model will be examined using experiments in the next section.

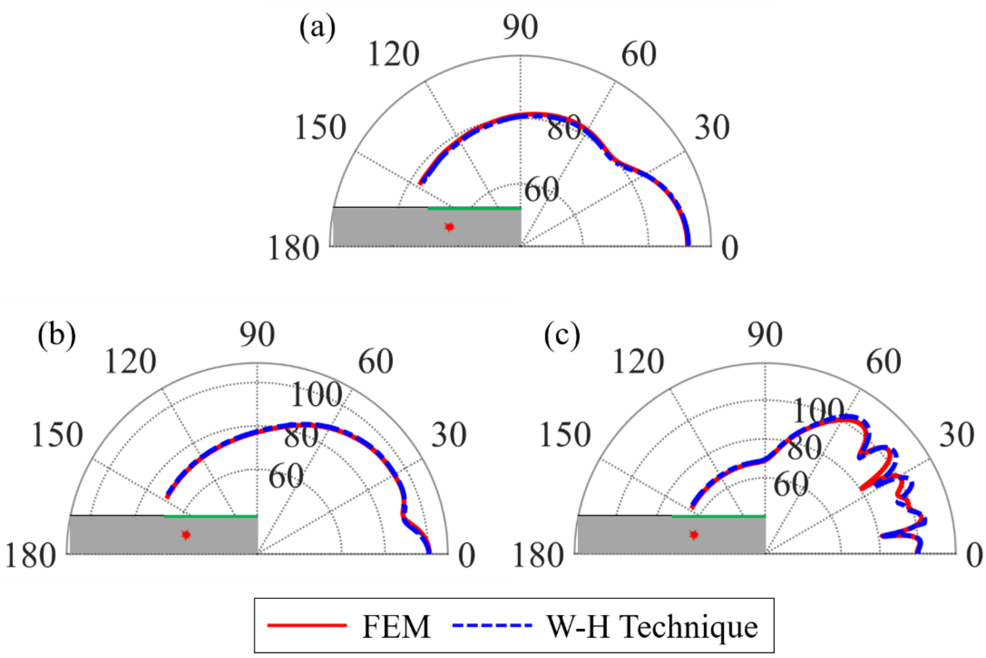

Figure 3.13 Directivity pattern of the radiated SPL field obtained by the FEM and W-H technique at (a) 200 Hz, (b) 680 Hz, and (c) 1700 Hz.

3.4 Experimental validations

Experimental studies are performed to validate the theoretical model proposed in Section 3.2. The schematic diagram of the quasi-2D testing system is demonstrated in Figure 3.14 (a). A Detailed introduction about the measurement devices can be found in Section 2.4. Here, to mimic the ground, an acrylic plate is used to close one side of the quasi-2D space. Besides, another acrylic plate is inserted into the quasi-2D space to simulate the wall. Absorption materials and MPPA are attached to the inner wall of the long enclosure to mimic impedance boundary conditions.

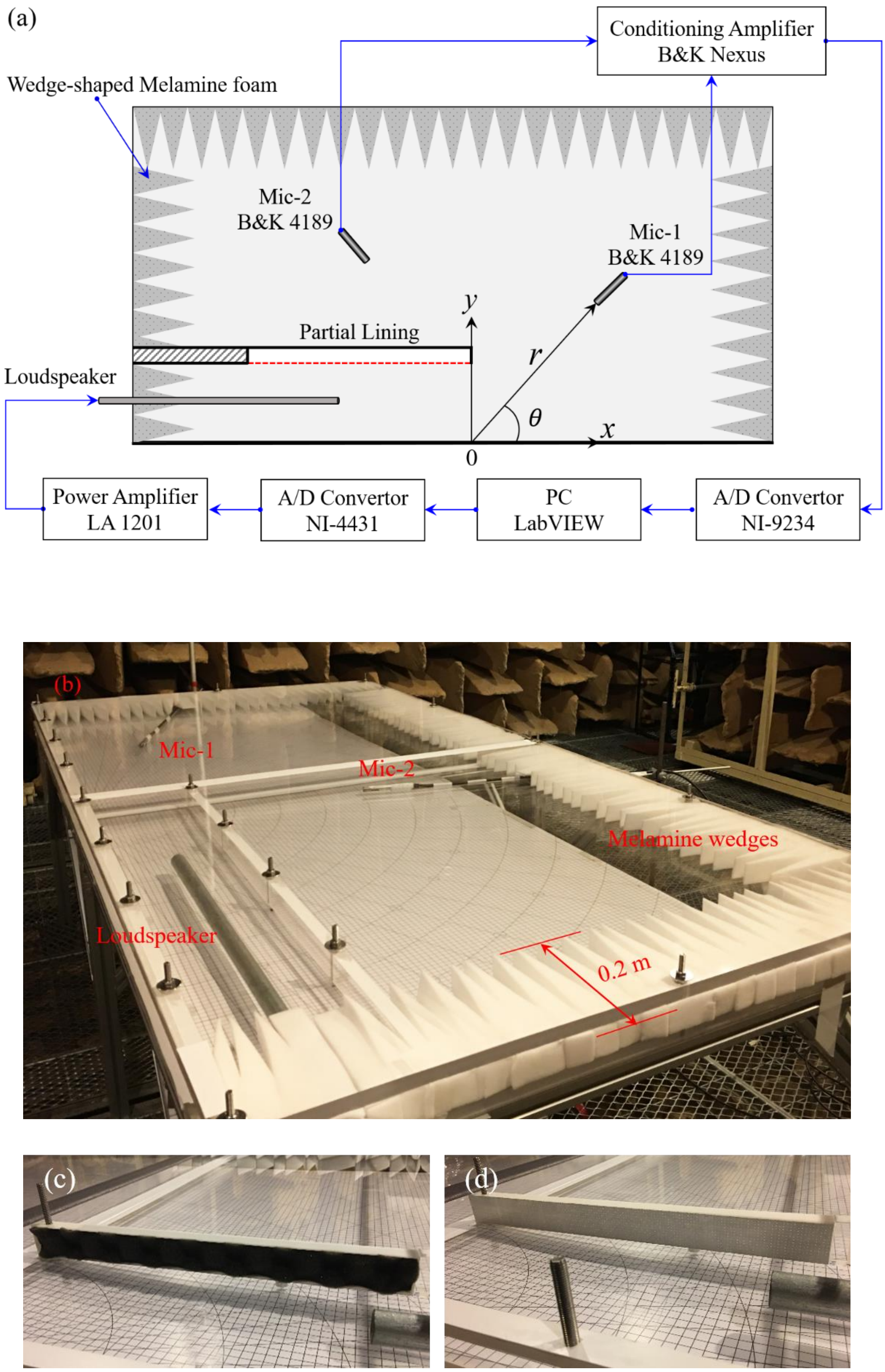
(a)
Conditioning Amplifier
B&K Nexus
Wedge-shaped Melamine foam
Mic-2
B&K 4189
Mic-1
B&K 4189
Partial Lining
Loudspeaker
y
r
θ
x
0
Power Amplifier
LA 1201
A/D Convertor
NI-4431
PC
LabVIEW
A/D Convertor
NI-9234
(b)
Mic-1
Mic-2
Melamine wedges
Loudspeaker
0.2 m
(c)
(d)

Figure 3.14 Experimental setups: (a) schematic diagram of the quasi-2D experimental test rig, (b) photography of the test rig, (c) partial lining of absorption materials, and (d) partial lining of MPPA.

To validate the proposed model, a layer of sound absorption material is used to simulate a partial lining. The acoustical impedance and sound absorption coefficient under normal plane wave incidence are obtained using an impedance tube as presented in Figure 3.15.

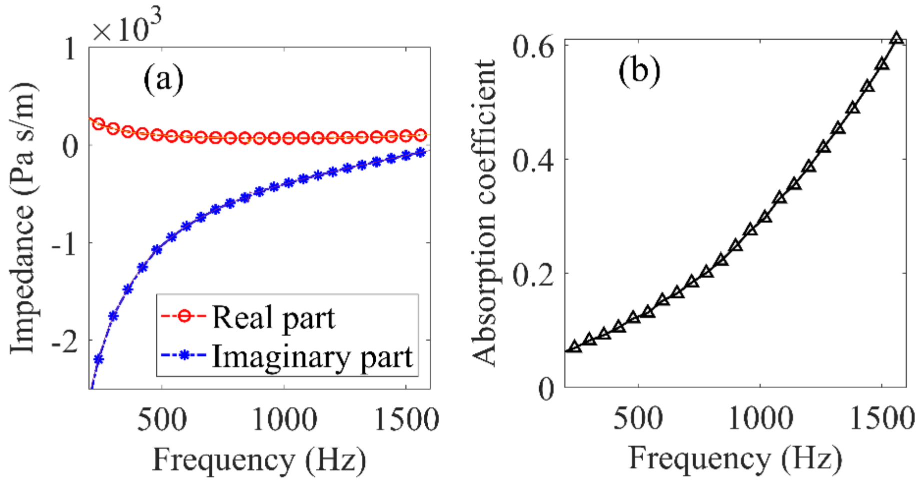

Figure 3.15 Acoustical impedance (a) and sound absorption coefficient (b) of sound absorption material obtained by an impedance tube.

The directivity patterns of the radiated SPL field obtained by the W-H technique and experiment are presented in Figure 3.16. The results are generally consistent in patterns, however, there are fluctuations in the experimental results, especially at the higher frequencies as presented in Figure 3.16 (c). These errors result from the shape effect of the sound absorption material. In the theoretical model, all the surfaces are assumed to be flat. Nevertheless, in the experiment, the rough surface of the material changes the reflected direction of the sound waves and the sound distribution inside the long enclosure changes as well. Then, the radiated sound field which is determined by the sound field inside the long enclosure varies accordingly. Besides, this effect becomes dominant when the wavelength of the incoming sound wave is smaller than the corrugation size of the rough surface, namely, at high frequencies.

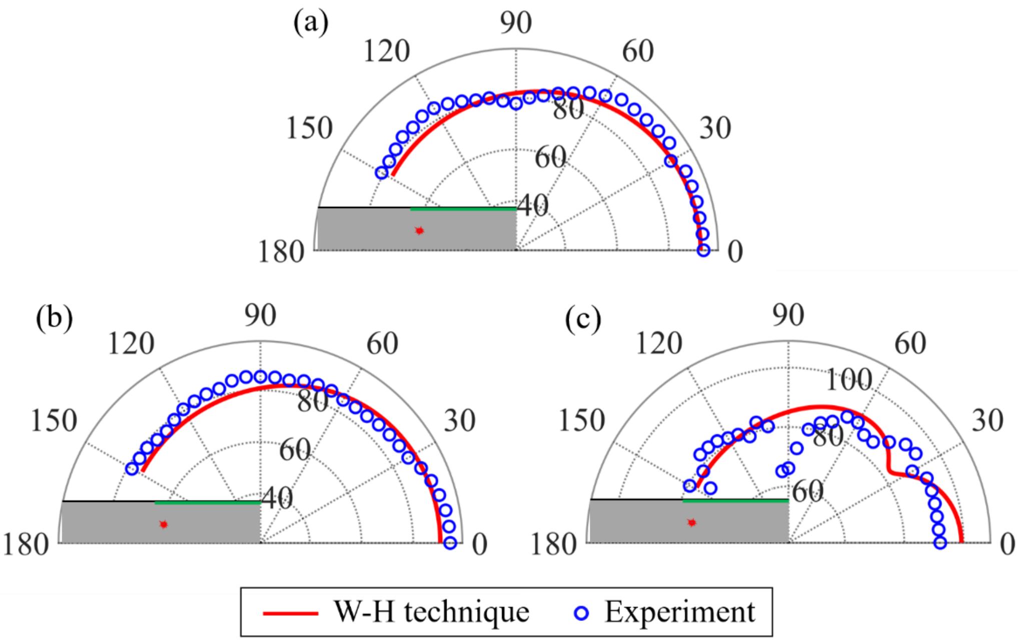

Figure 3.16 Directivity patterns of the radiated SPL field from a long enclosure with partially lined porous materials (a) 500 Hz, (b) 1000 Hz, and (c) 1500 Hz.

In addition, a partial lining of flat MPPA is used to validate the model. The basic parameters are listed in Table 3-3. The SPL spectra obtained by the W-H technique and experiment at receiver (-0.6 0.6) m are presented in Figure 3.17. The results agree well under 850 Hz and the patterns are similar in other frequencies. However, there are discrepancies between the results in the middle to high frequencies which result from manufacturing and assembling errors.

Table 3-3 Parameters of MPPA used in the experiment.

t_{MPP} (mm)	d_{MPP} (mm)	p_{MPP}	D (mm)	L_p (mm)
0.2	0.5	2%	18	435

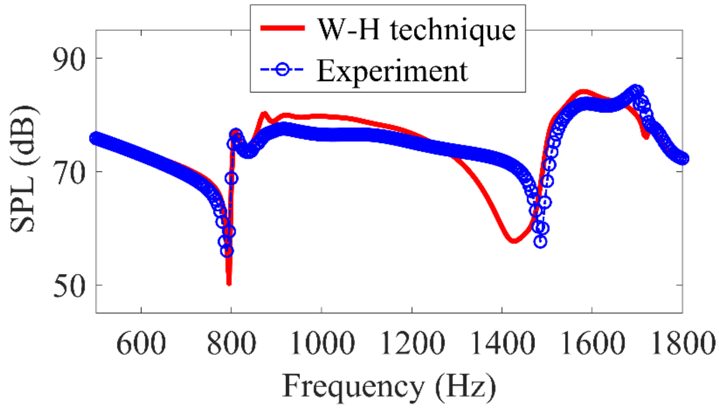

Figure 3.17 SPL spectra attained by the W-H technique and the experiment at receiver point (-0.6, 0.6) m.

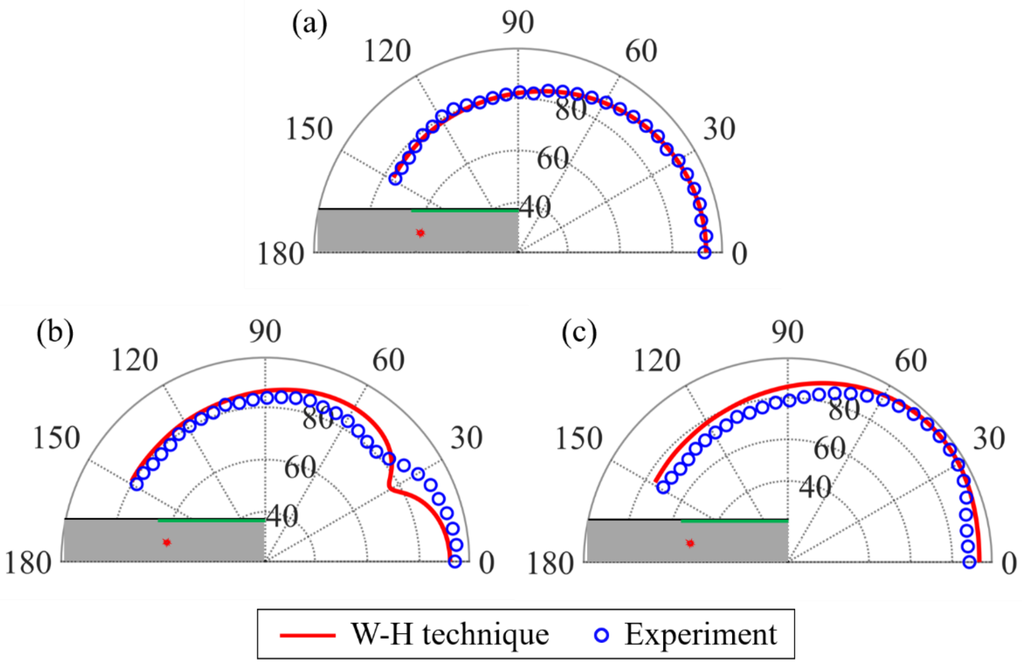

Figure 3.18 Directivity patterns of the radiated SPL field from a long enclosure with partially lined MPPA (a) 500 Hz, (b) 1000 Hz, and (c) 1500 Hz.

The directivity patterns of the radiated SPL field obtained by the W-H technique and experiment are presented in Figure 3.18. General patterns coincide with each other even though there are discrepancies between theoretical and experimental results. Due to the manufacturing error of the MPPA, the sound pressure field inside the unbaffled long enclosure has changed which gives rise to the change of the radiated directivity pattern. Combining the experimental results, the theoretical model is validated, even though there are certain errors that are within the acceptable range. However, it is unsuitable to use the proposed theoretical model to consider the impedance of a lining when its surface shape influences the sound distribution.

3.5 Summary

In this chapter, a rigorous and explicit model is established for the prediction of sound radiated from a semi-infinite long enclosure in which an unbaffled opening, the ground, and point-source excitation are taken into consideration simultaneously. The results obtained by the W-H technique and FEM are compared and discussed which indicates that the proposed method can predict the sound fields both inside and outside a long enclosure with high accuracy and efficiency.

The theoretical model can be applied to a broad frequency range, generalized to arbitrary boundary conditions. Besides, there is no size restriction for the acoustical domain. The performance of acoustical liners with constant impedances in attenuating the noise inside and outside a long enclosure is first investigated, based on which potential noise reduction approaches are introduced. The proposed model will be an effective tool for conducting parameter studies, explaining the physics behind the sound radiation phenomenon, and proposing appropriate noise control strategies.

Finally, quasi-2D experiments are carried out to validate the proposed models in which a layer of porous material and MPPA are used to provide different acoustical impedances. The radiated directivity patterns agree with each other in relatively low frequencies. However, discrepancies exist at middle to high frequencies as the shape of the material surface and the manufacturing error of MPP influence the distribution of sound inside the long enclosure. Combining the experimental results, the theoretical model is validated, even though there are certain errors that are within the acceptable range. However, it is unsuitable to use the proposed theoretical model to consider the impedance of a lining when its surface shape influences the sound distribution.

CHAPTER 4

SOUND RADIATION CONTROL OF AN UNBAFFLED LONG ENCLOSURE USING HELMHOLTZ RESONATORS

4.1 Introduction

In the last two Chapters, the W-H technique has been applied to model the sound radiated from unbaffled long enclosures with and without the ground effect, which are corresponding to ductwork systems and traffic tunnels in practice. The sound pressure field inside the unbaffled long enclosure was expressed in terms of the superposition of acoustic modes, while the radiated sound pressure field was described by the W-H technique. It is convenient to explain the radiation phenomenon through the classical mode theory, nevertheless, complicated to derive the modal response coefficients. In addition, despite that the radiated sound pressure field can be explicitly expressed in terms of observation radius and angle, which can deal with large acoustical domains with high efficiency, the sound pressure field is very difficult to obtain when there are discontinuous noise control devices mounting on the enclosure wall. For the FEM, it is convenient to calculate the sound pressure field inside an unbaffled long enclosure even when discrete acoustical silencers are mounted on the wall which is more flexible than the theoretical models. However, the calculation efficiency declines rapidly when dealing with large acoustical domains outside the long enclosure. Hence, to take the advantage of both the W-H technique and the FEM, a hybrid method is proposed in this chapter to calculate the sound radiation from an unbaffled long enclosure with the ground. The sound pressure field inside the long enclosure is first obtained by the FEM, while the radiated sound pressure field is calculated through the W-H technique using the calculated sound pressure and particle velocity at the opening. This hybrid method not only possesses the flexibility of the FEM to deal with complicated noise control devices and boundary conditions but also has the high efficiency of the W-H technique in the calculation of a large acoustic domain. Numerical implementation of the hybrid method is introduced which can deal with complex noise control devices mounting on the wall and calculate large acoustical domains.

To effectively reduce the noise radiated from the portals of a soundproof tunnel using a confined space on the wall, a simple, reliable, and compact noise control device is needed. Recently, Wang et al. (2015; 2017; 2018) proposed an active noise control (ANC) system which is called the planar virtual sound barrier to attenuate the noise radiated from a baffled rectangular cavity. Although substantial noise reductions were achieved near the resonant frequencies of the cavity using the ANC system, it can be hardly applied in practical traffic tunnels owing to the robust and complicated requirements of the ANC system. On the other hand, many passive noise attenuation techniques such as covering the surfaces of parallel barriers (Crombie & Hothersall, 1994), and ducts (Rawlins, 1978) with porous materials have been proposed to reduce the sound radiated from openings. However, the performance is undesirable at low frequencies and the porous materials may cause hygiene problems such as the accumulation of dust and bacteria. The concept of sound wave-trapping barriers was introduced (Yang et al., 2013) recently, where the inner walls of the barriers are coated by wedge-shaped structures. The sound waves are either redirected towards the ground or trapped within the parallel barriers so that the noise radiated to the outside is reduced. In order to suppress the sound radiated from parallel barriers, Helmholtz resonators (HRs) were adopted by Wang and Choy (2019a; 2019b) to modify the sound pressure distribution inside the parallel barriers so that the diffracted and the radiated sound around the targeted frequencies were reduced with an appropriate number and appropriate positions of HRs. The performance of HRs, however, is still limited by relatively narrow working frequency bands. To widen the stopband, a flexible panel device (FPD) was proposed to be mounted on the walls of the parallel barriers (Wang et al., 2020). An average insertion loss (IL) of approximately 5 dB was achieved in the frequency range between 80 Hz and 1000 Hz. Furthermore, with the advancement of acoustical meta-surfaces (AMS), parallel barriers of inhomogeneous impedance were constructed using an array of slender tubes with varying depths (Wang et al., 2015; 2016; Xiao et al., 2020). Reflected sound waves were manipulated applying the phase gradient of the walls so that the trapped acoustical energy inside the barrier was altered, which improved the sound reduction in the shadow zone.

To distort the sound distribution inside the unbaffled long enclosure, mounting HRs on the enclosure wall is proposed in this chapter. The modal response coefficients at the opening around the targeted frequencies are reduced, and the radiated noise in the shadow zone is expected to be suppressed. HRs have been adopted to attenuate the noise in open cavities (Wang & Choy, 2019a; 2019b), ducts (Seo & Kim, 2005; Cai & Mak, 2018), and enclosure systems (Li et al., 2007; Li & Cheng, 2007; Yu et al., 2008; Yu & Cheng, 2009), however, the interaction between HRs and the acoustic field inside an unbaffled long enclosure has seldom been investigated. Besides, the relationship between acoustical modes and the radiation patterns is analyzed. The HR array locations, optimized to reduce the radiated noise, are obtained. In addition, the influences of noise source types on the radiated acoustic field are explored. Finally, a quasi-two-dimensional experiment is carried out to verify the proposed model and examine the feasibility of HRs in suppressing the noise radiated from an unbaffled long enclosure including the ground.

4.2 Hybrid method

4.2.1 Formulation of the sound radiation problem

The schematic diagram of an FE-WH-based hybrid method to predict the sound radiated from an unbaffled long enclosure with the ground is shown in Figure 4.1. The sound pressure field inside a long enclosure is obtained by the FEM, while the radiated sound pressure field is determined by the W-H technique using the calculated pressure and particle velocity at the opening.

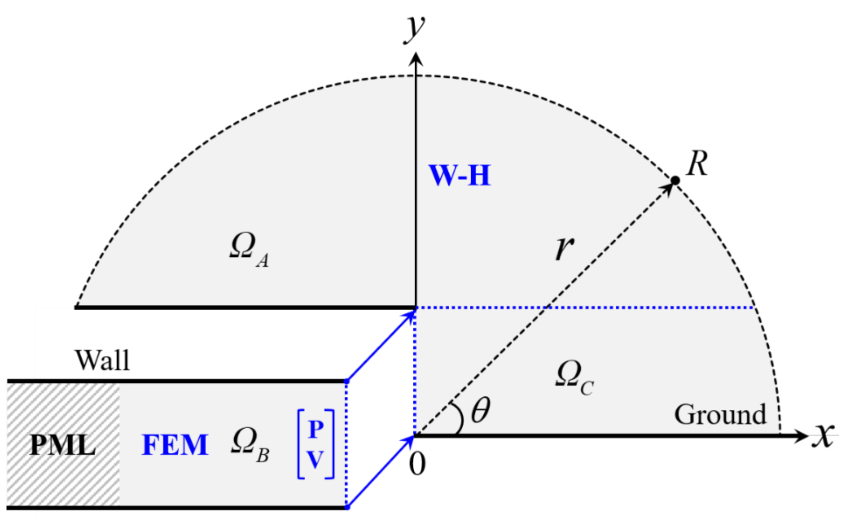

Figure 4.1 Schematic diagram of a hybrid method to predict sound radiation from an unbaffled long enclosure with the ground.

Applying the same procedures in chapter 2 and 3, the W-H solution for the rigid unbaffled long enclosure with the ground is obtained as follows:

$$\dot{P}_A^{+}(\alpha,h)=\sum_{m=0}^{\infty}(-1)^m \frac{f_m - i\alpha_m g_m}{2\alpha_m(\alpha+\alpha_m)} L^{+}(\alpha_m)\kappa^{+}(\alpha_m) L^{+}(\alpha)\kappa^{+}(\alpha) \tag{4.1}$$

The far-field directivity pattern of the radiated sound pressure field outside the unbaffled long enclosure is given by

$$p_A(r,\theta)=i\frac{e^{i\pi/4}}{\sqrt{2\pi}}\dot{P}_A^{+}(-k\cos\theta,h)e^{ik\sin\theta h}\frac{e^{-ikr}}{\sqrt{kr}} \tag{4.2}$$

From Eqs. (4.1) and (4.2), the radiated sound pressure field is determined by the modal response coefficients of sound pressure and pressure gradient along horizontal direction. To determine the coefficients, the continuity relations of sound pressure and pressure gradient at the opening of the unbaffled long enclosure are considered.

$$\begin{bmatrix} P_1 \\ P_2 \\ \vdots \\ P_n \end{bmatrix} = \begin{bmatrix} Y_1^C(y_1) & Y_2^C(y_1) & \cdots & Y_m^C(y_1) \\ \vdots & \vdots & \vdots & \vdots \\ \vdots & \vdots & \vdots & \vdots \\ Y_1^C(y_n) & Y_2^C(y_n) & \cdots & Y_m^C(y_n) \end{bmatrix} \begin{bmatrix} g_1 \\ g_2 \\ \vdots \\ g_m \end{bmatrix} \tag{4.3}$$

and

$$\begin{bmatrix} V_1 \\ V_2 \\ \vdots \\ V_n \end{bmatrix} = \begin{bmatrix} Y_1^C(y_1) & Y_2^C(y_1) & \cdots & Y_m^C(y_1) \\ \vdots & \vdots & \vdots & \vdots \\ \vdots & \vdots & \vdots & \vdots \\ Y_1^C(y_n) & Y_2^C(y_n) & \cdots & Y_m^C(y_n) \end{bmatrix} \begin{bmatrix} f_1 \\ f_2 \\ \vdots \\ f_m \end{bmatrix} \tag{4.4}$$

where P_n and V_n are the sound pressure and horizontal pressure gradient on meshing nodes $(0,y_n)$ along the enclosure opening. Modal function of region Ω_C is denoted by Y_m^C which can be obtained by the Helmholtz equation and the boundary condition on the ground.

Rewriting Eq. (4.3) and Eq. (4.4) in matrix form, we have

$$\mathbf{P}=\mathbf{MG} \tag{4.5}$$

$$\mathbf{V}=\mathbf{MF} \tag{4.6}$$

where matrices $\mathbf{P}$ and $\mathbf{V}$ can be obtained using FEM, while $\mathbf{M}$ can be constructed using Eq. (4.3). After solving Eqs. (4.5) and (4.6), the modal response coefficients at the opening $\mathbf{G}$ and $\mathbf{F}$ can be obtained. Then, the directivity pattern of the radiated sound pressure can be calculated using Eqs. (4.1) and (4.2).

4.2.2 Implementation of the hybrid method

In this section, the hybrid model is implemented numerically. The configuration of the unbaffled long enclosure, air properties, and the monopole point source are listed in Table 4-1.

Table 4-1 Configuration of the unbaffled long enclosure, air properties, the monopole point source, and the far-field directivity.

Air Properties		**Monopole Point Source**	
Density	1.225 kg/m^3	Location	(-2, 0.5) m
Sound speed	340 m/s	Volume velocity strength	0.01 m^2/s
Unbaffled Long Enclosure		**Directivity Patterns**	
Height	1 m	Far-field radius	5 m
Truncated length	5 m	Observation angle	[0, 150] degrees

An unbaffled long enclosure of 5 m in length and 1 m in height is considered here. A monopole point source is located at (-2, 0.5) m and the volume velocity strength is 0.01 m^2/s. The far-field observation radius is 5 m and the observation angle is in the range of [0, 150] degrees. Besides, the speed of sound and density of the air are 340 m/s and 1.225 kg/m^3, respectively.

In the first place, the sound pressure field inside the long enclosure is calculated using the FEM. To ensure the accuracy of the results, the mesh grids along the opening are refined as presented in Figure 4.2. Besides, a geometrical singularity exists at the enclosure edge, where the pressure gradient at this point may be wrong. Hence, more grids are needed near this point and the horizontal pressure gradient at this point is replaced by that of the nearest point in the following calculations. Such replacement may give rise to certain errors of the radiated sound pressure field. however, the direct use of the horizontal pressure gradient at the edge will lead to wrong results.

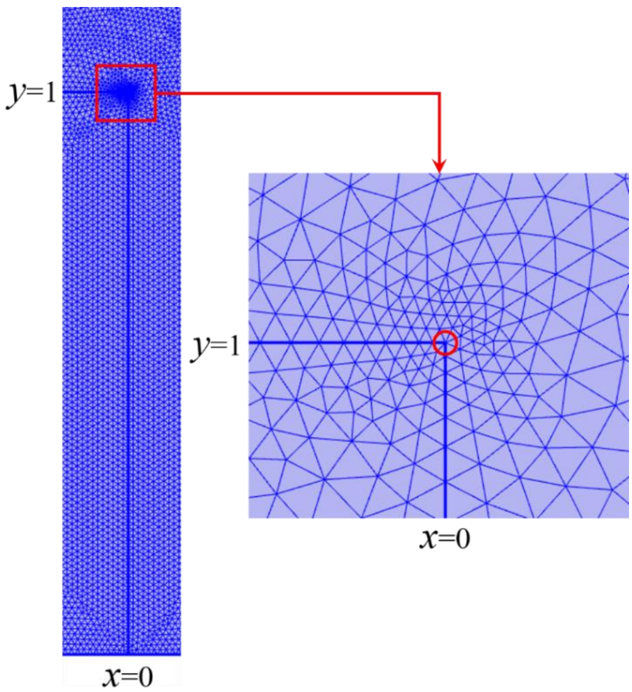

Figure 4.2 Refinement of the meshing grids along the enclosure opening and at the sharp edge.

The sound pressure and the horizontal particle velocity along the opening at 340 Hz, 510 Hz, and 1190 Hz are presented in Figure 4.3. Using Eqs. (4.5) and (4.6), the modal response coefficients of sound pressure and horizontal pressure gradient can be obtained. Then, using Eqs. (4.1) and (4.2), the directivity pattern of the radiated sound field from the unbaffled long enclosure can be obtained.

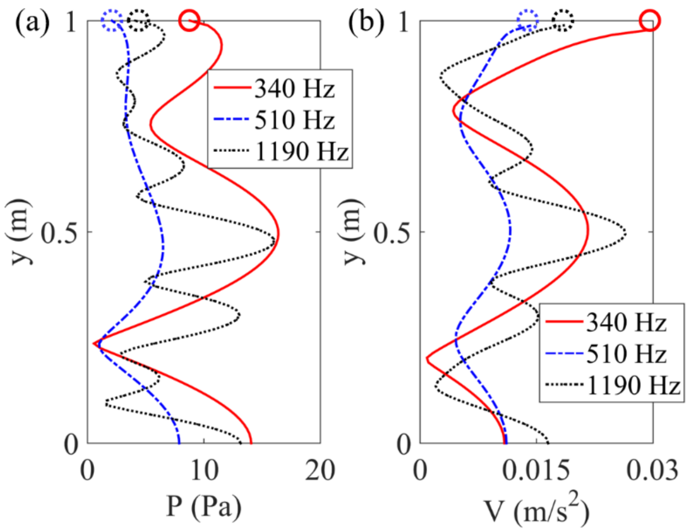

Figure 4.3 Distribution of absolute sound pressure (a) and particle velocity (b) along the opening at 340 Hz, 510 Hz, and 1190 Hz.

Figure 4.4 compares the directivity patterns of the radiated SPL field obtained by the FEM and the hybrid method. Generally, the results agree well with each other even though small discrepancies exist in the shadow zone which must result from the approximation at the edge. The distribution patterns of the radiated sound field can be briefly explained from the perspective of acoustical rays applying Figure 4.5. In the shadow zone, the sound field is only composed of diffracted rays that depend on the acoustical properties near the edge. The distribution of SPL in this region appears to be uniform. The SPL distribution in the illuminated zone, however, is complex, which is formed by direct sound propagation, sound reflection from the ground and wall, and sound diffraction at the sharp edge. These sound waves propagate to the receiver with different phases and over different distances. Consequently, their superposition leads to directivity lobes in front of the enclosure opening.

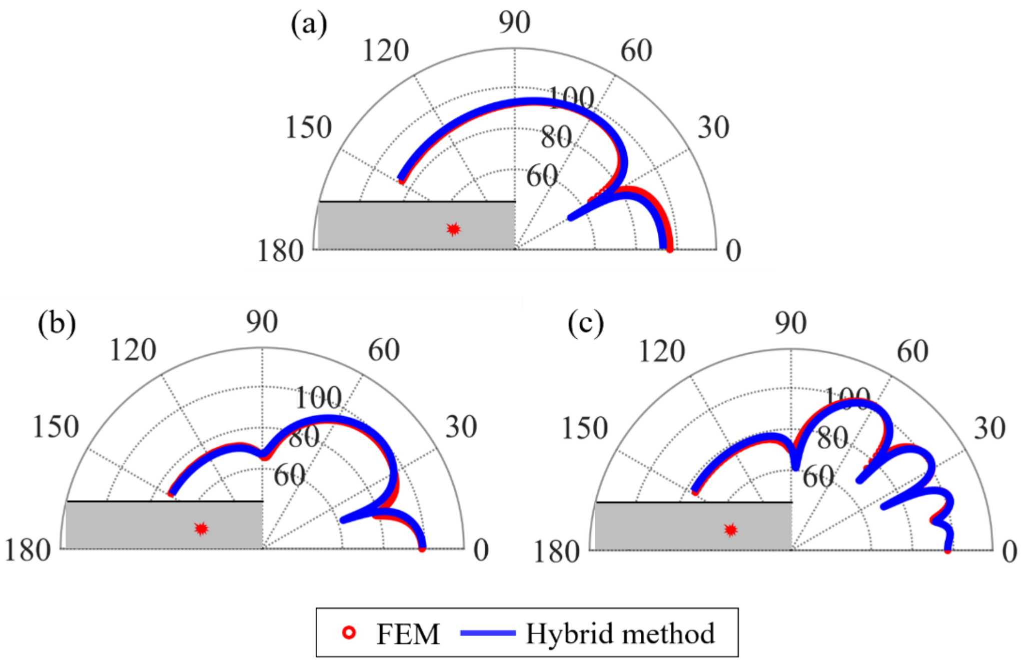

Figure 4.4 Directivity patterns of the radiated SPL field obtained by the FEM and the proposed hybrid method at (a) 340 Hz, (b) 510 Hz, and (c) 1190 Hz.

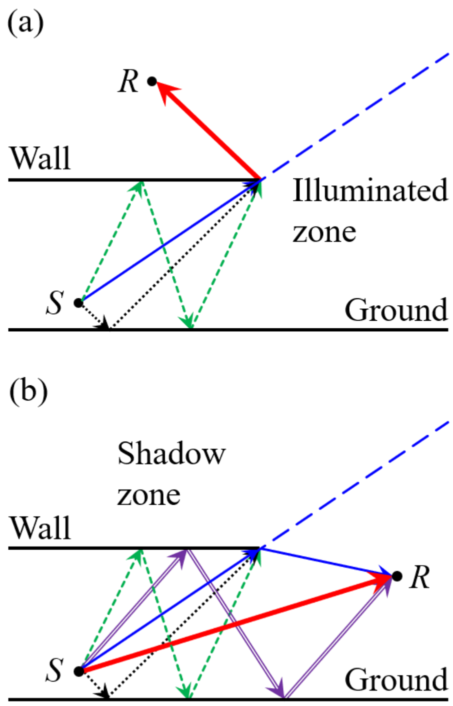

Figure 4.5 Acoustical rays from the sound source to the (a) shadow and (b) illuminated zones of an unbaffled long enclosure with the ground.

As the directivity polar plots can only show the patterns of the radiated sound field at specific frequencies, SPL spectra of two randomly picked receiving points R1 (-1, 0.5) m and R2 (-3, 3) m are used to represent the characteristics of sound fields inside and in the shadow zone of the long enclosure. The comparison between the SPLs obtained by the W-H technique and the hybrid method in the targeted frequency range at the receivers is illustrated in Figure 4.6. Good agreement can be observed between the results, which along with Figure 4.4, verifies the proposed hybrid model in the calculation of sound fields inside and outside an unbaffled long enclosure.

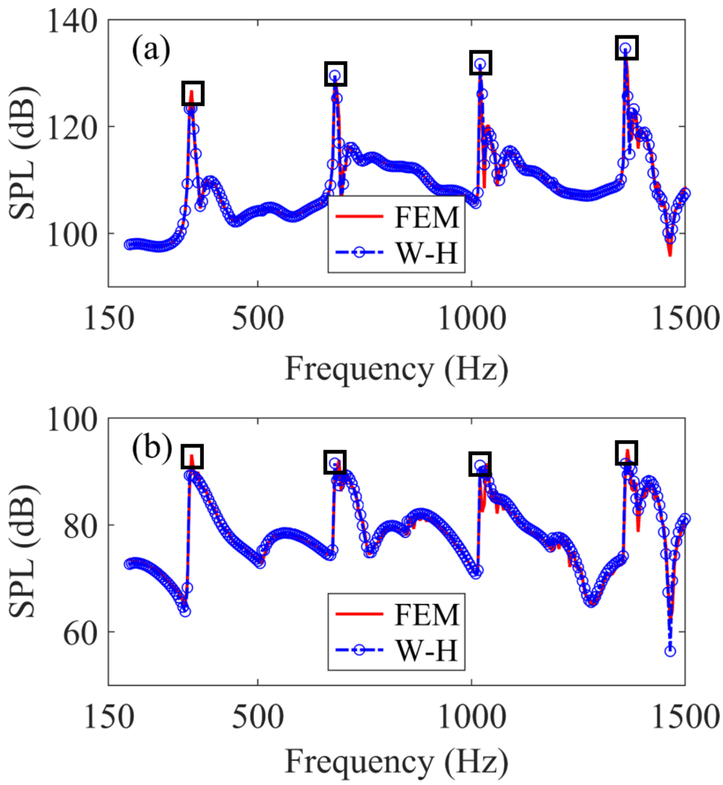

Figure 4.6 Comparison of SPL spectra of receivers inside and outside the unbaffled long enclosure at (a) R1 (-1, 0.5) m and (b) R2 (-3, 3) m.

4.3 Sound suppression of an unbaffled long enclosure using HRs

4.3.1 Mechanism investigations

As demonstrated in Figure 4.6, SPL peaks can be observed around 340 Hz, 680 Hz, 1020 Hz, and 1360 Hz (denoted by squares) inside and at the shadow zone of the long enclosure. They are the resonant frequencies of the long enclosure along the vertical direction. In order to explore the formation mechanisms of sound peaks and then suppress the radiated noise at peak frequencies, HRs are proposed to reduce the relevant modal responses inside the long enclosure so that the radiated sound field around the peak frequencies are expected to be controlled. Generally, the acoustical coupling between a long enclosure and an HR is strong when the resonator is close to the anti-node regions or near the primary sound sources. In addition, the acoustical properties at the enclosure edge, according to the geometrical theory of diffraction (GTD), have a great influence on the diffracted sound field. Hence, we choose two HR locations L1 (-2, 1) m and L2 (0, 1) m to explore their influences on the sound radiation phenomenon. Figure 4.7 (a), (b), and (c) show the SPL distributions inside and outside a long enclosure at 340 Hz for rigid wall without and with HRs at locations L1 (denoted by HR340, L1) and L2 (denoted by HR340, L2), respectively. Using the hybrid method, the effect from the HR profiles on the radiated sound pressure field is ignored. The HRs in Figure 4.7 are used mainly to illustrate their locations. In Figure 4.7 (a), due to multiple reflections on the rigid ground and wall, an acoustic mode can be observed, and the SPL is generally high inside the long enclosure. However, in the horizontal direction, standing waves can be hardly seen because the reflected sound is relatively small which just influences the sound distribution near the opening. Outside the long enclosure, the principal lobe (the lobe with the highest SPL near the enclosure edge) locates at about 70 degrees. Figure 4.7 (b) shows that when the resonator is located exactly above the sound source, the SPL distribution in the long enclosure is greatly changed and the sound energy radiates mainly toward 10 degrees. Besides, the amplitude of the principal lobe is greatly reduced and its angle shifts to a lower degree compared with the rigid case. In Figure 4.7 (c), the HR340 is mounted near the edge, the SPL distribution inside the long enclosure remains almost the same as the rigid case without a resonator. The amplitude of the principal lobe, however, is reduced and its angle shifts to a lower degree as well.

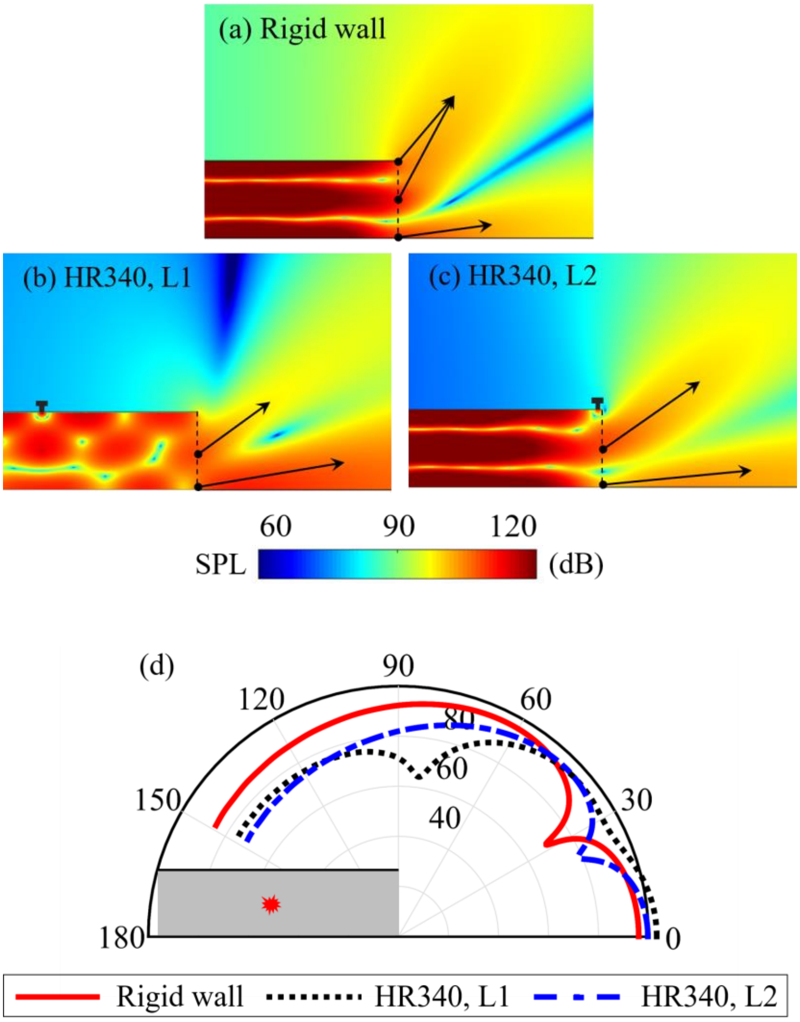

Figure 4.7 SPL distributions of the sound fields at 340 Hz: (a) Rigid wall, (b) HR340 at L1, (c) HR340 at L2; and (d) far-field directivity patterns.

Figure 4.7 (d) illustrates the comparison of SPL directivity patterns outside the long enclosure. The SPL distribution patterns along the observation radius are like the near-field results. However, the amplitudes and sizes of lobes are different among these three situations. The sound is significantly reduced above the observation angle of 50 degrees when an HR340 is mounted on the enclosure wall. However, the SPLs under the observation angle of 50 degrees are mostly larger than the rigid case which implies that more sound energy radiates to the lower observation angles when an HR340 is mounted. Besides, the performance of HR340 at L2 is better than L1 when the observation angle is larger than 120 degrees. This is caused by the diffracted sound when the HR340 is located at L1 which forms a small lobe in the shadow zone.

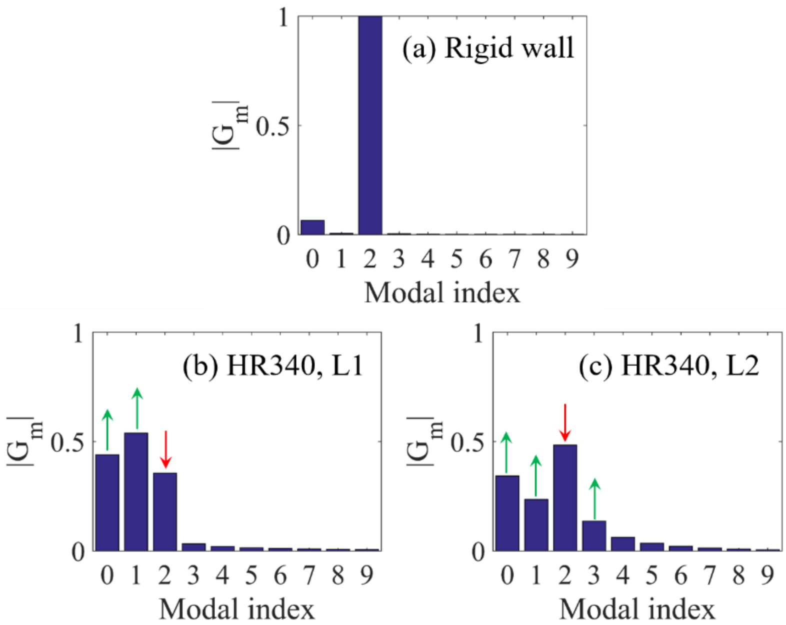

Figure 4.8 Absolute modal response coefficients at the opening normalized by the rigid case: (a) Rigid wall, (b) HR340 at L1, and (c) HR340 at L2.

To better understand the physics behind the sound radiation control of using an HR, acoustical modal analysis is conducted. Figure 4.8 illustrates the absolute modal response coefficients $|G_m|$ for the long enclosure with and without an HR340. In the rigid case, as presented in Figure 4.8 (a), the second acoustic mode is dominant. The amplitudes of the second modal responses are significantly reduced when an HR340 is mounted at L1 and L2 as demonstrated in Figure 4.8 (b) and (c), respectively. The contributions from the adjacent acoustical modes, however, increase as well, which attributes to the energy conservation. Figure 4.8 (b) demonstrated that the zeroth and the first acoustical modes become the main contributors to the total sound pressure field, while Figure 4.8 (c) displays that the first four acoustical modes contribute to the total sound pressure field. Different combinations of these modes form the sound pressure distributions as illustrated in Figure 4.7 (a), (b), and (c), respectively.

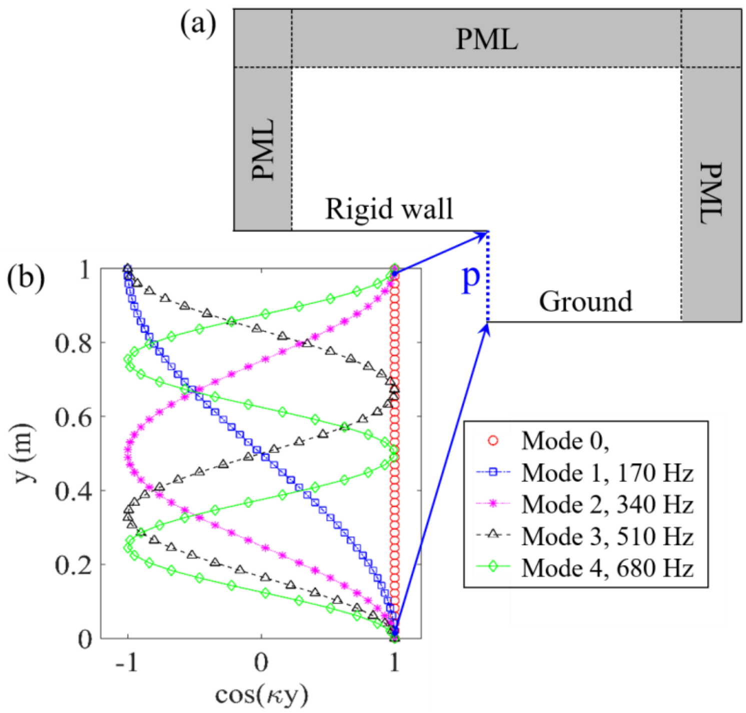

Figure 4.9 Schematic diagram of the hybrid method, (a) the transversal modal shapes of the rigid long enclosure and the corresponding eigen-frequencies, (b) calculation domain in COMSOL.

To find the connections between acoustical modes and the SPL distributions of the radiated sound field, the radiation pattern of each single-mode incidence from the enclosure opening is investigated using the hybrid method. The transversal acoustic mode shapes of the rigid long enclosure and the corresponding eigenfrequencies are displayed in Figure 4.9 (b). These modes are imposed on the enclosure opening as pressure boundary conditions in COMSOL so that their radiation patterns can be obtained as shown in Figure 4.9 (a). Perfectly matched layers (PMLs) are applied to simulate the reflectionless boundaries.

As can be observed in Figure 4.10, the radiation patterns of the zeroth to the fifth mode at 340 Hz are not symmetric about the centerline of the opening as shown in the paper of Tong et al. (2017) and the results in Figure 2.13 and Figure 2.14. However, the radiated acoustical modes from the opening tend to propagate upward due to the ground reflection. Besides, the number of radiation lobes at the opening increase with the modal index, and it is greater than the index by one. Also, it is found that the higher-order acoustical modes are quite easy to dissipate and small lobes merge to form large ones during the radiation process as demonstrated from Figure 4.10 (d) to (f). In the far-field results, as presented in Figure 4.10 (g), the radiation directivities of the acoustical modes differ from each other mainly in front of the opening. By doing the modal decomposition analysis, we find the dominant modal contributors to the radiated field. The sound peaks in the shadow zone can then be suppressed by controlling the modal responses of these modes using HRs.

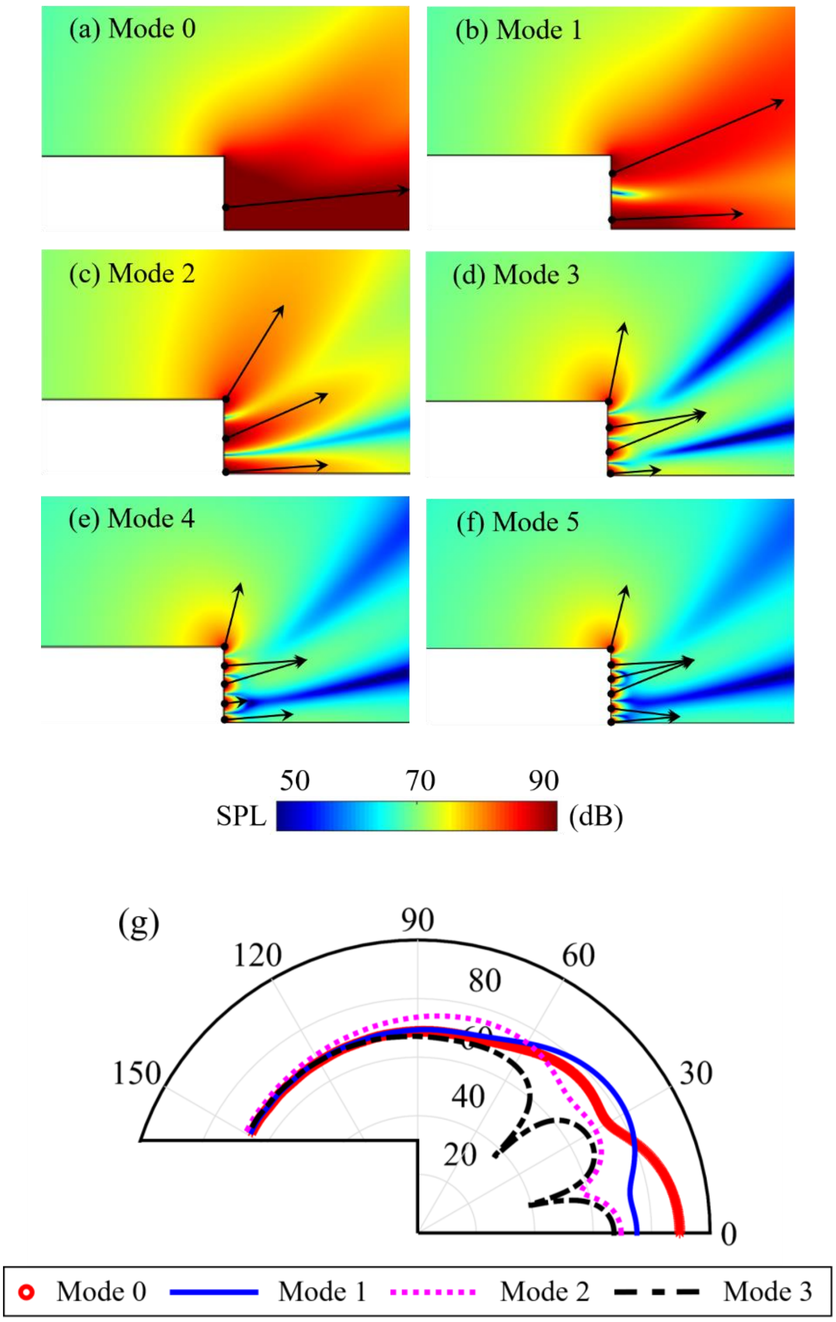

Figure 4.10 Radiated SPL fields under single-mode incidence at 340 Hz: (a) Mode 0, (b) Mode 1, (c) Mode 2, (d) Mode 3, (e) Mode 4, (f) Mode 5, and (g) far-field directivity patterns of Mode 0 to Mode 3.

4.3.2 Diffraction effect at the enclosure edge

Since only the diffracted sound waves propagate into the shadow zone of the long enclosure, the acoustic properties at the sharp edge which can be considered as a diffraction point need to be further studied. According to the GTD proposed by Keller (1962), the diffracted sound pressure field can be calculated by

$$p_d = C_d p_i \frac{e^{ikl}}{\sqrt{l}} \tag{4.7}$$

where p_d and p_i are, respectively, the sound pressure at the receiving and diffracting points, and l is the distance between them. An asymptotical expanded form of the diffraction coefficient is given by

$$C_d = -\frac{e^{i\pi/4}}{2\sqrt{2\pi k}}\left[\sec\left(\frac{\varphi-\phi}{2}\right)+\sec\left(\frac{\varphi+\phi}{2}\right)\right] \tag{4.8}$$

where φ and ϕ are the incident and diffraction angles, respectively.

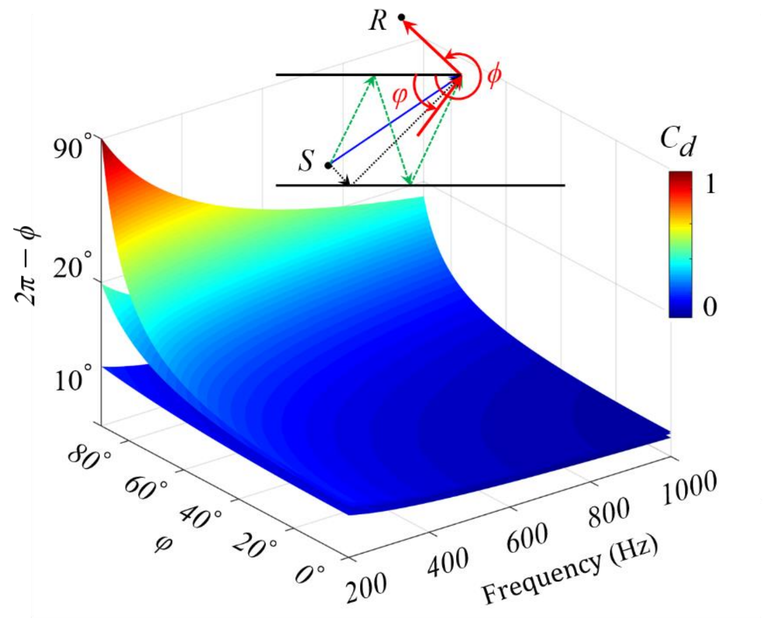

Figure 4.11 Change in the diffraction coefficient regarding frequency, the incident and diffraction angles.

The change of diffraction coefficient against frequency, incident, and diffraction angles is shown in Figure 4.11. The diffraction coefficient decreases as the frequency increases. This implies that a sound wave with a long wave length will be diffracted with higher efficiency. In addition, at a specific frequency, the increase of the incident angle obtains a larger diffraction coefficient. This means that the sound wave will be diffracted more effectively if the incident wave impinges normally to the enclosure wall. On the contrary, if the incident wave propagates along a parallel direction to the enclosure wall, a minimum diffraction coefficient will be observed. Besides, as the diffraction angle increases, it becomes more difficult for sound waves to be diffracted which results in the uniform decrease of SPL at higher observation angles in Figure 4.7 (d).

Combining Eqs. (4.1) and (4.2), the radiated sound pressure field is determined by the modal response coefficients of sound pressure and pressure gradient at the opening. Specifically, they correspond to the amplitude and angle of the incident sound pressure at the edge for the diffraction effect. Their joint effects on the diffraction phenomenon can be represented by a vector quantity, namely, sound intensity. Therefore, attention is then paid to the intensity field around the sharp edge. The sound intensity fields near the enclosure edge with and without HR340 are presented in Figure 4.12 using arrow line plots. The length of the line represents the amplitude and the arrow shows the direction. In the rigid case, as shown in Figure 4.12 (a), a ring-shaped sound intensity distribution that rotates counterclockwise is formed near the opening. The incident sound waves reach the sharp edge almost at a perpendicular angle to the wall. The diffraction coefficient, according to the GTD, is close to the maximum. As a result, the far-field SPL at an observation angle of 120 degrees in the shadow zone stands at about 88 dB as presented in Figure 4.7 (d). After mounting an HR340 on the wall at L1 and L2, the sound intensities in the shadow zone are both reduced as shown in Figure 4.12 (b) and (c), respectively. However, the physics behind these two cases are different. In Figure 4.12 (b), the HR340 is mounted exactly above the sound source. The coupling between the HR340 and the sound field inside the long enclosure is strong which distorts the sound distribution near the opening. The sound waves propagate to the diffraction point at a grazing angle to the wall. In this case, the diffraction coefficient is close to the minimum based on the GTD. In Figure 4.12 (c), the HR340 is mounted near the edge. It produces little effect on the sound field inside the long enclosure. Nevertheless, the sound pressure around the sharp edge is greatly reduced which also gives rise to the suppression of sound in the shadow zone. Therefore, as demonstrated in Figure 4.7 (d), the SPLs at an observation angle of 120 degrees in the shadow zone are 76 dB and 74 dB when an HR340 is mounted at L1 and L2, respectively. The difference between these two cases is that the sound energy propagates mainly along the ground in Figure 4.12 (b) while to the sky in Figure 4.12 (c).

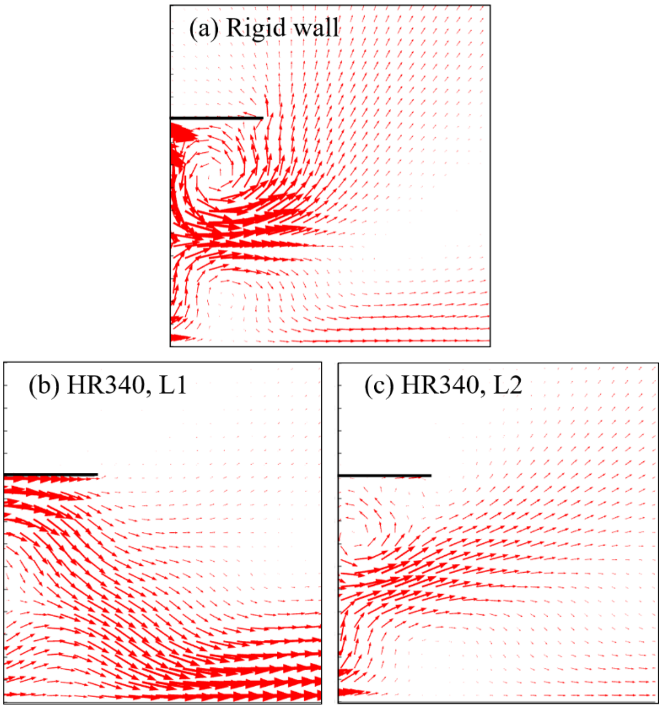

Figure 4.12 Sound intensity field near the sharp edge of the long enclosure at 340 Hz: (a) Rigid case, (b) HR340 at L1, and (c) HR340 at L2.

4.3.3 Use of multiple HRs

A resonator array consisting of HRs with different natural frequencies can be adopted to reduce the noise level at multiple sound peaks. Therefore, according to the SPL spectra presented in, four HRs, namely, HR340, HR680, HR1020, and HR1360 are designed to suppress the sound peaks at 340 Hz, 680 Hz, 1020 Hz, and 1360 Hz, respectively. The geometrical configurations of these HRs are presented in Table 4-2. To begin with, the optimized locations of HRs are obtained based on the maximum mean IL over a frequency bandwidth (20 Hz) centered at the resonant frequencies of HRs. Receiver R2 (-3, 3) m is chosen to represent the properties of the sound field in the shadow zone. As the HRs are moving on the enclosure wall, the IL is a function of horizontal locations of HRs. Mathematically, it is expressed as follows:

$$\begin{aligned} & \max\left[IL_{\text{mean}}\left(f,x\right)\right] \\ & IL_{\text{mean}}\left(f,x\right)=\frac{\sum_{f-10}^{f+10}\left[SPL_{Rigid}\left(f,x\right)-SPL_{HR}\left(f,x\right)\right]}{N_f} \\ & \text{subjected to: } x\in\left[-3,0\right] \end{aligned} \tag{4.9}$$

where subscripts ‘Rigid’ and ‘HR’ represent the cases without and with the HR, respectively. N_f denotes the total number of sampling frequencies used to calculate the SPL. Figure 4.13 indicates the variation of mean ILs at receiving point R2 (-3, 3) m when different HRs are placed on different locations of the enclosure wall. Small and negative ILs can be observed when the HRs are mounted at the left-hand side of the sound source. This implies that the acoustical coupling between HRs and the long enclosure is weak when they are away from the point source. Generally, the optimized locations are between the point source and the sharp edge, and the maximum ILs of HRs decline with the increase of frequency. An exception is that two optimal locations are observed for HR680. However, we use (-0.6, 1) m in the following calculations to avoid unfavorable interactions between HRs when the distance between them is too short.

Table 4-2 Geometrical configurations and the optimized locations of HRs in reducing the noise radiated from an unbaffled long enclosure.

Resonator types	Neck width (m)	Neck length (m)	Cavity width (m)	Cavity length (m)	Optimized Locations (m)
HR340	0.02	0.0381	0.14	0.05	(-1.19, 1)
HR680	0.02	0.02	0.052	0.05	(-1.6,1), (-0.6, 1)
HR1020	0.016	0.02	0.0572	0.02	(-1.8, 1)
HR1360	0.01	0.012	0.028	0.0215	(-2.01, 1)

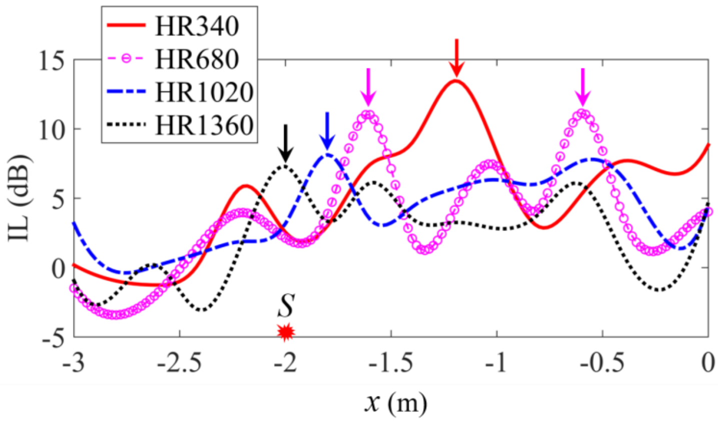

Figure 4.13 Mean IL over the frequency bandwidth of 20 Hz centered at the resonant frequencies of HRs against their locations.

The directivity patterns of the radiated sound field with a single HR and multiple HRs are shown in Figure 4.14. Compared with the rigid case without a resonator, the

SPLs in the shadow zone are significantly reduced both by a single HR and multiple HRs. Due to the favorable or unfavorable interactions among HRs and the long enclosure, the performance of multiple HRs is superior to a single HR at 340 Hz and 1360 Hz, while inferior to a single HR at 1020 Hz. Overall, multiple HRs can reduce multiple SPL peaks. In order to examine whether there are undesirable results in this optimized configuration, the ILs of a single HR and multiple HRs are compared in Figure 4.15. In general, as presented in Figure 4.15 (a), (b), and (d), the performance of multiple HRs can maintain the performance of corresponding single HR in the certain frequency bandwidth. In Figure 4.15 (c), the IL of multiple HRs is smaller than that of a single HR1020 which is resulted from undesirable interactions among HRs and the long enclosure. However, two unexpected IL peaks appear in other frequency ranges which result from favorable interactions among HRs and the sound field inside the long enclosure. From the above analysis, a resonator array consisting of HRs with different natural frequencies can be adopted to reduce the noise level at multiple sound peaks if their locations are optimized.

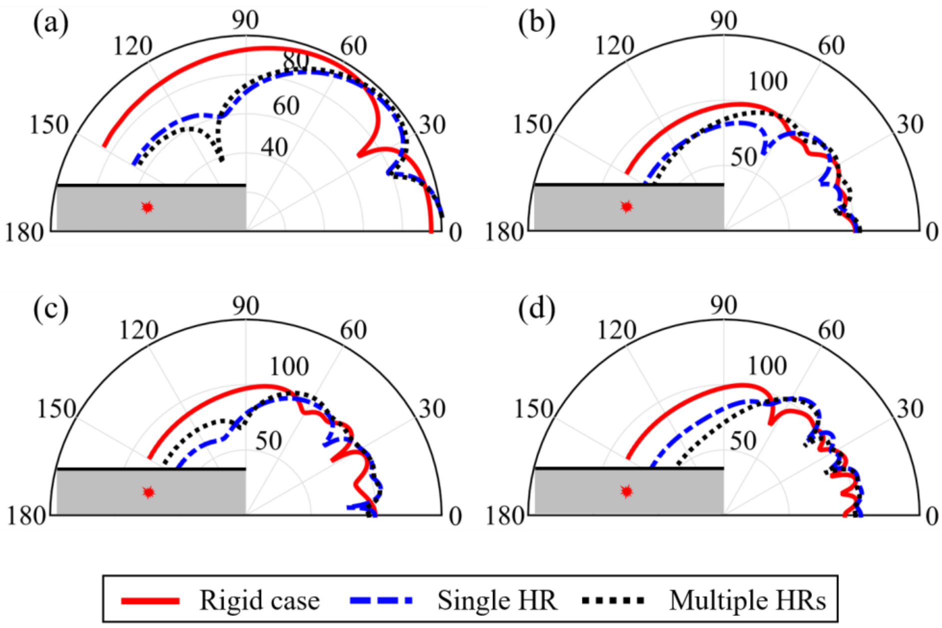

Figure 4.14 Far-field directivity patterns (dB) of the radiated sound field in rigid, single, and multiple HRs conditions at (a) 340 Hz, (b) 680 Hz, (c) 1020 Hz, and (d) 1360 Hz.

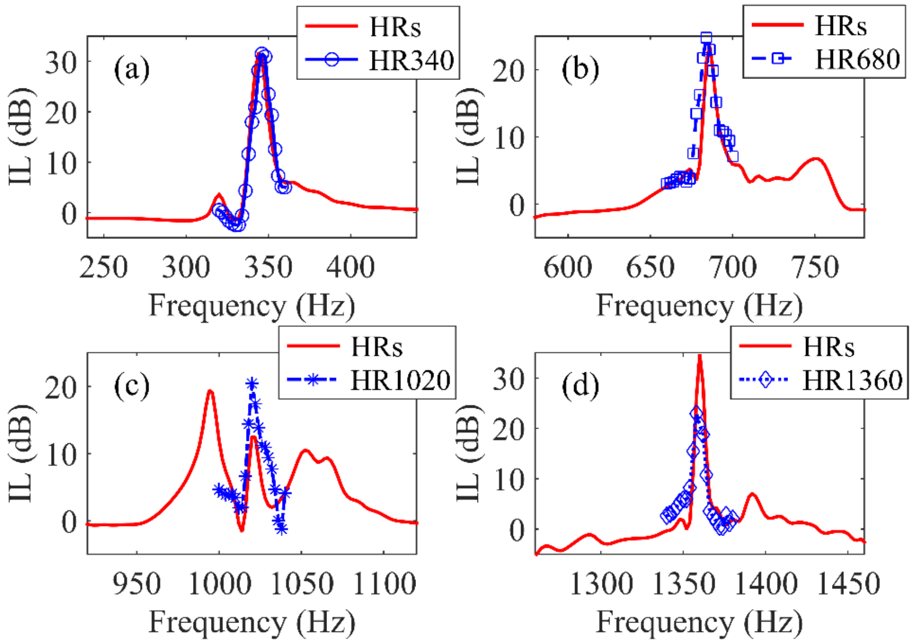

Figure 4.15 Comparison of ILs between HR array and single HR at R2, (a) HR340, (b) HR680, (c) HR1020, and (d) HR1360.

4.3.4 Source effect

In practice, there are various types of noise sources inside an unbaffled long enclosure. Therefore, preliminary investigations are conducted to explore the effects of the source on the sound radiation phenomenon. Four cases, namely, (1) plane-wave incidence with amplitude of 1 Pa, (2) single point source Q_1=0.01 m^2/s at (-2, 0.5) m, (3) single point source Q_2=0.02 m^2/s at (-1, 0.5) m, and (4) two point sources Q_1 and Q_2 at (-2, 0.5) m and (-1, 0.5) m, respectively, are considered here. Directivity patterns of the radiated sound fields at specific frequencies are presented in Figure 4.16.

As illustrated in Figure 4.16 (a), the radiation patterns of the plane-wave and point source cases are similar at 300 Hz. This implies that plane-wave is the dominant mode radiating from the enclosure opening when the frequency of interest is relatively low. However, the size of the lobes in the point source cases becomes large at high frequency compared with the plane-wave case, as presented in Figure 4.16 (b). This is the result of the superposition of higher-order modes radiation. As a result, plane wave incidence is not suitable to represent the sound source in traffic tunnel where higher-order acoustical modes must be considered. In addition, the SPLs are very similar for the case of multiple sources and the source Q_2 case, as the sound field is dominated by the source with a higher volume velocity strength. Besides, the amplitude and location of the point sources also influence the radiated sound field which will be analyzed in future work.

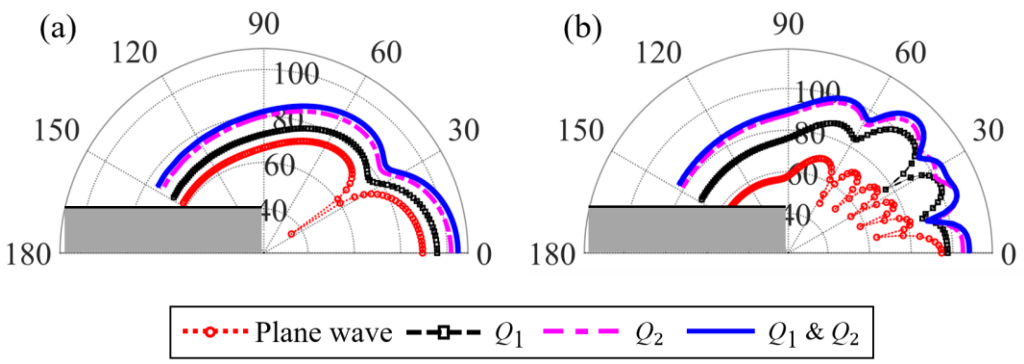

Figure 4.16 Directivity patterns of the radiated sound field with different types of sound sources at (a) 300 Hz and (b) 1000 Hz.

4.4 Experimental studies

The schematic diagram of a quasi-2D experimental test rig to study the sound radiation from an unbaffled long enclosure is shown in Figure 4.17 (a). The photos of the test rig in an anechoic chamber and the HRs on the wall are demonstrated in Figure

4.17 (b) and (c), respectively. Detailed introductions about the testing system can be found in Section 2.4. In addition, 2D Helmholtz resonators are used in the theoretical model to explain the physics behind the sound attenuation phenomenon. However, in reality, 3D Helmholtz resonators are applied to verify their sound reduction abilities instead of validate the theoretical model.

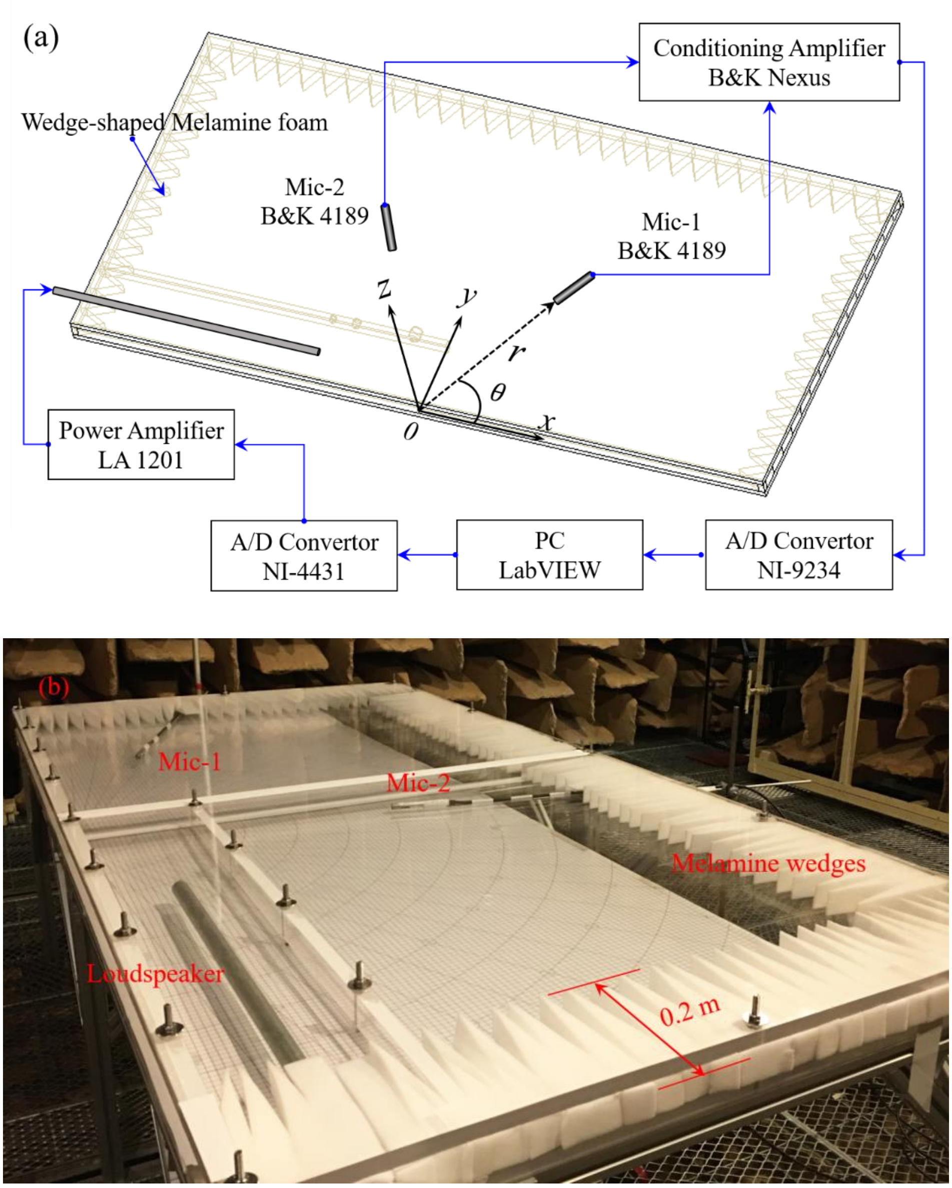

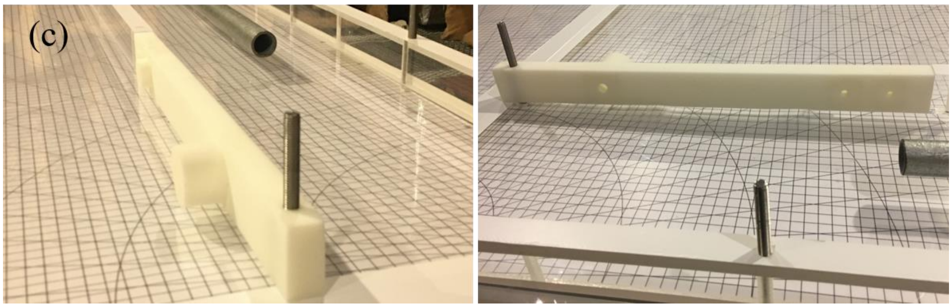

Figure 4.17 Experimental setups: (a) schematic diagram of the quasi-2D experimental test rig, (b) photography of the test rig, and (c) Helmholtz resonators on the wall.

Considering the performance of the loudspeaker and the dimensions of the test rig, the location and volume velocity strength of the monopole point source, the observation radius are set as (-0.4, 0.1) m, 0.002 m^2/s, and 0.6 m, respectively, in the experiment. In the first place, the far-field directivity patterns of the radiated SPL field are measured and compared with the theoretical results as presented in Figure 4.18. Good agreement can be observed between the theory and experiment even though discrepancies exist. They are caused by various factors such as the installation accuracy of the test rig, the quality of the loudspeaker, the performance of the Melamine foam wedges, and the precision of positioning.

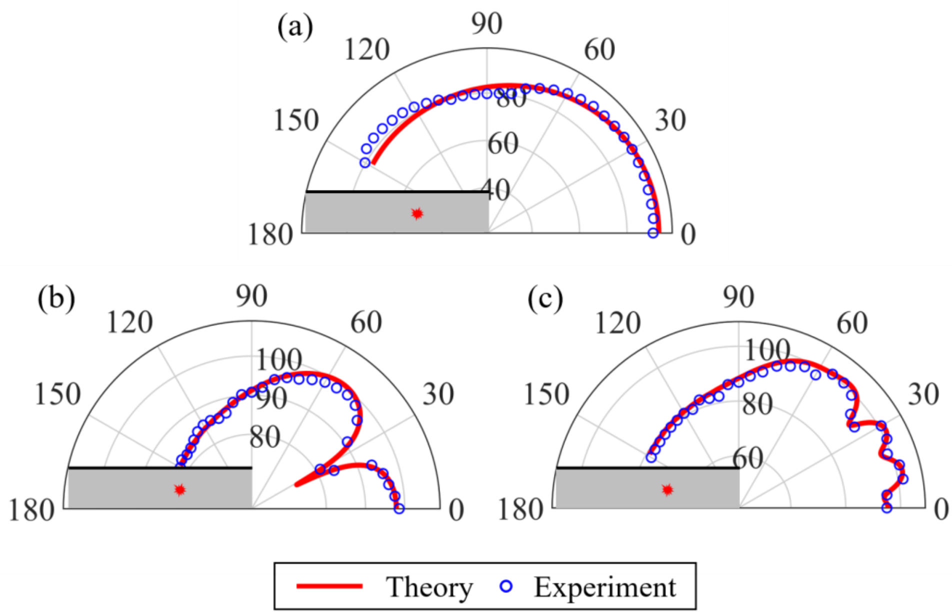

Figure 4.18 Directivity patterns of the radiated SPL field obtained by the W-H technique and experiment at (a) 500 Hz, (b) 2000 Hz, and (c) 4000 Hz.

Then, the feasibility of using HRs to reduce the radiated noise from a long enclosure is verified by the experiment. Considering the height of the long enclosure in the test rig, the first SPL peak appears at 1700 Hz. However, the corresponding HRs will be too small to manufacture and install if we adopt a one-fifth scaled-down model of the long enclosure considered in Section 4.3. Besides, HR340 is too big to be mounted in the quasi-2D space. Therefore, only three cylindrical HRs: HR680, HR1020, and HR1360, fabricated of photosensitive resin using 3D printing technique are mounted on the enclosure wall to reduce the radiated noise even though SPL peaks will not appear in the targeted frequency range. Experimental results of SPL spectra at (-0.6, 0.6) m are presented in Figure 4.19. Clear sound reductions can be observed around 680 Hz, 1020 Hz, and 1360 Hz. The average ILs reach 2.1 dB, 8.3 dB, and 11.9 dB within the bandwidth of 20 Hz centered at these frequencies.

Besides, measured directivity patterns of the radiated SPL field with and without

HR array at 680 Hz, 1020 Hz, and 1360 Hz are presented in Figure 4.20. Clear sound reductions are obtained especially in the shadow zone. In brief, the experimental results demonstrate that using an HR array can reduce the noise in the shadow zone around the targeted frequencies.

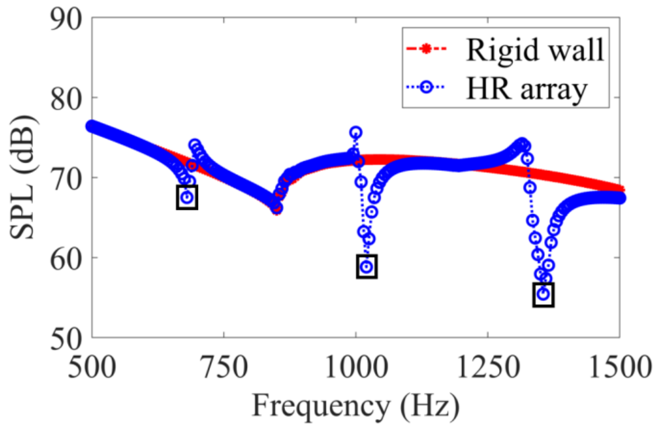

Figure 4.19 Experimental results of SPL spectra at (-0.6, 0.6) m with and without the HR array.

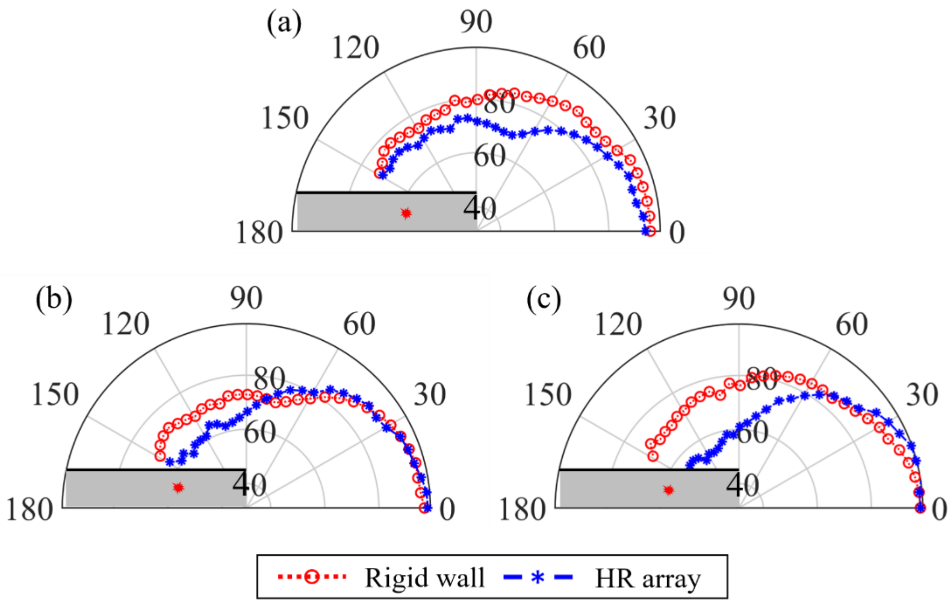

Figure 4.20 Measured directivity patterns of the radiated SPL field with and without HR array at (a) 680 Hz, (b) 1020 Hz, and (c) 1360 Hz.

4.5 Summary

The prediction and suppression of the noise inside and outside an unbaffled long enclosure are theoretically, numerically, and experimentally investigated. Formation mechanisms of the radiation directivity patterns are explored. HRs are employed to attenuate the radiated noise. The following conclusions are made:

A hybrid method capable of coupling the interior and exterior acoustical fields of an unbaffled long enclosure including the ground is established. It is proven to be an effective tool for the analysis of sound radiation phenomena and the introduction of appropriate noise control approaches. The sound peaks and directivity patterns are closely related to the acoustical modes and the modal responses at the opening. With the appropriate design of HRs, the dominant modal responses at the peak frequencies of the SPL spectra are significantly reduced, which results in the amplitude reduction of the incident sound wave at the top edge of the enclosure. In addition, the direction of the incident sound wave bends slightly towards the parallel direction along the wall surface. Thus, the diffraction wave that propagates from the sharp edge to the shadow zone is attenuated. Quasi-2D experiments were implemented to verify the proposed theoretical model and demonstrate the feasibility of using HRs to attenuate radiated noise. Three resonators, HR680, HR1020, and HR1360, were applied to reduce the noise at 680 Hz, 1020 Hz, and 1360 Hz, respectively. The average ILs at receiver point (-0.6, 0.6) m reach 2.1 dB, 8.3 dB, and 11.9 dB, respectively, within a bandwidth of 20 Hz centered at these frequencies.

CHAPTER 5

SOUND ABSORPTION CHARACTERISTICS OF Z-SHAPED MICRO-PERFORATED PANEL ABSORBERS

5.1 Introduction

From the previous Chapters, the sound pressure distribution inside an unbaffled long enclosure is complicated, which is formed by the linear superposition of multiple higher-order acoustical modes. In chapter 4, HRs have been proposed to suppress the sound peaks inside the unbaffled long enclosure so that the radiated SPL field around the resonant frequencies of the HRs can be attenuated. However, the noise reduction performance of an array of HRs is still unsatisfactory which is limited by their narrow working frequency bandwidths. Therefore, A simple, compact, and broadband noised suppression device is needed. The feasibility of applying two-dimensional hard rough surfaces to attenuate the noise level inside a traffic tunnel has been examined by Law et al. (2008). It was observed that an average sound reduction of about 3 dB over the frequency range from 500 Hz to 5000 Hz could be obtained. Aiming at absorbing the higher-order acoustical modes inside a duct, the interactions between these modes and a perforated liner system were investigated by Eldredge (2004). Later, enlightened by the research of Eldredge, a broadband acoustical liner with multiple cavity resonances was designed, and the acoustical performance of the liner was investigated (Jing et al., 2007; Zhou et al., 2016).

From the above introductions, acoustical liners consisting of micro-perforated panel absorbers (MPPAs) are promising noise control devices to attenuate the noise consisting of higher-order acoustical modes. Apart from applying the multiple cavity resonances, MPPAs with trapezoidal (Wang et al., 2010) and L-shaped (Gai et al., 2017) cavities are proposed. More acoustical modes that are initially decoupled with the MPP backed by a rectangular cavity are coupled with the MPP backed by cavities with irregular shapes. Compared with a flat MPPA backed by a constant air gap, the irregular-shaped MPPAs provide more spectral peaks and achieve good absorption performance at the dips in the sound absorption coefficient curve. These designs are from the perspective of the backing cavity and the incident plane waves are normal to the MPP. However, in practice, the distribution of sound pressure fields is complex in the duct, enclosure, and cavity systems. The amplitudes and incident angles of sound pressure along MPP surfaces are different. Consequently, the in-situ performance of the MPPAs is usually inferior to the theoretical results as the normal sound absorption coefficient of the MPPAs is inapplicable. Hence, to investigate the performance of an MPPA in practical acoustical environments, researches on the performance of MPPAs under oblique and random plane-wave incidences have been carried out (Yang et al., 2013; Wang et al., 2014; Liu et al., 2020). Results show that shape designs of cavities are not enough for a broadband sound absorption performance of an MPPA, especially when the sound waves are impinging tangentially or at a large incident angle on the flat MPP. To further improve the sound absorption performance of an MPPA under an oblique plane-wave incidence or in the diffuse field, a corrugated MPPA (CMPPA) with a sinusoidal MPP profile is proposed (Wang & Liu, 2020). Both the plane-wave incident angle to the local surface and the cavity shape of the MPPA are changed by introducing the corrugated MPP, which enhanced the sound absorption at the troughs and more spectral peaks can be observed. A key parameter that influences the sound absorption performance of a CMPPA is the corrugation depth. The corrugated profile of MPP, however, is determined when the corrugation depth and width of the MPPA are chosen, which is lacking flexibility for higher sound absorption performance.

To find a more flexible configuration of the corrugated MPP profile, a Z-shaped micro-perforated panel absorber (ZMPPA) is proposed in this Chapter. It is targeted for the absorption of higher-order acoustical modes inside an unbaffled long enclosure so that the radiated sound field can be attenuated. In addition to the advantages of the CMPPA, a ZMPPA is more versatile and flexible, which is promising for broadband noise control in large spaces and buildings. The remainder of this chapter is organized as follows. A numerical approach is first proposed to calculate the sound absorption coefficients of MPPAs under an oblique plane-wave incidence. The proposed method is then validated using theoretical formulas. After that, the acoustical performance of the ZMPPA is investigated. The effects of the key parameters, such as the corrugation depth and offset distance, on the oblique sound absorption coefficient of the ZMPPA are explored. The random sound absorption coefficients of the MPPAs are calculated and compared to evaluate their performance in complex situations. In addition, a liner comprising of ZMPPAs is applied to attenuate the sound radiated from an unbaffled long enclosure with the ground. Finally, experimental results are presented to validate the numerical model and examine the performance of the ZMPPA. Results show that the ZMPPA can attenuate the radiated noise in a wide frequency band which proves that the ZMPPA is a promising noise control device in practical applications.

5.2 Numerical model

5.2.1 The sound absorption coefficient of an MPPA under an oblique plane-wave incidence

A schematic diagram of the micro-perforated panel absorber (MPPA) under an oblique plane-wave incidence is illustrated in Figure 5.1.

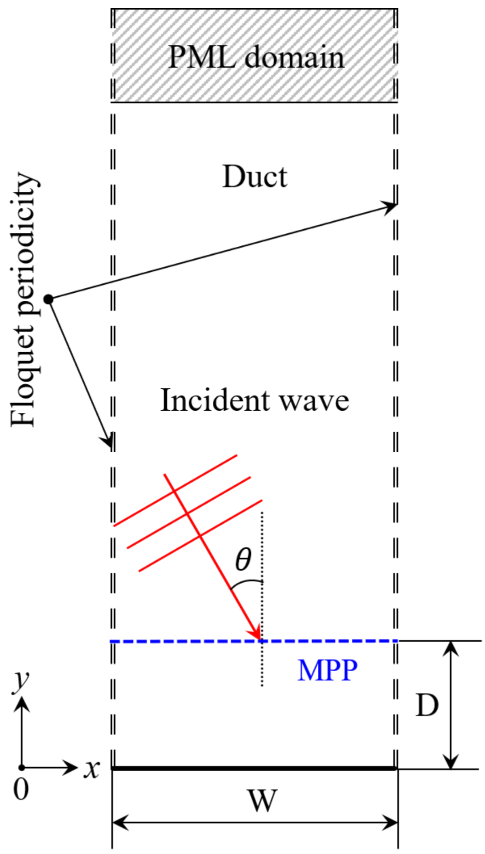

Figure 5.1 A schematic diagram of the micro-perforated panel absorber (MPPA) under an oblique plane-wave incidence.

The width of the acoustical domain is W, and the depth of the cavity is D. The bottom wall of the cavity is rigid, while the sidewalls of the acoustical domain are periodic to simulate an MPPA of infinite length. In addition, a non-reflection domain is applied at the inlet of the duct to ensure that the reflected and scattered sound waves can propagate to the outside without any reflection. Assume that a plane-wave of unit amplitude is incident obliquely on the MPP surface which can be expressed by

$$p_{incident} = \exp\left[-ik\left(\sin\theta x - \cos\theta y\right)\right] \tag{5.1}$$

where k stands for the wavenumber in the free space, and θ represents the incident angle. Part of the incident sound energy is reflected or scattered by the MPP while the rest is absorbed by the MPPA. The sound fields in the virtue duct and backing cavity satisfy the Helmholtz equation as

$$\left(\nabla^2 + k^2\right) p_{total} = 0 \tag{5.2}$$

On two sides of the MPP, the normal particle velocity must be continuous along the MPP surface:

$$u_n = \frac{p_{cavity} - p_{duct}}{Z_{MPP}} \tag{5.3}$$

where p_{cavity} and p_{duct} denote, respectively, the sound pressure field inside the cavity and duct. The acoustical impedance of the MPP can be calculated by Maa's equation as given in Eq. (3.59). The MPPs considered in this thesis are assumed to be rigid and therefore, the vibration effects of the MPP panels are ignored. To include the vibration effect of MPP panel, Eq.(5.3) is replace by the coupled normal particle velocity of air and MPP (Takahashi & Tanaka, 2002; Wang et al., 2012).

In order to account for the infinite size of the MPPA system, periodic boundary conditions are applied on sidewalls of the backing cavity and virtual duct which are described as

$$p_L = p_R e^{-ik\sin\theta W} \tag{5.4}$$

where subscripts ‘L’ and ‘R’ denote the left and right boundaries, respectively. For the inlet of the duct, A Dirichlet-to-Neumann boundary (DtN) Boundary condition is imposed to simulate a non-reflection boundary. For the bottom wall, a rigid boundary condition is applied which is expressed as

$$\left.\frac{\partial p_{total}}{\partial y}\right|_{y=-D} = 0 \tag{5.5}$$

The governing Helmholtz equation and the boundary conditions are considered using the FE software package COMSOL Multiphysics. Eq. (5.3) is implemented by specifying the surface of the MPP as an ‘interior impedance’ boundary. The sidewalls of the virtual duct and cavity are set as ‘Floquet periodicity’ and the bottom wall of the backing cavity is set as ‘acoustically rigid wall’ in COMSOL. A perfectly matched layer (PML) is specified on top of the duct to simulate a non-reflection domain, and the ‘background pressure field’ is used to define an oblique plane-wave incidence. In the numerical model, the backing cavity and the exterior virtual duct are meshed using triangular elements while the PML domain is discretized by structured grids. In order to ensure the accuracy of the model, 20 elements per wavelength are applied to mesh the acoustical domain. After solving the problem, the sound absorption coefficient of an MPPA under an oblique plane-wave incidence is calculated by

$$\alpha_\theta = \frac{-\rho c_0 \int\limits_{inlet} \mathrm{Re}\left(p u_y^*\right) dx}{W \cos\theta}, \tag{5.6}$$

where the asterisk denotes the complex conjugate and the sound absorption coefficient under a random plane-wave incidence is calculated by

$$\alpha_r = \int_0^{\pi/2} \alpha_\theta \sin\left(2\theta\right) d\theta \tag{5.7}$$

The numerical model is applied to investigate the sound absorption performance of different types of MPPAs as shown in Figure 5.2. For a flat MPP as demonstrated in Figure 5.2 (a), the acoustical impedance is determined by Maa's formula. The sound properties of a corrugated micro-perforated panel absorber (CMPPA) were explored by Wang and Liu (2021), as presented in Figure 5.2 (b). The volume of the CMPPA is kept the same as that of an FMPPA. The sound absorption coefficient of the CMPPA increases considerably at the troughs of the sound absorption coefficient curve, which is a favorable characteristic for broadband random noise attenuation in large buildings and spaces. The sound absorption coefficient is mainly determined by the corrugation depth. However, once the height of the backing cavity and the width of the MPPA are chosen, the sinusoidal profile and the corrugation depth of the CMPP are determined which is lacking flexibility. In this regard, a Z-shaped micro-perforated panel absorber (ZMPPA) is proposed as shown in Figure 5.2 (c) and (d), which have the same volume and height as that of an FMPPA, respectively.

The profile of a ZMPP is an interpolation curve that is determined by the cavity width W, height D, corrugation depth H, and an offset distance O from the central line as presented in Figure 5.2 (d). In such a configuration, the air gap between the ZMPP and the bottom wall forms an irregular-shaped backing cavity, which gives rise to the variation of the cavity depth. Therefore, the distance from the middle line of the ZMPP to the bottom wall is defined as the cavity depth D, so that the volume of the cavity is the same as that of an FMPPA. Due to the introduction of an offset distance, the shape of the ZMPPA is changeable which may provide more potential for the absorption of noise. Compared with the CMPPA, apart from the variation of the corrugation depth $H \in [0, D]$; the offset distance $O \in [0, W/2]$. However, to keep the same cavity volume as an FMPPA, the profiles of the CMPP and ZMPP protrude outward for a corrugation depth which enlarges the thickness of the MPPAs. To propose compact absorbers, the acoustical performance of a ZMPPA of the same height as the FMPPA is investigated as demonstrated in Figure 5.2 (c). Such a configuration sacrifices a part of the cavity volume; however, the corrugation depth and offset distance are changeable which may provide unexpected performance. The positions of points that determine the profile of the ZMPP (red circles) are all changeable, as presented in Figure 5.2 (c).

Since a ZMPP can be obtained by reshaping an FMPP, the acoustical impedance over the ZMPP profile is the same as the FMPP. However, the actual length, as well as the perforation area of the ZMPP are, respectively, longer and larger than that of the FMPP. So, the bulk perforation ratio of the ZMPP, which indicates the ratio of the total perforated area to the incident plane area is applied:

$$p_{ZMPP} = \frac{W}{L_{ZMPP}} p_{FMPP} , \tag{5.8}$$

where L_{ZMPP} denotes the arc length of the ZMPP. The bulk perforation ratio is applied on the CMPPA as well.

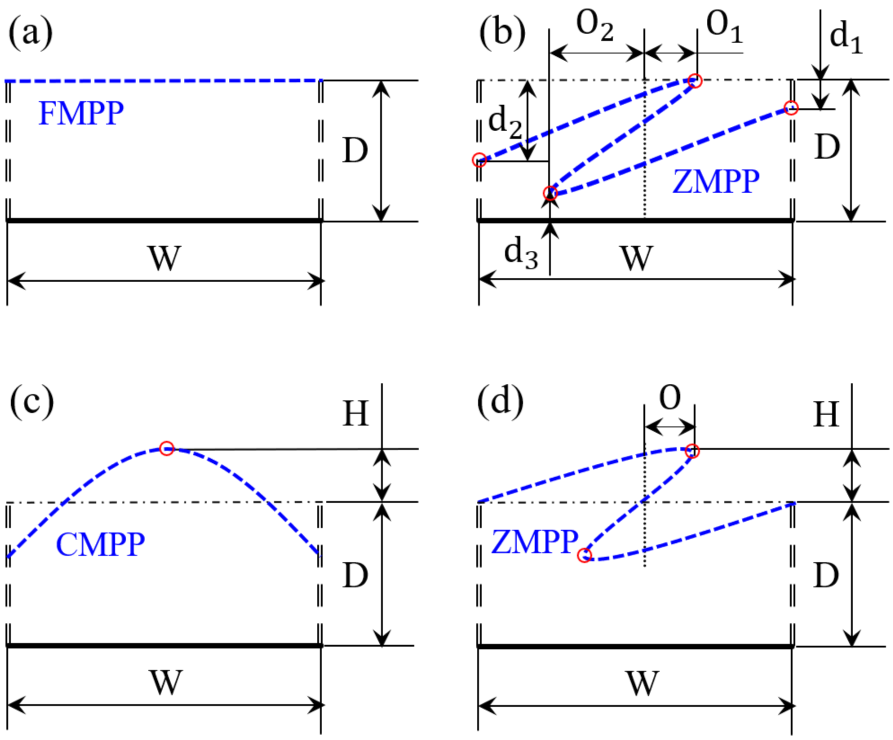

Figure 5.2 Different configurations of MPPAs. (a) an FMPPA, (b) a ZMPPA with the same height as the FMPPA, (c) a CMPPA with the same volume as the FMPPA, (d) a ZMPPA with the same volume as the FMPPA.

5.2.2 Model validation using theoretical formulas

For an infinite long FMPPA with a constant air gap, the path difference between the incident and reflected acoustical waves from the cavity wall varies regarding the incidence angle. The sound absorption coefficient of the FMPPA under an oblique plane-wave incidence is calculated by (Maa, 1998)

$$\alpha_\theta = \frac{4\,\mathrm{Re}\left(Z_{MPP}\right)\cos\theta}{\left[1+\mathrm{Re}\left(Z_{MPP}\right)\cos\theta\right]^2+\left[\mathrm{Im}\left(Z_{MPP}\right)\cos\theta-\cot\left(kD\cos\theta\right)\right]^2} \tag{5.9}$$

For an FMPP that is backed by several sub-cavities, the MPPA can be treated as a locally reacting surface. The sound absorption coefficient of the MPPA under an oblique plane-wave incidence can be estimated by (Wang et al., 2014)

$$\alpha_\theta = \frac{4\,\mathrm{Re}\left(Z_{MPPA}\right)\cos\theta}{\left[1+\mathrm{Re}\left(Z_{MPPA}\right)\cos\theta\right]^2+\left[\mathrm{Im}\left(Z_{MPPA}\right)\cos\theta\right]^2} \tag{5.10}$$

where the surface impedance can be obtained by the equivalent circuit method.

To validate the proposed model using these theoretical formulas, three cases are considered, namely, (a) a normal plane-wave incidence on an FMPPA, (b) an oblique plane-wave incidence on the FMPPA (45 degrees), and (c) an Oblique plane-wave incidence on an FMPPA with sub-cavities (45 degrees). The parameters of MPPAs are listed in Table 5-1. As presented in Figure 5.3 (a) and (b), the results obtained by the current numerical method agree well with that calculated using Eq. (5.9) under normal and oblique plane-wave incidences. In Figure 5.3 (c), however, discrepancies can be observed between the results obtained by the current method and Eq. (5.10) under an oblique plane-wave incidence. The oblique sound absorption coefficient of an MPPA array is a function of the geometrical size of the sub-cavities, the incidence angle, and so on. However, Eq. (5.10) only takes the effect of the incidence angle into consideration while the influence by other parameters is ignored. An extreme situation is described using Eq. (5.10), in which the sizes of the sub-cavities are infinitesimal compared with the acoustical wavelength. As a result, the sound absorption coefficient of an MPPA with sub-cavities under an oblique plane-wave incidence can be roughly evaluated by Eq. (5.10). However, accurate numerical approaches, such as the current one, are necessary for the actual acoustical performance of the MPPA array.

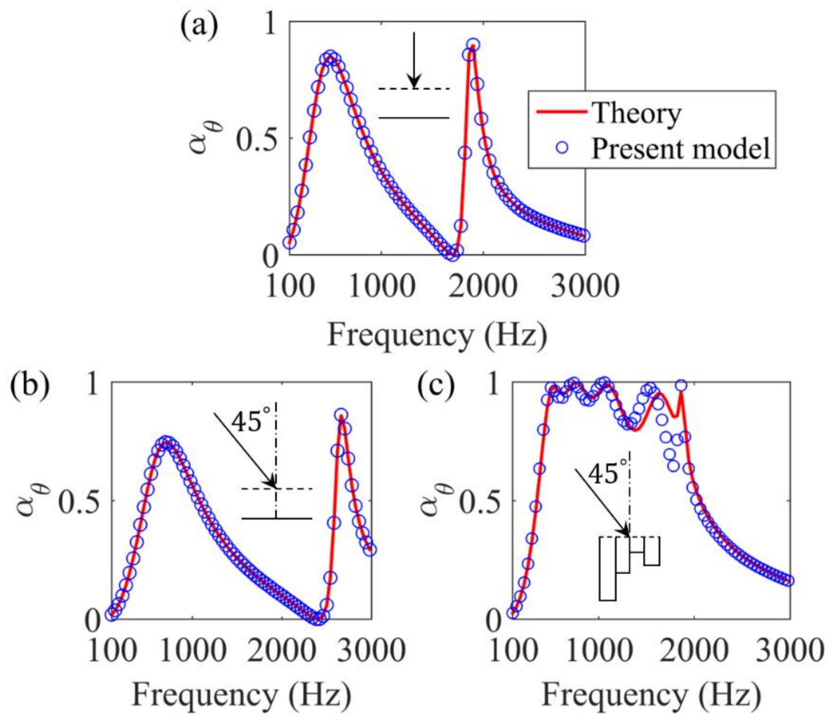

Figure 5.3 Sound absorption coefficients of MPPAs: (a) normal plane-wave incidence on an FMPPA, (b) oblique (45 degrees) plane-wave incidence on the FMPPA, and (c) oblique (45 degrees) plane-wave incidence on an MPPA with sub-cavities.

Table 5-1 Parameters of MPPA used to validate the numerical model.

MPP parameters			Cavity parameters (mm)				
t_{MPP}	d_{MPP}	p_{MPP}	D_{FMPP}	D_1	D_2	D_3	D_4
0.4 (mm)	0.4 (mm)	1/100	100	100	50	12	25

5.3 Acoustical properties of a ZMPPA

5.3.1 ZMPPA of the same volume as the FMPPA

The acoustical properties of the ZMPPA are investigated in this section. MPPA parameters used in the calculations are listed in Table 5-2. The MPP parameters are arbitrarily chosen for the purpose of revealing the sound absorption mechanisms. The optimized configurations will be presented later.

Table 5-2 Parameters of MPPAs used in the calculations.

MPP parameters			Cavity shape (mm)		Corrugation profile (mm)	
t_{MPP}	d_{MPP}	p_{MPP}	D	W	H=D/4	O=D/4
0.4 (mm)	0.4 (mm)	1/100	100	100	25	25

- **Normal plane-wave incidence**

The sound absorption coefficients of the FMPPA, CMPPA, and ZMPPA under a normal plane-wave incidence are compared in Figure 5.4. First, the sound absorption coefficient of the ZMPPA at the first trough (1075 Hz) is improved compared with that of the CMPPA (1580 Hz) and FMPPA (1700 Hz). This is advantageous for the broadband attenuation of a highly reverberated acoustical field. Second, the first sound absorption peak of the ZMPPA shifts to a lower frequency (385 Hz) compared with that of the FMPPA and CMPPA (500 Hz), which is promising for the suppression of low-frequency noise. Besides, there are three sound absorption peaks between the frequency range of 1500 Hz and 2300 Hz, which also improves the sound absorption performance of the ZMPPA within the middle to high-frequency range. Besides, the CMPPA performs almost the same as the FMPPA below approximately 700 Hz which is determined by the ratio of the corrugation depth to the wavelength of the incident sound wave. However, the performance of the ZMPPA is not influenced by the ratio in this frequency range. As the sound dips and peaks are determined by the resonances of the cavity and mass-spring system composed of the air inside the perforations and the cavity, respectively. The frequency shift of the first peak, the enhancement of the first trough, and the appearance of extra peaks in the middle-frequency range indicate that the sound absorption mechanisms of the ZMPPA are different from the FMPPA and CMPPA.

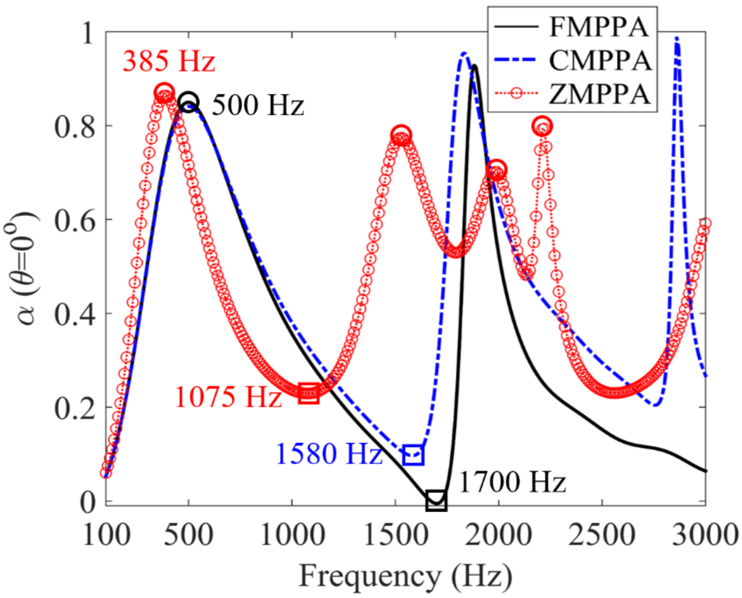

Figure 5.4 Sound absorption coefficients of the FMPPA, CMPPA, and ZMPPA under a normal plane-wave incidence.

The dips in the sound absorption coefficient curve of an MPPA result from the resonances of the backing cavity. At the resonant frequencies of a cavity, the stiffness of the air gap becomes infinity. Consequently, the air inside the perforations is unable to vibrate so that no energy dissipation occurs. Figure 5.5 demonstrates the first modal shapes and eigenfrequencies of the FMPPA, CMPPA, and ZMPPA, respectively. As presented in Figure 5.5 (a), for the FMPPA, the first resonant frequency of the cavity is 1700 Hz. The sound pressure along the MPP is large, which leads to the dip of the sound absorption coefficient. For the CMPPA, the resonant frequency is 1573 Hz. The sound pressure along the MPP is still large but shows a decreasing trend towards two sides as shown in Figure 5.5 (b). A small part of the sound energy is absorbed and the first dip in the sound absorption coefficient curve increases as well. For a ZMPPA, as demonstrated in Figure 5.5 (c), the first resonant frequency of the cavity is located at 1165 Hz. However, the cavity is partitioned into two parts by the Z-shaped MPP. The sound pressure in the upper part of the sub-cavity is large, however, the sound pressure along the MPP of the lower part is moderate, which allows more sound energy to be absorbed. Therefore, the sound absorption coefficient at the fist dip has been enhanced considerably compared with the FMPPA and CMPPA. In addition, the first trough of the FMPPA is located at 1700 Hz which is the same as the resonant frequency of the cavity. This implies that only the resonant mode contributes to the sound absorption performance of an FMPPA at 1700 Hz. However, for the CMPPA and ZMPPA, the frequencies of the first troughs shift compared with the resonant frequencies of the cavities which indicates that apart from the dominant mode, adjacent acoustical modes also contribute to the sound absorption performance. Furthermore, the Z-shaped MPP profile also plays the role of a multi-layered MPP, which introduces the peaks in the middle to high-frequency range. Although the second sound absorption peaks of the FMPPA and CMPPA are larger than that of the ZMPPA. The bandwidth of the peaks for half sound absorption is narrow. The second to fourth sound absorption peaks of the ZMPPA are moderate, however, the frequency band for half sound absorption is wide, which is favorable for broadband sound reduction.

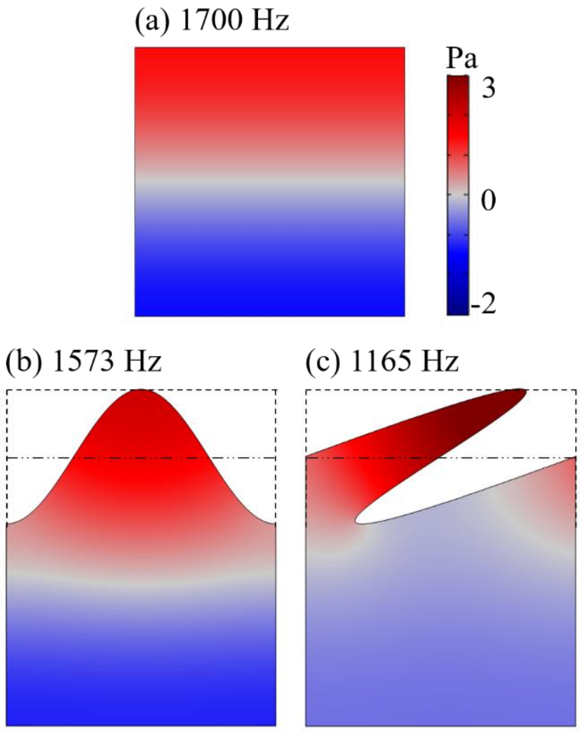

Figure 5.5 The first cavity modal shapes and eigenfrequencies of the (a) FMPPA, (b) CMPPA, and (c) ZMPPA of the same volume.

- **Oblique plane-wave incidence**

The sound absorption coefficients of the FMPPA, CMPPA, and ZMPPA under an oblique plane-wave incidence are demonstrated in Figure 5.6. At 30 degrees of the incident angle, as shown in Figure 5.6 (a), apart from the properties of low-frequency shift for the first peak and the sound absorption enhancement of the first dip in the normal plane-wave incidence, the peaks in the sound absorption coefficient curve of ZMPPA between 1500 Hz and 2000 Hz improve considerably compared with that of the normal-incidence counterpart. The first trough almost disappears at 60 degrees of the incident angle as illustrated in Figure 5.6 (b). The sound absorption coefficients are larger than 0.5 in the frequency range of 500 Hz to 1850 Hz, and the performance of the ZMPPA is superior to the FMPPA and CMPPA under about 800 Hz. At 85 degrees of the incident angle, as displayed in Figure 5.6 (c), the FMPPA almost loses its sound absorption ability, however, the CMPPA and ZMPPA can still absorb sound energy due to the curved MPP profiles, and the ZMPPA presents better performance than the CMPPA.

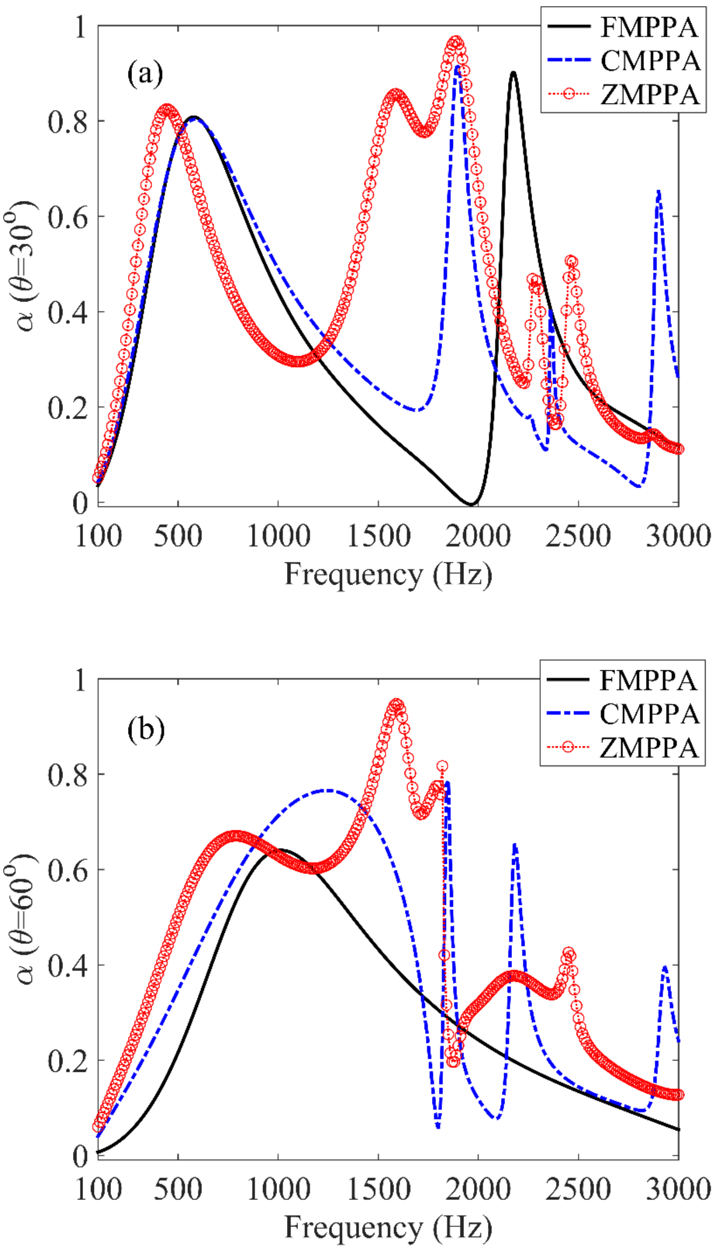

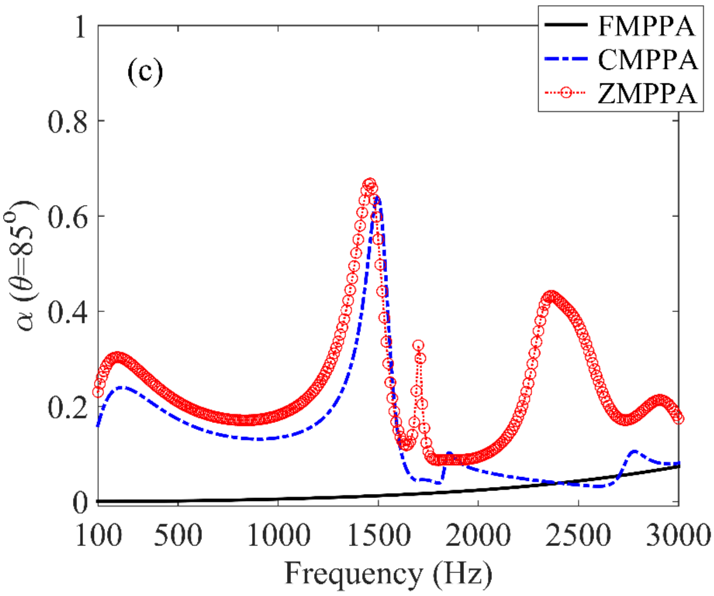

Figure 5.6 Oblique sound absorption coefficients of the FMPPA, CMPPA, and ZMPPA at (a) 30 degrees, (b) 60 degrees, and (c) 85 degrees.

Another observation is found that with the increase of the incident angle, the sound absorption curve shifts to higher frequencies. The MPPs are locally reacting whose acoustical impedances are independent of the incident angle, however, the acoustical impedances of the cavities vary with the incident angle which gives rise to the shift of the sound absorption coefficient curve. From the above analysis, the sound absorption performance of the curved MPPAs under an oblique plane-wave incidence is better than the normal counterparts, especially at large incident angles.

Also, the sound absorption performance of the ZMPPA and CMPPA improve noticeably under oblique incidence while drops greatly for the FMPPA, especially at large incident angles. This is due to the curved MPP profiles where the local incident angle of the plane sound wave does not change in the same pattern as the angle of the background sound field, as presented in Figure 5.7. Imagine an extreme case when the incident angle of the background sound field reaches 90 degrees, the sound wave propagates to the FMPP in a grazing angle while to the CMPP and ZMPP in certain local incident angles. This explains the results showed in Figure 5.6 (c).

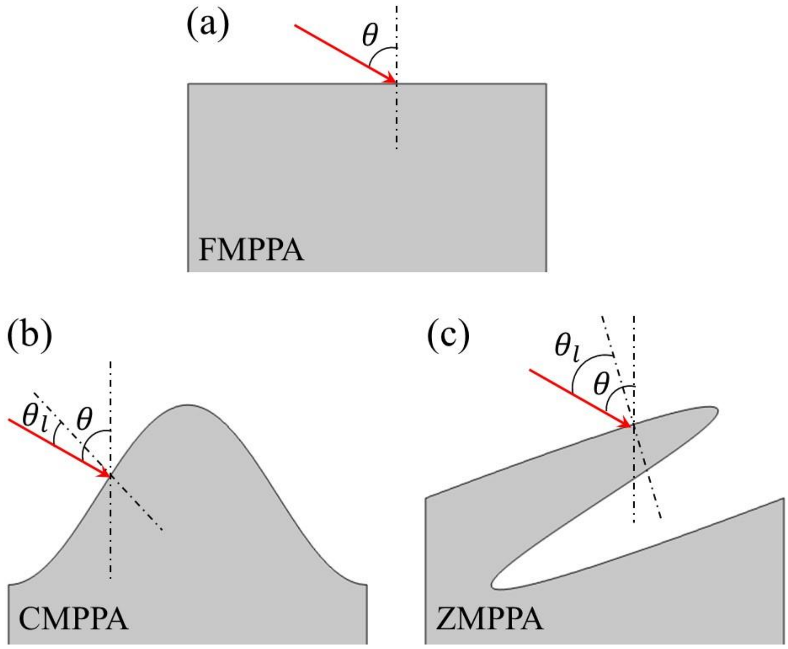

Figure 5.7 Oblique incident angle and the local incident angle on the MPP surfaces. (a) FMPPA, (b) CMPPA, and (c) ZMPPA.

5.3.2 Effect of the offset distance

As introduced before, the Z-shaped MPP profile introduces the performance of a multi-layered MPPA, while the curve is determined by the offset distance. So, the effect of the offset distance on the oblique sound absorption coefficient of the ZMPPA is investigated. The changes in the oblique sound absorption coefficient regarding the offset distance are presented in Figure 5.7. At 0 degrees, the first sound absorption peak shifts to lower frequency with increasing offset distance, along with the decrease of the bandwidth. This principle applies to 30 degrees as well. Besides, double peaks can be observed when the offset distance is larger than 20 mm. At 60 degrees, the first sound absorption peak decreases; however, the bandwidth increases remarkably. In addition, double sound absorption peaks can be observed between the frequency range from 1200 Hz to 1800 Hz. The frequency interval between the peaks decreases with the increasing offset distance. At 85 degrees, the sound absorption only happens at a small frequency band, and the peak increase with the increasing offset distance.

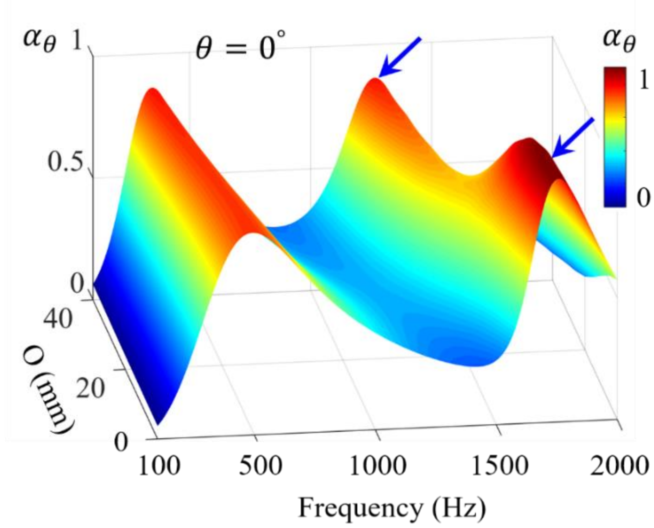

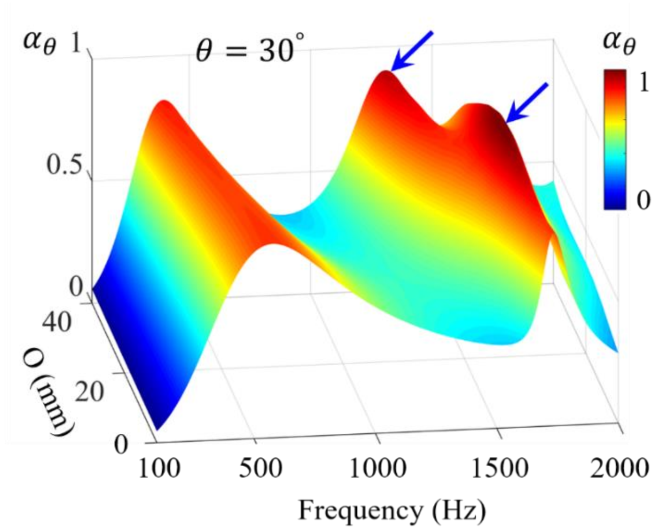

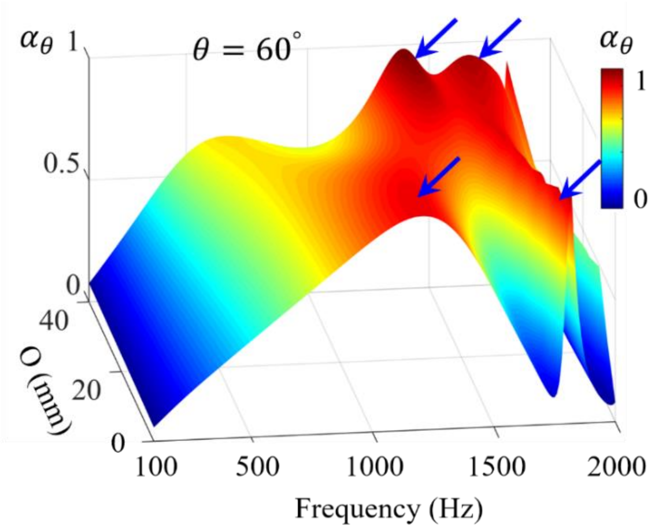

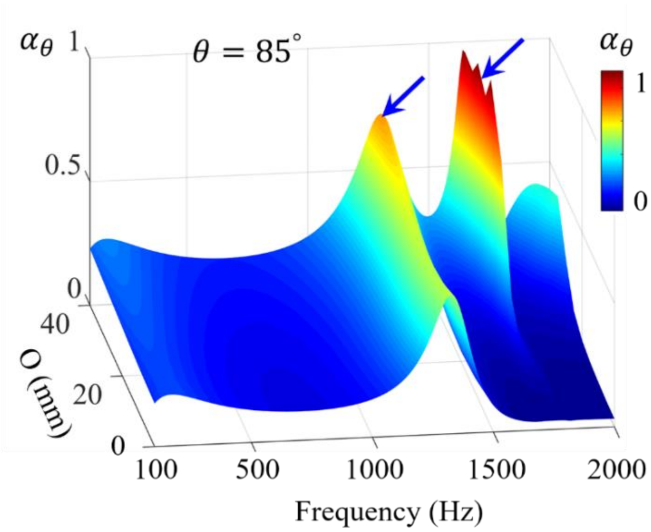

Figure 5.8 Influence of the offset distance on the oblique sound absorption coefficient at 0 degree, 30 degrees, 60 degrees, and 85 degrees, respectively.

5.3.3 Effect of the corrugation depth

Another key parameter that influences the sound absorption performance of the ZMPPA is the corrugation depth H. Keeping the other parameters constant, the change in the sound absorption coefficient regarding the corrugation depth is demonstrated in Figure 5.9. At 0 and 30 degrees of the incident angle, the first sound absorption peaks decrease slightly and shift to higher frequencies with the increase of the corrugation depth, along with the improvement of the first sound absorption dips. The sound absorption coefficients of the second peaks increase with increasing corrugation depth. At 60 degrees of the incident angle, the peaks and dips disappear which are replaced by a broadband sound absorption curve. Besides, the peak sound absorption reaches 1 when H is large than 60 mm. At 85 degrees of the incident angle, the corrugation depth has little effect on the sound absorption coefficient of the ZMPPA.

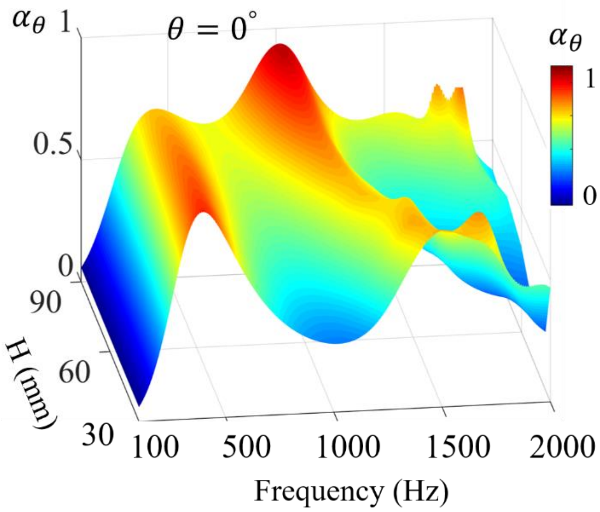

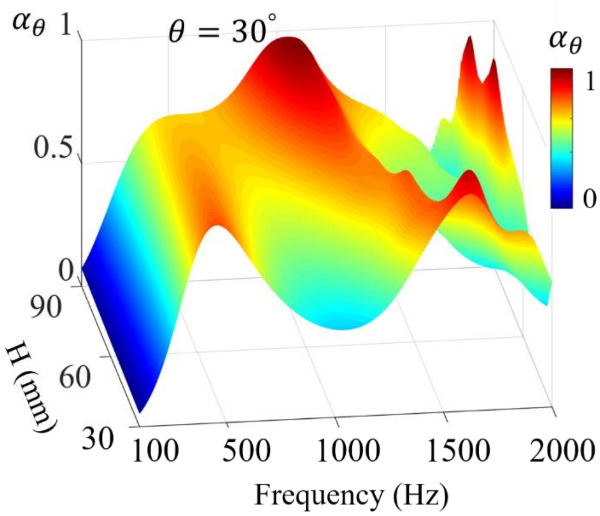

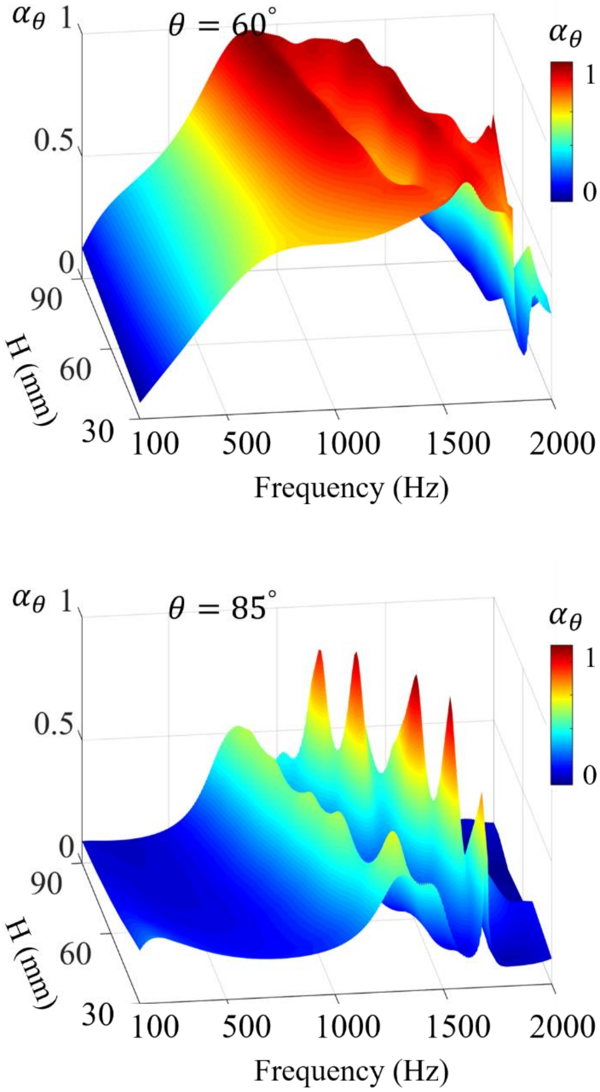

Figure 5.9 Effect of corrugation depth on the oblique sound absorption coefficient at 0 degree, 30 degrees, 60 degrees, and 85 degrees, respectively.

5.3.4 ZMPPA of the same height as the FMPPA

In the above analysis, the cavity volumes of the MPPAs are maintained the same to make fair comparisons. However, the CMPPA and ZMPPA occupy more space than the FMPPA because of the protruding corrugation profiles. This is not favorable for a compact noise control device. Therefore, the acoustical properties of a ZMPPA and a CMPPA that are as high as an FMPPA are investigated.

- **Normal plane-wave incidence**

The sound absorption coefficients of the FMPPA, CMPPA, and the proposed ZMPPA under a normal plane wave incidence are shown in Figure 5.10. As the heights of the MPPAs are kept the same in this comparison, the cavity volumes of the CMPPA and ZMPPA are smaller than the FMPPA. Consequently, for the CMPPA, the first dip of the sound absorption coefficient curve shifts to a higher frequency (1965 Hz) comparing with 1580 Hz in Figure 5.4. For the ZMPPA, the first dip shifts to a higher frequency (1135 Hz) as well compared with 1075 Hz in Figure 5.4. However, it is still smaller than that of the FMPPA (1700 Hz) which results from the offset distance of the ZMPP profile. This phenomenon can also be observed at the first peaks of the CMPPA and ZMPPA with their frequencies shift to 610 Hz and 460 Hz, respectively. However, for the ZMPPA, the first peak frequency is still lower than that of the FMPPA (500 Hz). In other words, the offset distance of the ZMPPA compensates for the frequency shift caused by the volume sacrifice. Besides, the broadband sound absorption performance in the middle frequency range remains.

Figure 5.11 demonstrates the first cavity modal shapes and eigenfrequencies of the FMPPA, CMPPA, and ZMPPA. The heights of the MPPAs are kept the same. The eigenfrequencies increase to 1923 Hz and 1243 Hz for the cavities of the CMPPA and ZMPPA, respectively, compared with Figure 5.5. However, due to the corrugation profiles of the CMPP and ZMPP, the sound pressure distributions along their surfaces are not all large, which gives rise to the enhancement of the sound absorption at the dips. Besides, apart from the first cavity mode, adjacent acoustical modes contribute to the sound absorption performance of the CMPPA and ZMPPA.

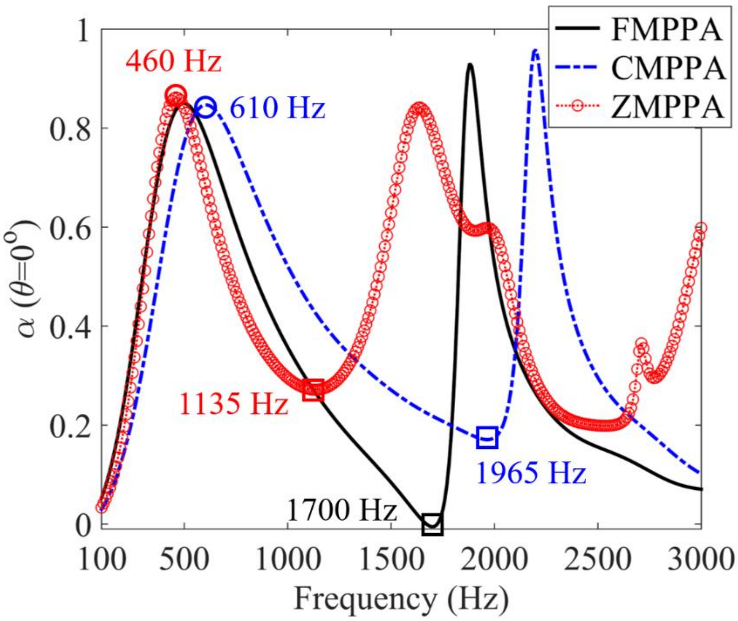

Figure 5.10 Sound absorption coefficients of the FMPPA, CMPPA, and ZMPPA with the same height under a normal plane-wave incidence.

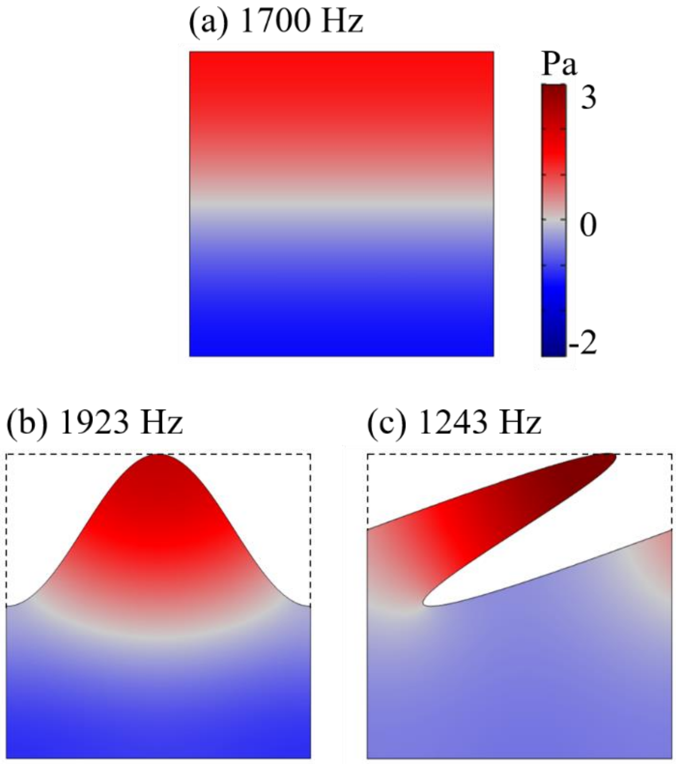

Figure 5.11 The first cavity modal shapes and eigenfrequencies of the (a) FMPPA, (b) CMPPA, and (c) ZMPPA with the same height.

- **Oblique plane-wave incidence**

The sound absorption coefficients of FMPPA, CMPPA, and ZMPPA under the oblique plane-wave incidence are presented in Figure 5.12. At 30 and 60 degrees of the incident angle, apart from the properties of low-frequency shift for the first peak and the absorption enhancement of the first dip in the normal plane-wave incidence, two peaks can be observed between 1500 Hz and 2000 Hz for the ZMPPA which is good for broadband noise control. At 85 degrees of the incident angle, the FMPPA almost loses its sound absorption ability, however, the CMPPA and ZMPPA can still absorb sound energy due to their curved MPP profiles. Figure 5.12 and Figure 5.6 show similar results. The main difference between them is that the sound absorption curves of MPPAs shift to higher frequencies due to volume sacrifice. However, the ZMPPA can maintain good performance compared with the CMPPA which is mainly attributed to the Z-shaped MPP profile, especially the introduction of offset distance.

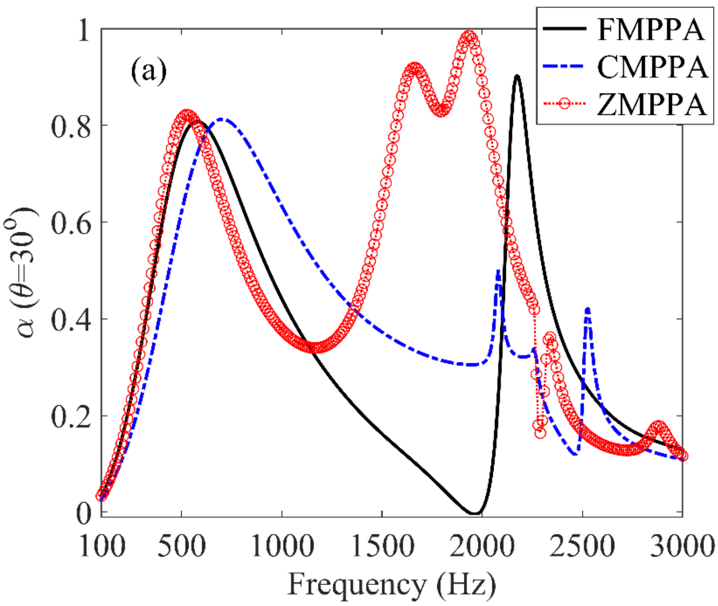

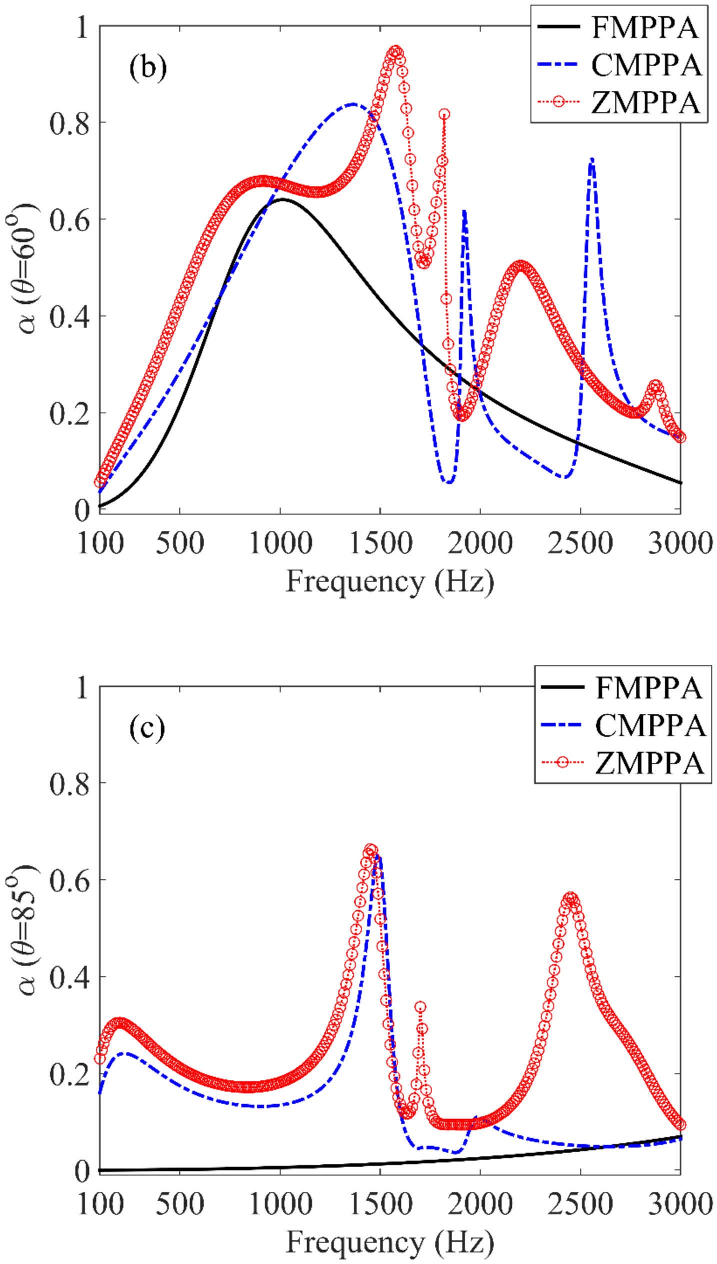

Figure 5.12 Oblique sound absorption coefficients of FMPPA, CMPPA, and ZMPPA of the same height at (a) 30 degrees, (b) 60 degrees, and (c) 85 degrees.

The effect of the offset distance on the oblique sound absorption coefficient of a ZMPPA with the same height as the FMPPA is demonstrated in Figure 5.13. At the normal incidence case, with the increase of the offset distance, the low-frequency shift characteristic exhibits and the amplitudes of the sound absorption peaks increase as well. At the oblique incidence case (45 degrees), two peaks are observed within the middle-frequency range.

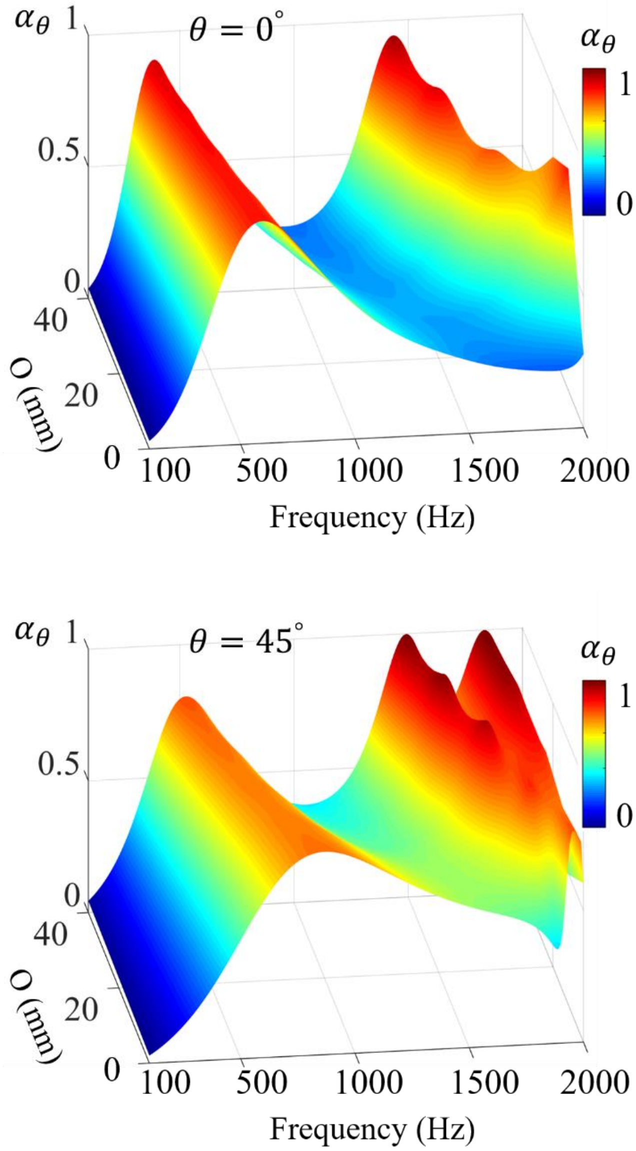

Figure 5.13 Effect of the offset distance on the oblique sound absorption coefficient of a ZMPPA with the same height as the FMPPA.

5.3.5 Random sound absorption coefficients of MPPAs

In a complex acoustical field, the incident sound waves propagate to the MPPAs at random angles. Therefore, the random sound absorption coefficients of the FMPPA, CMPPA, and ZMPPA are obtained and compared in Figure 5.14. Within the presented frequency range, the ZMPPA and the CMPPA perform better than the FMPPA, and the random sound absorption coefficients of the ZMPPA are almost larger than that of the CMPPA, especially in the frequency range between 1000 Hz and 1800 Hz. All the results presented above are calculated using the default values of the parameters of MPPAs. In parametrical studies, better performance can be achieved by tuning the configuration of the ZMPPA.

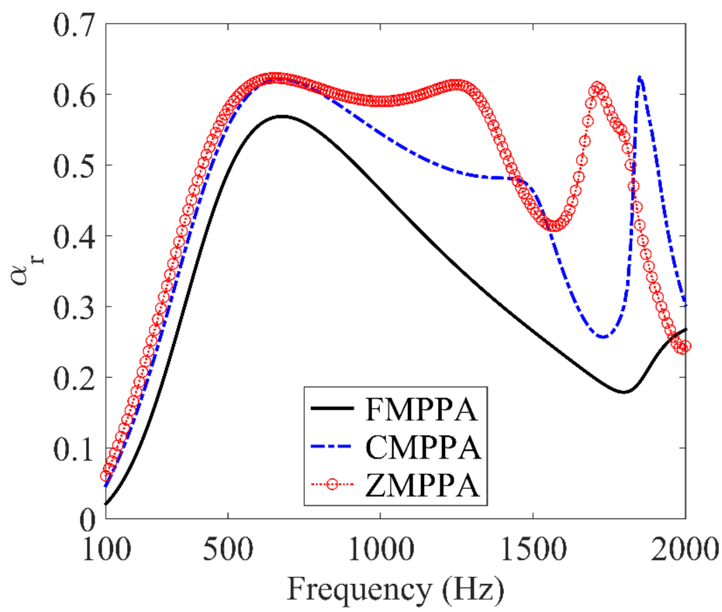

Figure 5.14 Comparisons of the random sound absorption coefficients between the FMPPA, CMPPA, and ZMPPA.

5.4 Sound suppression of an unbaffled long enclosure using the ZMPPA

Figure 5.15 illustrates the suppression of sound radiated from an unbaffled long enclosure using a liner comprising an array of ZMPPAs. The hybrid method proposed in chapter 4 is applied to calculate the acoustical field. Besides, acoustical liners made of FMPPA and CMPPA are also applied to make comparisons. The liners are 3 m in length and the source is located at (-2, 0.5) m. MPP parameters are kept the same as Table 5-2.

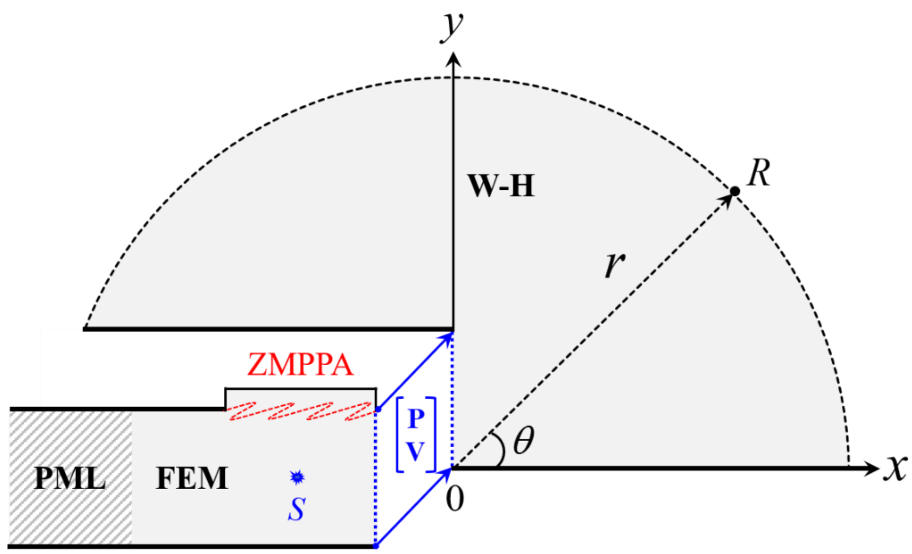

Figure 5.15 Suppression of sound radiated from an unbaffled long enclosure using a liner comprising of ZMPPAs.

Comparisons of ILs obtained by the liners made of FMPPAs, CMPPAs, and ZMPPAs are demonstrated in Figure 5.16. All the liners exhibit negative ILs below about 300 Hz which indicates that the designed liners are not suitable for the control of low-frequency noise. From 500 Hz to 2000 Hz, the sound absorption performance of liners made of CMPPAs and ZMPPAs is superior to the liner made of FMPPAs which implies that the corrugation profiles of CMPP and ZMPP start to play important role in attenuating higher-order acoustical modes. Furthermore, from 1300 Hz to 1800 Hz, the performance of the liner made of ZMPPAs is better than the liner made of

CMPPAs, even though there is a big trough at about 1600 Hz. This results from the flexible corrugation profile of the ZMPP which can achieve the performance of double layered MPPA in the middle to high-frequency range.

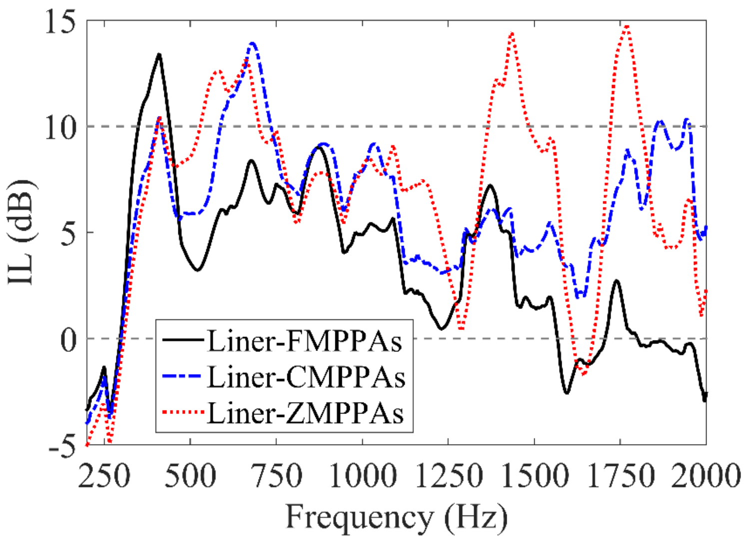

Figure 5.16 Comparison of ILs obtained by the liners made of FMPPAs, CMPPAs, and ZMPPAs.

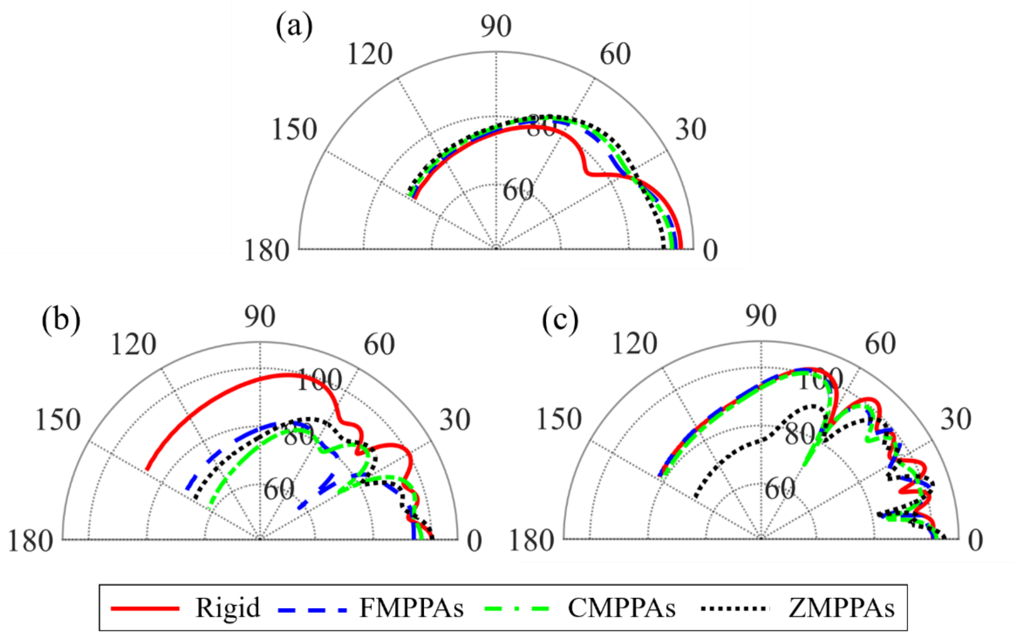

Figure 5.17 Directivity patterns of the radiated SPL fields at (a) 265 Hz, (b) 680 Hz, and (c) 1435 Hz.

The directivity patterns of the radiated SPL fields are shown in Figure 5.17. At 265 Hz, the liners loss their sound absorption abilities. At the resonance frequency of the unbaffled long enclosure 680 Hz, introducing liners can significantly reduce the radiated noise, especially in the shadow zone. At 1435 Hz, the liner made of ZMPPAs reached its best performance.

5.5 Experimental studies

5.5.1 Normal sound absorption coefficients of MPPAs

The sound absorption coefficients of the FMPPA, CMPPA, and ZMPPA under a normal plane-wave incidence are measured by the two-microphone transfer function method. The experimental setup is demonstrated in Figure 5.18. A sinusoidal signal is generated by the LabVIEW program, which is then converted by a digital-to-analog convertor (DAC, NI PCI-M10-16E-1), amplified by a power amplifier (B&K Lab Gruppen 300), and played by a loudspeaker. The cross-section of the duct is 100×100 mm^2, which can maintain the plane-wave condition under 1700 Hz. The acoustical signals inside the rectangular duct are collected by a pair of microphones (B&K type 4947), amplified by a conditioning amplifier (B&K Nexus 2693), and digitized by an analog-to-digital convertor (ADC, NI PCI-4452). The testing system is controlled by a LabVIEW program which has the advantages of excellent stability and real-time performance.

The FMPPs are fabricated of stainless steel through the etching technique. The profiles of the CMPP and ZMPP are then obtained by reshaping the FMPP on prepared molds which are made of 3D printing, as demonstrated in Figure 5.19. The parameters of the MPPAs applied in the experiment are illustrated in Table 5-3. The effective perforation ratios of all MPPs are 0.4/100.

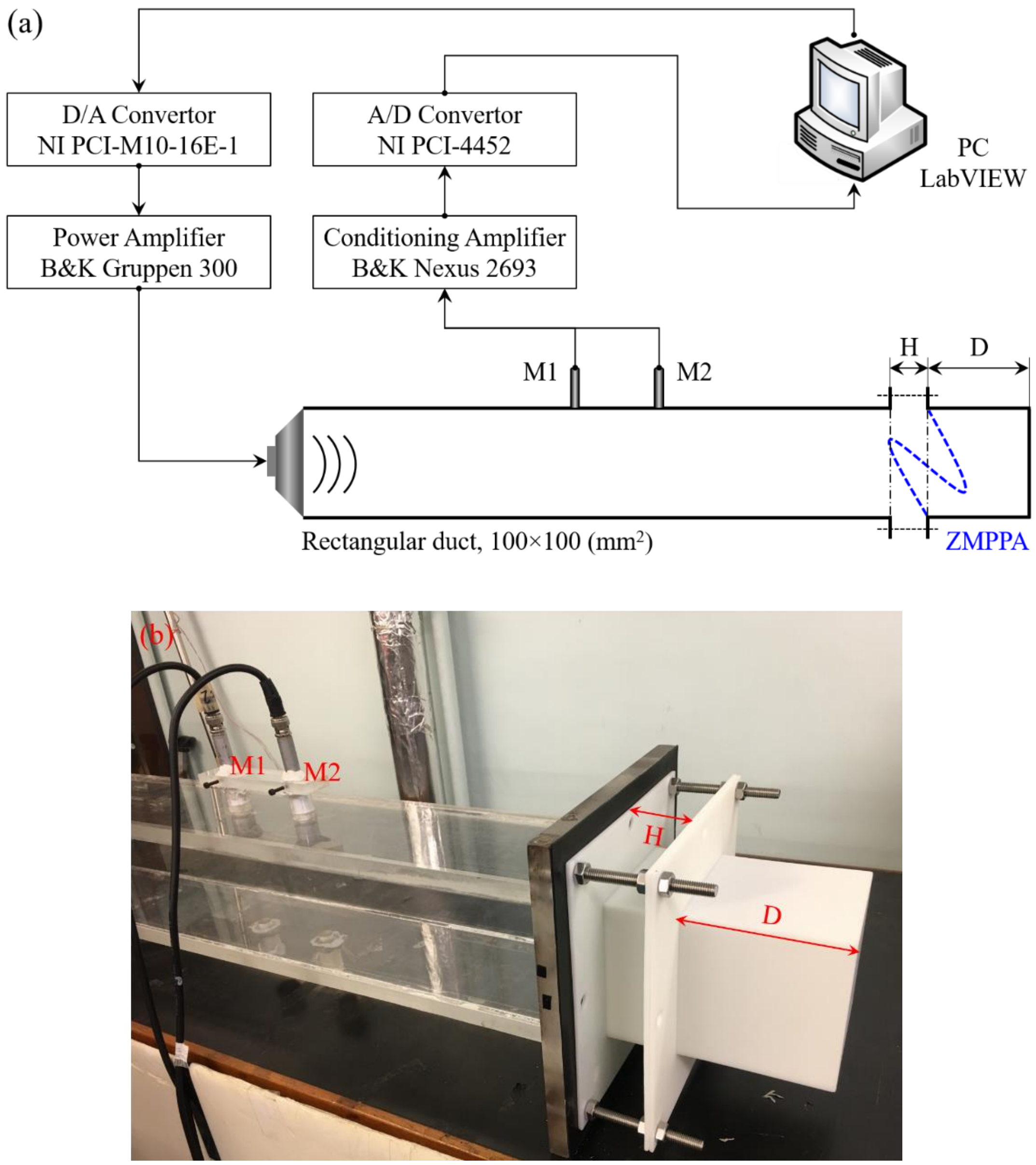

Figure 5.18 Experimental setup for the measurement of the normal sound absorption coefficients of MPPAs, (a) schematic diagram, (b) photography.

The normal sound absorption coefficients obtained by the numerical model and the experiment are compared in Figure 5.20. Good agreement can be observed in the targeted frequency range which validate the proposed numerical model. Above about

600 Hz, discrepancies can be found between the results. They result from the error of the testing system, manufacturing accuracy and the mounting precision.

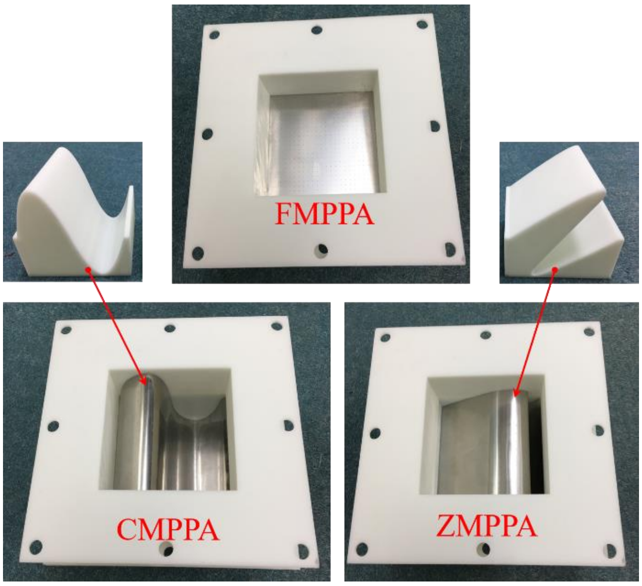

Figure 5.19 Photos of MPPAs and shaping molds of the CMPP and ZMPP.

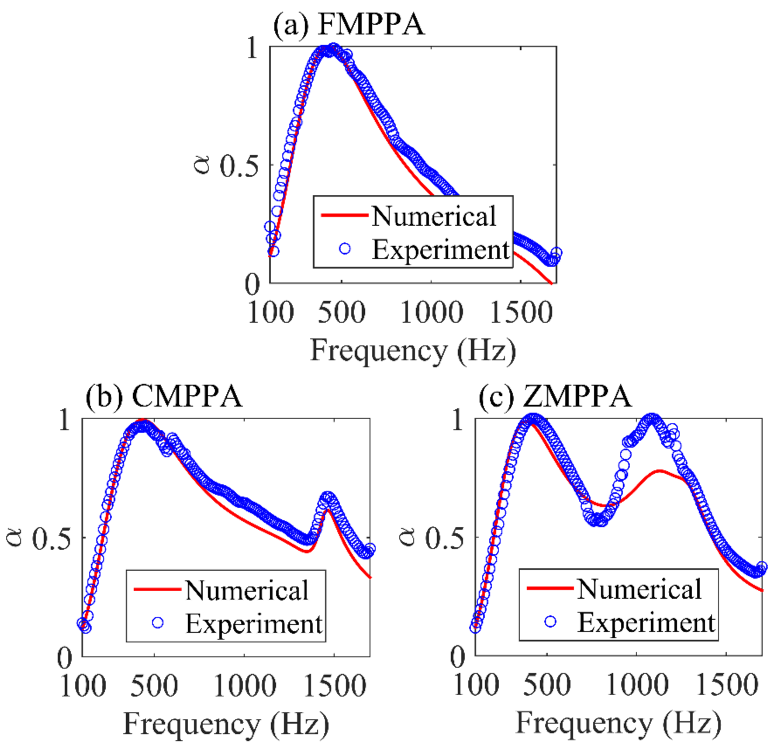

Figure 5.20 Normal sound absorption coefficients obtained by the numerical model and experiments. (a) FMPPA, (b) CMPPA, and (c) ZMPPA.

Table 5-3 Parameters of MPPAs used in the experiment.

MPPA parameters (mm)			Corrugation profile (mm)		
t_{MPP}	d_{MPP}	D	W	H	O
0.2	0.3	100	100	50	25

5.5.2 Quasi-2D experiment

The performance of the ZMPPA, CMPPA, and FMPPA in reducing the radiated noise from an unbaffled long enclosure is examined using quasi-2D experiments. A schematic diagram of the test rig is presented in Figure 5.21 (a).

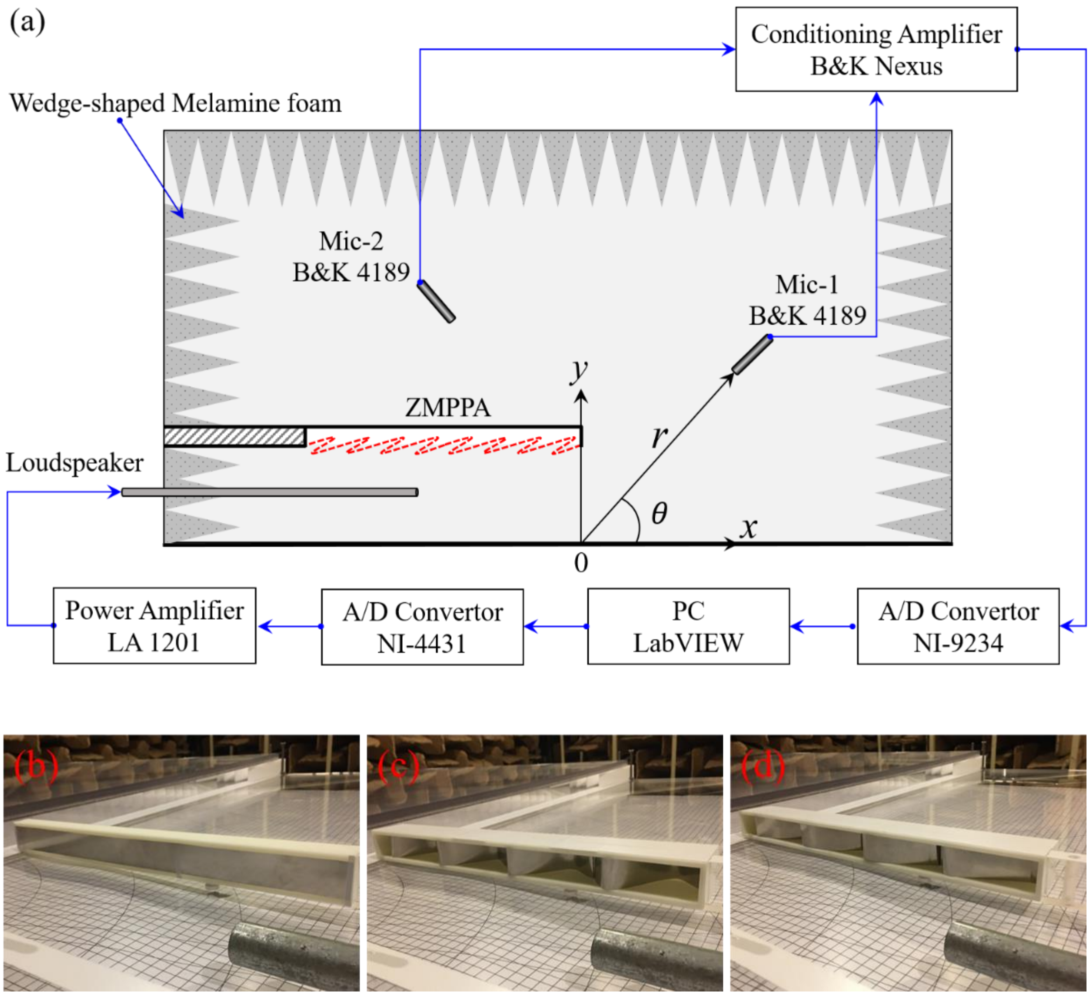

Figure 5.21 Experimental setups. (a) schematic diagram of the test rig, (b) a liner made of FMPPAs, (c) a liner made of CMPPAs, and (d) a liner made of ZMPPAs.

The photography of the test rig can be found in the previous chapters such as Figure 3.14 (b) and Figure 4.17 (b). Here, 3 types of liners are mounting on the inner wall of the long enclosure as presented from Figure 5.21 (b) to (d). Each liner is assembled by four FMPPAs, CMPPAs, and ZMPPAs, respectively. The cavity width and depth of each unit are 100 mm and 50 mm, respectively. The corrugation depth and offset distance are 25 mm and 40 mm, respectively. A comparison between the ILs obtained by liners made of FMPPAs, CMPPAs, and ZMPPAs is demonstrated in Figure 5.22. From 500 Hz to 1600 Hz, the ILs are stands at about 5 dB to 8 dB which results from the shallow cavities of the MPPAs. Besides, in the frequency range of 1200 Hz to 1700 Hz, the FMPPAs outperform the CMPPAs and ZMPPAs. The liner made of ZMPPAs starts to show its advantages in the frequency range between 1700 Hz and 2000 Hz, in which high ILs are achieved. In this frequency interval, the sound field inside the long enclosure become complex. More random incident sound can be absorbed by the ZMPPAs.

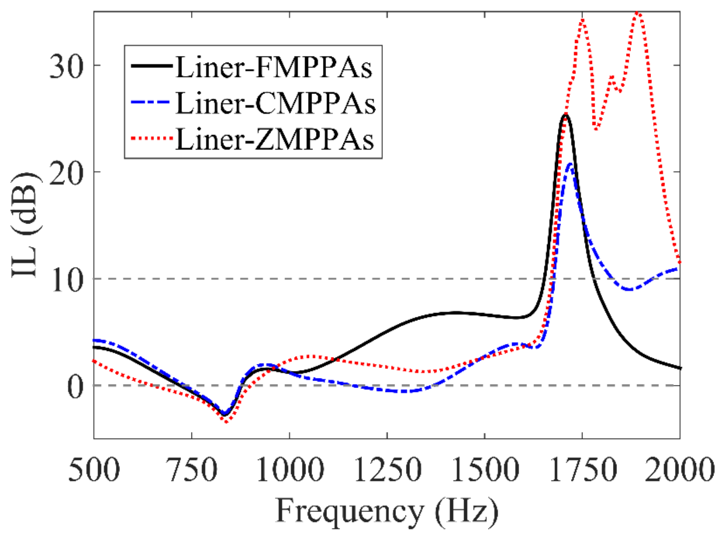

Figure 5.22 Comparison of Insertion losses obtained by liners made of (a) FMPPAs, (b) CMPPAs, and (c) ZMPPAs.

5.6 Summary

To evaluate the sound absorption performance of an MPPA in practical sound fields, a numerical model is established which can calculate the oblique and random sound absorption coefficients of MPPAs. For the purpose of proposing a broadband noise control device, the sound absorption performance of a ZMPPA is thoroughly investigated using the numerical scheme. Owning to the offset distance, the sound absorption curve of the ZMPPA shift to lower frequencies which is favorable for the reduction of low-frequency noise. In addition, the profile of the ZMPP also introduces the properties of double-layered MPPAs, in which extra sound absorption peaks can be observed in the middle to high frequency range which is promising for broadband diffuse sound attenuation. However, due to the protruding MPP profile, the corrugated MPPAs are not as compact as the FMPPA of the same cavity volume. Therefore, the sound absorption performance of the ZMPPA with the same high as the FMPPA is also investigated. It is demonstrated that the sound absorption curve shifts to higher frequencies owning to the volume sacrifice. However, the broadband performance of ZMPPAs in the middle to high frequency range still maintains which is superior to the CMPPA and suitable for broadband noise attenuation.

Besides, to attenuate the noise radiated from an unbaffled long enclosure with the ground, a liner consisting of an array of MPPAs is employed to absorb the multiple higher-order acoustical modes inside the long enclosure so that the radiated noised can be reduced. The obtained insertion losses show that the ZMPPA can attenuate the noise in a broad frequency range.

To validate the proposed numerical model and examine the sound absorption performance of the proposed ZMPPA, the normal sound absorption coefficients of the ZMPPA, CMPPA, and FMPPA are measured and compared. In addition, a quasi 2D experiment is conducted to explore the sound absorption performance of an array of ZMPPA in reducing the sound radiated from an unbaffled long enclosure with the ground. Satisfactory insertion loss is obtained.

CHAPTER 6

CONCLUSIONS AND RECOMMENDATIONS

6.1 Conclusions

The thesis focuses mainly on the modelling of unbaffled long enclosures for the prediction and reduction of sound radiated from pipework systems and sound-proof tunnels. The formation mechanisms of sound fields and the physics behind the sound radiation phenomenon are investigated. Besides, HRs and ZMPPAs are proposed to attenuate the noise radiated from long enclosures. In summary, the main conclusions are drawn as follows:

(1) To investigate the properties of sound radiated from a pipework system, a theoretical model is established combining the mode-matching method and the W-H technique. The formulation and implementation procedures of the proposed method are introduced which provides a theoretical foundation for sound radiation problems. In addition, the relationships between the radiated directivity patterns and the acoustical modes inside the long enclosure are explored. The theoretical model is proven to be an effective tool for the analysis of sound radiation phenomenon and the introduction of appropriate noise control strategies.

(2) Sound radiation from an unbaffled long enclosure with the ground effect is modeled and studied. Point source excitation, the ground, and the impedance boundary conditions are considered to simulate the sound-proof tunnels in

practice. Complex wavenumbers and modal functions are introduced which explains the dissipation of sound energy. The effects of impedance on each boundary are evaluated. The results indicate that the inner wall of the long enclosure is the best location for mounting noise control devices. A partial lining is then employed to reduce the radiated noise and good performance is obtained.

(3) Multiple sound peaks can be found inside and in the shadow zone of a rigid long enclosure. They resulted from the resonant modes along the transversal direction. HRs mounting on the enclosure wall are proposed to control the response coefficients of the resonant modes so that the SPLs around the peak frequencies are attenuated. A hybrid method is first put forward to deal with discrete noise control devices like HRs. The interaction between HRs and the acoustical field inside the long enclosure is investigated using the hybrid method. With the appropriate design, number, and location of HRs, the sound diffraction at the edge is reduced. Therefore, the radiated noise level in the shadow zone is attenuated.

(4) To achieve a broader bandwidth of the sound absorption curve, a Z-shaped micro-perforated panel absorber is proposed. A numerical scheme is applied to evaluate the acoustical properties of the ZMPPA. The sound absorption coefficient of the ZMPPA under an oblique plane-wave incidence is attained and compared with that of the FMPPA and CMPPA. The ZMPPA exhibits a promising sound absorption coefficient at low frequency and demonstrates a broadband sound absorption curve in the middle frequency range. An array of ZMPPA is then applied to attenuate the sound radiated from an unbaffled

long enclosure. Excellent insertion loss is obtained.

(5) To figure out the spectral characteristics of noise radiated from ventilation systems and traffic tunnels, indoor and outdoor experimental investigations are carried out. Besides, quasi-two-dimensional experiments are conducted to validate the theoretical models and examine the performance of proposed noised control devices in attenuating the sound radiated from unbaffled long enclosures.

6.2 Recommendations for future study

Theoretical, numerical, and experimental investigated are presented in the thesis to predict and suppress the sound radiated from unbaffled long enclosures. To enhance the understanding of the physics behind the sound radiation phenomena, improve the sound attenuation performance of HRs and ZMPPAs, and extend the proposed models to practical applications, several future studies are proposed as follows:

(1) 2D configurations of unbaffled long enclosures are adopted in the theoretical models. However, they cannot fully represent the pipework and traffic tunnels in practice, which are in 3D configurations. A prediction model for the sound radiated from a long enclosure in a 3D configuration is needed for practical applications.

(2) Monopole point sources are applied in this thesis to mimic the noise produced by vehicles. Whereas, there are various kinds of theoretical sound sources such as dipole source, line source, surface source, etc. The radiation characteristics of these sources need to be further investigated. Besides, the noise sources in

practice can be more complicated. The propagation, radiation, and dissipation of practical noise should be studied.

(3) HRs and ZMPPAs mounting on the enclosure wall are proposed to attenuate the radiated noise. Nevertheless, only the simplest configurations of them are applied in the thesis to reveal the physical aspect of the problem. Optimized configurations of HRs and ZMPPAs and other updated noise control devices can be adopted to attenuate the radiated noise.

(4) Passive noise control devices are employed to dissipate the sound energy so that the SPLs in the shadow zone can be reduced. The SPL distribution in the illuminated zone, however, is complex and irregular. In practice, the radiated noise towards the high-rise buildings also needs to be considered. Advanced meta-surfaces such as inhomogeneous impedance have the potential to change the radiation directivity so that the radiated noise towards a specific angle can be shifted or reduced.

APPENDIX-A

PROCEDURES TO SOLVE A WIENER-HOPF EQUATION

In general, the W-H equation can be obtained using the continuity relations of sound pressure at an imaginary interface. For a waveguide structure, the standard form of a W-H equation can be expressed as

$$\Phi^{+}(\alpha)\mathrm{K}(\alpha)=\mathrm{A}^{+}(\alpha)-\mathrm{B}^{-}(\alpha) \tag{A-1}$$

where $\Phi^{+}(\alpha)$ and $\mathrm{B}^{-}(\alpha)$ are unknowns, while $\mathrm{A}^{+}(\alpha)$ and $\mathrm{K}(\alpha)$ are functions in the complex α-plane. The first step to solve the W-H equation is to factorize the entire function into a product of two functions which are regular in the upper and lower half complex α- plane, respectively.

$$\mathrm{K}(\alpha)=\mathrm{K}^{+}(\alpha)\mathrm{K}^{-}(\alpha) \tag{A-2}$$

The factorization process can be accomplished using the method introduced by Mittra (1971). Since $\mathrm{K}^{-}(\alpha)$ is nonzero, we have the following identity:

$$\Phi^{+}(\alpha)\mathrm{K}^{+}(\alpha)=\frac{\mathrm{A}^{+}(\alpha)}{\mathrm{K}^{-}(\alpha)}-\frac{\mathrm{B}^{-}(\alpha)}{\mathrm{K}^{-}(\alpha)} \tag{A-3}$$

The term on the left-hand side of the equation $\Phi^{+}(\alpha)\mathrm{K}^{+}(\alpha)$ is regular in the upper half complex α-plane; $\mathrm{B}^{-}(\alpha)/\mathrm{K}^{-}(\alpha)$ is regular in the lower half complex α-plane; however, the characteristics of $\mathrm{A}^{+}(\alpha)/\mathrm{K}^{-}(\alpha)$ are not determined.

The next step is to decompose the term into a sum of two functions which are regular in the upper and lower half complex α-plane, respectively.

$$\frac{A^+(\alpha)}{K^-(\alpha)} = P^+(\alpha) + P^-(\alpha) \tag{A-4}$$

Combining Eqs. (A-3) and (A-4), we have the following identity:

$$\Phi^+(\alpha)K^+(\alpha) - P^+(\alpha) = P^-(\alpha) - \frac{B^-(\alpha)}{K^-(\alpha)} \tag{A-5}$$

Note that the terms on the left-hand side of Eq. (A-5) are regular in the upper half complex α-plane, and the terms on the right-hand side of the equation are regular in the lower half complex α-plane. These two half planes have a common overlapped region. By analytic continuation, both sides of the equation must equal to an entire function. Recall that an entire function is regular in the whole complex plane and it behaves algebraically at infinity. By an application of Liouville's theorem which state that a bounded entire function is a constant, it is uniquely determined to be identically zero.

$$\Phi^+(\alpha)K^+(\alpha) - P^+(\alpha) = 0, \quad P^-(\alpha) - \frac{B^-(\alpha)}{K^-(\alpha)} = 0 \tag{A-6}$$

So finally, the original W-H equation is divided into two, and the two unknowns can be obtained immediately.

APPENDIX-B

DERIVATION OF THE FAR-FIELD APPROXIMATION

In order to deal with problems of sound radiation from open structures using the W-H technique, the radiated sound pressure field is expressed in terms of the inverse Fourier transform as shown in Eq. (2.70). Except for a few special cases, however, the explicit expression of the integral cannot be obtained. Fortunately, the far-field result which is frequently applied in engineering applications, can be expressed in a simple form applying the saddle-point method. Taking the following equation for example

$$p_A(r,\theta) = -\frac{i}{2\pi}\int_{\Gamma_w} \dot{P}_A^+(-k\cos w, h)e^{-ikh\sin w}e^{krg(w)}dw \tag{B-1}$$

where Γ_w represents the integration path in the complex w-plane, and

$$g(w) = -i\cos(w+\theta) \tag{B-2}$$

The leading term of Eq. (B-1) can be attained using the exponentially decaying property of $e^{krg(w)}$ in the integrand of Eq. (B-1). In the far-field, the main contribution to the integration of Eq. (B-1) comes from a small segment near the saddle point. The following approximation can be used:

$$\dot{P}_A^+(-k\cos w, h)e^{-ik\sin wh} \approx \dot{P}_A^+(-k\cos\theta, h)e^{ik\sin\theta h}, w \in \Delta P_s \tag{B-3}$$

where ΔP_s denotes a small segment near the saddle point.

Also, $g(w)$ can be approximated by the first three terms of Taylor expansion as follows:

$$g(w) \approx g(w_s) + g'(w_s)(w-w_s) + g''(w_s)(w-w_s)^2 / 2$$
$$= -i + i(w+\theta)^2 / 2, w \in \Delta P_s \tag{B-4}$$

Substituting Eqs. (B-3) and (B-4) into Eq. (B-1) gives

$$p_A(r,\theta) = -\frac{i}{2\pi} \dot{P}_A^+(-k\cos\theta, h) e^{ikh\sin\theta} e^{-ikr} \int_{\Delta P_s} e^{(ikr/2)(w+\theta)^2} dw \tag{B-5}$$

Next, we introduce a change of variable $w' = w + \theta$, and note that the new path makes an angle of $3\pi/4$ with the real axis in the upper half of the complex w-plane, and $-\pi/4$ in the lower half of the complex w-plane. It follows that

$$w' = \begin{cases} |w'| e^{i\pi/4}, & w' \in \Delta P_s, \nu > 0 \\ |w'| e^{-3i\pi/4}, & w' \in \Delta P_s, \nu < 0 \end{cases} \tag{B-6}$$

And consequently, Eq. (B-5) becomes

$$\int_{\Delta P_s} e^{(ikr/2)(w+\theta)^2} dw = 2\int_0^{\Delta\Gamma} e^{(ikr/2)\left(|w'|e^{i\pi/4}\right)^2} d\left(|w'|e^{i\pi/4}\right)$$
$$= 2e^{i\pi/4} \int_0^{\Delta\Gamma} e^{(-kr/2)(|w'|)^2} d(|w'|) \tag{B-7}$$

where $\Delta\Gamma$ is the distance between the saddle point to either end of ΔP_s. Therefore, it is a small number. Making full use of the error function

$$\int_0^{T} e^{(-1/2)kr|w'|^2} d(|w'|) = \sqrt{\frac{\pi}{2kr}} \operatorname{erf}\left(\sqrt{\frac{kr}{2}} T\right)$$
$$\approx \sqrt{\frac{\pi}{2kr}}, \; kr \to \infty \tag{B-8}$$

So finally, combining Eqs. (B-5) to Eq. (8), we have

$$p_A(r,\theta) = \frac{i}{\sqrt{2\pi kr}} \dot{P}_A^+(-k\cos\theta, h) e^{\frac{i\pi}{4}} e^{ik\sin\theta h} e^{-ikr} \operatorname{erf}\left(\sqrt{\frac{kr}{2}} \Delta\Gamma\right) \tag{B-9}$$

REFERENCES

Abom, M., & Allam, S. (2013). Dissipative silencers based on micro-perforated plates (No. 2013-24-0071). SAE Technical Paper.

Allam, S., & Abom, M. (2011). A new type of muffler based on microperforated tubes. Journal of vibration and acoustics, 133(3).

Asdrubali, F., & Pispola, G. (2007). Properties of transparent sound-absorbing panels for use in noise barriers. The Journal of the Acoustical Society of America, 121(1), 214-221.

Attenborough, K. (1985). Acoustical impedance models for outdoor ground surfaces. Journal of Sound and Vibration, 99(4), 521-544.

Ayub, M., Khan, T. A., & Jilani, K. (2016). Effect of cold plasma permittivity on the radiation of the dominant TEM-wave by an impedance loaded parallel-plate wave guide radiator. Mathematical Methods in the Applied Sciences, 39(1), 134-143.

Bauer, A. B. (1977). Impedance theory and measurements on porous acoustic liners. Journal of Aircraft, 14(8), 720-728.

Birbir, F., & Buyukaksoy, A. (2000). Radiation from an impedance loaded parallel-plate waveguide. Turkish journal of electrical engineering & computer sciences, 8(2), 81-91.

Brambley, E. J. (2011). Well-posed boundary condition for acoustic liners in straight ducts with flow. AIAA journal, 49(6), 1272-1282.

Bravo, T., Maury, C., & Pinhede, C. (2012a). Sound absorption and transmission through flexible micro-perforated panels backed by an air layer and a thin plate. The Journal of the Acoustical Society of America, 131(5), 3853-3863.

Bravo, T., Maury, C., & Pinhede, C. (2012b). Vibroacoustic properties of thin micro-perforated panel absorbers. The Journal of the Acoustical Society of America, 132(2), 789-798.

Bravo, T., Maury, C., & Pinhede, C. (2017). Absorption and transmission of boundary layer noise through flexible multi-layer micro-perforated structures. Journal of Sound and Vibration, 395, 201-223.

Bucciarelli, F., Fierro, G. M., & Meo, M. (2019). A multilayer microperforated panel prototype for broadband sound absorption at low frequencies. Applied Acoustics, 146, 134-144.

Buyukaksoy, A., & Birbir, F. (1998). Analysis of an Impedance Loaded Parallel-Plate Waveguide Radiator. Journal of electromagnetic waves and applications, 12(11), 1509-1525.

Buyukaksoy, A., & Cinar, G. (2005). Solution of a matrix Wiener-Hopf equation connected with the plane wave diffraction by an impedance loaded parallel plate waveguide. Mathematical Methods in the applied Sciences, 28(14), 1633-1645.

Cai, C., & Mak, C. M. (2018). Acoustic performance of different Helmholtz resonator array configurations. Applied Acoustics, 130, 204-209.

Can, A., Leclercq, L., Lelong, J., & Botteldooren, D. (2010). Traffic noise spectrum analysis: Dynamic modeling vs. experimental observations. Applied Acoustics, 71(8), 764-770.

Chang, D., Lu, F., Jin, W., & Liu, B. (2018). Low-frequency sound absorptive properties of double-layer perforated plate under grazing flow. Applied Acoustics, 130, 115-123.

Chapman, C. J. (1994). Sound radiation from a cylindrical duct. Part 1. Ray structure of the duct modes and of the external field. Journal of Fluid Mechanics, 281, 293-311.

Chen, K. T., Chen, Y. H., Lin, K. Y., & Weng, C. C. (1998). The improvement on the transmission loss of a duct by adding Helmholtz resonators. Applied Acoustics, 54(1), 71-82.

Crombie, D. H., & Hothersall, D. C. (1994). The performance of multiple noise barriers. Journal of sound and vibration, 176(4), 459-473.

Demir, A., & Buyukaksoy, A. (2005). Wiener-Hopf approach for predicting the transmission loss of a circular silencer with a locally reacting lining. International journal of engineering science, 43(5-6), 398-416.

Demir, A., & Rienstra, S. (2006). Sound Radiation from an Annular Duct with Jet Flow and a Lined Center Body. In 12th AIAA/CEAS Aeroacoustics Conference (27th AIAA Aeroacoustics Conference) (p. 2718).

Demir, A., & Rienstra, S. (2010). Sound radiation from a lined exhaust duct with lined afterbody. In 16th AIAA/CEAS aeroacoustics conference (p. 3947).

Doak, P. E. (1973). Excitation, transmission and radiation of sound from source distributions in hard-walled ducts of finite length (I): The effects of duct cross-section geometry and source distribution space-time pattern. Journal of Sound and Vibration, 31(1), 1-72.

Duan, W., & Kirby, R. (2012). A hybrid finite element approach to modeling sound radiation from circular and rectangular ducts. The Journal of the Acoustical Society of America, 131(5), 3638-3649.

Dupont, T., Pavic, G., & Laulagnet, B. (2003). Acoustic properties of lightweight micro-perforated plate systems. Acta Acustica united with Acustica, 89(2), 201-212.

Eldredge, J. D. (2004). On the interaction of higher duct modes with a perforated liner system with bias flow. Journal of Fluid Mechanics, 510, 303-331.

Fang, Y., Zhang, X., Zhou, J., Guo, J., & Huang, X. (2019). Acoustic meta-porous layer with composite structures for perfect and quasi-omnidirectional sound absorption. Composite Structures, 223, 110948.

Fei, M., & Xing, Z. Y. (2013). Highway Tunnel Acoustic Environment Simulation Calculation. Electronic Journal of Geotechnical Engineering, 18.

Felix, S., Doc, J. B., & Boucher, M. A. (2018). Modeling of the multimodal radiation from an open-ended waveguide. The Journal of the Acoustical Society of America, 143(6), 3520-3528.

Fuchs, H. V., & Zha, X. (2006). Micro-perforated structures as sound absorbers-a review and outlook. Acta acustica united with acustica, 92(1), 139-146.

Gabard, G., & Astley, R. J. (2006). Theoretical model for sound radiation from annular jet pipes: far-and near-field solutions. Journal of Fluid Mechanics, 549, 315-341.

Gai, X. L., Xing, T., Li, X. H., Zhang, B., Wang, F., Cai, Z. N., & Han, Y. (2017). Sound absorption of microperforated panel with L shape division cavity structure. Applied Acoustics, 122, 41-50.

Goyder, H. G. D. (2011, January). Modelling Acoustic Sources in Pipework. In Pressure Vessels and Piping Conference (Vol. 44540, pp. 297-307).

Guo, J., Zhang, X., Fang, Y., & Fattah, R. (2018). Reflected wave manipulation by inhomogeneous impedance via varying-depth acoustic liners. Journal of Applied Physics, 123(17), 174902.

Hames, Y. (2011). Investigation of Thickness Effects on the TM-Wave Radiation from a Thick Impedance-Loaded Parallel-Plate Radiator. Electromagnetics, 31(6), 429-447.

Hein, S., Hohage, T., & Koch, W. (2004). On resonances in open systems. Journal of Fluid Mechanics, 506, 255.

Herrin, D., Liu, J., & Seybert, A. (2011). Properties and applications of microperforated panels. Sound & vibration, 45(7), 6-9.

Heutschi, K., & Bayer, R. (2006). Sound radiation from railway tunnel openings. Acta acustica united with acustica, 92 (4), 567-573.

Hocter, S. T. (1999). Exact and approximate directivity patterns of the sound radiated from a cylindrical duct. Journal of Sound and Vibration, 227(2), 397-407.

Hocter, S. T. (2000). Sound radiated from a cylindrical duct with Keller's geometrical theory. Journal of sound and vibration, 231(5), 1243-1256.

Homicz, G. F., & Lordi, J. A. (1975). A note on the radiative directivity patterns of duct acoustic modes. Journal of Sound and Vibration, 41(3), 283-290.

Huang, L. H., Chen, G. R., & Hwang, W. S. (2001). Sound propagation near tunnel outlets. Journal of the Chinese Institute of Engineers, 24(3), 321-328.

Ishizuka, T., & Fujiwara, K. (2004). Performance of noise barriers with various edge shapes and acoustical conditions. Applied Acoustics, 65(2), 125-141.

Iu, K. K., & Li, K. M. (2002). The propagation of sound in narrow street canyons. The Journal of the Acoustical Society of America, 112(2), 537-550.

Ji, G., Fang, Y., & Zhou, J. (2020). Porous acoustic metamaterials in an inverted wedge shape. Extreme Mechanics Letters, 36, 100648.

Jing, X., Wang, X., & Sun, X. (2007). Broadband acoustic liner based on the mechanism of multiple cavity resonance. AIAA journal, 45(10), 2429-2437.

Jiang, C., Zhang, S., & Huang, L. (2016). On the acoustic wedge design and simulation of anechoic chamber. Journal of Sound and Vibration, 381, 139-155.

Jones, M., Watson, W., & Parrott, T. (2005, January). Benchmark data for evaluation of aeroacoustics propagation codes with grazing flow. In 11th AIAA/CEAS Aeroacoustics Conference (p. 2853).

Kang, J. (1996a). Acoustics in long enclosures with multiple sources. The Journal of the Acoustical Society of America, 99(2), 985-989.

Kang, J. (1996b). Reverberation in rectangular long enclosures with geometrically reflecting boundaries. Acta Acustica united with Acustica, 82(3), 509-516.

Kang, J. (1996c). Sound attenuation in long enclosures. Building and environment, 31(3), 245-253.

Kang, J. (1997). A method for predicting acoustic indices in long enclosures. Applied Acoustics, 51(2), 169-180.

Kang, J. (1998). Scale modelling for improving the speech intelligibility from multiple loudspeakers in long enclosures by architectural acoustic treatments. Acta Acustica united with Acustica, 84(4), 689-700.

Kang, J. (2002). Reverberation in rectangular long enclosures with diffusely reflecting boundaries. Acta Acustica United with Acustica, 88(1), 77-87.

Kang, J., & Brocklesby, M. W. (2005). Feasibility of applying micro-perforated absorbers in acoustic window systems. Applied Acoustics, 66(6), 669-689.

Keller, J. B. (1962). Geometrical theory of diffraction. Josa, 52(2), 116-130.

Khan, T. A., Ayub, M., & Jilani, K. (2014). E-polarized plane wave diffraction by an impedance loaded parallel-plate waveguide located in cold plasma. Physica Scripta, 89(9), 095207.

Kirby, R. (2008). Modeling sound propagation in acoustic waveguides using a hybrid numerical method. The Journal of the Acoustical Society of America, 124(4), 1930-1940.

Law, M. K., Li, K. M., & Leung, C. W. (2008). Noise reduction in tunnels by hard rough surfaces. The Journal of the Acoustical Society of America, 124(2), 961-972.

Lee, D. H., & Kwon, Y. P. (2004). Estimation of the absorption performance of multiple layer perforated panel systems by transfer matrix method. Journal of sound and vibration, 278(4-5), 847-860.

Lee, Y. Y., Lee, E. W. M., & Ng, C. F. (2005). Sound absorption of a finite flexible micro-perforated panel backed by an air cavity. Journal of Sound and Vibration, 287(1-2), 227-243.

Lemire, G., & Nicolas, J. (1989). Aerial propagation of spherical sound waves in bounded spaces. The Journal of the Acoustical Society of America, 86(5), 1845-1853.

Levine, H., & Schwinger, J. (1948). On the radiation of sound from an un-flanged circular pipe. Physical review, 73(4), 383.

Li, D., Chang, D., & Liu, B. (2016). Enhancing the low frequency sound absorption of a perforated panel by parallel-arranged extended tubes. Applied Acoustics, 102, 126-132.

Li, D., Cheng, L., Yu, G. H., & Vipperman, J. S. (2007). Noise control in enclosures: Modeling and experiments with T-shaped acoustic resonators. the Journal of the Acoustical Society of America, 122(5), 2615-2625.

Li, D., & Cheng, L. (2007). Acoustically coupled model of an enclosure and a Helmholtz resonator array. Journal of sound and vibration, 305(1-2), 272-288.

Li, G., & Mechefske, C. K. (2010). A comprehensive experimental study of micro-perforated panel acoustic absorbers in MRI scanners. Magnetic Resonance Materials in Physics, Biology and Medicine, 23(3), 177-185.

Li, K. M., & Iu, K. K. (2002). The propagation of sound in tunnels. The Journal of the Acoustical Society of America, 112(5), 2437-2437.

Li, K. M., & Iu, K. K. (2004). Propagation of sound in long enclosures. The Journal of the Acoustical Society of America, 116(5), 2759-2770.

Li, K. M., & Iu, K. K. (2005). Full-scale measurements for noise transmission in tunnels. The Journal of the Acoustical Society of America, 117(3), 1138-1145.

Li, K. M., Kwok, M. P., & Law, M. K. (2008). A ray model for hard parallel noise barriers in high-rise cities. The Journal of the Acoustical Society of America, 123(1), 121-132.

Li, K. M., Law, M. K., & Kwok, M. P. (2008). Absorbent parallel noise barriers in urban environments. Journal of sound and vibration, 315(1-2), 239-257.

Liu, J., & Herrin, D. W. (2010). Enhancing micro-perforated panel attenuation by partitioning the adjoining cavity. Applied Acoustics, 71(2), 120-127.

Liu, Y., Zhang, Y., Chen, K., & Ma, X. (2020). Oblique incidence sound absorption of a hybrid structure using a micro-perforated panel and a planar actuator. Applied Physics Express, 13(5), 057001.

Lordi, J., Homicz, G., & Rehm, R. (1974). Effects of finite duct length and blade chord on noise generation by a rotating blade row. In 7th Fluid and Plasma Dynamics Conference (p. 555).

Maa, D. Y. (1987). Microperforated-panel wideband absorbers. Noise control engineering journal, 29(3), 77-84.

Maa, D. Y. (1998). Potential of microperforated panel absorber. the Journal of the Acoustical Society of America, 104(5), 2861-2866.

Maekawa, Z. (1968). Noise reduction by screens. Applied acoustics, 1(3), 157-173.

Maxit, L., Yang, C., Cheng, L., & Guyader, J. L. (2012). Modeling of micro-perforated panels in a complex vibro-acoustic environment using patch transfer function approach. The Journal of the Acoustical Society of America, 131(3), 2118-2130.

McAlpine, A., Daymond-King, A. P., & Kempton, A. J. (2012). Sound radiation from a flanged inclined duct. The Journal of the Acoustical Society of America, 132(6), 3637-3646.

Min, H., Chen, W., & Qiu, X. (2011). Single frequency sound propagation in flat waveguides with locally reactive impedance boundaries. The Journal of the Acoustical Society of America, 130(2), 772-782.

Min, H., Chen, Y., & Qiu, X. (2014, October). A coherent image source method for sound prediction in long spaces with a sound absorbent ceiling. In INTER-NOISE and NOISE-CON Congress and Conference Proceedings (Vol. 249, No. 2, pp. 4994-5002). Institute of Noise Control Engineering.

Mittra, R. (1971). Analytical techniques in the theory of guided waves. Macmillan Series in Electrical Science.

Mosa, A. I., Putra, A., Ramlan, R., Prasetiyo, I., & Esraa, A. A. (2019). Theoretical model of absorption coefficient of an inhomogeneous MPP absorber with multi-cavity depths. Applied Acoustics, 146, 409-419.

Mosa, A. I., Putra, A., Ramlan, R., & Esraa, A. A. (2020). Wideband sound absorption of a double-layer microperforated panel with inhomogeneous perforation. Applied Acoustics, 161, 107167.

Olafsen, S. (1996). Noise from road tunnel openings: An engineering approach. In Inter-Noise 96.

Ortiz, S., Le Plenier, C., & Cobo, P. (2013). Efficient modeling and experimental validation of acoustic resonances in three-dimensional rectangular open cavities. Applied acoustics, 74(7), 949-957.

Ortiz, S., González, L. M., Díaz, C. G., Svensson, U. P., & Cobo, P. (2016). Acoustic resonances in a 3D open cavity with non-parallel walls. Journal of Sound and Vibration, 363, 181-198.

Pamies, T., Romeu, J., Genesca, M., & Balastegui, A. (2011). Sound radiation from an aperture in a rectangular enclosure under low modal conditions. The Journal of the Acoustical Society of America, 130(1), 239-248.

Park, S. H. (2013). Acoustic properties of micro-perforated panel absorbers backed by Helmholtz resonators for the improvement of low-frequency sound absorption. Journal of Sound and Vibration, 332(20), 4895-4911.

Peake, N., & Abrahams, I. D. (2020). Sound radiation from a semi-infinite lined duct. Wave Motion, 92, 102407.

Pierce, A. D., & Acoustics, A. (1981). Introduction to its Physical Principles and Applications. Acoustical Society of America and American Institute of Physics, 122.

Polat, B. (1998). Plane wave diffraction by a semi-infinite soft/hard parallel-plate waveguide. Canadian journal of physics, 76(10), 771.

Prasetiyo, I., Sarwono, J., & Sihar, I. (2016). Study on inhomogeneous perforation thick micro-perforated panel sound absorbers. Journal of Mechanical Engineering and Sciences (JMES), 10(3), 2350-2362.

Qian, Y. J., Zhang, J., Sun, N., Kong, D. Y., & Zhang, X. X. (2017). Pilot study on wideband sound absorber obtained by adopting a serial-parallel coupling manner. Applied Acoustics, 124, 48-51.

Rawlins, A. D. (1978). Radiation of sound from an unflanged rigid cylindrical duct with an acoustically absorbing internal surface. Proceedings of the Royal Society of London. A. Mathematical and Physical Sciences, 361(1704), 65-91.

Redmore, T. L. (1982). A theoretical analysis and experimental study of the behavior of sound in corridors. Applied Acoustics, 15(3), 161-170.

Sakagami, K., Yairi, M., & Morimoto, M. (2010). Multiple-leaf sound absorbers with microperforated panels: an overview. Acoustics Australia, 38(2), 76-81.

Sakamoto, S. (2015). Road traffic noise prediction model “ASJ RTN-Model 2013”: Report of the Research Committee on Road Traffic Noise. Acoustical Science and Technology, 36(2), 49-108.

Sakamoto, S., Matsumoto, T., & Funahashi, O. (2020). Validation of calculation method of tunnel portal noise in ASJ RTN-Model 2018 by a field experiment. Acoustical Science and Technology, 41(3), 614-621.

Sasaki, M. (1984). Discussion on the prediction method of traffic noise in the vicinity of road interchange. The Journal of the Acoustical Society of Japan, 40(9), 638-642.

Seo, S. H., & Kim, Y. H. (2005). Silencer design by using array resonators for low-frequency band noise reduction. The Journal of the Acoustical Society of America, 118(4), 2332-2338.

Shimokura, R., & Soeta, Y. (2011). Characteristics of train noise in above-ground and underground stations with side and island platforms. Journal of Sound and Vibration, 330(8), 1621-1633.

Seo, S. H., & Kim, Y. H. (2005). Silencer design by using array resonators for low-frequency band noise reduction. The Journal of the Acoustical Society of America, 118(4), 2332-2338.

Tachibana, H., Sakamoto, S., & Nakai, A. (1999). Scale model experiment on sound radiation from a tunnel mouth. In proceedings of inter-noise 99.

Takahashi, D., & Tanaka, M. (2002). Flexural vibration of perforated plated and porous elastic materials under acoustic loading. The Journal of the Acoustical Society of America, 112(4), 1456-1464.

Tam, C. K., Kurbatskii, K. A., Ahuja, K. K., & Gaeta Jr, R. J. (2001). A numerical and experimental investigation of the dissipation mechanisms of resonant acoustic liners. Journal of Sound and Vibration, 245(3), 545-557.

Tiryakioglu, B. (2019). Sound radiation from the perforated end of a lined duct. Acta Acustica united with Acustica, 105(4), 591-599.

Tong, Y., Kou, Y., & Pan, J. (2017). Forced acoustical response of a cavity coupled with a semi-infinite space using coupled mode theory. Wave Motion, 73, 11-23.

Wang, C., Cheng, L., Pan, J., & Yu, G. (2010). Sound absorption of a micro-perforated panel backed by an irregular-shaped cavity. The Journal of the Acoustical Society of America, 127(1), 238-246.

Wang, C., & Huang, L. (2011). On the acoustic properties of parallel arrangement of multiple micro-perforated panel absorbers with different cavity depths. The Journal of the Acoustical Society of America, 130(1), 208-218.

Wang, C., Huang, L., & Zhang, Y. (2014). Oblique incidence sound absorption of parallel arrangement of multiple micro-perforated panel absorbers in a periodic pattern. Journal of Sound and Vibration, 333(25), 6828-6842.

Wang, C., & Liu, X. (2020). Investigation of the acoustic properties of corrugated micro-perforated panel backed by a rigid wall. Mechanical Systems and Signal Processing, 140, 106699.

Wang, S., Tao, J., & Qiu, X. (2015). Performance of a planar virtual sound barrier at the baffled opening of a rectangular cavity. The Journal of the Acoustical Society of America, 138(5), 2836-2847.

Wang, S., Tao, J., & Qiu, X. (2017). Controlling sound radiation through an opening with secondary loudspeakers along its boundaries. Scientific reports, 7(1), 1-6.

Wang, S., Tao, J., Qiu, X., & Pan, J. (2018). Mechanisms of active control of sound radiation from an opening with boundary installed secondary sources. The Journal of the Acoustical Society of America, 143(6), 3345-3351.

Wang, X., Mao, D., Yu, W., & Jiang, Z. (2015). Sound barriers from materials of inhomogeneous impedance. The Journal of the Acoustical Society of America, 137(6), 3190-3197.

Wang, X. N., Choy, Y. S., & Cheng, L. (2012). Hybrid noise control in a duct using a light micro-perforated plate. The Journal of the Acoustical Society of America, 132(6), 3778-3787.

Wang, X., Wang, X., Yu, W., Jiang, Z., & Mao, D. (2016). A theoretical model of barriers having inhomogeneous impedance surfaces. The Journal of the Acoustical Society of America, 139(3), EL63-EL69.

Wang, X., Yu, W., Zhu, X., Jiang, Z., & Mao, D. (2017). Effects of ceiling phase gradients on the acoustic environment on roadside balconies. The Journal of the Acoustical Society of America, 141(2), EL146-EL152.

Wang, Z., & Choy, Y. (2019a). Acoustical coupling and radiation control of open cavity using an array of Helmholtz resonators. Mechanical Systems and Signal Processing, 130, 632-648.

Wang, Z. B., & Choy, Y. S. (2019b). Tunable parallel barriers using Helmholtz resonator. Journal of Sound and Vibration, 443, 109-123.

Wang, Z., Choy, Y. S., & Wang, C. (2020). Vibro-acoustic analysis of parallel barriers integrated with flexible panels. Journal of Sound and Vibration, 489, 115653.

Woehner, H. (1992). Sound propagation at tunnel openings. Noise control engineering journal, 39(2), 47-56.

Wu, M. Q. (1997). Micro-perforated panels for duct silencing. Noise Control Engineering Journal, 45(2), 69-77.

Xiao, Y., Lai, H., Li, Q., Wang, X., & Wang, X. (2020). Improved interference-type sound barriers: Use of hyperbolic phase modulation. Applied Acoustics, 161, 107186.

Yairi, M., Sakagami, K., Takebayashi, K., & Morimoto, M. (2011). Excess sound absorption at normal incidence by two microperforated panel absorbers with different impedance. Acoustical Science and Technology, 32(5), 194-200.

Yamamoto, K., & Takagi, K. (1992). Expressions of Maekawa's chart for computation. Applied Acoustics, 37(1), 75-82.

Yang, C., & Cheng, L. (2016). Sound absorption of microperforated panels inside compact acoustic enclosures. Journal of sound and vibration, 360, 140-155.

Yang, C., Cheng, L., & Pan, J. (2013). Absorption of oblique incidence sound by a finite micro-perforated panel absorber. The Journal of the Acoustical Society of America, 133(1), 201-209.

Yang, C., Fang, Y., Zhao, C., & Zhang, X. (2018). On modeling the sound propagation through a lined duct with a modified Ingard-Myers boundary condition. Journal of Sound and Vibration, 424, 173-191.

Yang, C., Pan, J., & Cheng, L. (2013). A mechanism study of sound wave-trapping barriers. The Journal of the Acoustical Society of America, 134(3), 1960-1969.

Yang, L., & Shield, B. M. (2001). The prediction of speech intelligibility in underground stations of rectangular cross section. The Journal of the Acoustical Society of America, 109(1), 266-273.

Yang, W., Wang, Z., & Choy, Y. (2021). Prediction of sound radiation from an unbaffled long enclosure with the ground. Mechanical Systems and Signal Processing, 149, 107232.

Yu, G., Li, D., & Cheng, L. (2008). Effect of internal resistance of a Helmholtz resonator on acoustic energy reduction in enclosures. The Journal of the Acoustical Society of America, 124(6), 3534-3543.

Yu, G., & Cheng, L. (2009). Location optimization of a long T-shaped acoustic resonator array in noise control of enclosures. Journal of sound and vibration, 328(1-2), 42-56.

Zhou, D., Wang, X., Jing, X., & Sun, X. (2016). Acoustic properties of multiple cavity resonance liner for absorbing higher-order duct modes. The Journal of the Acoustical Society of America, 140(2), 1251-1267.